

The MODEST catalog of depth-dependent spatially coupled inversions of sunspots observed by Hinode/SOT-SP

J. S. Castellanos Durán^{1,2*}, N. Milanovic¹, A. Korpi-Lagg^{1,3}, B. Löptien¹, M. van Noort¹, and S. K. Solanki^{1,4}

¹ Max Planck Institute for Solar System Research, Justus-von-Liebig-Weg 3, D-37077, Göttingen, Germany

² Georg-August-Universität Göttingen, Friedrich-Hund-Platz 1, D-37077, Göttingen, Germany

³ Department of Computer Science, Aalto University, PO Box 15400, FI-00076 Aalto, Finland

⁴ School of Space Research, Kyung Hee University, Yongin, 446-101, Gyeonggi, Republic of Korea

Submitted: January 19, 2024; accepted: February 22, 2024

ABSTRACT

We present a catalog that we named MODEST containing depth-dependent information on the atmospheric conditions inside sunspot groups of all types. The catalog is currently composed of 942 observations of 117 individual active regions with sunspots that cover all types of features observed in the solar photosphere. We use the SPINOR-2D code to perform spatially coupled inversions of the Stokes profiles observed by Hinode/SOT-SP at high spatial resolution. SPINOR-2D accounts for the unavoidable degradation of the spatial information due to the point spread function of the telescope. The sunspot sample focuses on complex sunspot groups, but simple sunspots are also part of the catalog for completeness. Sunspots were observed from 2006 to 2019, covering parts of solar cycles 23 and 24. The catalog is a living resource, as with time, more sunspot groups will be included.

Key words. Sunspots; Sun: photosphere; Sun: magnetic fields

1. Introduction

Sunspots are magnetic structures that are comparatively cool and hence dark in continuum images with respect to their surroundings and form the hearts of active regions (for a review see e.g., Solanki 2003; Borrero & Ichimoto 2011). They play a central role in and are often used as tracers of solar magnetic activity. Although sunspots have been studied for over four centuries, many of their properties are still not well known or understood. In an effort to change this, we provide a new catalog of high resolution maps of physical parameters within the sunspots and in their surroundings.

The thermal, magnetic field and dynamic properties of magnetic features in the lower solar atmosphere, such as sunspots, pores, plage regions, etc., are encoded in the intensity and polarization properties of the solar spectrum. The polarization state of sunlight is fully described by the Stokes profiles, where the intensity of the light is represented by Stokes $I(\lambda)$, the linear polarization by Stokes $Q(\lambda)$ and $U(\lambda)$, and the circular polarization by Stokes $V(\lambda)$.

It is necessary to solve an *inverse problem* to retrieve the conditions in the solar atmosphere from the measured Stokes parameters (see del Toro Iniesta & Ruiz Cobo 2016, for a review). These so-called inversions use as input the atomic data relevant to the transitions underlying the spectral lines in the solar spectrum. In a first step, a model of the solar atmosphere is formulated. The complexity of this model varies, depending on the type of available observations and the level of detail of the involved physical processes. Then the radiative transfer equation of polarized light is solved to produce synthetic Stokes profiles that are compared with the observations. The model is iteratively modified until the synthetic Stokes profiles match the

observations. The χ^2 -merit function is usually used as a quantitative measure of the quality of the fit.

The atmospheric conditions retrieved from an inversion depend on the simplifications entering into the atmospheric model underlying the inversions. The atmosphere recovered for a given model does not have to resemble the true stratification of the solar atmosphere at the analyzed location. Inversions are usually done by integrating the radiative transfer equation numerically and the propagation of numerical errors is intrinsic. Different physical parameters might leave very similar imprints in the observable (the polarization state and intensity of light), which can lead to ambiguities. It is customary to use the merit function χ^2 as a metric of how well the atmospheric model resembles the observations. However, there is no guarantee that the χ^2 -hypersurface has a single minimum so that the final result can in some ill-posed cases depend on the initial guess. Taken together, the above points make inversions a fine art, requiring experience and thorough interpretation of the obtained results.

The plane-parallel Milne-Eddington (ME) approximation is the simplest atmospheric model. Inversion codes that apply this approximation are extremely useful when quick inversions are needed (e.g., Borrero et al. 2011). This model is commonly used because a ME-type atmosphere has an analytical solution (Unno 1956; Rachkovsky 1962, 1967). As a result, inversion codes that rely on ME-type atmospheres can be almost straightforwardly turned into pipelines to retrieve information on some atmospheric properties at the average height of formation of the spectral lines. Milne-Eddington inversions can also be used to infer chromospheric magnetic fields and line-of-sight velocities for the He I triplet at 10830 Å as these form in a thin layer (e.g., Rüedi et al. 1995; Lagg et al. 2004, 2009; Sowmya et al. 2022). Milne-Eddington inversions are a fast and convenient tool to find the *average* atmospheric parameters over the height range where

* e-mail: castellanos@mps.mpg.de

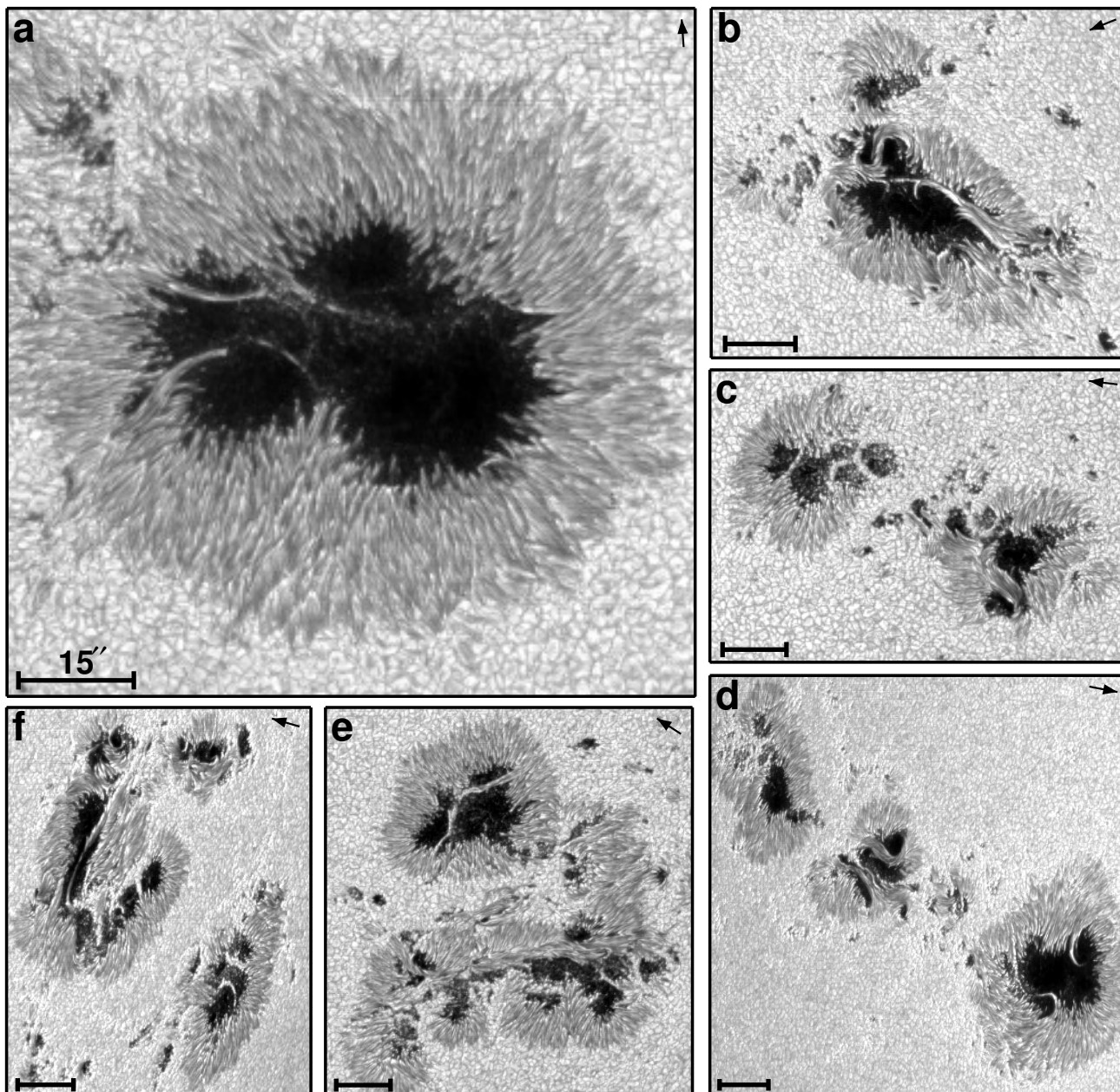


Fig. 1: Best-fit continuum images of sunspot groups part of MODEST. Panels display continuum images of the sunspot groups AR 11943 (2014 January 7; a), AR 11726 (2013 April 23; b), AR 12645 (2017 April 3; c), AR 11295 (2011 September 24; d), AR 12242 (2014 December 19; e), and AR 12673 (2017 September 8; f). Bars on the bottom-left have a length of $15'' \approx 10\,800$ km (no foreshortening correction applied). Arrows located on the top-right part of each image mark the direction of solar disk center.

the spectral line is formed when inverting large datasets. In particular for data taken by the Spectro-Polarimeter (SP; [Ichimoto et al. 2008](#)) onboard the Japanese Hinode solar mission ([Kosugi et al. 2007](#)), the ME-inversion is a part of the standard data processing pipeline (Level-2 data product). The code used by the Hinode consortium is the Milne-Eddington gRid Linear Inversion Network (MERLIN; [Skumanich & Lites 1987](#)). MERLIN inversions of Hinode data are provided by the [Community Spectropolarimetric Analysis Center \(2006\)](#).

Different parts of an absorption line are formed at different heights in the solar atmosphere. The core of the line forms in higher layers than its wings. Any variation or gradient in the atmosphere where the line is formed can leave an imprint on

its shape and polarization. For example, gradients in the velocity and the magnetic field result in asymmetric or even complex Stokes profiles ([Solanki & Pahlke 1988](#); [Solanki & Montavon 1993](#)), which are ubiquitous ([Solanki & Stenflo 1984](#); [Sigwarth et al. 1999](#)). Unfortunately, by construction, the ME-inversions fail to model the observed Stokes profiles when such gradients along the line-of-sight exist, since they can only reproduce simple profiles without asymmetries; a significant shortcoming given the strong asymmetries almost invariably present outside sunspot umbrae.

Depth-dependent codes are commonly used in solar physics to model stratified atmospheres (e.g., SIR ([Ruiz Cobo & del Toro Iniesta 1992](#)), NICOLE ([Socas-Navarro et al. 1998, 2015](#)),

Table 1: Atomic information of the observed spectral lines.

element	wavelength (Å)	lower level	upper level	g_{lower}	g_{upper}	g_{eff}	$\log(g_l^* f)$	energy lower [eV]	abundance	1st ionization potential [eV]	2nd ionization potential [eV]
Fe I	6301.5012	$z^5P_2^o$	$-e^5D_2$	1.83	1.5	1.67	-0.745	3.654	7.50	7.9024	16.1879
Fe I	6302.4936	$z^5P_1^o$	$-e^5D_0$	2.50	–	2.50	-1.203	3.687			

SPINOR (Solanki 1987; Frutiger et al. 2000), SNAPI (Milić & van Noort 2018), among others). Such height-stratified inversions are able to retrieve variations of the physical conditions with optical depth (for a review see e.g., de la Cruz Rodríguez & van Noort 2017). However, depending on the photospheric features of interest, the model used to interpret the observations might need to be adjusted. For example, the formation height of the same spectral line from quiet Sun to sunspots can differ by hundreds of kilometers (see e.g., Fig. 2 of Smitha et al. 2021a). This large difference requires a change in the grid locations where the atmospheric parameters are determined.

Typically, it is difficult to obtain excellent fits to all pixels inside the field of view (FOV) if a single atmospheric model is used. It has been customary that different features, such as the quiet sun, plage, penumbra, and umbra, were modeled with different settings for the atmospheric parameters (e.g. Collados et al. 1994; Bellot Rubio et al. 2003). Depth-dependent spatially coupled inversions were proposed to solve this as well as other problems (van Noort 2012; van Noort et al. 2013, hereafter coupled inversions). They account for the parasitic light coming from adjacent pixels due to the unavoidable blurring caused by the point spread function (PSF) of the telescope. The coupled inversions applied to Hinode/SOT-SP data have been used to study different features of the solar photosphere such as, among others, the umbral dots (Riethmüller et al. 2013), the Wilson depression (Löptien et al. 2020a), the umbra-penumbra boundary (Löptien et al. 2020b), light bridges (Lagg et al. 2014; Castellanos Durán et al. 2020), penumbral filaments (van Noort et al. 2013; Tiwari et al. 2013), counter Evershed flows (Siu-Tapia et al. 2017, 2019; Castellanos Durán et al. 2023).

Recently, the concept behind the coupled inversions was generalized by de la Cruz Rodríguez (2019) to account for observations taken by different facilities that may have different spatial, or spectral resolutions, or that are rotated relative to each other (see, e.g., Rouppe van der Voort et al. 2020, for a multi-observatory dataset where such inversions could be applied). To our knowledge, there is only one existing photospheric catalog of depth-dependent inversions, which mainly focuses on simple sunspots and covers ~50 Hinode/SOT-SP scans (see e.g., Löptien et al. 2018).

In this work, we present the Max-Planck Open Database of Elaborate inversions of SunspotTs or MODEST for short. The MODEST catalog of sunspot groups covers different types of active regions (ARs) with sunspots, including the most complex ones. Figure 1 shows examples of different ARs that are part of MODEST. For many ARs, MODEST also provides some (limited) temporal coverage as they cross the solar disk. MODEST is one of the first catalogs of stratified sunspots inversions where the same atmospheric model was used for all observations while being able to fit all types of features observed on the Sun with one set of free atmospheric parameters. The MODEST catalog will enable statistical studies of depth-dependent conditions inside a large variety of sunspots.

2. Data and sunspot sample

2.1. Data calibration

The MODEST catalog uses spectropolarimetric data taken by the Spectropolarimeter (SP; Ichimoto et al. 2008) attached to the Solar Optical Telescope (SOT; Tsuneta et al. 2008) onboard Hinode (Kosugi et al. 2007). Hinode/SOT-SP performs high spectral and spatial resolution spectropolarimetric observations of the solar photosphere in the line pair Fe I 6301.5 Å and 6302.5 Å. The magnetic sensitivity of these lines, given by the effective Landé factor (g_{eff}), is 1.67 and 2.5 respectively (cf. Solanki & Stenflo 1985). Table 1 summarizes the atomic parameters of these transitions.

Hinode/SOT-SP has a spectral sampling of 21.5 mÅ, while the spatial resolution varies depending on the observing mode, with the “fast” mode having 0′′297×0′′32 pixel size and the “normal” mode 0′′149×0′′16. The fast mode decreases the time needed to scan a given area on the solar surface, to the detriment of the spatial resolution with respect to the normal mode. Depending on the science case, either mode can be more suitable, and therefore the sample of sunspots presented here contains observations taken in both modes. The data were calibrated using the standard `sp_prep` routines that are part of the Solarsoft package and were reduced using the nominal Hinode/SOT-SP pipeline (Lites & Ichimoto 2013). In addition, all data were checked for continuum polarization that is sometimes observed in Stokes $Q(\lambda)$, $U(\lambda)$ and $V(\lambda)$ (see Fig. 1 in Okamoto & Sakurai 2018). In case such an offset was found in the polarization, we removed the offset by requiring the continuum polarization to be zero. No additional correction to account for gray spectral stray light was applied (see Appendix A). In addition, for some particularly large Hinode/SOT-SP scans, we did not invert the full scan, but we rather manually centered the sunspot group and cut the scan in the spatial plane (See Sect. 3.4).

2.2. Sample of sunspots

Since coupled inversions are computationally expensive, only a small subset of all Hinode observations could be included in the MODEST database, so that we need to select. We made use of the Lockheed Martin Solar and Astrophysics Laboratory (LMSAL) database¹ Hinode/SOT-SP to select the sample of sunspot groups to invert. This database contains ME-inversions of all Hinode/SOT-SP observations, which were performed with the MERLIN code. However, this database does not specify whether individual scans include a specific AR or not. On the date we started selecting our sample (2019 July 27), more than 22 000 scans were available.

We started by creating an initial list of all ARs with sunspots that were visible on the Sun from the date when Hinode started observing until 2019 July 27. Here we used the Solar Re-

¹ <http://sot.lmsal.com/data/sot/level2d/>

gions Summaries² made by the Space Weather Prediction Center. These are daily reports about all visible ARs on the Sun. For each visible AR with sunspots, the SRS reports contain the NOAA number, the estimated area, the latitude and longitude, the modified Zürich class (McIntosh 1990), magnetic sunspot class (Hale et al. 1919; Künzel 1960, 1965), among others. If an AR was observed for more than one day, it occurs more than once on the initial list. To see which of these ARs were observed by Hinode/SOT-SP, we used the SOT planning files³. We kept only ARs that were visible on dates that appeared in the SOT planning files or that had a NOAA number that was mentioned in those. Finally, we also excluded all regions that had an estimated sunspot area smaller than 100 MSH, where MSH stands for a millionth of the solar hemisphere, i.e., $1\mu\text{SH} = (6'')^2$. This filtering reduced the number of scans that we further investigated from more than 22 000 to about 9 100.

These conditions could not completely exclude other types of Hinode/SOT-SP observations that were performed on the same day as an observation of a suitable active region, however. These scans were excluded in the subsequent filtering process. Sunspots can be identified easily in maps of the magnetic field strength. Hence, to select only scans including sunspots, we made use of maps of the magnetic field strength provided by the MERLIN inversions in the LMSAL Level-2 database. With the help of the ME-inversions, we checked for each scan in our sample if it had at least one connected region, where the inferred magnetic field strength was greater than 2 kG, and where the area of the region was larger or equal to $(10'')^2$.

This approach did not work well for wide scans that included the limb. Sometimes the MERLIN inversion assigns very strong magnetic fields to the parts of the FOV outside the limb (usually 5 kG, which is the upper limit in the MERLIN code), which would be falsely classified as sunspots by our approach. Consequently, we removed scans including the limb from the sample, by checking if the center of the connected region is too close to or even outside the limb (if its central pixel lies at a radius greater than the disk radius minus $50''$, which corresponds to $\mu \approx 0.35$). After applying these conditions, we were left with a sample of about 4500 “suitable” scans. Unfortunately, some of these scans still contained off-limb regions, since the coordinates of the center of the FOV in the Level-2 data header were not always accurate (cf. Fouhey et al. 2022) or the scans were too wide.

Initially, MODEST was conceived to study statistically superstrong magnetic fields observed in sunspots (cf. Okamoto & Sakurai 2018; Castellanos Durán et al. 2020). For this reason, we sorted the “suitable” scans of sunspot groups in descending order, according to the number of pixels inside the connected regions that had magnetic field strength of exactly 5 kG, which is the maximum value allowed of the magnetic field strength in the MERLIN inversions. From this point on, we inspected each of the remaining scans manually before deciding whether to invert it or not. This step reduced the number of scans by another factor of ~ 4 .

As we were originally interested in complex sunspots with very strong magnetic fields, in particular in bipolar light bridges, the current MODEST sample focuses on complex ARs with sunspots, in particular δ -groups. To increase the usability of our catalog also for other studies involving sunspots, we later added scans of α and β spots, and we will continue to do so in the future. Figure 2 shows a summary of the current sample of sunspot

groups that are part of MODEST. As of now, MODEST consists of 942 scans of 117 individual ARs with sunspots (either whole or part of them), and most of the inverted scans contain multiple sunspots. Panel (2a) displays the density of all scans projected onto the solar disk. Panel (2b) shows the heliocentric angle of the center of each scan. Multiple scans were inverted for many ARs to provide information on the temporal evolution of at least some of the ARs. Panel (2c) compiles the number of scans that cover a given AR, or part of it. Panel (2d) arranges all sunspot groups in terms of their magnetic class.

The current MODEST’s sample covers ARs located roughly within $\pm 60^\circ$ of longitude and $\pm 25^\circ$ in latitude on the solar disk. Table D.1 summarizes the sample of the scans inverted so far. Table D.1 lists information about the inverted scans: the OBS_ID, NOAA number, date, time, type of the Hinode scan (either fast with a pixel size $\sim 0'':32$ or normal $\sim 0'':16$), coordinates of the FOV, μ -value (cosine of the heliocentric angle), number of tiles that the FOV was divided into (see below), size of the FOV, and area, Zürich classification and magnetic classification of the AR.

3. Inversion approach

3.1. Spatially coupled inversions

In this work, we applied the so-called spatially coupled inversions (van Noort 2012; van Noort et al. 2013), which make use of the knowledge of the telescope PSF to remove its effects at the same time as obtaining information on the solar atmosphere from the measured Stokes profiles. The recorded images at the entrance slit of the SP are the result of the convolution of the undisturbed solar image with the PSF of the aplanatic 50-cm $f/9$ Gregorian telescope. The PSF includes the effects of the spider holding the M2 mirror and the central obscuration (see Fig. 10 in van Noort 2012). As a result of this convolution, the information of a given pixel is distributed over its surroundings. To account for these effects, van Noort (2012) proposed to include the effects of the PSF in the inversion procedure.

The inversions are performed using the SPINOR code (Frutiger et al. 2000). SPINOR fits the spectropolarimetric observations with a stratified model of the solar atmosphere. SPINOR uses the STOPRO routines that solve the radiative transfer equation of polarized light (Solanki 1987), and employs the Levenberg-Marquardt minimization algorithm (Levenberg 1944; Marquardt 1963) to fit the synthetic Stokes profiles to the observed ones. The module for spatially coupled inversions in the SPINOR code can be activated when the PSF of the instrument is known (SPINOR-2D inversions).

Table 1 summarizes the atomic parameters used in the inversion procedure, where g_{lower} and g_{upper} are the Landé factors of the lower and upper energy levels of the considered transitions, and $\log(g_l^* f)$ is the weighted oscillator strength of the line. The Landé factors are calculated from the atomic configuration assuming LS -coupling. The effective (triplet) Landé factors are shown for completeness but are not used during the inversion.

3.2. Node position and free parameters

The number of free parameters in the atmospheric model is related (1) to the number of nodes placed at different depths at which the parameters are determined, and (2) to the physical quantities that play a role in the formation of the spectral line. A larger number of free parameters generally improves the quality of the fit. This can come at the cost of the uniqueness of the solution, in particular, if some free parameters are not sufficiently

² <ftp://ftp.swpc.noaa.gov/pub/warehouse>

³ <https://sot.lmsal.com/operations/timeline/>

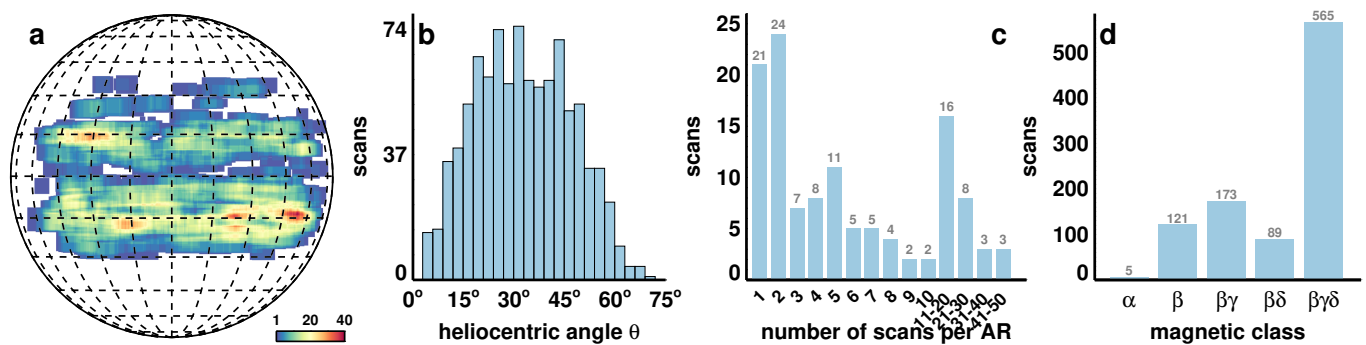


Fig. 2: Characteristics of the sample of sunspots in the archive. (a) Location of all scans on the solar disk. The color gives the number of scans observed at roughly the same location on the disk. (b) Heliocentric angle of the center of each field of view. (c) Number of scans of a given sunspot group (or part of it). (d) Magnetic classification of the sunspot group, with each scan being counted separately.

independent of each other. For the MODEST catalog, we use 16 free parameters to model a stratified solar photosphere. The temperature (T), magnetic field strength (B), inclination (γ), azimuth (φ) and line-of-sight velocity (v_{LOS}) each contribute with three free parameters located at different optical depths. The micro-turbulence (v_{micro}) was modeled without depth-dependence (one free parameter) as the χ^2 -hypersurface is relatively insensitive to depth-dependent changes due to micro-turbulence velocities (Frutiger et al. 2000). We convolve the synthetic profile with the measured SP spectral transmission profile, which has a FWHM of 24.3 mÅ and extended wings, so no other parameter was necessary to account for the broadening of the Fe I line pair.

The node positions were located at $\log \tau_c = 0.0, -0.8, -2.0$, where τ_c represents the continuum optical depth at 5000 Å. The position of the top node at $\log \tau_c = -2.0$ was chosen following Danilovic et al. (2016) as large parts of the FOV might be filled with quiet Sun. These authors demonstrated that this node position is well-suited under quiet-Sun conditions, but it also does not adversely affect the retrieved atmospheres for complex profiles (see the discussion in Sect. 4.1; cf. Figs. 4-6). The atmospheric stratification is computed from the coarse three-node grid onto a fine depth grid with a sampling of $\Delta \log(\tau) = 0.05$ using a spline approximation (see Frutiger 2000). The atmosphere was extrapolated using a linear function based on the slope of the spline interpolated between the nodes for optical depths ranging between $\log \tau_c < -6.0$ and $\log \tau_c > 1.5$.

3.3. Inversion strategy

Selecting a balanced inversion strategy helps to avoid getting stuck in a local minimum in the χ^2 -hypersurface. There is the possible existence of extreme cases where any of the retrieved parameters can have an extreme value (e.g., $v_{\text{LOS}} > 7 \text{ km s}^{-1}$ - photospheric sound speed - or $B > 4 \text{ kG}$). In addition, gradients of the v_{LOS} and the magnetic field, at different heights where the lines are formed, can create complex Stokes profiles (Solanki & Montavon 1993).

To account for these possibilities, each observation was inverted ten times as suggested by van Noort et al. (2013). After each inversion run, the output atmosphere for each pixel was smoothed with the surrounding neighbors in case the solution in the pixel reaches a local minimum in the χ^2 -hypersurface (see below). Then, that smoothed atmosphere was used as the initial condition for the next inversion run applied to the same set of

pixels. In the first inversion run, for the initial conditions we give the average quiet-Sun conditions, weakly magnetized and at rest (e.g., Danilovic et al. 2016). We used quiet-Sun conditions to initialize the inversions, as 68.2 % of the pixels inside the FOVs belong to quiet Sun, active region plage or network.

The number of maximum iterations allow to find the best match between the observed and synthetic Stokes vector increases in each inversion run. The first inversion run has a maximum of 10 iterations and this number is increased after each inversion run until up to 100 iterations (van Noort 2012).

The allowed ranges (“limits”) of the atmospheric parameters during the first run were chosen to cover typical values that contain quiet sun, penumbral, and umbral regions (see below). In the subsequent runs, the parameter space was slowly increased. This allowed adequately fitting ever more complex profiles while ensuring that the fits to simple Stokes profiles remained of high quality. In particular, to avoid the inversion reaching extreme values the limits for the magnetic field strength and v_{LOS} were smoothly increased for each inversion run. For the first three runs B and v_{LOS} were limited to $B \leq 3 \text{ kG}$ and $|v_{\text{LOS}}| \leq 5 \text{ km s}^{-1}$. This limit accounts for the subsonic pixels in the quiet sun, penumbrae, and the not-too-dark parts of umbrae (i.e. in umbral dots and the diffuse background, e.g., Socas-Navarro et al. 2004; Riethmüller et al. 2008, 2013). This limit covers the values reached in the majority of the pixels. In case a larger value of either of these quantities would be required to reproduce a particular set of Stokes profiles, the inversion saturates at this limit, but then, the saturated value is used as an input for the next inversion run.

During inversion runs 4 and 5, the v_{LOS} limits start covering the supersonic regime to $|v_{\text{LOS}}| \leq 8 \text{ km s}^{-1}$ and $\leq 10 \text{ km s}^{-1}$, and also the maximum field strength is increased such that $B \leq 5 \text{ kG}$. The last 5 inversion runs are devoted to finding the best fits for extreme cases for the supersonic LOS velocities (e.g. del Toro Iniesta et al. 2001; van Noort et al. 2013; Esteban Pozuelo et al. 2016; Siu-Tapia et al. 2017) and superstrong magnetic field strengths (van Noort et al. 2013; Okamoto & Sakurai 2018; Siu-Tapia et al. 2019; Castellanos Durán 2022), while further loosening the limits in each run. In the last run, the maximum values for the magnetic field strength and line-of-sight velocity were set to 15 kG and 30 km s⁻¹, respectively.

During a given inversion run, the global minimum of the χ^2 -hypersurface can be located inside the allowed parameter space or not, depending on the complexity of the atmosphere. When increasing the limits of the parameters in the next inversion run, the previously fitted atmosphere is only affected if the “real” global

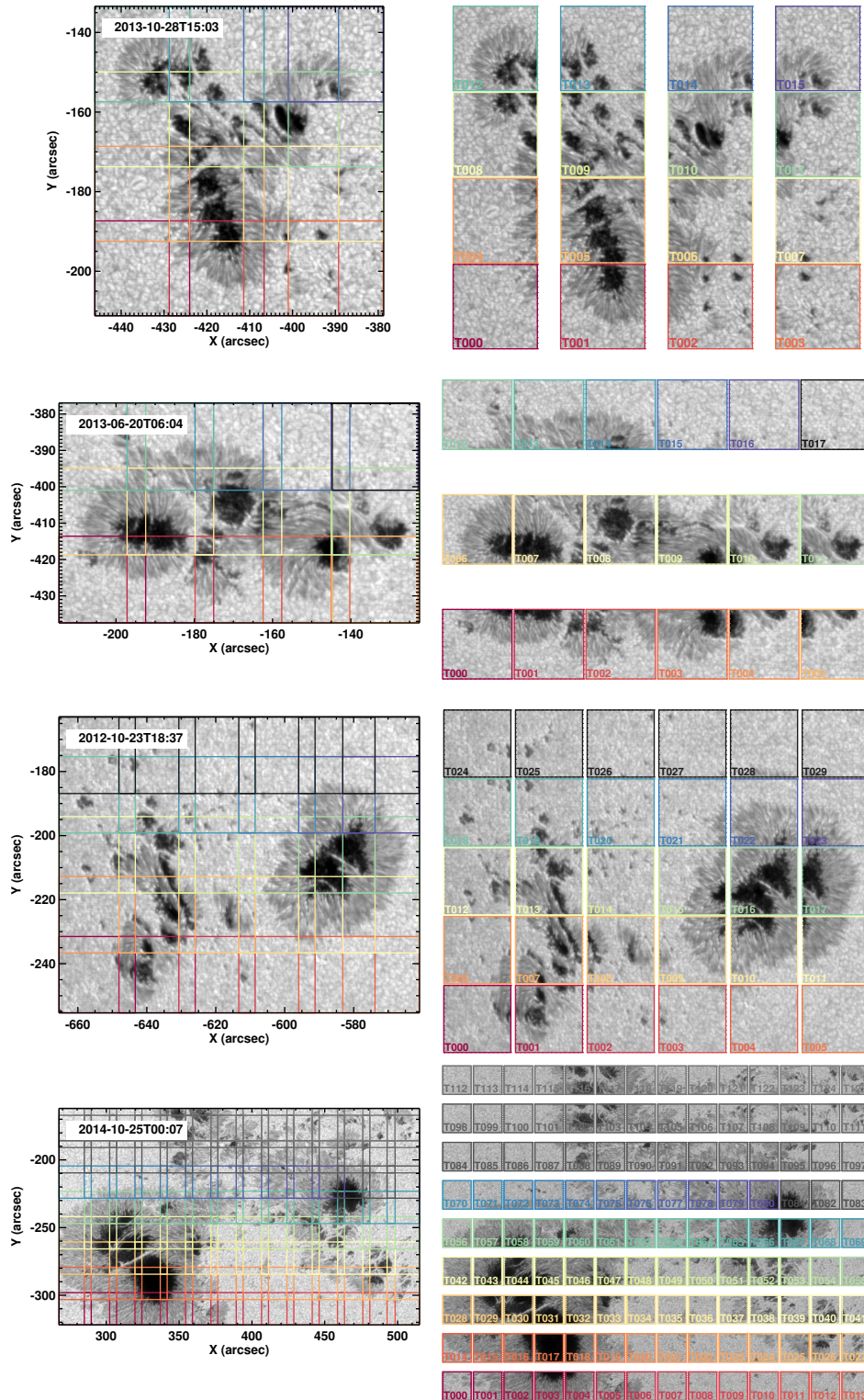


Fig. 3: Illustration of the division of the FOV into tiles for the coupled inversions. From top to bottom, the continuum maps as observed by Hinode/SOT-SP of AR 11882, AR 11775, AR 11560, and AR 12192. Colored lines mark the location of the tiles in which the FOV is divided (left). Notice that the tiles are designed to overlap. Right column shows the individual continuum maps of each individual tile.

minimum of the χ^2 -hypersurface was not part of the parameter space. Then the next inversion run will improve the solution by increasing the size of the χ^2 -hypersurface in each step until the “real” global minimum is part of the parameter space. However, by extending limits the global minimum for a given atmosphere

does not change the solution if it represents the global minimum also in the increased parameter search space.

In addition, if the previous best-fit atmosphere was stuck in a local minimum, we help the inversion to go out of it by starting the new inversion run with an offset given by the “invert-

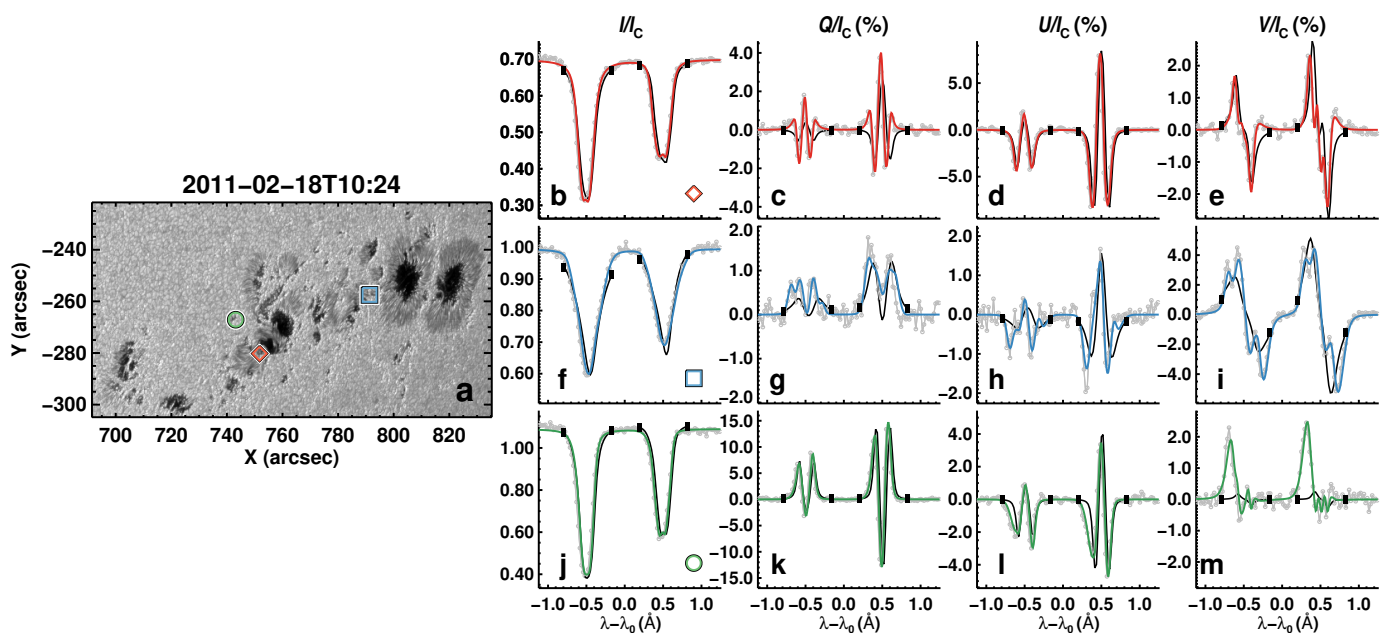


Fig. 4: Fits obtained by the coupled inversions to the observed Stokes profiles. Panel (a) shows the continuum image of the AR 11158 when it was located at $\mu \approx 0.6$. Columns 2 to 5 show the observed Stokes profiles (gray dotted lines) and the retrieved fits obtained by the coupled inversions (colored lines), and the ME-inversion by MERLIN (black lines). Vertical black bars mark the spectral windows that MERLIN uses for the Level-2 inversions. The locations of the plotted profiles are marked on the continuum images by the colored symbols. $\lambda_0 = 6302 \text{ \AA}$.

smooth-invert” approach. This approach assumes that adjacent pixels may have relatively similar atmospheres. Consequently, when using the smoothed atmosphere as an input of the next inversion run, the inversion is likely to find the global minimum easier, avoiding getting stuck in a local minimum. Furthermore, every time the inversion is restarted, the so-called Marquardt parameter is also reset (see e.g., Eq. 4 of van Noort (2012)). The Marquardt parameter is used to find the minimum in a χ^2 -hypersurface, since it regulates the amount of linearization assumed by the algorithm. We help the algorithm to leave the local minimum by resetting the Marquardt parameter. The effect of the “invert-smooth-invert” approach can be directly seen working in the quiet sun, where the low signal-to-noise tends to retrieve *noisy* maps. Other spatial-regularization schemes are found in the literature (see e.g., de la Cruz Rodríguez 2019), but they have not been implemented in the SPINOR code yet. The opted simple spatial-regularization “invert-smooth-invert” scheme is applied after each inversion run. Therefore, it is straightforwardly applied to any other type of inversion that uses a gradient-based minimization (e.g., SIR-inversions) to fit synthetic Stokes profiles to the observed ones.

As suggested by van Noort et al. (2013), data were upsampled before the inversion by a factor of 2 in Fourier space to keep the noise level constant (see Fig. 5 in van Noort et al. (2013) for illustration). The upsampled data are then inverted by the coupled inversions, which means that the number of pixels inside the same FOV is four times larger than for the original sampling. For normal [fast] maps, the approximate pixel size is $0''.16$ [$0''.32$]. The inversion is done on upsampled pixels with a size of $0''.08$ [$0''.16$]. The output of the coupled inversion is later downsampled with the same procedure in Fourier space to return to the nominal scale of the observed FOV, i.e., the final pixels have again a size of $0''.16$ [$0''.32$]. The upsampled inversions are not presented as a default in the current catalog, but are available on request. The upsampling (and later downsampling) steps are needed to

fit substructures that are below the pixel size, but which affect the observed Stokes profiles. As explained by van Noort et al. (2013), this approach is similar to having multiple atmospheres within the pixel that are assigned different filling factors. Since these atmospheres or components are coupled by the PSF, this allows the coupled inversions to infer the atmospheric conditions up to the diffraction limit of the telescope when the PSF of the optical system is known and the data are reordered without seeing disturbances. See van Noort (2017) for estimating the PSF and restoration of solar spectra when observations are taken by a ground-based facility.

3.4. Tiling the FOV

During the inversion, a minimization procedure is applied to find the best match between the observed Stokes profiles and the synthetic Stokes profiles that are obtained after the solution of the radiative transfer equation of polarized light for a given atmospheric model. In the classic pixel-to-pixel inversions, every pixel inside the FOV is treated independently. This implies that the size of the matrices needed to be inverted during the minimization procedure is independent of the size of the FOV. Hence, classic inversions are fast and easy to parallelize, and not very demanding in terms of memory usage.

For coupled inversions, all profiles within the FOV must be inverted simultaneously. The coupling of the solutions between the pixels rapidly increases the size of the matrices needing to be inverted during the minimization procedure with the number of pixels, N . The size of the matrix computations roughly increases $\propto N^3$, which places greater demands on computer memory with increasing size of the scan (see further details in van Noort 2012).

The number of pixels in the scans selected for MODEST ranges from $N_{\text{smallest}} \sim 8500$ ($\approx 22'' \times 36''$; fast mode) to

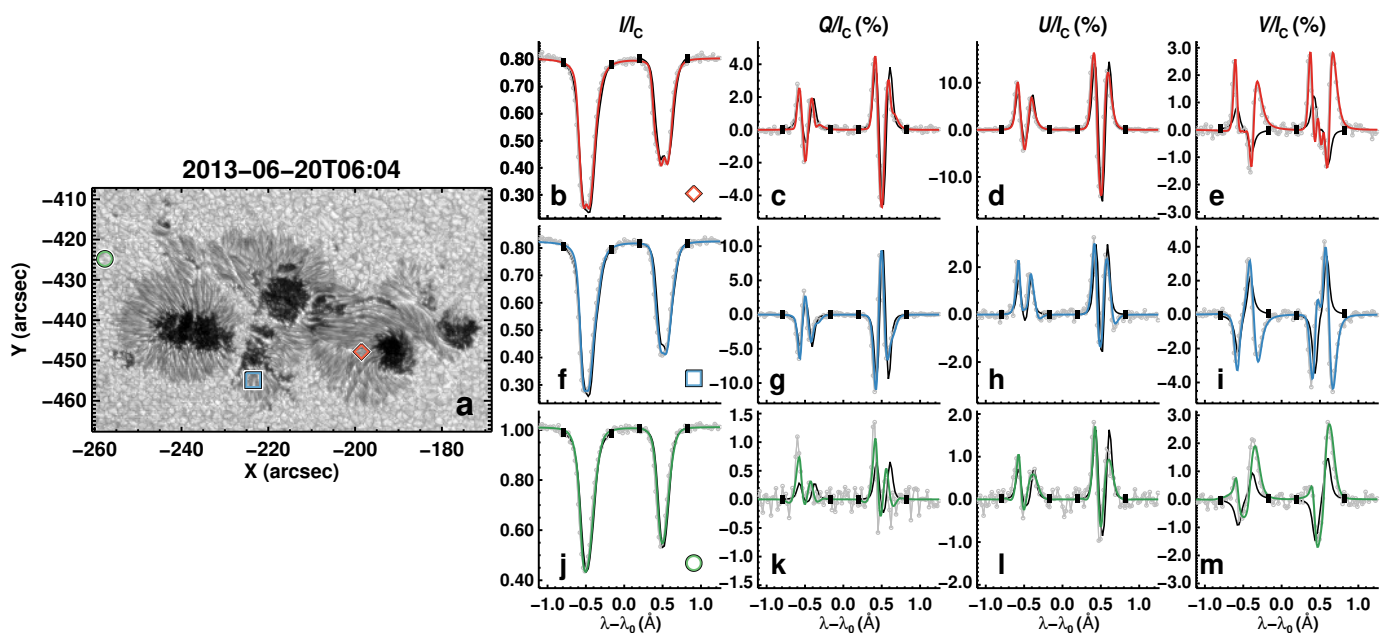


Fig. 5: The same as Fig. 4 for a sunspot group belonging to AR 11775, when it was located at $\mu \approx 0.8$.

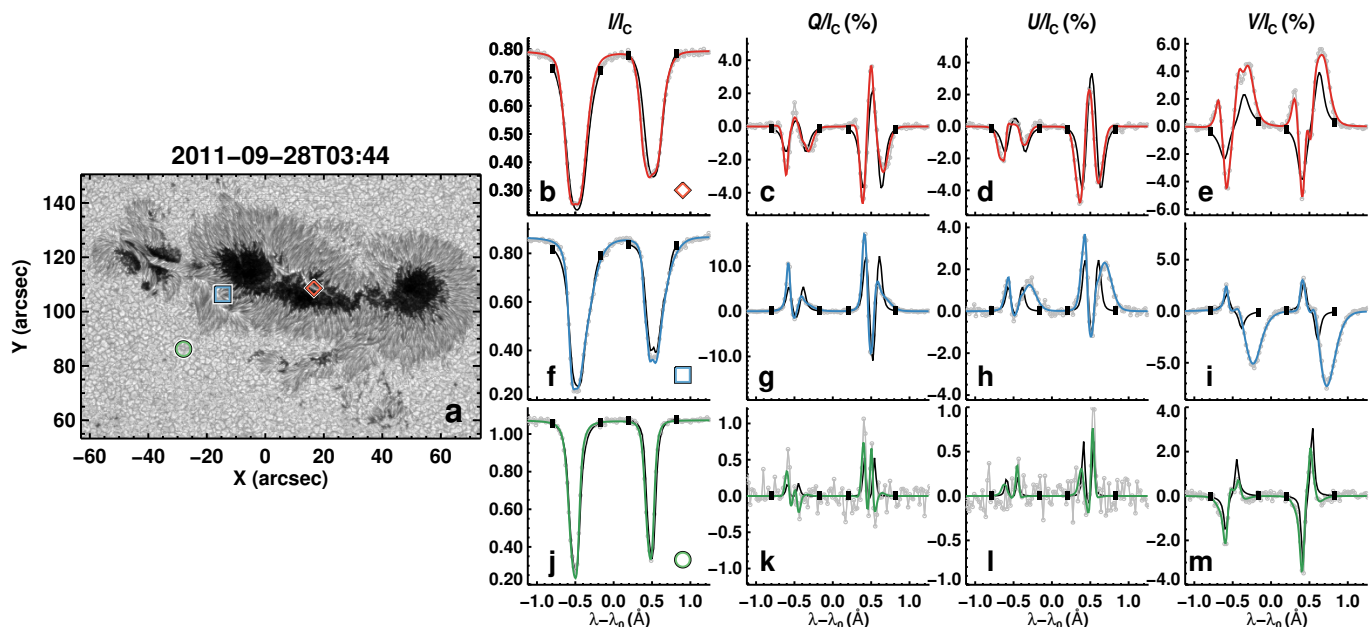


Fig. 6: The same as Fig. 4 for a sunspot group belonging to AR 11302, when it was located at $\mu \approx 1.0$.

$N_{\text{largest}} \sim 591\,000$ ($\approx 125'' \times 110''$; normal mode). In addition, after upsampling the number of pixels increases by a factor of four. Many of the scans are much too large to be handled in one go. One solution is to split the larger scans into sufficiently overlapping tiles. In addition, we were able to use three different computing facilities to perform our inversions. However, this also implied that we had to account for the differences between the facilities such as the type of processors, the available storage, the maximum runtime per job, and the read/write I/O characteristics among others. We chose to divide all scans into tiles of the same size based on all these constraints and for consistency. We obtained good results by dividing each upsampled FOV into tiles of 150×150 spatial pixels resulting in a maximum memory usage of 2 GBytes per tile (see Fig. 3). Maps on the left side of Fig. 3

mark the location of each tile within the FOV, where different colors represent each tile. Note the overlap between tiles.

We performed tests by varying the overlapping area between tiles to determine how much overlap is needed to ensure that there are no discontinuities when stitching the atmospheres retrieved in the individual tiles together. These tests allowed us to ensure that the overlap between the tiles was at least twice the width of the core of the PSF that covers most of the power in Fourier space. A conservative value for this overlap was chosen to be 16 pixels. This was done to ensure a homogeneous quality of inversion after all the tiles (now containing the best-fit profiles and resulting atmospheres) are arranged in their original positions (see also Appendix B).

Table 2: Features covered by the sample

Pixels	Fast mode		Normal mode		Total	
	(Num. px)	(Percen.)	(Num. px)	(Percen.)	(Num. px)	(Percen.)
Quiet Sun/plage/network	9.1×10^7	68.8 %	6.2×10^6	60.6 %	9.7×10^7	68.2 %
Penumbra	3.3×10^7	25.1 %	3.2×10^6	31.8 %	3.6×10^7	25.6 %
Warm umbra	7.1×10^6	5.4 %	6.6×10^5	6.5 %	7.7×10^6	5.5 %
Cold umbra	9.1×10^5	0.7 %	1.2×10^5	1.1 %	1.0×10^6	0.7 %
Masked	7.6×10^4	0.06 %	1.9×10^4	0.18 %	9.4×10^4	0.07 %
Total	1.3×10^8	100.0 %	1.0×10^7	100.0 %	1.4×10^8	100.0 %

Maps on the right side of Fig. 3 show each tile within the FOV that then was inverted. After the inversion, tiles were stitched together by removing the outer added edge between neighboring tiles. No boundary or edge effects were visible after putting together the tiles on the large map. No smoothing at the boundaries was required, indicating that the independent inversions of the adjacent tiles found the same global minimum for the pixels located in both tiles, and that the chosen overlap of 16 pixels was sufficiently large.

Appendix B shows a quantitative test on the effects of tiling the FOV. A scan of AR 11748 was inverted without tiling the FOV on a so-called “fat node” with large memory. This scan contains all types of features (umbrae, penumbrae, and quiet Sun) at the location where the tiles are put together. The inversion was carried out following the same steps as presented in Secs. 3.1–3.3. As the last step, the whole FOV was downsampled to its original size, thus reversing the Fourier upsampling procedure mentioned above. This inversion was then compared with the nominal “tiled” MODEST inversion (Fig. B.1). This test demonstrates that the effects of tiling the FOV are negligible.

4. Results

The MODEST catalog contains the atmospheric conditions of sunspot groups that were located roughly within a longitude of $\pm 60^\circ$ and $\pm 25^\circ$ in latitude on the solar disk. MODEST started out focusing on the more complex sunspot groups (Fig. 2d). Later, simpler sunspots were added. All ARs with sunspots were observed by Hinode/SOT-SP and span the last part of solar cycle 23, and almost the full cycle 24. Currently, MODEST is composed of 942 scans of 117 individual ARs with sunspots (or parts of these active regions). The inverted scans frequently show multiple sunspots. The total number of spatial xy -pixels is 1.4×10^8 , and the total number of data points⁴ that was fitted is 6.3×10^{10} .

In December 2006, i.e. still in the early stages of the mission, a hardware failure in the X-band at 8.4 GHz reduced the downlink transmission bandwidth between Hinode and ground stations considerably. In terms of data volume, fast mode scans with a spatial sampling of $0''.32$ are considerably smaller than normal scans with a spatial sampling of $0''.16$. Due to the technical problem with the X-band, the majority of the Hinode/SOT-SP scans are therefore taken in fast mode (the fifth column in Table D.1 lists whether the scan was taken in the fast or normal mode).

⁴ One data point is considered to be a monochromatic Stokes profile value. A typical xy -pixel has 444 data points, which corresponds to a full Stokes vector at a given wavelength (I, Q, U, V)(λ) times ~ 111 spectral wavelength positions covered by each Stokes profile. The number of wavelength positions may vary depending on the observing mode.

Table 2 summarizes the total number of xy -pixels covering different solar features depending on whether they were observed in the fast or normal mode, and the combined total. Roughly 69% of the areas of the scans observe quiet Sun, active region plage, and network regions surrounding sunspot groups, while 25% of the pixels cover sunspot penumbrae and 5% belong to sunspots umbrae. In addition, Figs. D.1 to D.44 show a mosaic of the best-fit continuum images as well as the line-of-sight magnetograms of the current sample of MODEST (see also summary Table D.1).

The following sub-sections present examples taken from the catalog. They include examples of typical fits to the observed Stokes vectors at different μ -values of different solar structures, the retrieved atmospheric maps for different ARs, as well as the intrinsic limitations of the Fe I pair at 6302 Å, comparison with the standard Level-2 data product and the 6302 Å lines when observed in cold umbrae.

4.1. Modeling of the observed Stokes vector

The spatially coupled inversions apply a one-component depth-dependent atmospheric model to each pixel of an FOV, irrespective of the type of (photospheric) solar features observed. Figures 4 to 6 show three scans at μ -values of 0.6, 0.8 and 1.0, respectively. Panel (a) shows the best-fit continuum image of the scan, while columns 2 to 5 present three pixels within the FOV selected on the basis of the complexity of their observed Stokes spectra. The observed Stokes profiles are shown by the gray-dotted lines, while the best fits obtained by the inversions are presented by the colored lines. Pixels in the bottom row belong to the quiet Sun (green line), while the middle and top rows show pixels taken from penumbrae (blue and green lines, sometimes these pixels are located in light bridges). For comparison, the standard MERLIN inversions, that are a part of the Hinode/SOT-SP pipeline (Level-2 data product), are shown by the black lines. The vertical bars mark the reduced spectral window used by the standard Level-2 inversions. Figures 4 to 6 corroborate that, regardless of the μ -value of the scan and the photospheric feature, the spatially coupled inversions can retrieve fairly good fits to the sometimes very complex observed Stokes vector using a single atmospheric model. Further examples of typical good fits to complex atmospheres obtained by coupled inversions have been presented by van Noort et al. (2013); Siu-Tapia et al. (2017, 2019); Castellanos Durán et al. (2020, 2023).

4.2. Physical parameters of the atmospheres

In this section, we present examples of the maps of atmospheric physical parameters contained in the MODEST catalog, with an

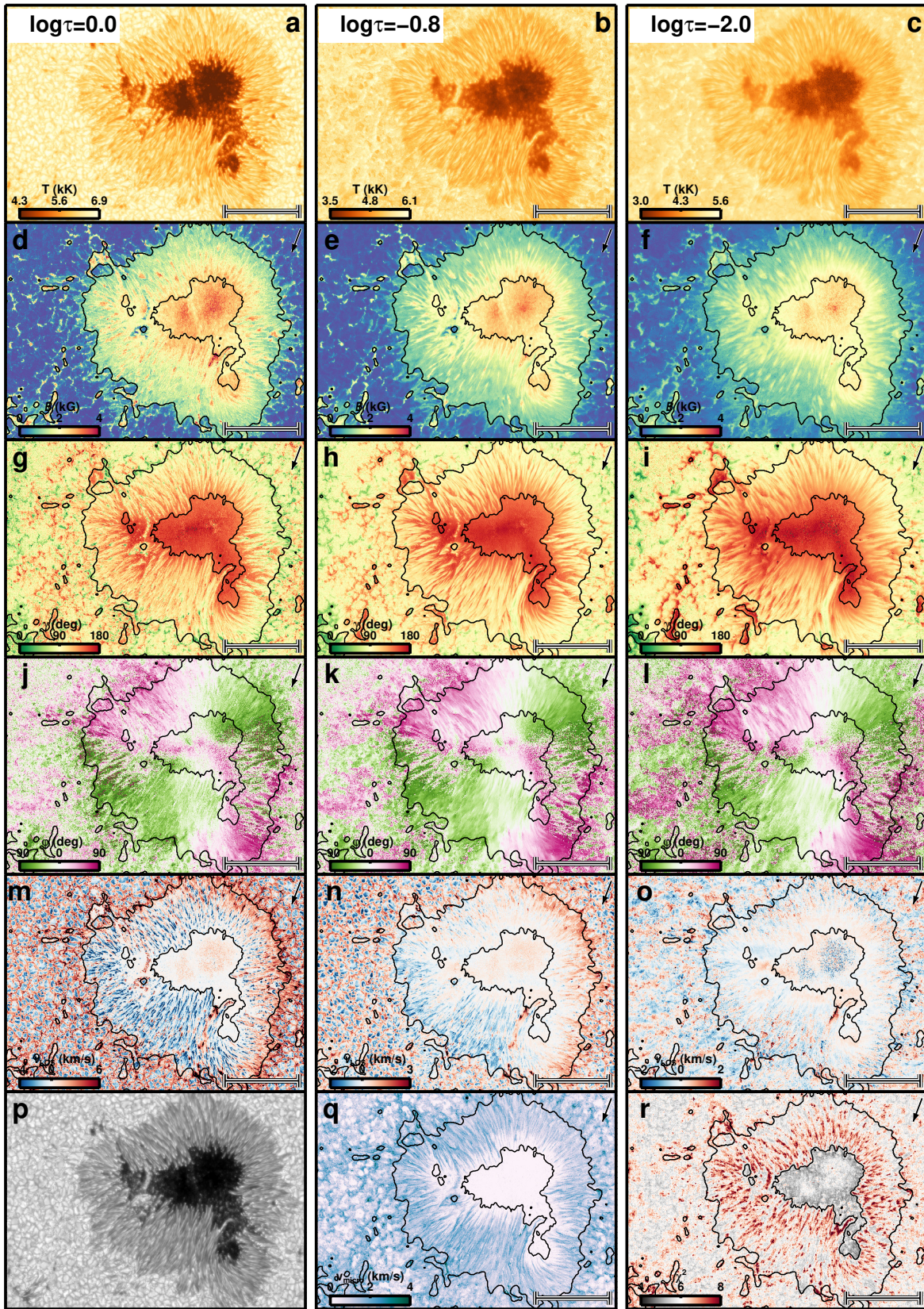


Fig. 7: Depth-dependent atmospheric conditions retrieved by the coupled inversions of AR 10953 (2007 May 1). Rows from top to bottom show maps of temperature, magnetic field strength, inclination, azimuth, and line-of-sight velocity, while explanations for the quantities plotted in the bottom row are given below. In the first five rows, the columns show from left to right these quantities retrieved at $\log \tau = 0, -0.8$ and -2.0 , i.e. at the bottom, middle, and top nodes. Panels (p)-(r) display the best-fit continuum, microturbulence, and χ^2_{reg} maps. This scan was observed in the normal mode with a pixel size of $0''.16$. The FOV is composed of 8×10 tiles.

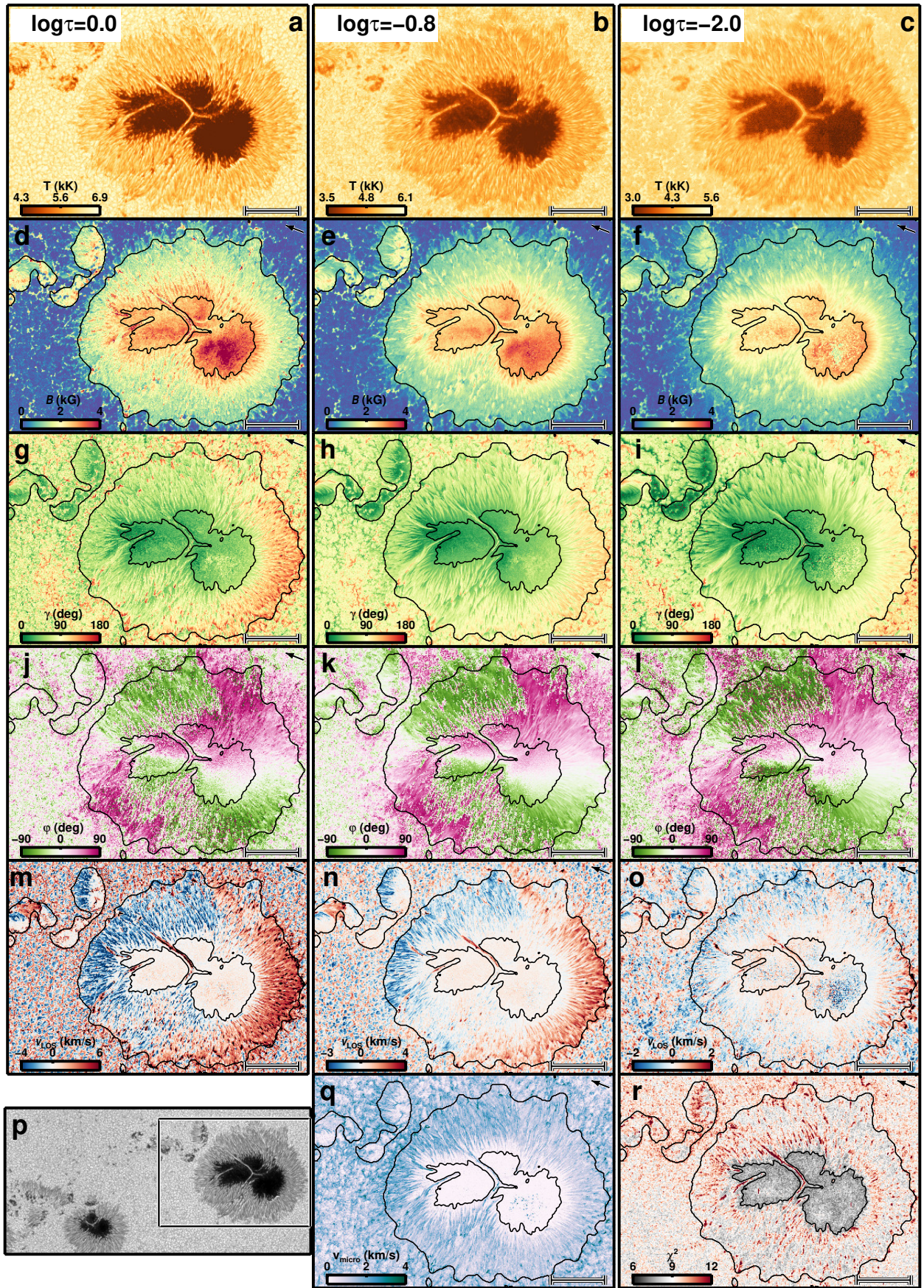


Fig. 8: Same as Fig. 7, but for of part of AR 11944 (2014 January 9). This scan was observed in the fast mode with a pixel size of $0''.32$. The black rectangle inlaid in panel (p) marks the FOV covered by the other panels. The full FOV is composed of 13×6 tiles.

inverted normal mode scan being plotted in Fig. 7 and a fast mode scan in Fig. 8. From top to bottom, the first five rows show temperature, magnetic field strength, line-of-sight inclination and azimuth of the magnetic field, and line-of-sight velocity, respectively. Each column depicts the atmospheric quantities at $\log(\tau) = 0$ (left), $\log(\tau) = -0.8$ (middle) and $\log(\tau) = -2.0$ (right). The bottom row displays the best-fit continuum (panel (p)), micro-turbulence (panel (q)), and the χ^2 -map (panel (r)).

The magnetic field is in the line-of-sight reference frame. To transform the magnetic vector to the local reference frame, the intrinsic ambiguity of the magnetic field's azimuth must be taken into account. Tests have been performed with currently available techniques (Leka et al. 2009), however, the disambiguation is currently not part of the MODEST pipeline (see Section 5.3).

Atmospheric maps show emblematic features observed in the solar photosphere. For example: outside the sunspot, the up-flows in the granules and downflows in the intergranular lanes are well visible (panel (m)) as is the concentration of the magnetic field in the intergranular lanes. Also, the well-known drop of the magnetic field strength of the sunspots from inside the umbra towards the outer parts of the penumbra is clearly visible. The magnetic field decreases with height and the magnetic field canopy is observed when comparing panels (d) and (f). The temperature variation between penumbral spines and intraspines is clearly visible (panels (a)-(c), see also e.g., Schmidt et al. 1992; Lites et al. 1993; Title et al. 1993; Langhans et al. 2005), which is associated with changes in the magnetic field inclination (panels (g)-(h), cf. Tiwari et al. 2013). The normal Evershed flow pattern is seen as a blueshift in the center-side penumbra and as a redshift in the limb-side penumbra (panel (8m) in Fig. 8, cf. Evershed 1909). The same panel (8m) also shows elongated counter Evershed flows associated with a filamentary light bridge (cf. Castellanos Durán et al. 2021), as well as small-scale penumbral downflows (cf. Katsukawa & Jurčák 2010; Jurčák & Katsukawa 2010; van Noort et al. 2013).

5. Discussion

5.1. Comparison with the standard Level-2 inversions

We present two examples of the depth-dependent atmospheric conditions retrieved using coupled inversions and compare them with the standard Level-2 ME-inversions that are a part of the Hinode/SOT-SP pipeline. Figure 9 is a normal-mode scan, while Fig. 10 presents a fast-mode scan. The panels in Figs. 9 and 10 show the best-fit continuum image (a), χ^2 (b), magnetic field strength (c), line-of-sight velocity (d), magnetic field inclination (e) and the magnetic field azimuth (f). Each panel is diagonally split into two halves, with the top-left half showing the results of the 2D coupled inversions presented in this paper. All these maps show the results for the middle node ($\log \tau_c = -0.8$), which is best suited for comparison with ME results (cf. Orozco Suárez et al. 2010). The bottom-right halves of the same panels show the same atmospheric quantities returned by the Level-2 ME-inversions of the complementary part of the same dataset. The continuum images in panels (a) have slightly different brightnesses in the two halves, likely because the SPINOR and MERLIN codes normalize the observed Stokes profiles differently during the inversion. This should not affect the rest of the parameters, however.

Not seen in the examples shown here is that coupled inversions provide depth-dependent information that a ME-inversion cannot provide by design. This is a qualitative difference be-

tween the atmospheres provided in the MODEST database and those obtained by inversions with MERLIN.

Equally important is the relative goodness of fit, or χ^2 . For direct comparison of the standard Level-2 with the coupled inversion, the χ^2 -maps were estimated by adopting the generic form of the merit function

$$\chi^2 = \frac{1}{4N_\lambda - \varrho} \sum_{i=1}^{N_\lambda} \sum_{j=1}^4 \frac{w_j^2}{\sigma_j^2} (I_{ij}^{\text{obs}} - I_{ij}^{\text{syn}})^2, \quad (1)$$

where j stands for the four Stokes profiles, i runs over the number of the observed wavelength points (N_λ), ϱ represents the number of free parameters of each inversion⁵, w_j is the weight applied to each Stokes profile, σ_j is the noise in the observed Stokes profile, and I_{ij}^{syn} and I_{ij}^{obs} are synthetic and observed Stokes profiles. In addition, χ^2 -values were estimated only within the two spectral windows that MERLIN fits (black lines in Figs. 4–6), and we use the same weights that MERLIN assumes. Even though these assumptions may favor the MERLIN inversions, the χ^2 -values obtained by coupled inversion are significantly smaller (see panel (b) in Figs. 9 and 10).

The superior visibility of the fine-scale structure from the SPINOR coupled inversions is evident. This difference is best visible in fast-mode scans (e.g. Fig. 10), but is also present for the normal-mode maps. One sign of the removal of the spatial degradation by the PSF by the coupled inversion is the enhanced contrast in the best-fit continuum map when comparing both inversions (panels (a)), as can be seen from Figs. 9 and 10. In addition, in the outer part of the penumbra, the Level-2 continuum maps show a “halo” in the outer penumbra boundary that extends into the surrounding granulation. This spatial contamination between different solar features is absent in the coupled inversions. This is a direct consequence of the spatially coupled inversions that account for the smearing by the PSF. Other atmospheric maps show comparable results at large scales, but on the smaller scales, the coupled inversions retrieve finer structures.

This smearing by the telescope PSF makes the Level-2 inversions look spatially smoother over scales of the PSF width. Inverting these smeared maps with Level-2 inversions maintains this smearing and results in apparently smoother maps. The 2D inversions act like a deconvolution of these smeared maps, bringing back the original fine structure with higher contrast in all physical quantities (see for example Fig. 11 of van Noort 2012, and compared Figs. 3 and 4 of Castellanos Durán et al. (2020)).

5.2. Molecular blends in the coolest parts of sunspot umbrae

In the comparatively cool environment of sunspot umbrae, diatomic molecules can form. Due to the large number of possible molecular transitions, molecular spectral lines appear as bands in many spectral regions (e.g., Berdyugina & Solanki 2002; Asensio Ramos et al. 2004). Of particular importance in the spectral window around 6302 Å are transitions of the CaH and TiO diatomic molecules (Berdyugina 2011, see also Berdyugina et al. (2003, 2005)).

Larger sunspots harbor darker and hence cooler umbrae (e.g., Mathew et al. 2007). In large dark umbrae the molecular blends are the strongest. Figure 11 shows five selected Stokes profiles arising along a line from the edge to the center of the umbra

⁵ The number of free parameters of the stratified-MODEST inversions and the ME-Level-2 inversions are $\varrho_{\text{MODEST}} = 16$ (Sect. 3.2) and $\varrho_{\text{MERLIN}} = 11$.

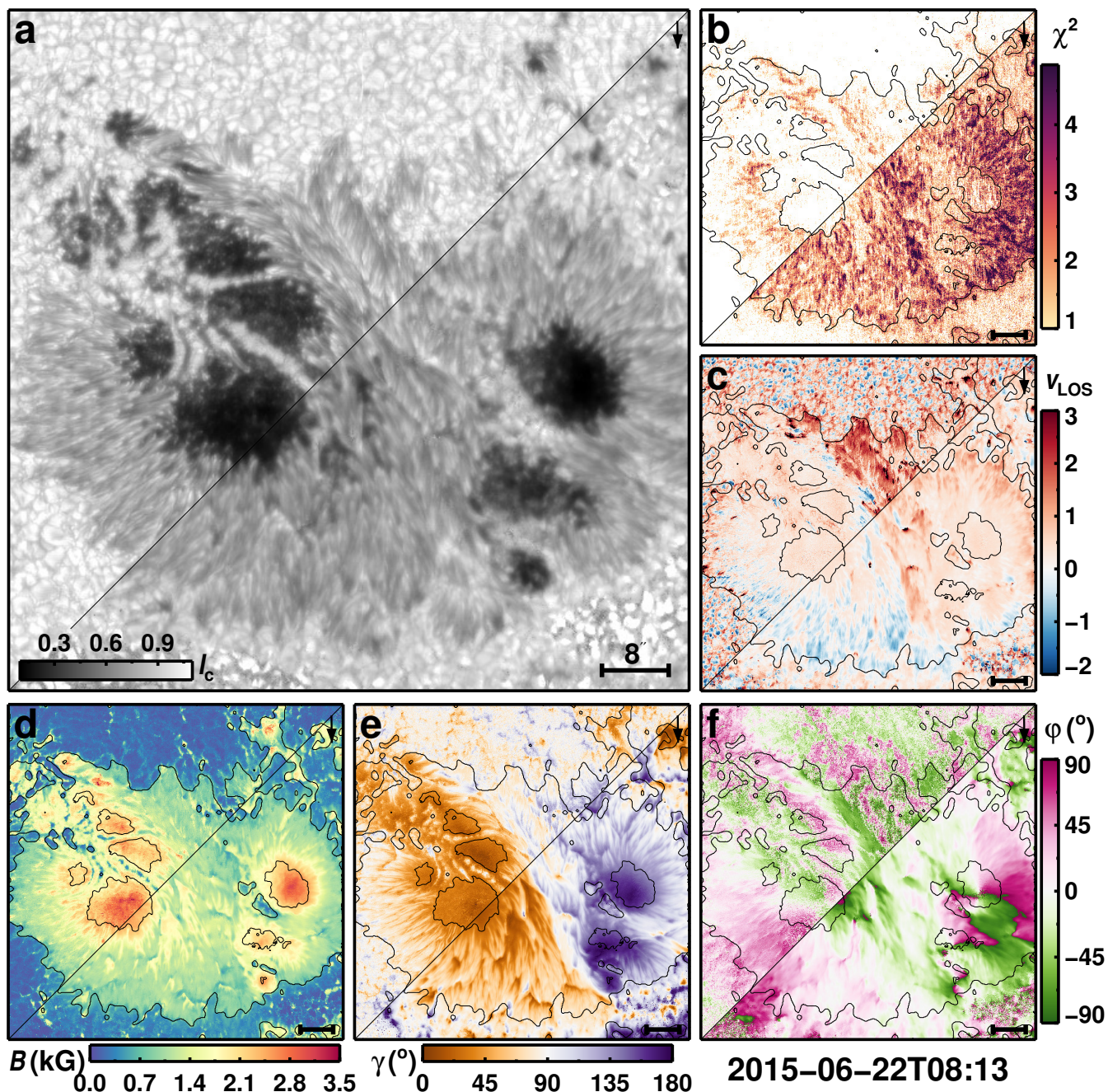


Fig. 9: Atmospheric maps of AR 12371 obtained with the spatially coupled inversions at the middle node ($\log \tau = -0.8$) (top-left half of each panel) and MERLIN (Level-2; bottom-right half). Panel (a) shows the best-fit continuum map. The atmospheric parameters retrieved by both inversion schemes are shown in the panels: (b) χ^2 -map, (c) line-of-sight velocity, (d) magnetic field strength, (e) magnetic field inclination relative to the line-of-sight, (f) azimuth relative to the line-of-sight. Atmospheric maps at the middle node were used for the coupled inversions. Horizontal bars on the bottom-right mark $8''$. This scan was observed in the normal mode with a pixel size of $0''.16$.

of a sunspot (AR 10930) that was located near the disk center. The main sunspot of AR 10930 is one of the largest spots in the sample. The pixels with the plotted profiles were chosen to sample umbra from warm ($I_c \approx 0.4 I_{qs}$; marked with the darkest blue color) to cold ($I_c \lesssim 0.15 I_{qs}$; marked with the lightest blue color). Vertical dashed lines in panel (11b) mark the most prominent (but by far not all the) molecular blends. At the lowest umbral temperatures, the Fe I line pair is of similar strength as the molecular lines, making it difficult for the inversion code to find the correct solution. Columns 2 to 5 show the observed Stokes vec-

tor and the obtained best fits. The blending molecular lines can make the identification of the correct position and splitting of the Fe I line pair at 6302 \AA difficult for the inversion code, potentially leading to errors in the field strength or the otherwise very robustly determined velocity. In Fig. 11v, the Stokes V of the Fe I line at 6302 \AA shows a “wobble” that the code sometimes fits by adding complexity to the atmosphere (e.g., unrealistically large line-of-sight velocities in umbrae). This “wobble” is thought to have a molecular origin, as it is not seen in the Fe I line at 6301 \AA .

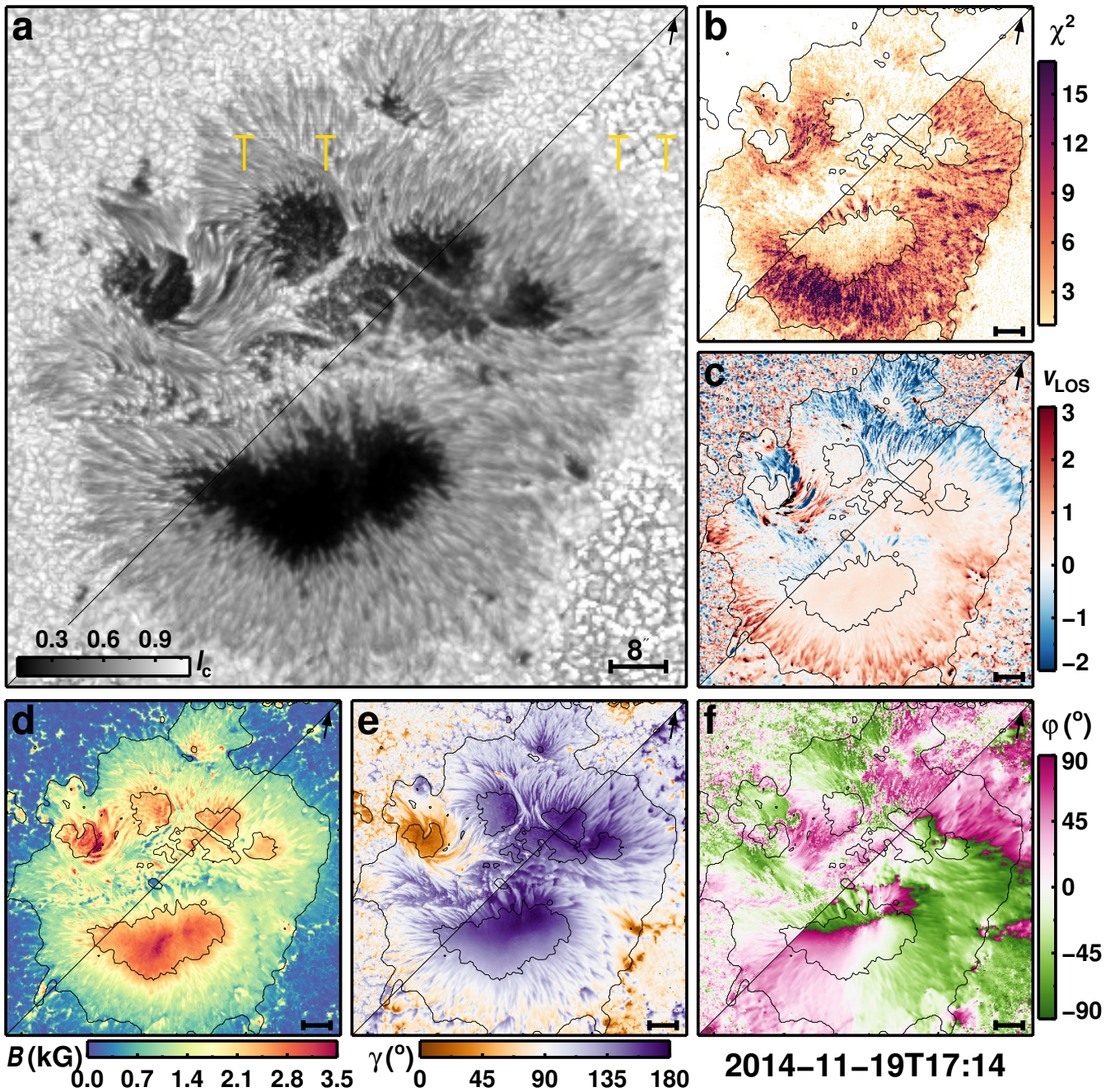


Fig. 10: Same as Fig. 9, but for of part of AR 12209. This scan was observed in the fast mode with a pixel size of $0''.32$.

Also, the continuum level is suppressed to an unknown value due to a molecular blend that appears at $\approx 6300.3 \text{ \AA}$. In addition to the molecular blends, the Fe I line pair 6302 \AA weakens in the coldest parts of umbrae due to their relatively high excitation potentials, making these lines not very sensitive to low temperatures (Smitha et al. 2021a). The issues presented by the appearance of molecular lines must be taken into account when analyzing the cold regions in sunspots. The user of the catalog must be aware of this issue and should use the inversion results from the regions where the spectra are affected by molecular lines with caution, or use masking techniques to avoid them completely.

Fortunately, umbral regions cold enough to form strong molecular lines do not appear too often on the Sun. In fact, pixels with low intensities $I_c < 0.15 I_{qs}$, where molecular blends

are sufficiently prominent to start affecting the inversion results, just represent 11.7% of all umbral pixels ($I_c \leq 0.5 I_{qs}$), and less than 0.7% of all pixels that are part of the MODEST catalog. All the same, these 11% of the umbrae are also the coldest and hence likely the parts with the strongest field strengths (see the relationship between temperature and field strength studied by, e.g., Kopp & Rabin (1992); Solanki et al. (1993); Mathew et al. (2004)), so that the properties of the strongest-field umbral regions may not be so reliable in MODEST as other parts of the sunspots.

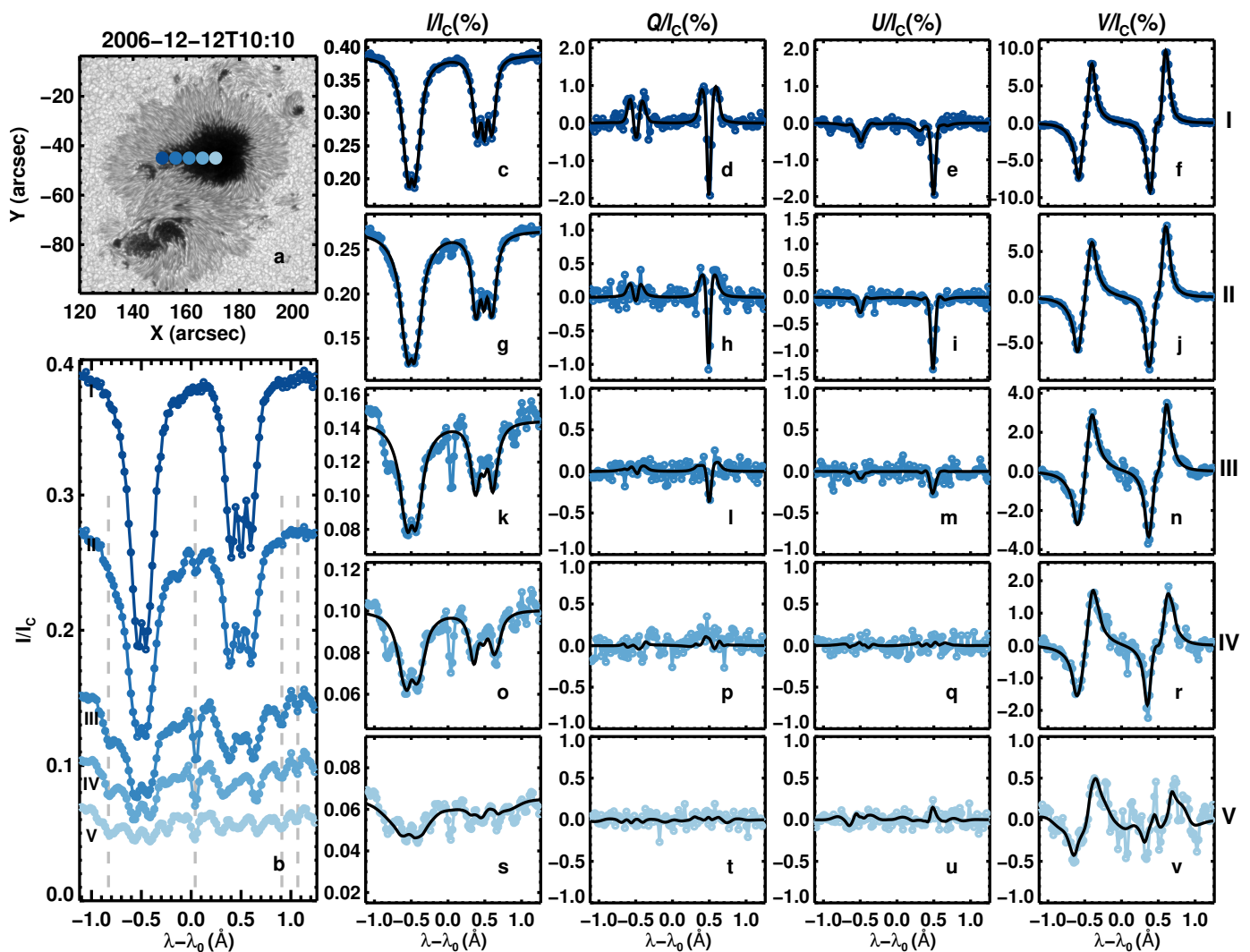


Fig. 11: Hinode/SOT-SP observations of AR 10930 observed almost at disk-center ($\mu = 0.99$). Panel (a) shows the continuum image. Blue circles overlotted on the continuum image mark the locations inside the umbra of the spectra plotted in the remaining panels, color-coded according to the region they were observed in. Lighter blue represents darker and cooler umbral regions, where blends with molecular lines appear. Panel (b) shows the five normalized Stokes $I(\lambda)$ profiles. The spectra are displayed on the same intensity scale for comparison (i.e. all spectra are normalized to the average quiet Sun continuum intensity). Dashed-gray vertical lines mark four prominent molecular blends identified at 6301.2 \AA , 6302.0 \AA , 6302.9 \AA , and 6303.1 \AA . Columns 2 to 5 (panels c-v) show the full observed Stokes vectors emerging at the same spatial pixels and the best fits found by the coupled inversions (black lines).

5.3. 180° disambiguation of the magnetic field

Measurements of the magnetic field based on the Zeeman effect have an intrinsic 180° ambiguity in the azimuthal angle of the component of the magnetic field transverse to the light-of-sight. Single-height-disambiguation techniques exist to solve the 180° ambiguity through minimizing a given parameter of the system (e.g., electric currents, free energy, etc. For a review see Leka et al. 2009). These single-height techniques are currently, to some extent, considered to be straightforward and they have been already automated for the ME-based inversions part of the SDO/HMI and Hinode/SOT-SP standard data products. These techniques work especially well in simple configurations but tend to struggle in more complex active regions. For example, the disambiguation techniques undergo problems in highly sheared regions and complex polarity inversion lines, which are present in many active regions.

Another more recently developed technique combines observations taken with different view-angles by two instruments (for example SO/PHI (Solanki et al. 2020) onboard Solar Orbiter (Müller et al. 2020) and Hinode/SOT-SP or SDO/HMI). This technique solves the 180° ambiguity by geometrical considerations without the need of minimizing any parameter (Valori et al. 2022, 2023). However, this technique also solves the 180° ambiguity at a single optical depth only, because of the limited number of wavelength points recorded by SO/PHI.

There is currently no standard technique available to properly disambiguate height-stratified inversions. Hence, current methods find the minimum of a given parameter for one height but these techniques do not find the global minimum for a stratified inversion. To avoid this problem, it is customary to disambiguate the data node by node, but that can easily result in inconsistent disambiguation for the different layers. If the sunspot is located close to the disk center and it is a relatively regular sunspot, the disambiguation can be applied to the middle node

and the same solutions can then be consistently applied to the other nodes. This choice assumes that the magnetic field does not change dramatically with height, which cannot be assumed in general. For example, it is expected that this approach will fail at the edges of facular magnetic concentrations, where the opposite polarity weak field lies under the expanding fields of the flux concentrations (see, e.g., [Buehler et al. 2015](#)). Similar problems are expected under the canopies surrounding sunspots.

Due to the current lack of an available disambiguation technique that fully accounts for the variation of the magnetic field with height, we opt, in this early phase of MODEST, to provide the magnetic field vector directly as it is obtained by the inversion, with the intrinsic 180° ambiguity. This also means that all quantities are given in the line-of-sight reference frame. Disambiguation codes can be easily found and the user of MODEST can select a map and apply a method of choice, bearing in mind the caveats given above.

5.4. Quality masks

After the inversion of a scan is fully converged, we create quality masks for that scan. Three different types of pixels are marked. These masks are not related to the quality of the fit to the observed Stokes vector, but rather to the integrity of each Hinode/SOT-SP scan. We define three quality levels:

- (I) Good-quality pixels
- (II) Medium-quality pixels. In rare events, there are sharp cuts found in the Hinode/SOT-SP data. These pixels in most cases are well fitted on both parts of the sharp cut. However, because of the coupled nature of the inversions, with the signal in nearby pixels being coupled to each other by the point spread function, we mark these places to warn the user that the results may be less reliable than for good-quality pixels. An example is shown on Fig. C.1 in Appendix C
- (III) Low-quality pixels. In a very small fraction of pixels, there are significant spikes in one of the Stokes profiles. These most likely come from cosmic rays or readout problems. As the inversion still finds the best possible fit to these pixels, including to the spike, unrealistic atmospheric conditions are retrieved in the pixel(s) and, due to the spatial coupling, their surroundings. All these types of pixels must be excluded from any type of analysis. An example is shown on Fig. C.2 in Appendix C.

Together, pixels of types (II) and (III) make up 0.07 % of all pixels within the catalog.

5.5. Residuals in the atmospheric maps

In some scans we observe a slight discontinuity of the atmospheric parameters for a certain pixel of the slit, resulting in spurious horizontal lines in the maps. These spurious residuals are best seen in the top node of the temperature maps, but they are also visible in the continuum maps. These spurious lines are most often located in the top part of the FOV (cf. Fig. 1 of [Tiwareti et al. 2013](#)). For some scans, these spurious lines can all be observed directly on the continuum maps of both, the coupled inversions and the standard Level-2 data. In Fig. 10 they are pointed out by the yellow marks on panel (10a). The dispersion of these residuals in the temperature maps is of the order of a few Kelvin, but it is difficult to separate this variation from the observed feature. This pattern highly resembles the Hinode/SOT-SP dark images (see Fig. 2 in [Lites & Ichimoto 2013](#)), and is seen

more often in scans taken after ~ 2014 . This might be an indication of some sort of degradation, but further analysis is needed. The magnitude of the residuals is small, so they could not be detected before the inversions. For the output of the inversion, we avoid removing these residuals ad-hoc and leave it up to the user of the catalog to either leave them as they are, or to apply a filter for their removal.

6. Summary and conclusions

In this paper, we introduced the MODEST catalog consisting of height-dependent maps of atmospheric parameters to study a wide range of phenomena in the photosphere of the Sun. The MODEST catalog encompasses all types of photospheric features, from umbral dots to network fields and quiet Sun regions. In addition, all types of sunspot groups from α -spots to complex δ ARs are covered by this catalog (Fig. 2). The catalog currently contains the outputs of inversion of 942 spatial scans by Hinode/SP of 117 individual sunspot groups, making a total of 1.4×10^8 spatial pixels with retrieved height-dependent physical conditions of the solar photosphere.

The large variety of scans, features, types of ARs, and locations on the solar disk that are contained in the MODEST catalog can be used to perform a range of studies, some of which are listed below. Thanks to the large number of inverted sunspots with height-dependent information, it may be possible to extend on existing studies.

- The photospheric structure of the penumbra (e.g., [Tiwareti et al. 2013, 2015](#)), its formation and temporal evolution on timescales of hours-days (e.g., [Scharmer et al. 2008](#); [Schlichenmaier et al. 2010](#); [Bello González et al. 2019](#)), as well as penumbral features such as penumbral grains (e.g., [Muller 1973a,b](#); [Sobotka et al. 1999](#); [Sobotka & Puschmann 2022](#); [Sobotka et al. 2023](#)) or orphan penumbrae (e.g., [Zirin & Wang 1991](#); [Löptien et al. 2023](#))
- Statistics of granular ([Vazquez 1973](#); [Lites et al. 1990, 1991](#); [Sobotka et al. 1993](#); [Roupe van der Voort et al. 2010](#); [Lagg et al. 2014](#); [Schlichenmaier et al. 2016](#); [Griñón-Marín et al. 2021](#)) and filamentary light bridges ([Adjabshirzadeh & Koutchmy 1980](#); [Rimmele 2008](#); [Katsukawa et al. 2007](#); [Guglielmino et al. 2017](#))
- Bipolar light bridges and the superstrong magnetic fields they harbor ([Zirin & Wang 1993](#); [Livingston et al. 2006](#); [Okamoto & Sakurai 2018](#); [Wang et al. 2018](#); [Castellanos Durán et al. 2020](#))
- The 3-D structure and evolution (on hours-days timescale) of the normal Evershed flow ([Evershed 1909](#); [Rimmele & Marino 2006](#)) and counter Evershed flow (e.g., [Schlichenmaier et al. 2011](#); [Kleint 2012](#); [Kleint & Sainz Dalda 2013](#); [Louis et al. 2014](#); [Siu-Tapia et al. 2017](#); [Castellanos Durán et al. 2021, 2023](#))
- Dependence of properties of sunspots on their size, shape, complexity, etc (e.g., [Collados et al. 1994](#); [Mathew et al. 2007](#); [Rezaei et al. 2012, 2015](#)). The physical structure of the umbra-penumbra boundary as a function of various sunspot parameters ([Jurčák 2011](#); [Jurčák et al. 2018](#); [Lindner et al. 2020](#); [Löptien et al. 2020b](#); [García-Rivas et al. 2021](#))
- Properties of the granulation (velocities, contrast, sizes, etc. as a function of height) (e.g., [Danilovic et al. 2008](#); [Hirzberger et al. 2010](#); [Ishikawa et al. 2020](#)), and of small-scale magnetic features (e.g., [Buehler et al. 2015, 2019](#); [Kahil et al. 2017, 2019](#)).

- Study changes in sunspot or granulation properties, or the amount of magnetic flux over the ~ 1.5 solar cycles that are currently covered by MODEST (see e.g., Muller & Roudier 1984; Mathew et al. 2007; Livingston et al. 2012; Buehler et al. 2013; Lites et al. 2014; Kiess et al. 2014)
- Use the large sample of ARs at different μ -values, for example, to train artificial neural networks (Carroll & Staude 2001; Socas-Navarro 2005; Asensio Ramos & Díaz Baso 2019; Milić & Gafeira 2020; Liu et al. 2020; Socas-Navarro & Asensio Ramos 2021; Centeno et al. 2022)
- The connection between flares and the detailed properties of underlying sunspots (e.g., Shimizu et al. 2014; Toriumi & Wang 2019; Yardley et al. 2022).

The spatially coupled inversions effectively retrieve excellent fits to the observed Stokes profiles for all kinds of solar features, almost irrespective of the complexity of the measured Stokes profile. Only in the very cold umbra are the inversions of lower quality, caused by the intrinsic problem of molecular lines appearing in the spectral window observed by Hinode/SOT-SP. In addition, recent works have demonstrated the significance of considering non-LTE effects on the formation of Iron lines in the photosphere (Smitha et al. 2020, 2021b, 2023). Compared to LTE-treated Stokes profiles, non-LTE Stokes profiles showed significant differences. In order to fully assert how non-LTE effects impact the retrieved atmospheric conditions, additional work is required.

Besides inverting the Hinode/SOT-SP scans of a larger number of active regions, additional improvements are conceivable. For example, modeling molecular lines and implementing them into the inversion procedure could improve the results obtained for the darkest parts of umbrae. The development and application of a disambiguation technique that covers the height dependence would open up new applications.

Observatory – Hinode (SOT-SP)

Computing facilities – HPC-GWDG (Göttingen, Germany), HPC-MPS (Göttingen, Germany), and HPC-MPCDF (Garching, Germany).

Acknowledgements. We are grateful to Rebecca Centeno Elliott for providing the MERLIN input files that were used to obtain synthetic Stokes profiles of standard Level-2 inversions. We thank Stephan Thoma (MPS) for his continuous support and development of a web-application to access the catalog. J. S. Castellanos Durán was funded by the Deutscher Akademischer Austauschdienst (DAAD) and the International Max Planck Research School (IMPRS) for Solar System Science at the University of Göttingen. This project has received funding from the European Research Council (ERC) under the European Union's Horizon 2020 research and innovation program (grant agreement No. 695075). Hinode is a Japanese mission developed and launched by ISAS/JAXA, with NAOJ as domestic partner and NASA and UKSA as international partners. It is operated by these agencies in cooperation with ESA and NSC (Norway).

References

Adjabshirzadeh, A. & Koutchmy, S. 1980, *A&A*, 89, 88
 Asensio Ramos, A. & Díaz Baso, C. J. 2019, *A&A*, 626, A102
 Asensio Ramos, A., Trujillo Bueno, J., & Collados, M. 2004, *ApJ*, 603, L125
 Bello González, N., Jurčák, J., Schlichenmaier, R., & Rezaei, R. 2019, in *Astronomical Society of the Pacific Conference Series*, Vol. 526, *Solar Polarization Workshop 8*, ed. L. Belluzzi, R. Casini, M. Romoli, & J. Trujillo Bueno, 261
 Bellot Rubio, L. R., Balthasar, H., Collados, M., & Schlichenmaier, R. 2003, *A&A*, 403, L47
 Berdyugina, S. V. 2011, in *Astronomical Society of the Pacific Conference Series*, Vol. 437, *Solar Polarization 6*, ed. J. R. Kuhn, D. M. Harrington, H. Lin, S. V. Berdyugina, J. Trujillo-Bueno, S. L. Keil, & T. Rimmele, 219
 Berdyugina, S. V., Braun, P. A., Fluri, D. M., & Solanki, S. K. 2005, *A&A*, 444, 947
 Berdyugina, S. V. & Solanki, S. K. 2002, *A&A*, 385, 701
 Berdyugina, S. V., Solanki, S. K., & Frutiger, C. 2003, *A&A*, 412, 513

Bianda, M., Solanki, S. K., & Stenflo, J. O. 1998, *A&A*, 331, 760
 Borrero, J. M. & Ichimoto, K. 2011, *Living Reviews in Solar Physics*, 8, 4
 Borrero, J. M., Tomczyk, S., Kubo, M., et al. 2011, *Sol. Phys.*, 273, 267
 Brault, J. W. 1976, *Journal of the Optical Society of America* (1917-1983), 66, 1081
 Brault, J. W. 1978, in *Future solar optical observations needs and constraints*, ed. G. Godoli, Vol. 106, 33
 Buehler, D., Lagg, A., & Solanki, S. K. 2013, *A&A*, 555, A33
 Buehler, D., Lagg, A., Solanki, S. K., & van Noort, M. 2015, *A&A*, 576, A27
 Buehler, D., Lagg, A., van Noort, M., & Solanki, S. K. 2019, *A&A*, 630, A86
 Carroll, T. A. & Staude, J. 2001, *A&A*, 378, 316
 Castellanos Durán, J. S. 2022, PhD thesis, University of Göttingen
 Castellanos Durán, J. S., Korpi-Lagg, A., & Solanki, S. K. 2023, *ApJ*, 952, 162
 Castellanos Durán, J. S., Lagg, A., & Solanki, S. K. 2021, *A&A*, 651, L1
 Castellanos Durán, J. S., Lagg, A., Solanki, S. K., & Noort, M. v. 2020, *ApJ*, 895, 129
 Centeno, R., Flyer, N., Mukherjee, L., et al. 2022, *ApJ*, 925, 176
 Collados, M., Martínez Pillet, V., Ruiz Cobo, B., del Toro Iniesta, J. C., & Vazquez, M. 1994, *A&A*, 291, 622
 Community Spectropolarimetric Analysis Center. 2006, *Hinode-Spectropolarimeter (SP) Level 2 (vector magnetic field) spectral line inversions*
 Danilovic, S., Gandorfer, A., Lagg, A., et al. 2008, *A&A*, 484, L17
 Danilovic, S., van Noort, M., & Rempel, M. 2016, *A&A*, 593, A93
 de la Cruz Rodríguez, J. 2019, *A&A*, 631, A153
 de la Cruz Rodríguez, J. & van Noort, M. 2017, *Space Sci. Rev.*, 210, 109
 del Toro Iniesta, J. C., Bellot Rubio, L. R., & Collados, M. 2001, *ApJ*, 549, L139
 del Toro Iniesta, J. C. & Ruiz Cobo, B. 2016, *Living Reviews in Solar Physics*, 13, 4
 Esteban Pozuelo, S., Bellot Rubio, L. R., & de la Cruz Rodríguez, J. 2016, *ApJ*, 832, 170
 Evershed, J. 1909, *MNRAS*, 69, 454
 Fouhey, D. F., Higgins, R. E. L., Antiochos, S. K., et al. 2022, arXiv e-prints, arXiv:2209.15036
 Frutiger, C. 2000, PhD thesis, ETH, Zürich
 Frutiger, C., Solanki, S. K., Fligge, M., & Bruls, J. H. M. J. 2000, *A&A*, 358, 1109
 García-Rivas, M., Jurčák, J., & Bello González, N. 2021, *A&A*, 649, A129
 Griñón-Marín, A. B., Pastor Yabar, A., Centeno, R., & Socas-Navarro, H. 2021, *A&A*, 647, A148
 Guglielmino, S. L., Romano, P., & Zuccarello, F. 2017, *ApJ*, 846, L16
 Hale, G. E., Ellerman, F., Nicholson, S. B., & Joy, A. H. 1919, *ApJ*, 49, 153
 Hirzberger, J., Feller, A., Riethmüller, T. L., et al. 2010, *ApJ*, 723, L154
 Ichimoto, K., Lites, B., Elmore, D., et al. 2008, *Sol. Phys.*, 249, 233
 Ishikawa, R. T., Katsukawa, Y., Oba, T., et al. 2020, *ApJ*, 890, 138
 Jurčák, J. 2011, *A&A*, 531, A118
 Jurčák, J. & Katsukawa, Y. 2010, *A&A*, 524, A21
 Jurčák, J., Rezaei, R., González, N. B., Schlichenmaier, R., & Vomlel, J. 2018, *A&A*, 611, L4
 Kabil, F., Riethmüller, T. L., & Solanki, S. K. 2017, *ApJS*, 229, 12
 Kabil, F., Riethmüller, T. L., & Solanki, S. K. 2019, *A&A*, 621, A78
 Katsukawa, Y. & Jurčák, J. 2010, *A&A*, 524, A20
 Katsukawa, Y., Yokoyama, T., Berger, T. E., et al. 2007, *PASJ*, 59, S577
 Kiess, C., Rezaei, R., & Schmidt, W. 2014, *A&A*, 565, A52
 Kleint, L. 2012, *ApJ*, 748, 138
 Kleint, L. & Sainz Dalda, A. 2013, *ApJ*, 770, 74
 Kopp, G. & Rabin, D. 1992, *Sol. Phys.*, 141, 253
 Kosugi, T., Matsuzaki, K., Sakao, T., et al. 2007, *Sol. Phys.*, 243, 3
 Künzel, H. 1960, *Astronomische Nachrichten*, 285, 271
 Künzel, H. 1965, *Astronomische Nachrichten*, 288, 177
 Lagg, A., Ishikawa, R., Merenda, L., et al. 2009, in *Astronomical Society of the Pacific Conference Series*, Vol. 415, *The Second Hinode Science Meeting: Beyond Discovery-Toward Understanding*, ed. B. Lites, M. Cheung, T. Magara, J. Mariska, & K. Reeves, 327
 Lagg, A., Solanki, S. K., van Noort, M., & Danilovic, S. 2014, *A&A*, 568, A60
 Lagg, A., Woch, J., Krupp, N., & Solanki, S. K. 2004, *A&A*, 414, 1109
 Langhans, K., Scharmer, G. B., Kiselman, D., Löfdahl, M. G., & Berger, T. E. 2005, *A&A*, 436, 1087
 Leka, K. D., Barnes, G., Crouch, A. D., et al. 2009, *Sol. Phys.*, 260, 83
 Levenberg, K. 1944, *Quar. Appl. Math.*, 2, 164
 Lindner, P., Schlichenmaier, R., & Bello González, N. 2020, *A&A*, 638, A25
 Lites, B. W., Bida, T. A., Johannesson, A., & Scharmer, G. B. 1991, *ApJ*, 373, 683
 Lites, B. W., Centeno, R., & McIntosh, S. W. 2014, *PASJ*, 66, S4
 Lites, B. W., Elmore, D. F., Seagraves, P., & Skumanich, A. P. 1993, *ApJ*, 418, 928
 Lites, B. W. & Ichimoto, K. 2013, *Sol. Phys.*, 283, 601
 Lites, B. W., Scharmer, G. B., & Skumanich, A. 1990, *ApJ*, 355, 329
 Liu, H., Xu, Y., Wang, J., et al. 2020, *ApJ*, 894, 70

- Livingston, W., Harvey, J. W., Malanushenko, O. V., & Webster, L. 2006, *Sol. Phys.*, 239, 41
- Livingston, W., Penn, M. J., & Svalgaard, L. 2012, *ApJ*, 757, L8
- Löptien, B., Castellanos Durán, J. S., Lagg-Korpi, A., van Noort, M., & Solanki, S. K. 2023, submitted to A&A
- Löptien, B., Lagg, A., van Noort, M., & Solanki, S. K. 2018, *A&A*, 619, A42
- Löptien, B., Lagg, A., van Noort, M., & Solanki, S. K. 2020a, *A&A*, 635, A202
- Löptien, B., Lagg, A., van Noort, M., & Solanki, S. K. 2020b, *A&A*, 639, A106
- Louis, R. E., Beck, C., Mathew, S. K., & Venkatakrishnan, P. 2014, *A&A*, 570, A92
- Marquardt, D. W. 1963, *SIAM J. Appl. Math.*, 11, 431
- Mathew, S. K., Martínez Pillet, V., Solanki, S. K., & Krivova, N. A. 2007, *A&A*, 465, 291
- Mathew, S. K., Solanki, S. K., Lagg, A., et al. 2004, *A&A*, 422, 693
- McIntosh, P. S. 1990, *Sol. Phys.*, 125, 251
- Milić, I. & Gafeira, R. 2020, *A&A*, 644, A129
- Milić, I. & van Noort, M. 2018, *A&A*, 617, A24
- Müller, D., St. Cyr, O. C., Zouganelis, I., et al. 2020, *A&A*, 642, A1
- Muller, R. 1973a, *Sol. Phys.*, 29, 55
- Muller, R. 1973b, *Sol. Phys.*, 32, 409
- Muller, R. & Roudier, T. 1984, *Sol. Phys.*, 94, 33
- Okamoto, T. J. & Sakurai, T. 2018, *ApJ*, 852, L16
- Orozco Suárez, D., Bellot Rubio, L. R., Vögler, A., & Del Toro Iniesta, J. C. 2010, *A&A*, 518, A2
- Rachkovsky, D. N. 1962, *Izvestiya Ordena Trudovogo Krasnogo Znameni Krymskoj Astrofizicheskoj Observatorii*, 28, 259
- Rachkovsky, D. N. 1967, *Izvestiya Ordena Trudovogo Krasnogo Znameni Krymskoj Astrofizicheskoj Observatorii*, 37, 56
- Rezaei, R., Beck, C., Lagg, A., et al. 2015, *A&A*, 578, A43
- Rezaei, R., Beck, C., & Schmidt, W. 2012, *A&A*, 541, A60
- Riethmüller, T. L., Solanki, S. K., & Lagg, A. 2008, *ApJ*, 678, L157
- Riethmüller, T. L., Solanki, S. K., van Noort, M., & Tiwari, S. K. 2013, *A&A*, 554, A53
- Rimmele, T. 2008, *ApJ*, 672, 684
- Rimmele, T. & Marino, J. 2006, *ApJ*, 646, 593
- Roupe van der Voort, L., Bellot Rubio, L. R., & Ortiz, A. 2010, *ApJ*, 718, L78
- Roupe van der Voort, L. H. M., De Pontieu, B., Carlsson, M., et al. 2020, *A&A*, 641, A146
- Rüedi, I., Solanki, S. K., & Livingston, W. C. 1995, *A&A*, 293, 252
- Ruiz Cobo, B. & del Toro Iniesta, J. C. 1992, *ApJ*, 398, 375
- Scharmer, G. B., Nordlund, Å., & Heinemann, T. 2008, *ApJ*, 677, L149
- Schlichenmaier, R., González, N. B., & Rezaei, R. 2011, in *Physics of Sun and Star Spots*, ed. D. Prasad Choudhary & K. G. Strassmeier, Vol. 273, 134–140
- Schlichenmaier, R., Rezaei, R., Bello González, N., & Waldmann, T. A. 2010, *A&A*, 512, L1
- Schlichenmaier, R., von der Lühe, O., Hoch, S., et al. 2016, *A&A*, 596, A7
- Schmidt, W., Hofmann, A., Balthasar, H., Tarbell, T. D., & Frank, Z. A. 1992, *A&A*, 264, L27
- Shimizu, T., Lites, B. W., & Bamba, Y. 2014, *PASJ*, 66, S14
- Sigwarth, M., Balasubramaniam, K. S., Knölker, M., & Schmidt, W. 1999, *A&A*, 349, 941
- Siu-Tapia, A., Lagg, A., Solanki, S. K., van Noort, M., & Jurčák, J. 2017, *A&A*, 607, A36
- Siu-Tapia, A., Lagg, A., van Noort, M., Rempel, M., & Solanki, S. K. 2019, *A&A*, 631, A99
- Skumanich, A. & Lites, B. W. 1987, *ApJ*, 322, 473
- Smitha, H. N., Castellanos Durán, J. S., Solanki, S. K., & Tiwari, S. K. 2021a, *A&A*, 653, A91
- Smitha, H. N., Holzreuter, R., van Noort, M., & Solanki, S. K. 2020, *A&A*, 633, A157
- Smitha, H. N., Holzreuter, R., van Noort, M., & Solanki, S. K. 2021b, *A&A*, 647, A46
- Smitha, H. N., van Noort, M., Solanki, S. K., & Castellanos Durán, J. S. 2023, *A&A*, 669, A144
- Sobotka, M., Bonet, J. A., & Vazquez, M. 1993, *ApJ*, 415, 832
- Sobotka, M., Brandt, P. N., & Simon, G. W. 1999, *A&A*, 348, 621
- Sobotka, M., Jurčák, J., Castellanos Durán, J. S., & García-Rivas, M. 2023, *A&ASubmitted*
- Sobotka, M. & Puschmann, K. G. 2022, *A&A*, 662, A13
- Socas-Navarro, H. 2005, *ApJ*, 621, 545
- Socas-Navarro, H. & Asensio Ramos, A. 2021, *A&A*, 652, A78
- Socas-Navarro, H., de la Cruz Rodríguez, J., Asensio Ramos, A., Trujillo Bueno, J., & Ruiz Cobo, B. 2015, *A&A*, 577, A7
- Socas-Navarro, H., Martínez Pillet, V., Sobotka, M., & Vázquez, M. 2004, *ApJ*, 614, 448
- Socas-Navarro, H., Ruiz Cobo, B., & Trujillo Bueno, J. 1998, *ApJ*, 507, 470
- Solanki, S. K. 1987, PhD thesis, ETH, Zürich
- Solanki, S. K. 2003, *A&A Rev.*, 11, 153
- Solanki, S. K., del Toro Iniesta, J. C., Woch, J., et al. 2020, *A&A*, 642, A11
- Solanki, S. K. & Montavon, C. A. P. 1993, *A&A*, 275, 283
- Solanki, S. K. & Pahlke, K. D. 1988, *A&A*, 201, 143
- Solanki, S. K. & Stenflo, J. O. 1984, *A&A*, 140, 185
- Solanki, S. K. & Stenflo, J. O. 1985, *A&A*, 148, 123
- Solanki, S. K., Walther, U., & Livingston, W. 1993, *A&A*, 277, 639
- Sowmya, K., Lagg, A., Solanki, S. K., & Castellanos Durán, J. S. 2022, *A&A*, 661, A122
- Title, A. M., Frank, Z. A., Shine, R. A., et al. 1993, *ApJ*, 403, 780
- Tiwari, S. K., van Noort, M., Lagg, A., & Solanki, S. K. 2013, *A&A*, 557, A25
- Tiwari, S. K., van Noort, M., Solanki, S. K., & Lagg, A. 2015, *A&A*, 583, A119
- Toriumi, S. & Wang, H. 2019, *Living Reviews in Solar Physics*, 16, 3
- Tsuneta, S., Ichimoto, K., Katsukawa, Y., et al. 2008, *Sol. Phys.*, 249, 167
- Unno, W. 1956, *PASJ*, 8, 108
- Valori, G., Calchetti, D., Moreno Vacas, A., et al. 2023, *A&A*, 677, A25
- Valori, G., Löschl, P., Stansby, D., et al. 2022, *Sol. Phys.*, 297, 12
- van Noort, M. 2012, *A&A*, 548, A5
- van Noort, M. 2017, *A&A*, 608, A76
- van Noort, M., Lagg, A., Tiwari, S. K., & Solanki, S. K. 2013, *A&A*, 557, A24
- Vazquez, M. 1973, *Sol. Phys.*, 31, 377
- Wang, H., Yurchyshyn, V., Liu, C., et al. 2018, *Research Notes of the American Astronomical Society*, 2, 8
- Yardley, S. L., Green, L. M., James, A. W., Stansby, D., & Mihailescu, T. 2022, *ApJ*, 937, 57
- Zirin, H. & Wang, H. 1991, *Advances in Space Research*, 11, 225
- Zirin, H. & Wang, H. 1993, *Sol. Phys.*, 144, 37

Appendix A: Spectral stray light and spurious polarization

We tested the influence of the spectral stray light on the atmospheric parameters retrieved by the inversions. We used Hinode/SOT-SP data of the quiet sun taken at disk center and compared it to the National Solar Observatory/Kitt Peak Fourier Transform Spectrometer atlas (FTS; Brault 1976, 1978). We found that the spectral stray light is up to $\zeta \sim 3\%$, which is consistent with the nominal values found by Lites & Ichimoto (2013). We chose a test FOV that contains quiet Sun, a small pore, part penumbra and umbra. We calibrated this FOV using the nominal Hinode/SOT-SP data, and created two datacubes: one with the nominal calibration, and another with $\zeta = 3\%$ spectral stray light subtracted. To apply this subtraction, we followed the approach described in Bianda et al. (1998). The corrected Stokes $I(\lambda)$ is given by

$$\left(\frac{I(\lambda)}{I_c}\right) = (1 + \zeta) \frac{I(\lambda)^{\text{corr}}}{I_c} - \zeta, \quad (\text{A.1})$$

where I_c is the continuum intensity. The corresponding Stokes profiles for the linear ($F_{Q,U}(\lambda)$) and circular polarization ($F_V(\lambda)$) are

$$F_{Q,U,V}(\lambda) = F_{Q,U,V}^{\text{corr}}(\lambda) + k_{Q,U,V}I(\lambda), \quad (\text{A.2})$$

$k_{Q,U,V}$ is the spurious polarization. $k_{Q,U,V}$ is usually well corrected by the `sp_prep` routines (Lites & Ichimoto 2013), however, it has been shown that $k_{Q,U,V}$ are not negligible in extreme cases (Okamoto & Sakurai 2018). Combining Eqs. (A.1)-(A.2), the corrected Stokes profiles are

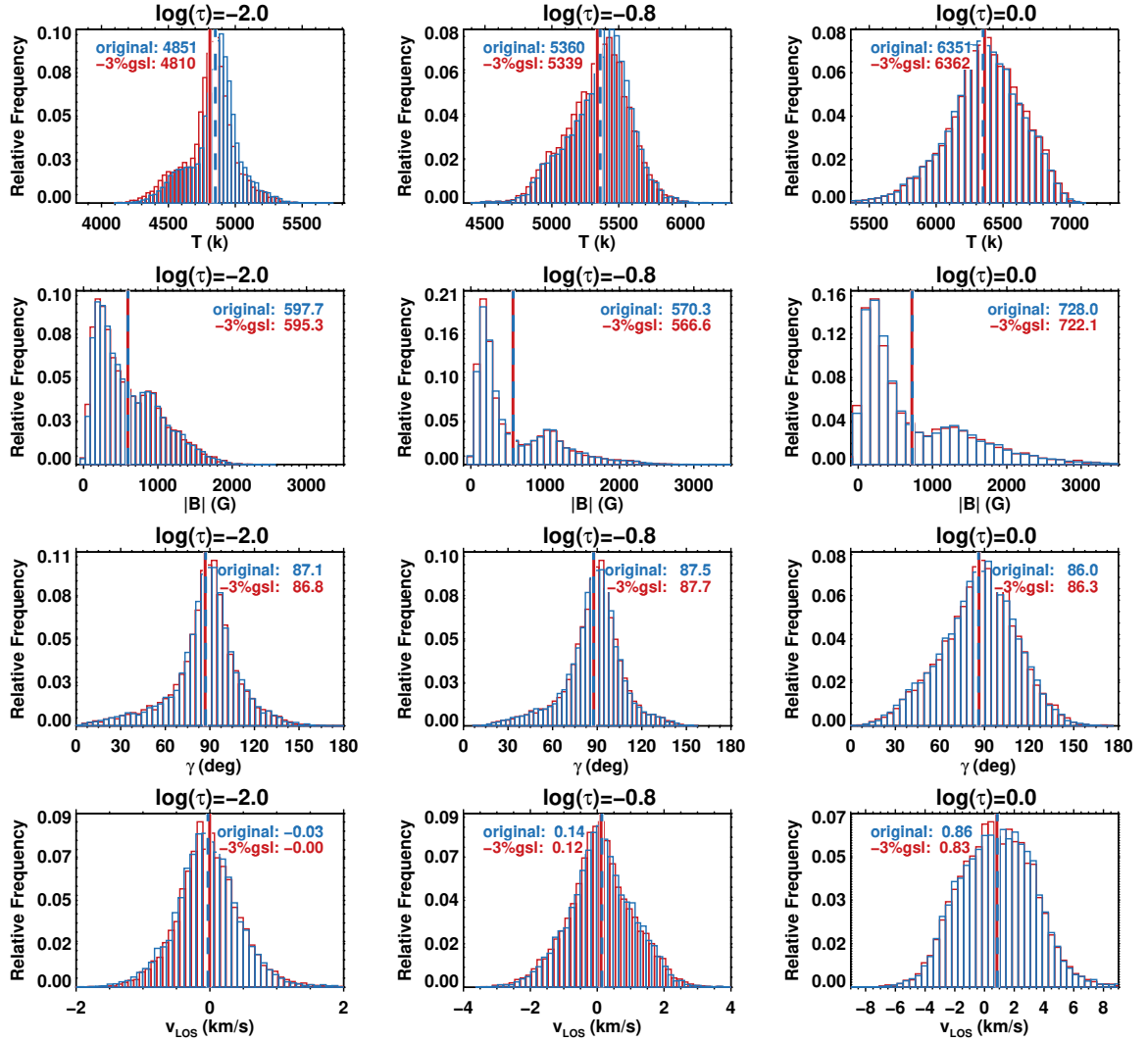


Fig. A.1: Effects of the gray stray light. Each column shows the retrieved atmospheric conditions for each node. Plotted from top to bottom rows are: the retrieved temperature, B , γ , and v_{LoS} . Results obtained from the original Hinode/SOT-SP data are in blue, and data corrected with 3% -level of gray stray light are red.

$$\left(\frac{F_{Q,U,V}(\lambda)}{I_c}\right)^{\text{corr}} = \frac{F_{Q,U,V}(\lambda)}{I_c \left(1 - \frac{\zeta}{1+\zeta}\right)}. \quad (\text{A.3})$$

Figure A.1 shows the results of this test, where labels “original” and “-3%gs!” mark the two datacubes. Panels in Fig. A.1 show the histograms of the same atmospheric quantity. No strong variation was observed with and without the 3% gray stray light. Based on these findings and as the gray stray light might change over time, no correction of this type was applied.

Appendix B: Effects of tiling the FOV

Splitting the FOV into multiple tiles was necessary to invert large Hinode/SOT-SP scans because of the high-computational demand of the coupled inversions, mainly in terms of memory usage. To mitigate boundary effects, the tiles need to overlap sufficiently. We chose this overlap region to be 3 times the FWHM of the PSF. In this appendix, we demonstrate that the tiling with this large spatial overlap does not produce any artifacts to the inversion results.

Figure B.1 shows an experiment where the same scan was inverted using two different approaches. The first inversion was performed for the full FOV without any tiling (B.1a). The second inversion used the same tiling scheme as in MODEST, and the FOV was divided into 16 tiles (B.1b). This scan was chosen because all types of features are present (the quiet Sun, penumbrae, and umbrae) in the area where the tiles are stitched together. These inversions were carried out following the same steps as in Secs. 3.1-3.3.

The results of these inversions are shown in Fig. B.1. Panels (B.1c) to (B.1f) depict the scatter plots of the retrieved atmospheric conditions for the three nodes combined. The abscissa results of the inversion where the FOV was divided, while the ordinate displays the inversion of the non-tiled FOV. Insets within panels (c)-(f) show the scatter of the difference between the atmospheric quantities from the two inversions for the three-node heights. The differences are Gaussian with a 1σ -level of 43 K for the temperature, 157 G for the magnetic field strength 0.6 km s^{-1} for the line-of-sight velocity, and 11 deg for the line-of-sight inclination of the magnetic field. As expected, the magnetic-field-inclination scatter is the largest. The match between the two inversions reveals that the effect of tiling the FOV is small.

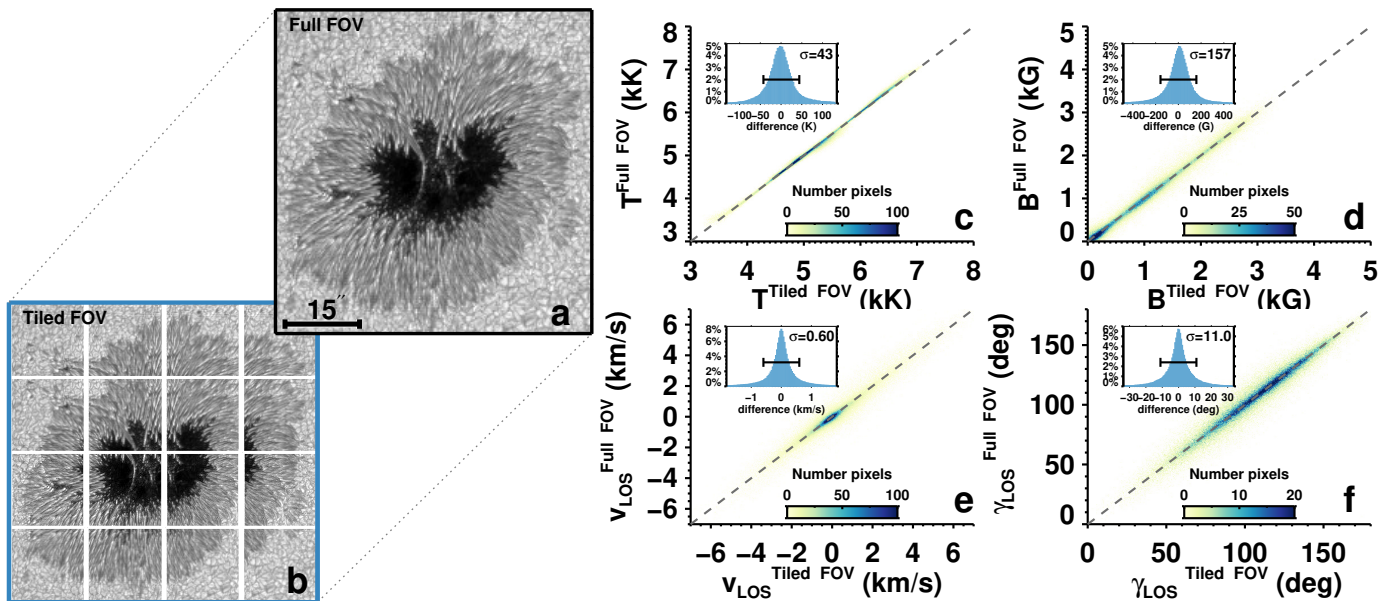


Fig. B.1: Effects of tiling the FOV. Panel (a) shows the full untiled continuum image of the AR 11748 when it was located close to disk center. Panel (b) shows the FOV broken up into overlapping tiles. The edges of each tile are marked by the white lines FOV. Scatter plots of atmospheric parameters obtained with or without the tiling are displayed in Panels (c)-(d). Data points from all three optical depth nodes are plotted in each panel. The individual panels display the temperature (c), magnetic field strength (d), line-of-sight velocity (e), and line-of-sight inclination of the magnetic field (f). The x -axis displays the inversions performed with the tiled FOV, while the y -axis shows the inversions for the whole FOV inverted in one go for the three-node height. The insets inside panels (c)-(f) show the histograms of differences between the two inversions, where the black bars indicate 1σ .

Appendix C: Medium- and low-quality pixels

Figures C.1 and C.2 show examples of pixels, which are likely affected by instrumental or data reduction artifacts, making them of only medium or low quality (see Sect. 5.4). The medium-quality pixels can easily be identified in maps of the Stokes parameters, and also in the corresponding maps of the inverted parameters, as sharp discontinuities in the vertical or horizontal direction.

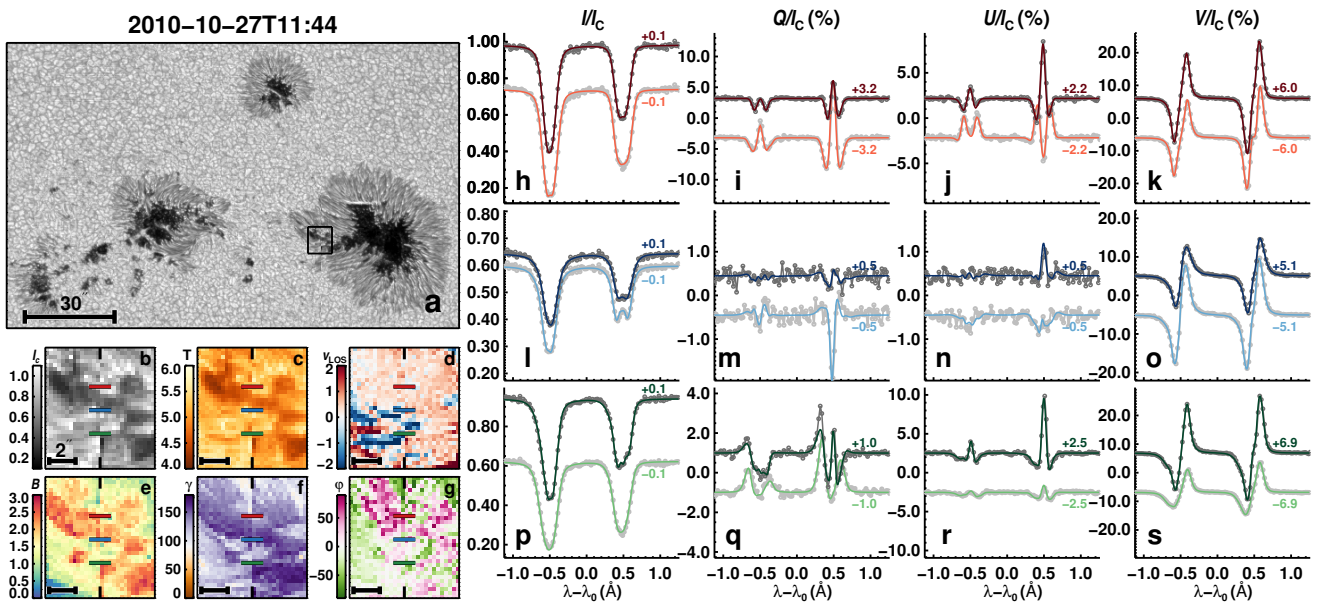


Fig. C.1: Fits obtained by the coupled inversions to the observed Stokes profiles for medium-quality pixels. Panel (a) shows the continuum image of the AR 11117 when it was located at $\mu \approx 0.9$. Maps in panels (b) to (g) display the continuum intensity (b), temperature (c), v_{LOS} (d), magnetic field strength (e), inclination (f), and azimuth (g). These maps are from the region outlined by the black rectangle in panel (a). Columns 2 to 5 show the observed Stokes profiles (gray dotted lines) and the best fits obtained by the coupled inversions (colored lines). A vertical shift was added to the Stokes profiles for better representation. The shift values are displayed on the right side of each profile. Each row shows two Stokes vectors coming from neighboring pixels lying immediately to the left (darker lines) and to the right (lighter lines) of a sharp discontinuity in the data (indicated by black vertical tickmarks in (b)–(g)). Colored horizontal lines in panels (b) to (g) mark the locations of the profiles. $\lambda_0 = 6302 \text{ \AA}$.

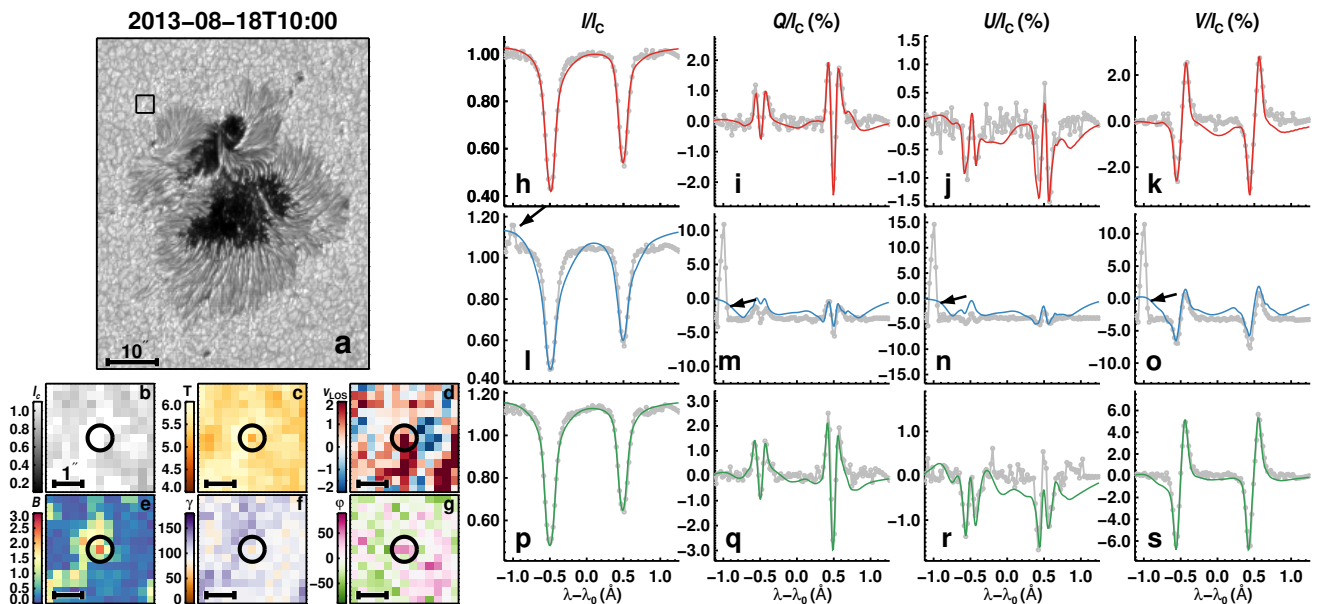


Fig. C.2: A low-quality pixel. Same as Fig. C.1 for a sunspot group belonging to AR 11818, when it was located at $\mu \approx 0.76$. The open circles mark the location of the low-quality pixel. Black arrows in panels (l) to (o) mark an artifact likely produced by a cosmic ray which strongly influences the fits.

Figure C.1 shows the atmospheric maps and the fits on both sides of one such discontinuity. The Stokes profiles are well-fitted as is common for medium-quality pixels. However, the fit values are likely not as reliable as for normal pixels due to the coupling of the pixels on both sides of the divide by the PSF.

Figure C.2 shows an example of a low-quality pixel. There are spikes in the Stokes profiles (black arrows in panels C.21 – C.2o). Especially in the polarized Stokes profiles the spike is much larger than the actual solar signals. The inversion still tries to invert this pixel and its surroundings (red and green profiles), but poor fits and unrealistic atmospheric conditions are retrieved in these pixels and in its surroundings (the latter again due to the coupling via the PSF).

Appendix D: Sample of sunspot groups observed by Hinode/SOT-SP part of the MODEST catalog

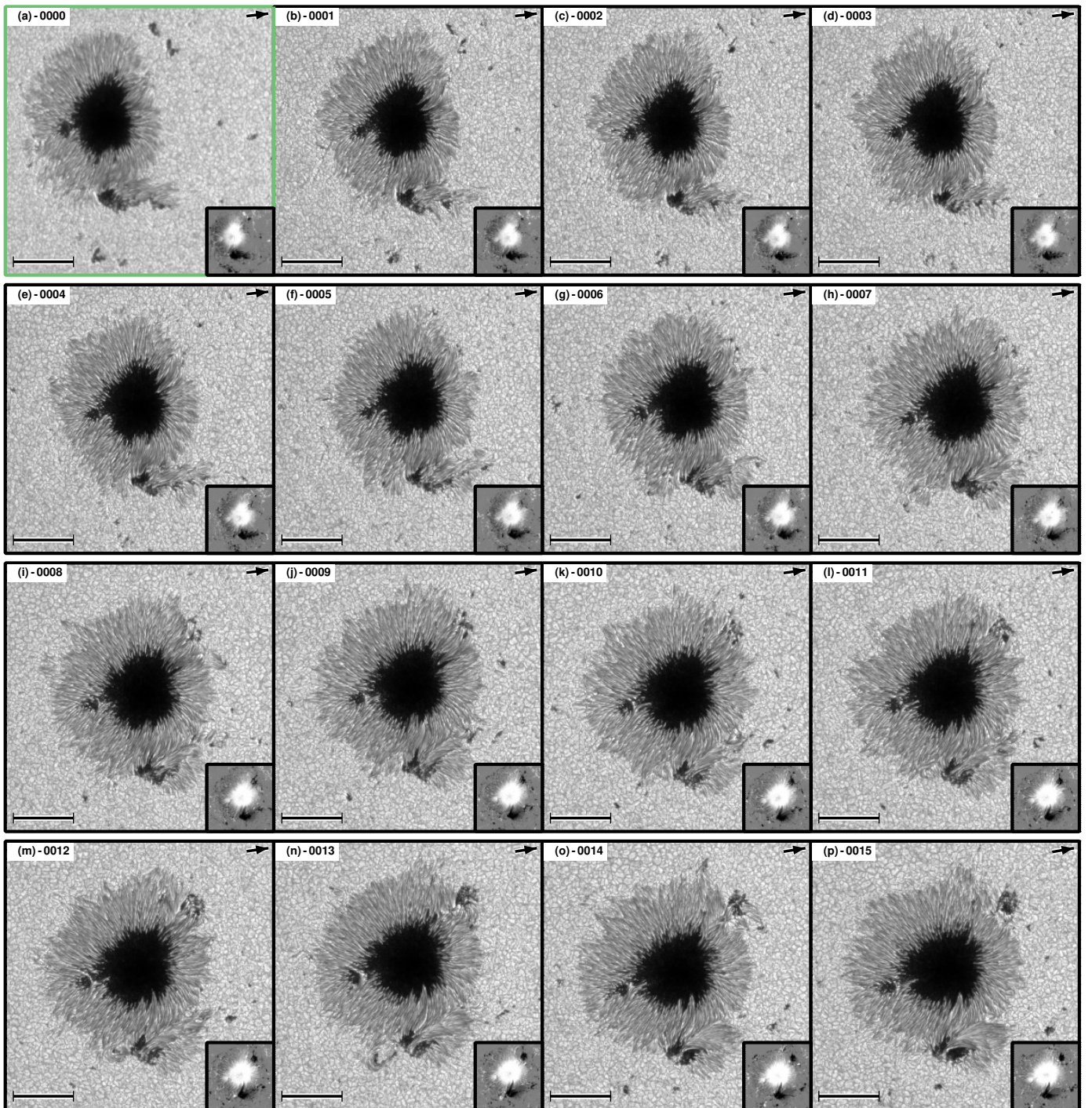


Fig. D.1: Best-fit continuum maps and magnetograms of the sample of sunspots in the MODEST catalog. Numbers on the upper-left part of each panel are the INV_ID of each inversion. INV_IDs can be found on the second column of Table D.1. Bars on the bottom-left corner have a length of $20''$, and arrows on the top-right corner point toward disk center. Insets on the lower-right show the magnetogram ($B \cos(\gamma_{\text{LOS}})$) in the LOS reference frame clipped at 1.5 kG obtained at the middle node. Axes colors display whether the scan was taken in fast (black) or normal mode (green).

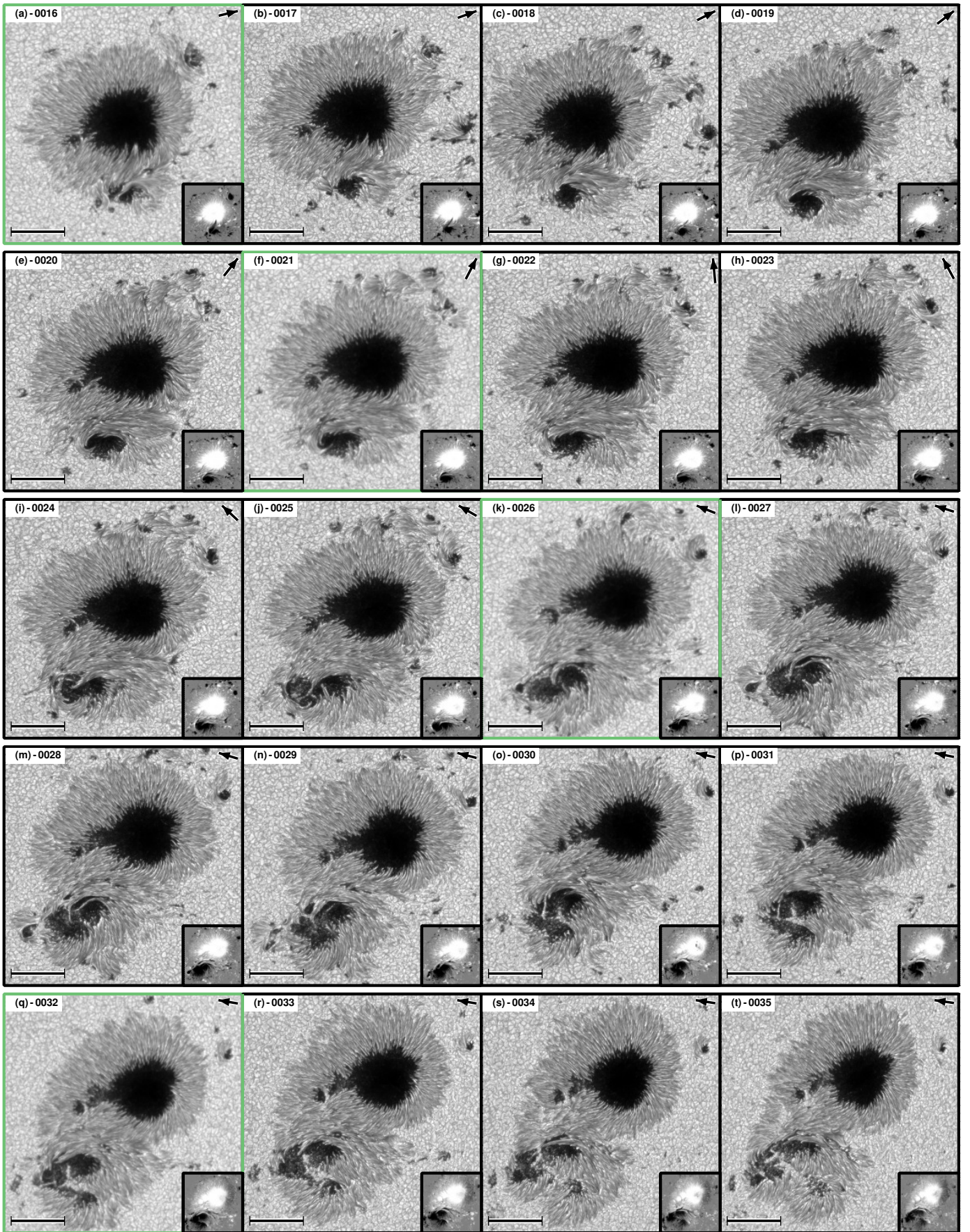


Fig. D.2: Same as Fig. D.1 on the preceding page. Axes colors display whether the scan was taken in fast mode (black) or normal mode (green).

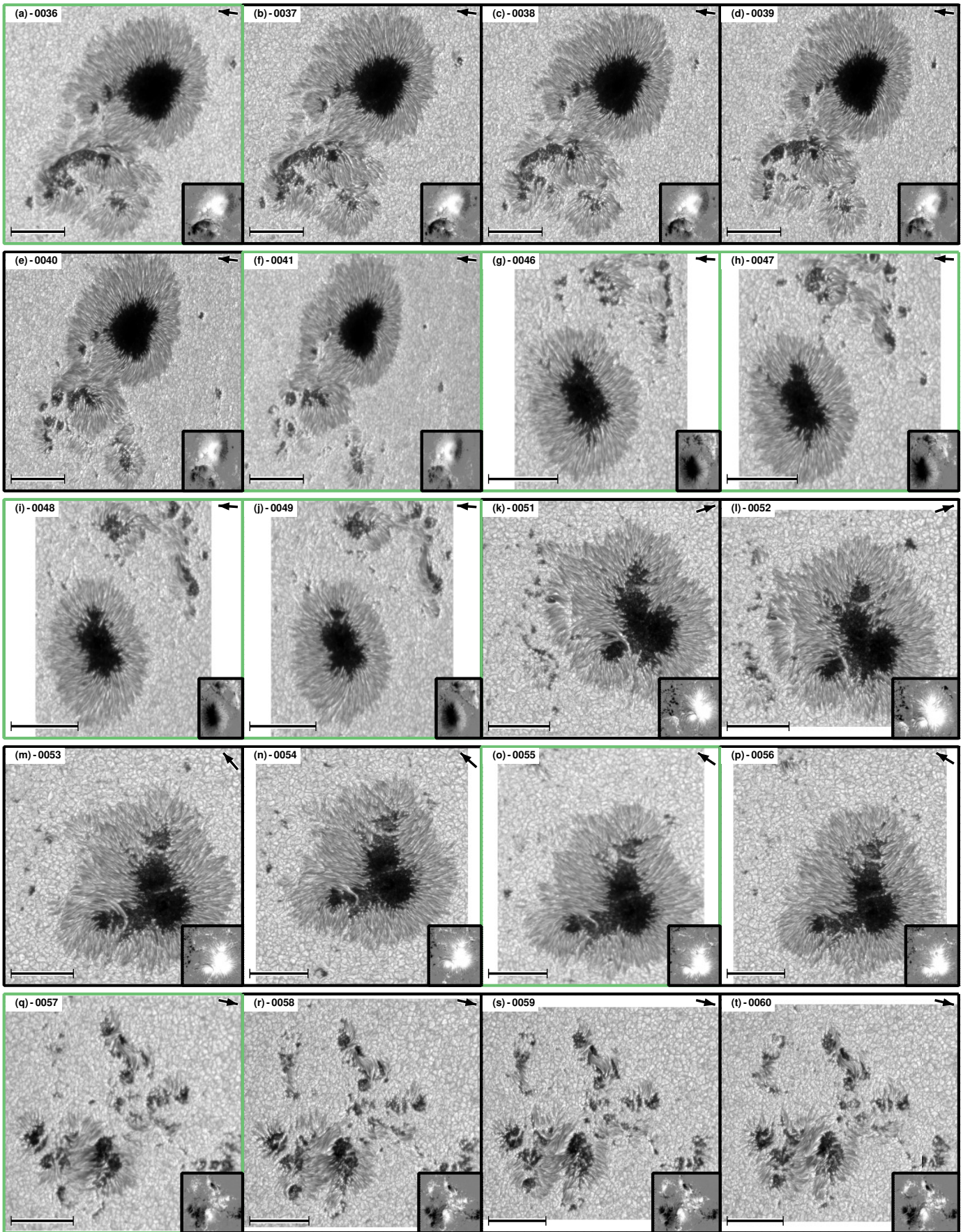


Fig. D.3: Same as Fig. D.1 on page 22. Axes colors display whether the scan was taken in fast mode (black) or normal mode (green).

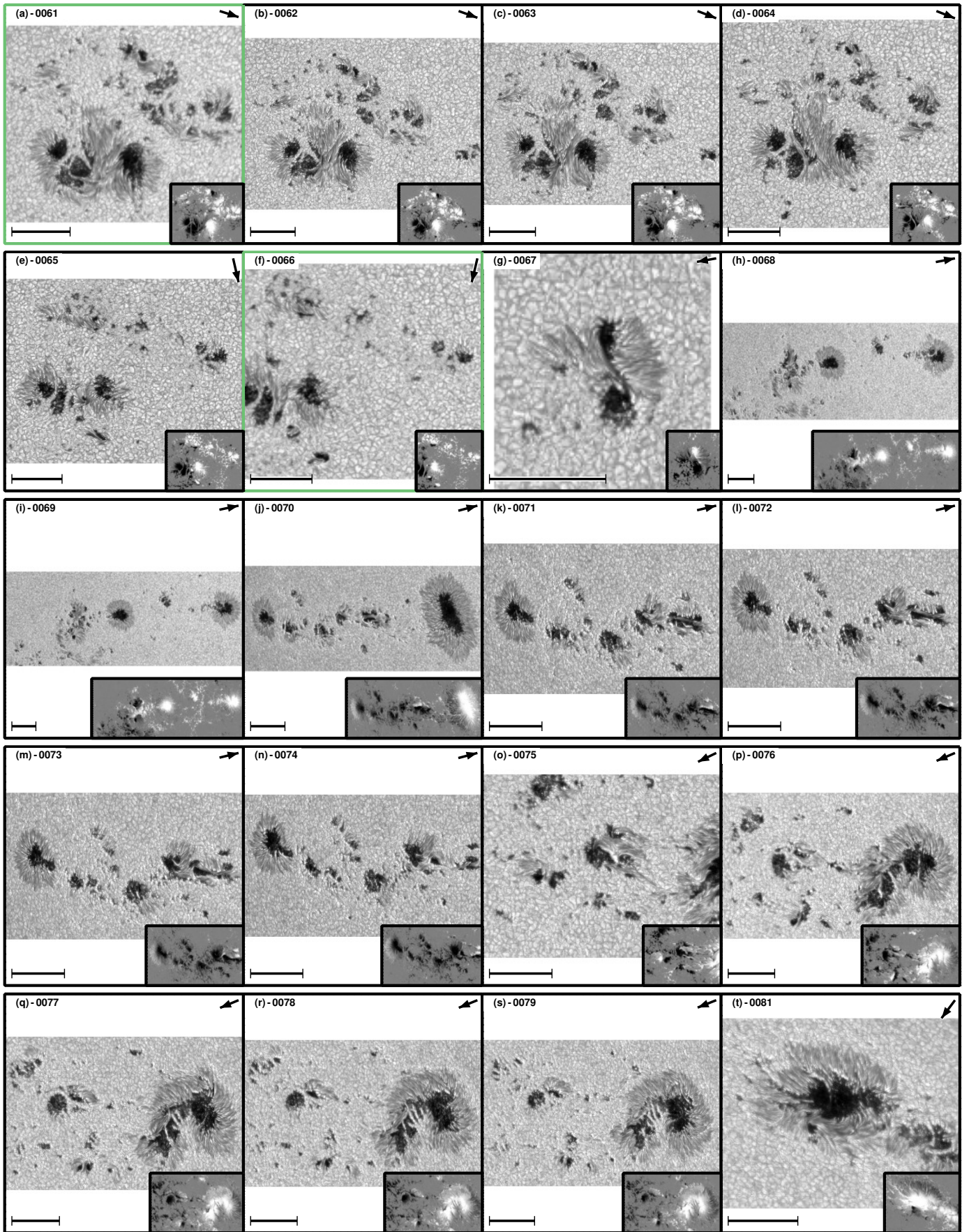


Fig. D.4: Same as Fig. D.1 on page 22. Axes colors display whether the scan was taken in fast mode (black) or normal mode (green).

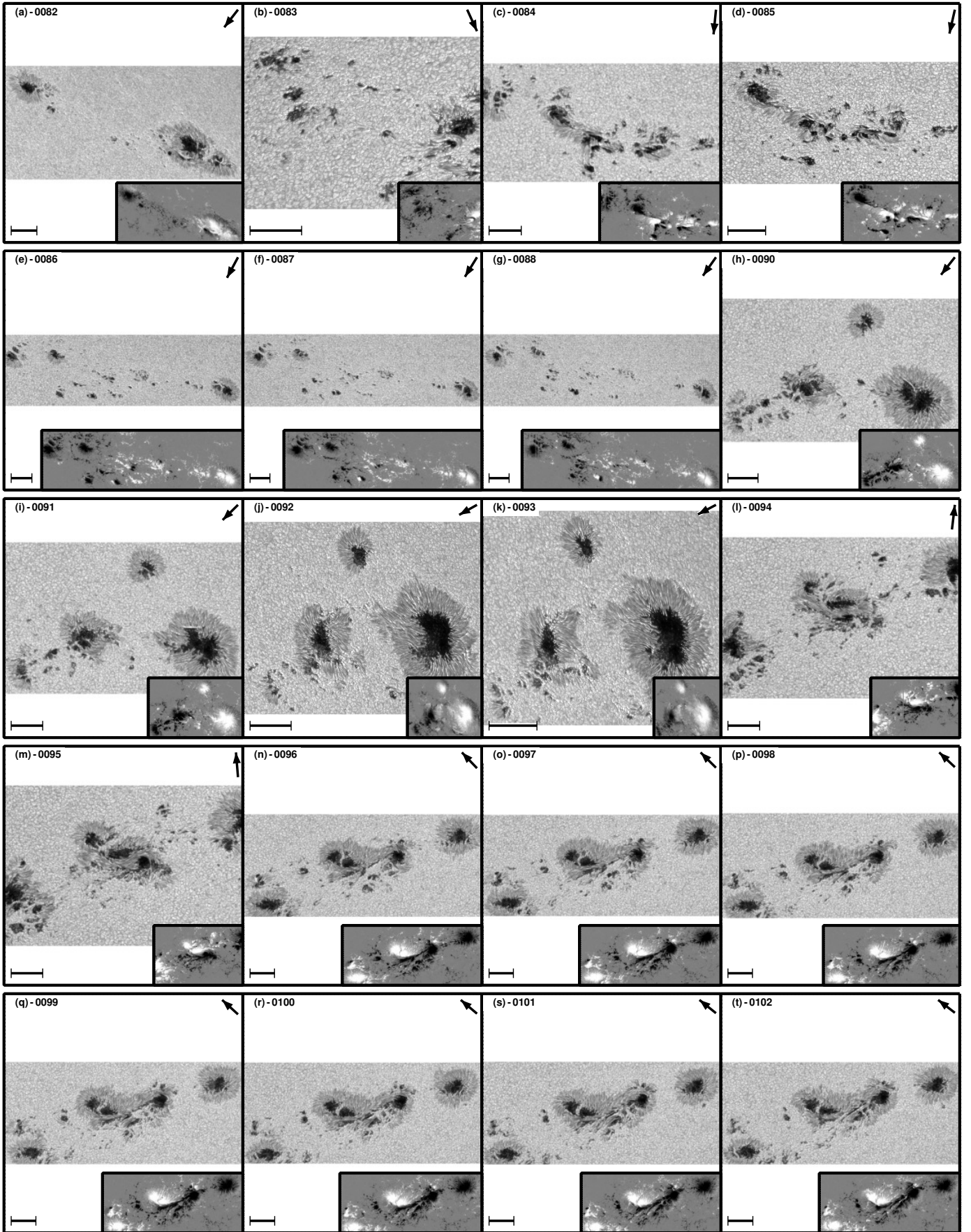


Fig. D.5: Same as Fig. D.1 on page 22. Axes colors display whether the scan was taken in fast mode (black) or normal mode (green).

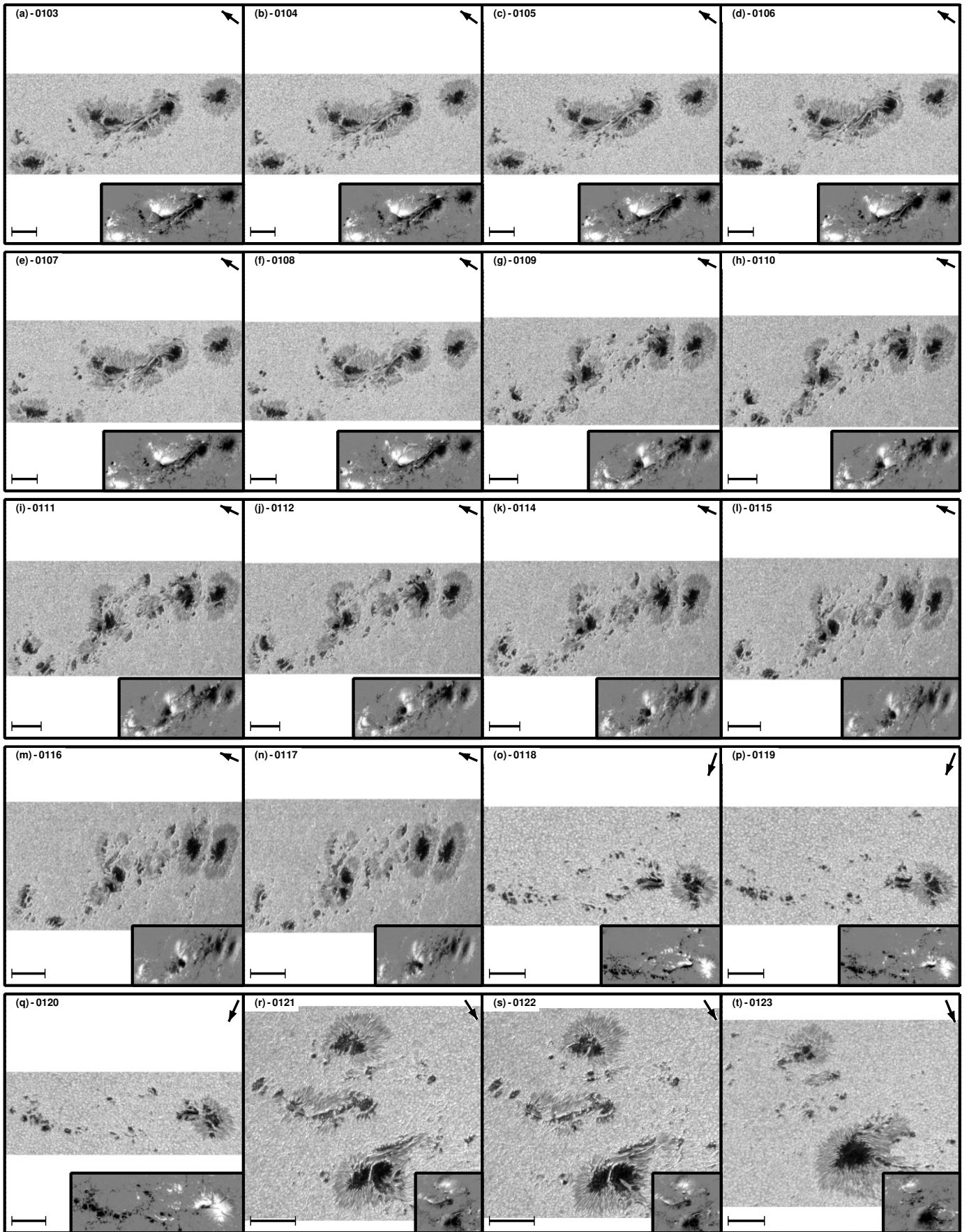


Fig. D.6: Same as Fig. D.1 on page 22. Axes colors display whether the scan was taken in fast mode (black) or normal mode (green).

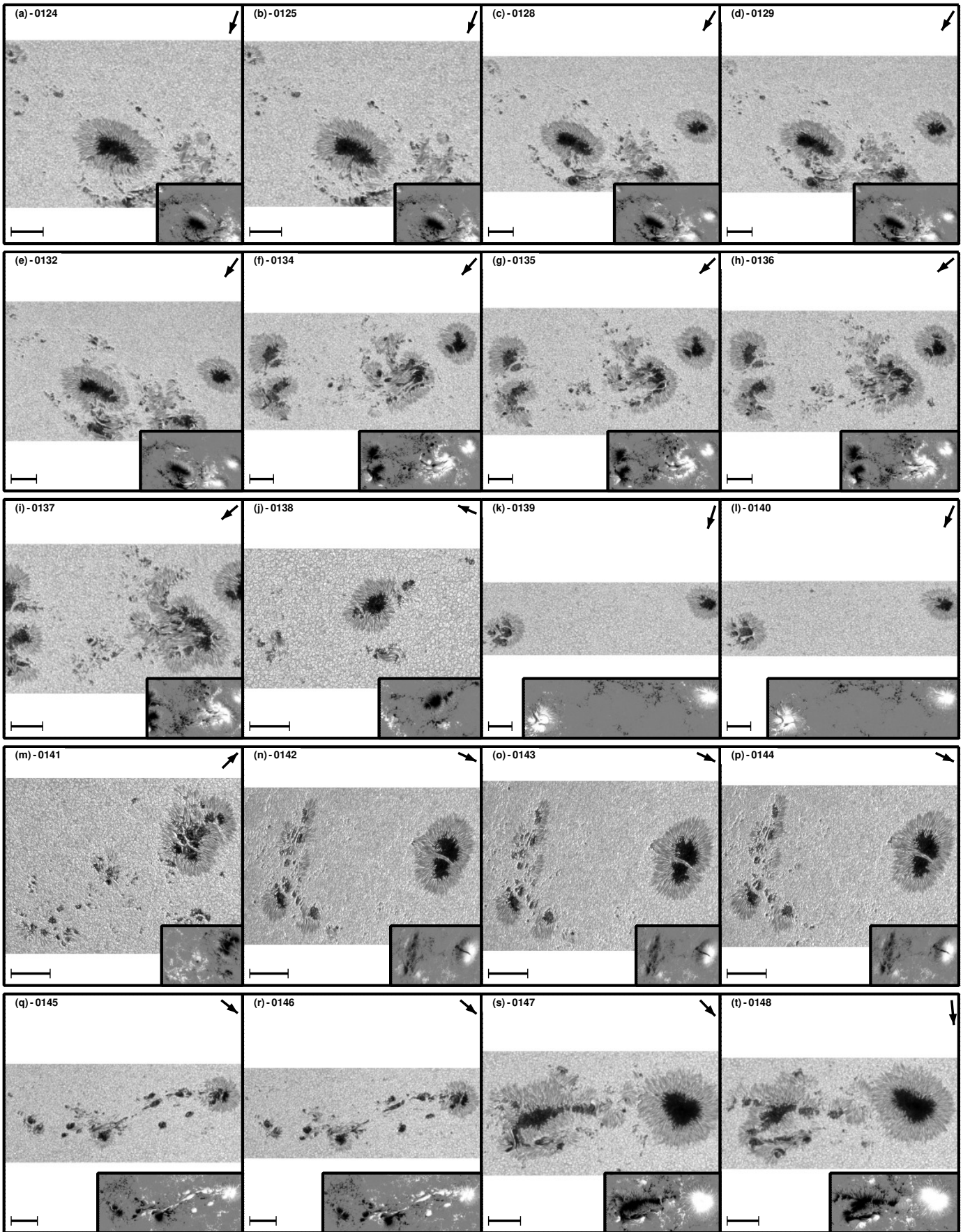


Fig. D.7: Same as Fig. D.1 on page 22. Axes colors display whether the scan was taken in fast mode (black) or normal mode (green).

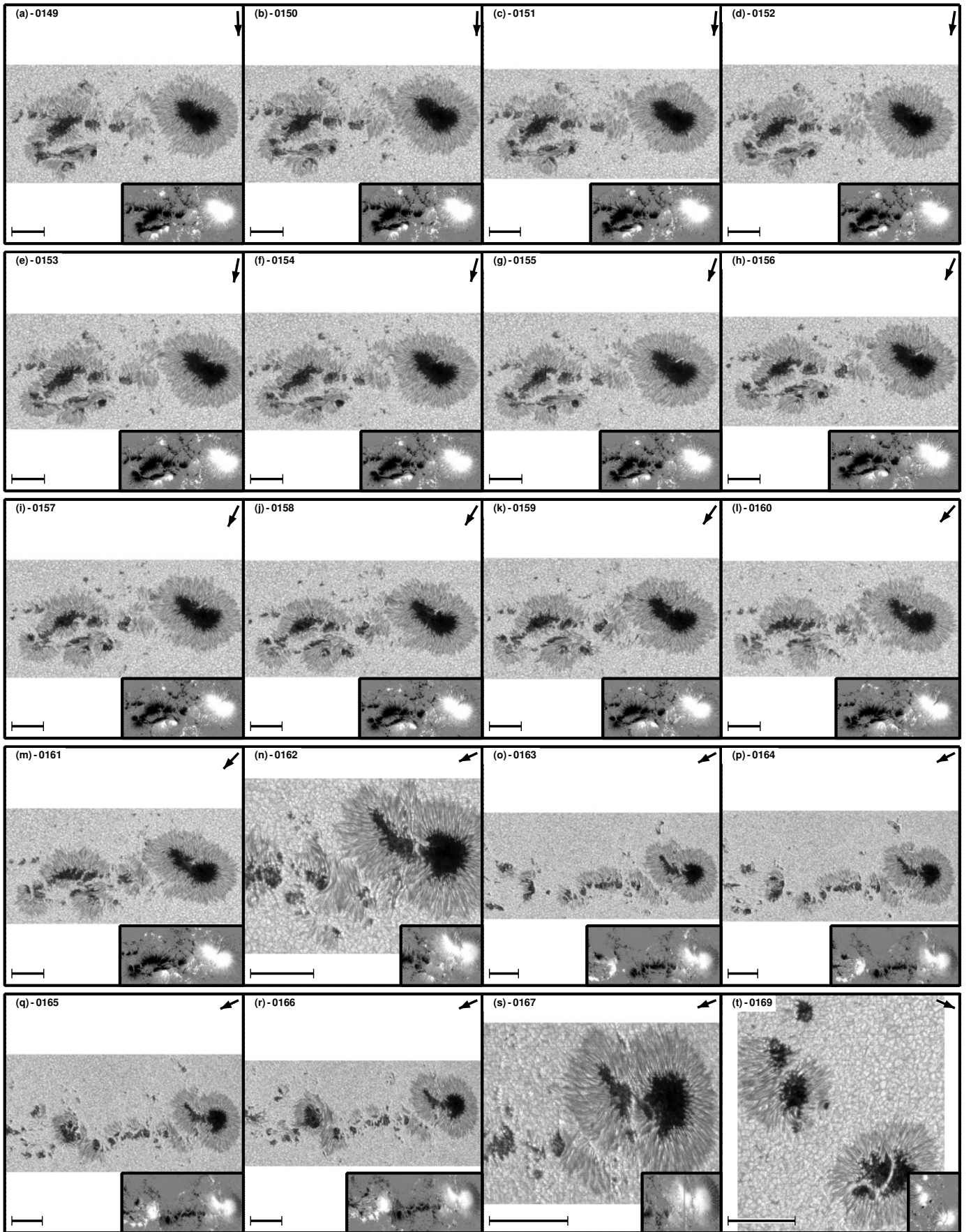


Fig. D.8: Same as Fig. D.1 on page 22. Axes colors display whether the scan was taken in fast mode (black) or normal mode (green).

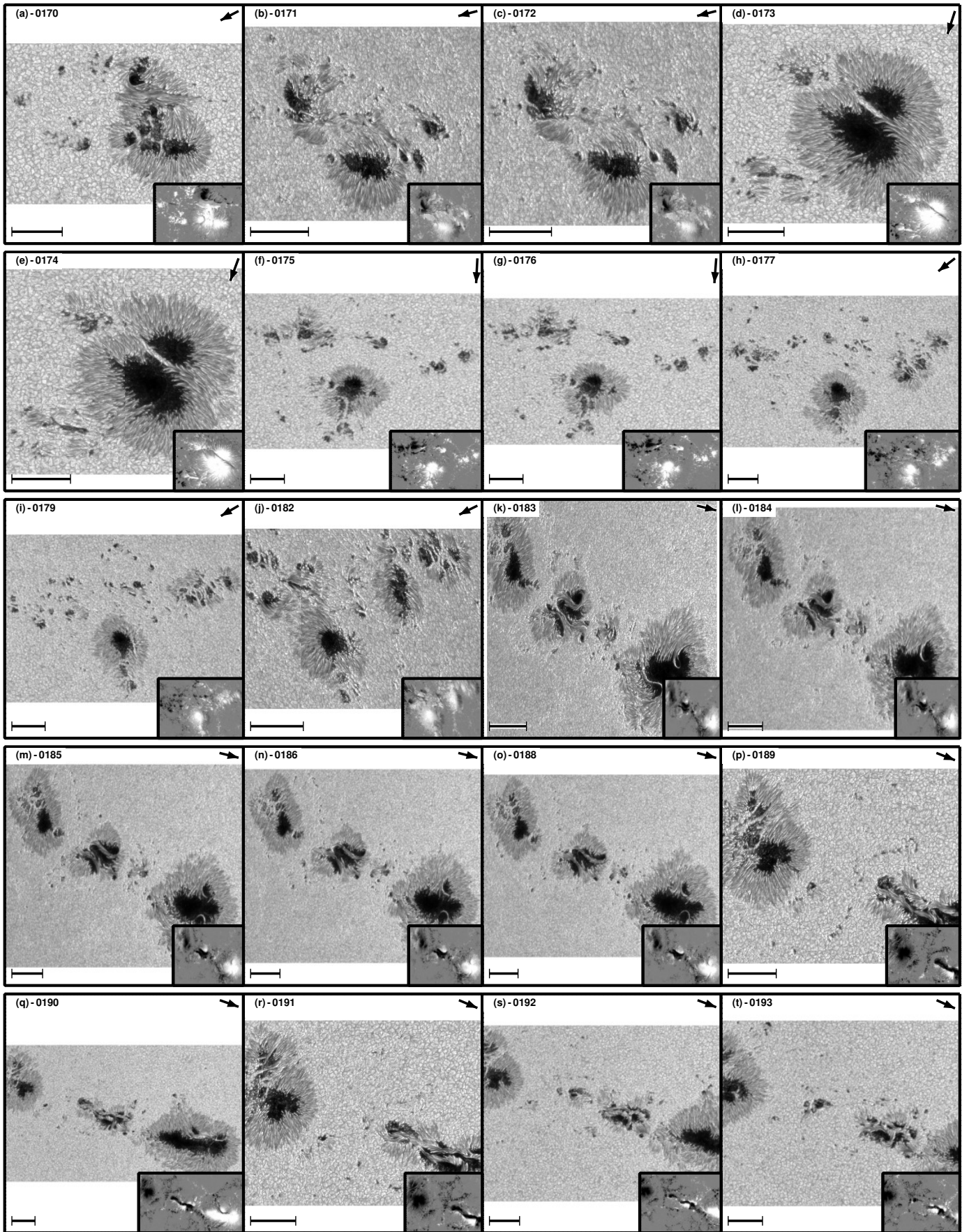


Fig. D.9: Same as Fig. D.1 on page 22. Axes colors display whether the scan was taken in fast mode (black) or normal mode (green).

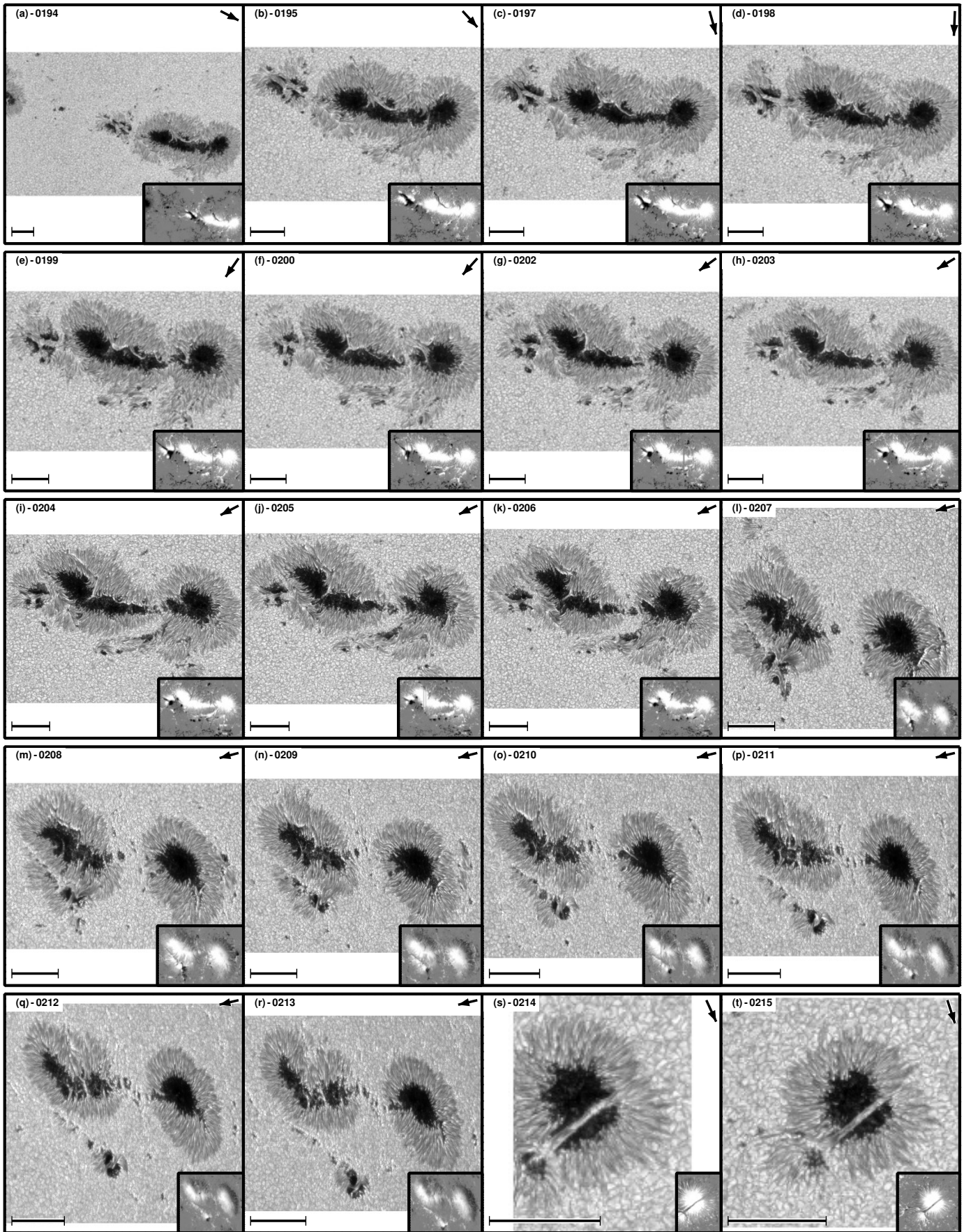


Fig. D.10: Same as Fig. D.1 on page 22. Axes colors display whether the scan was taken in fast mode (black) or normal mode (green).

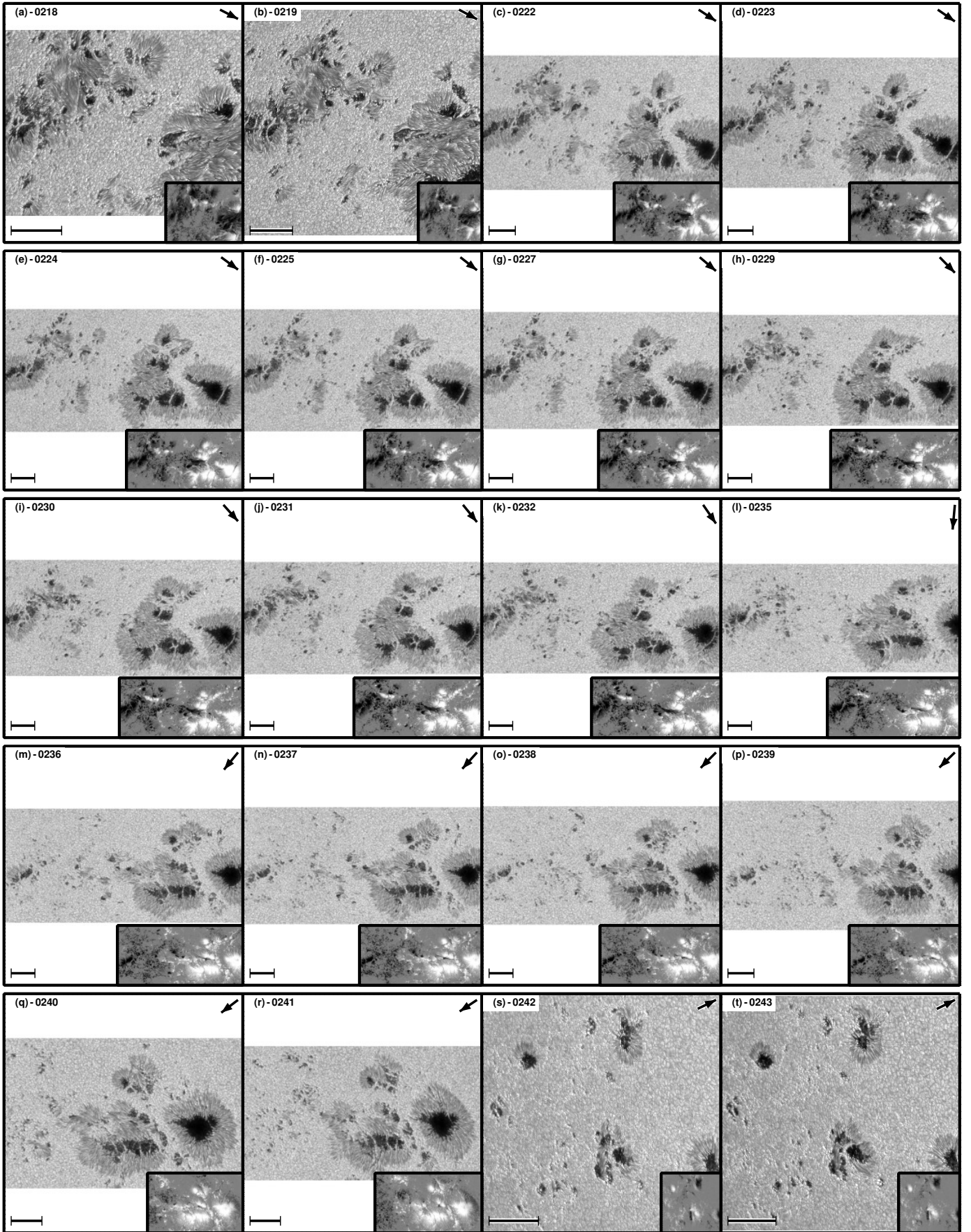


Fig. D.11: Same as Fig. D.1 on page 22. Axes colors display whether the scan was taken in fast mode (black) or normal mode (green).

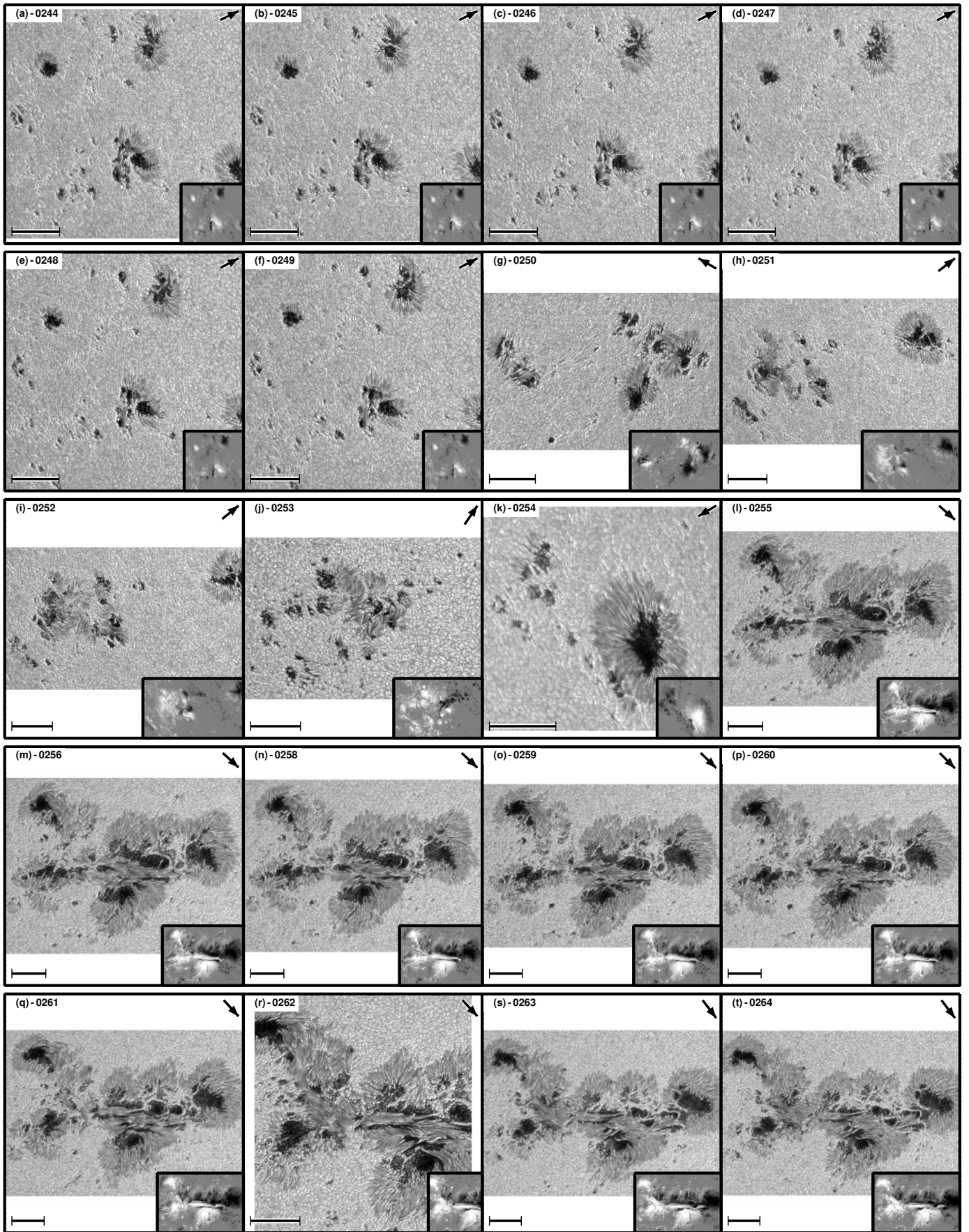


Fig. D.12: Same as Fig. D.1 on page 22. Axes colors display whether the scan was taken in fast mode (black) or normal mode (green).

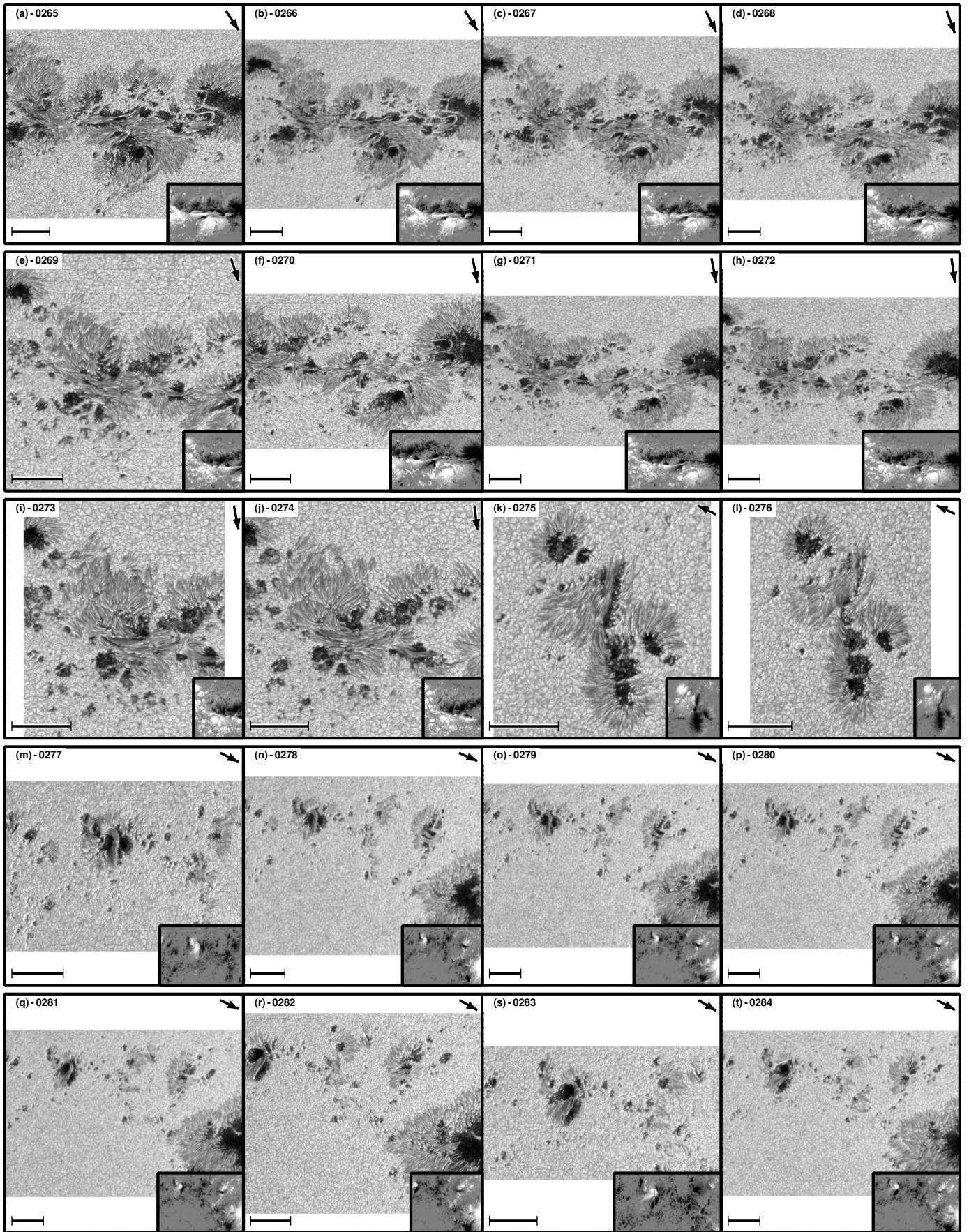


Fig. D.13: Same as Fig. D.1 on page 22. Axes colors display whether the scan was taken in fast mode (black) or normal mode (green).

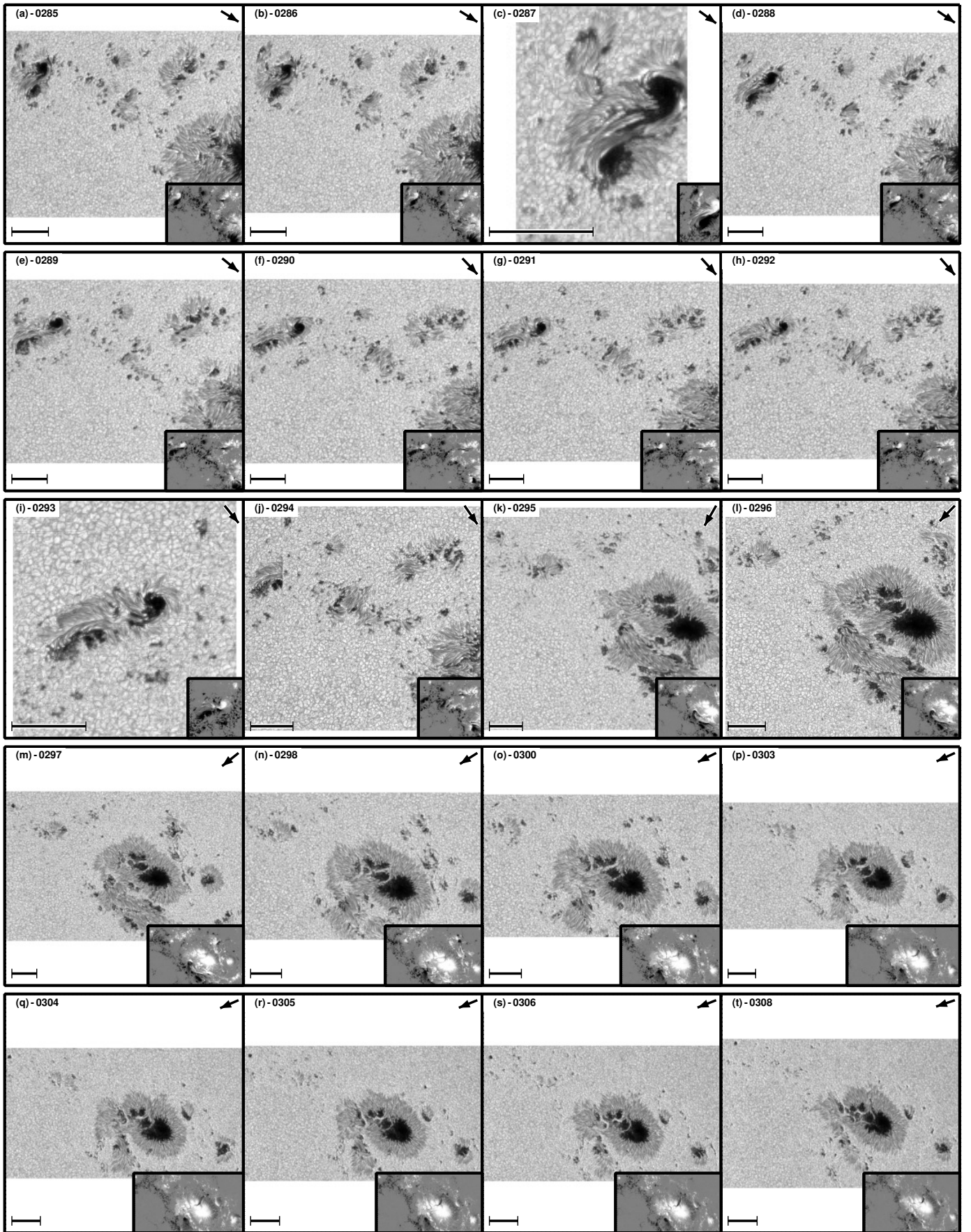


Fig. D.14: Same as Fig. D.1 on page 22. Axes colors display whether the scan was taken in fast mode (black) or normal mode (green).

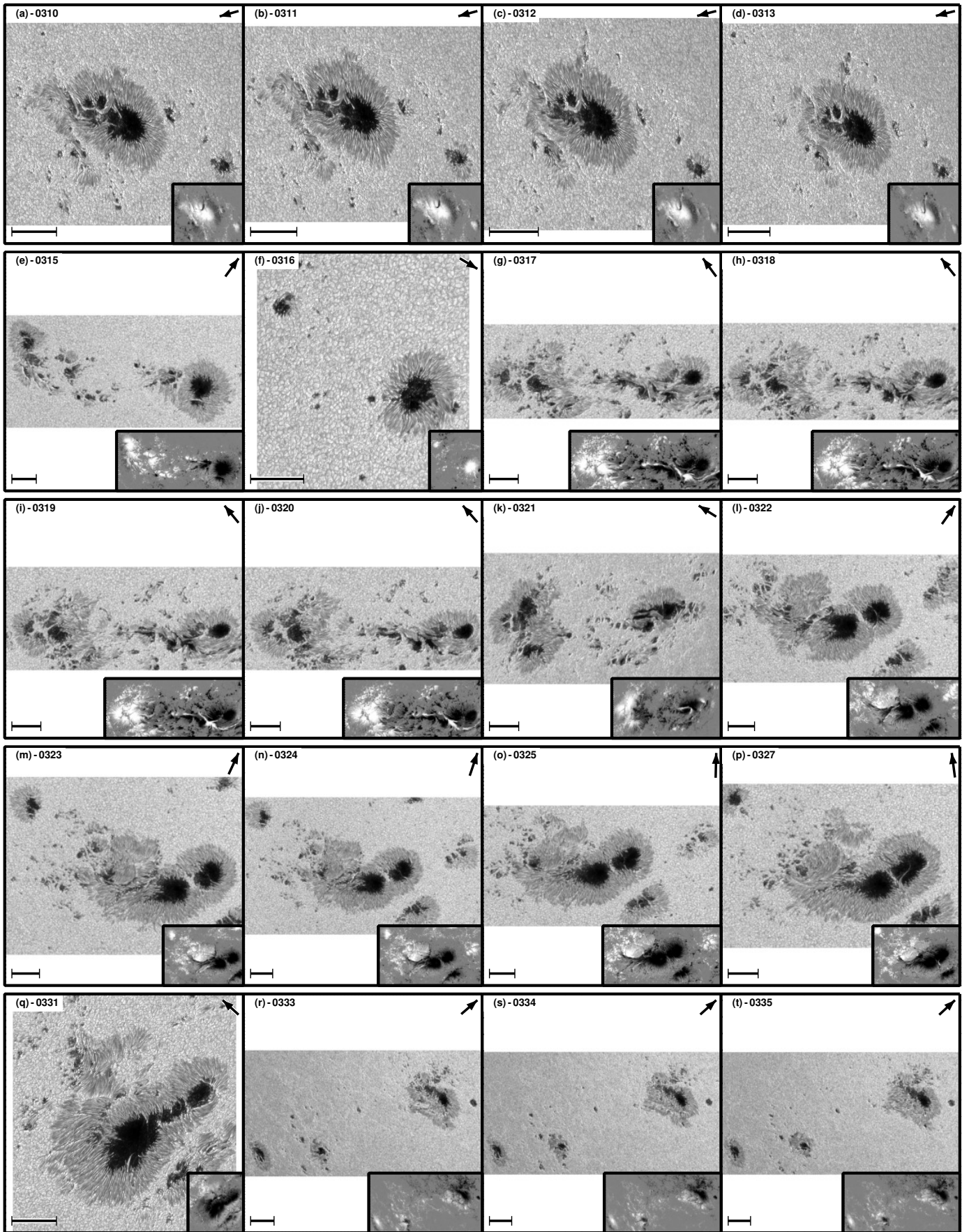


Fig. D.15: Same as Fig. D.1 on page 22. Axes colors display whether the scan was taken in fast mode (black) or normal mode (green).

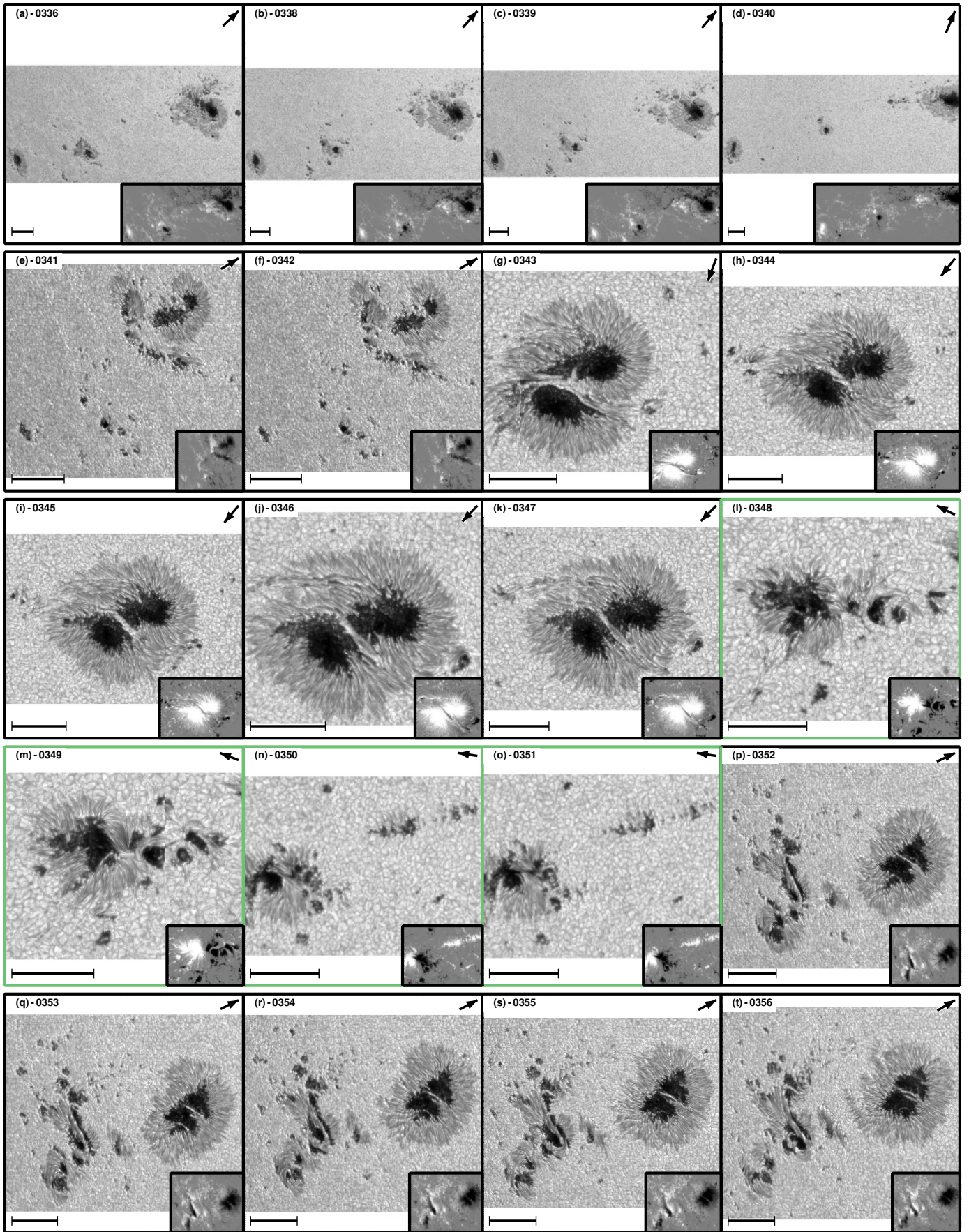


Fig. D.16: Same as Fig. D.1 on page 22. Axes colors display whether the scan was taken in fast mode (black) or normal mode (green).

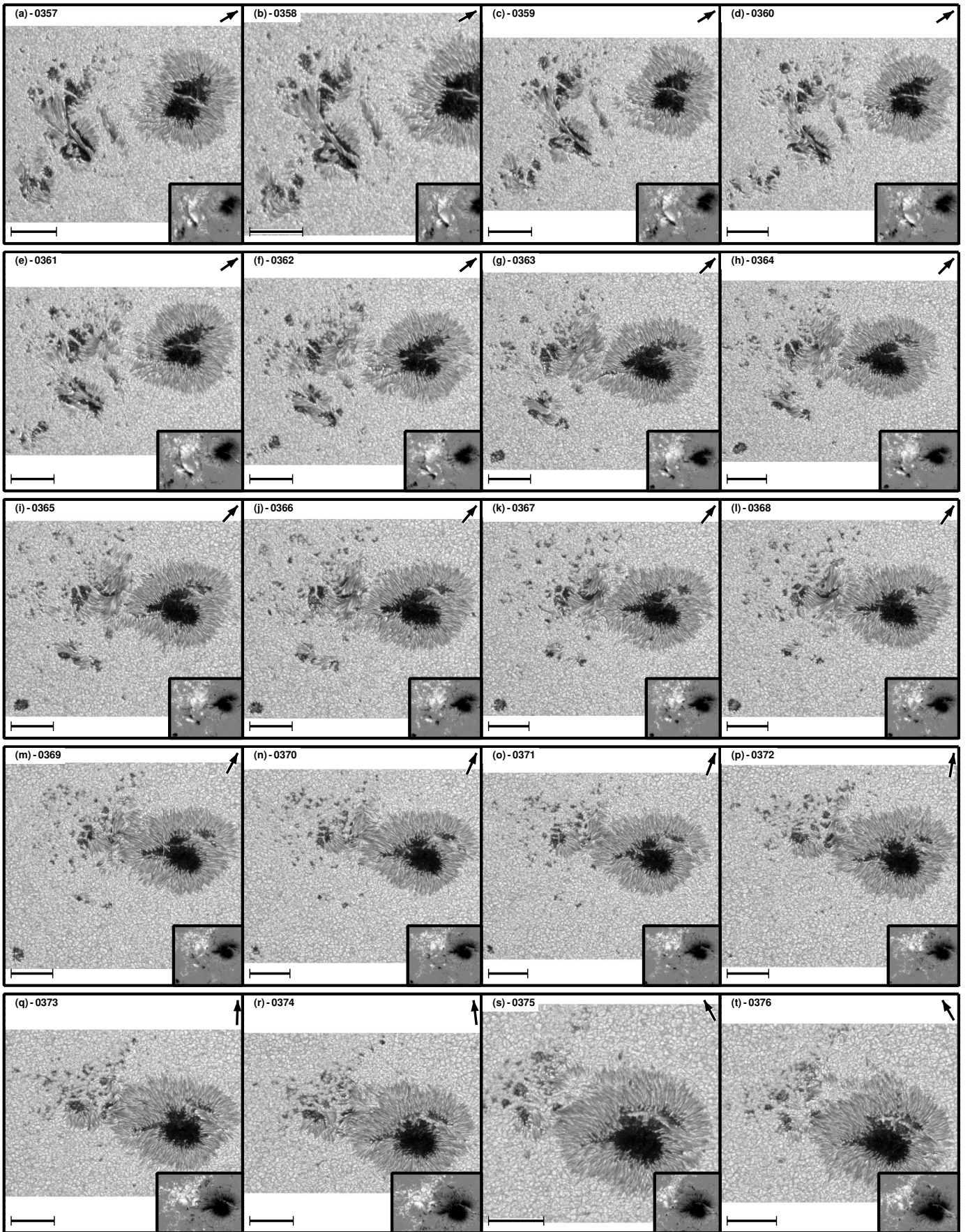


Fig. D.17: Same as Fig. D.1 on page 22. Axes colors display whether the scan was taken in fast mode (black) or normal mode (green).

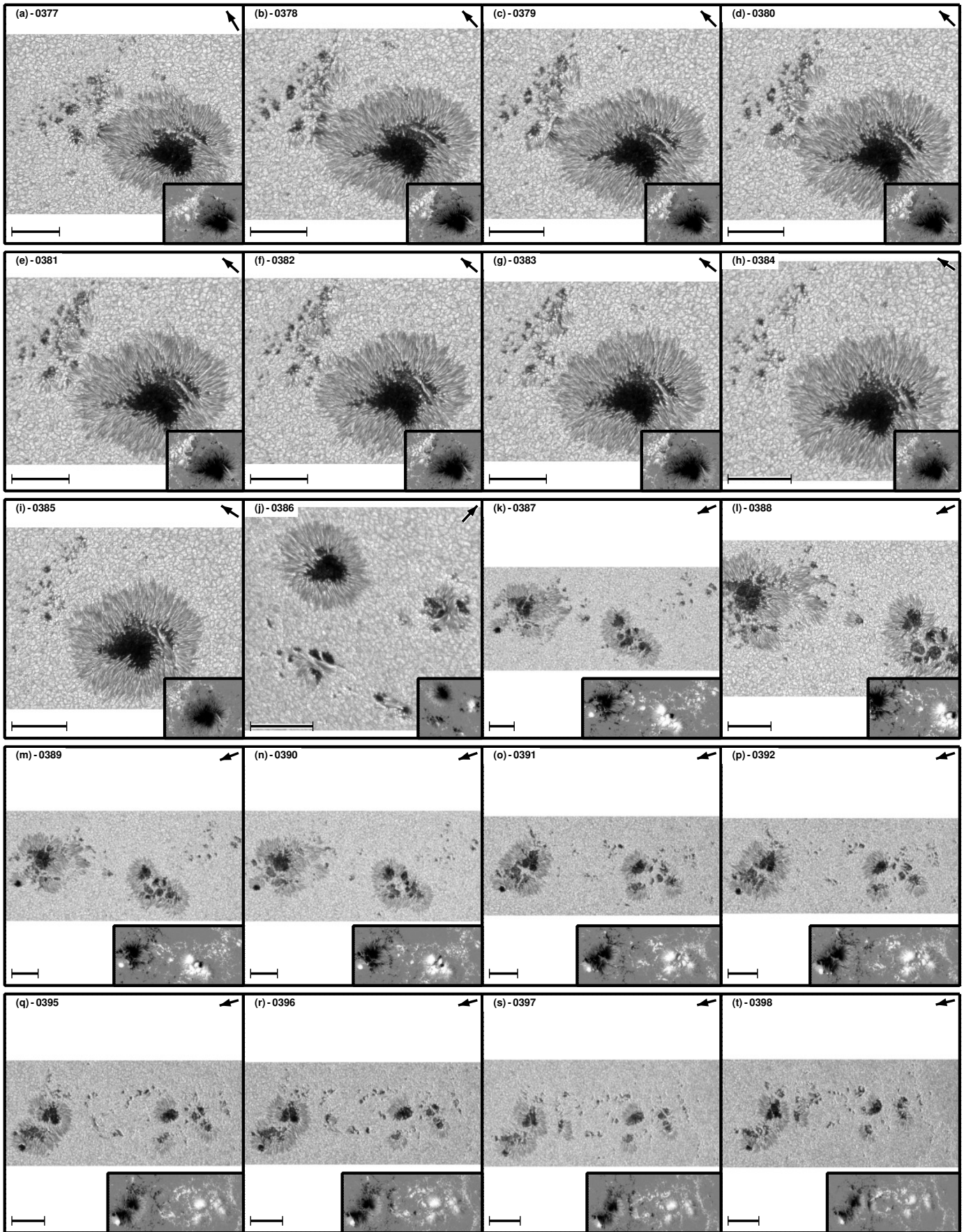


Fig. D.18: Same as Fig. D.1 on page 22. Axes colors display whether the scan was taken in fast mode (black) or normal mode (green).

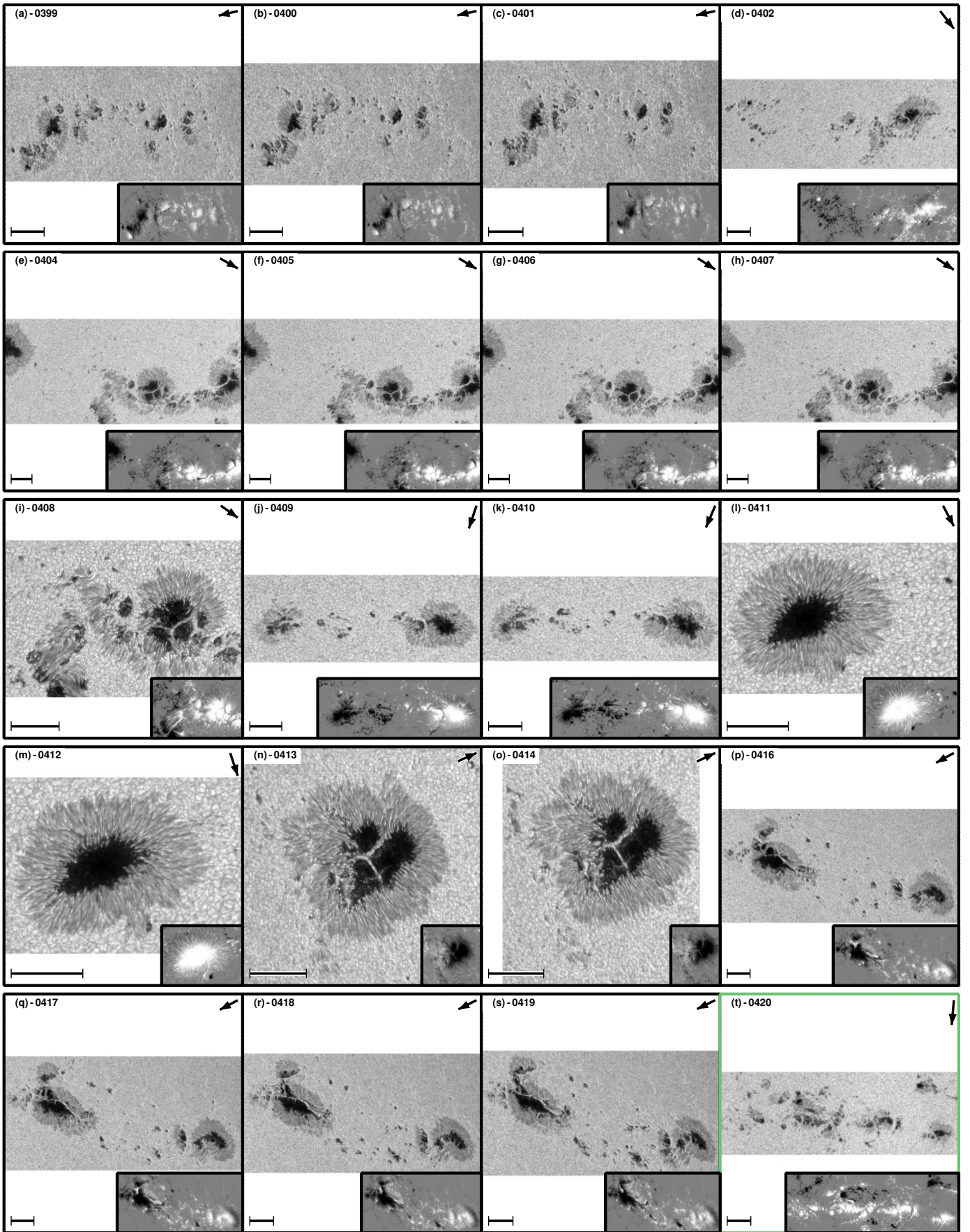


Fig. D.19: Same as Fig. D.1 on page 22. Axes colors display whether the scan was taken in fast mode (black) or normal mode (green).

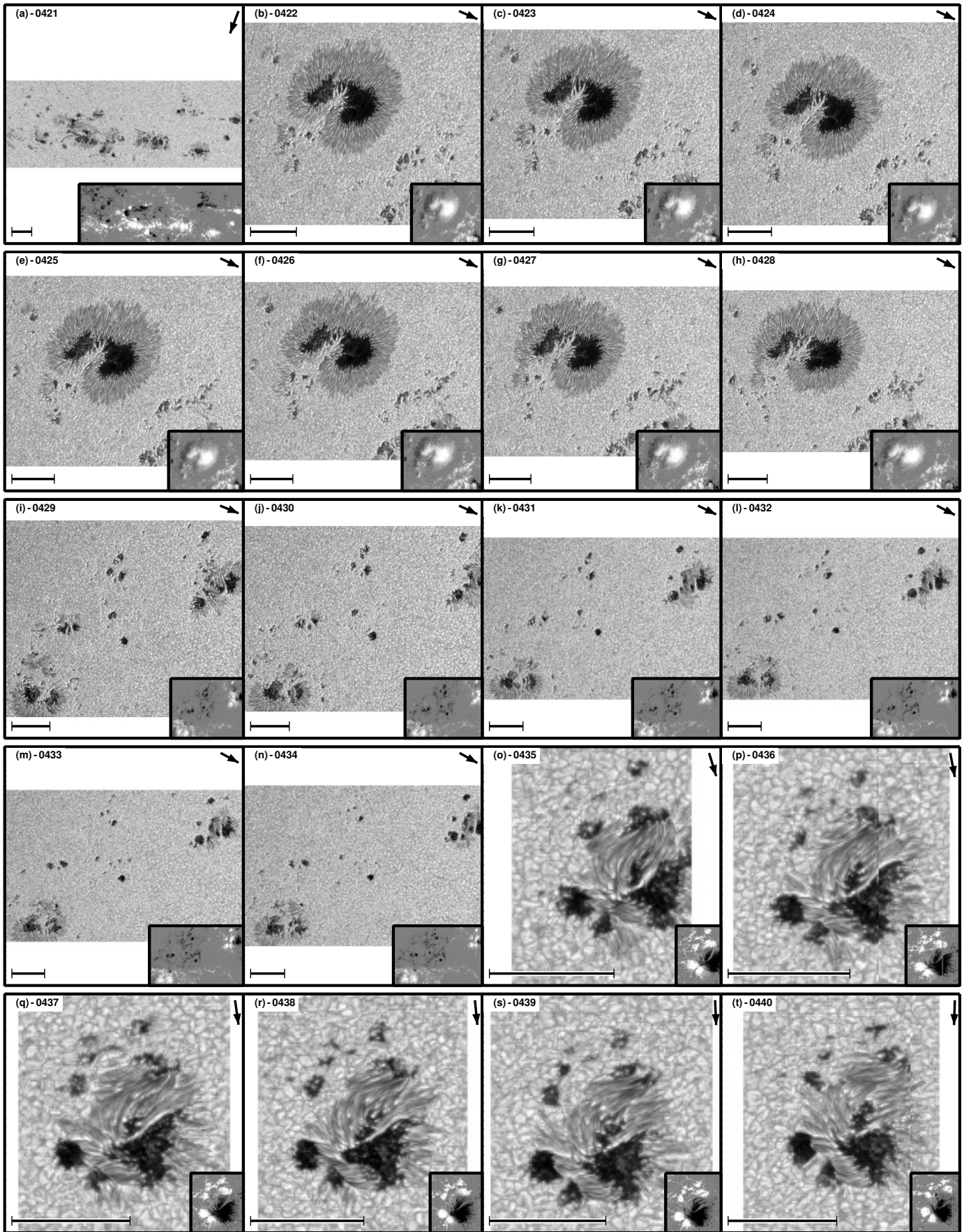


Fig. D.20: Same as Fig. D.1 on page 22. Axes colors display whether the scan was taken in fast mode (black) or normal mode (green).

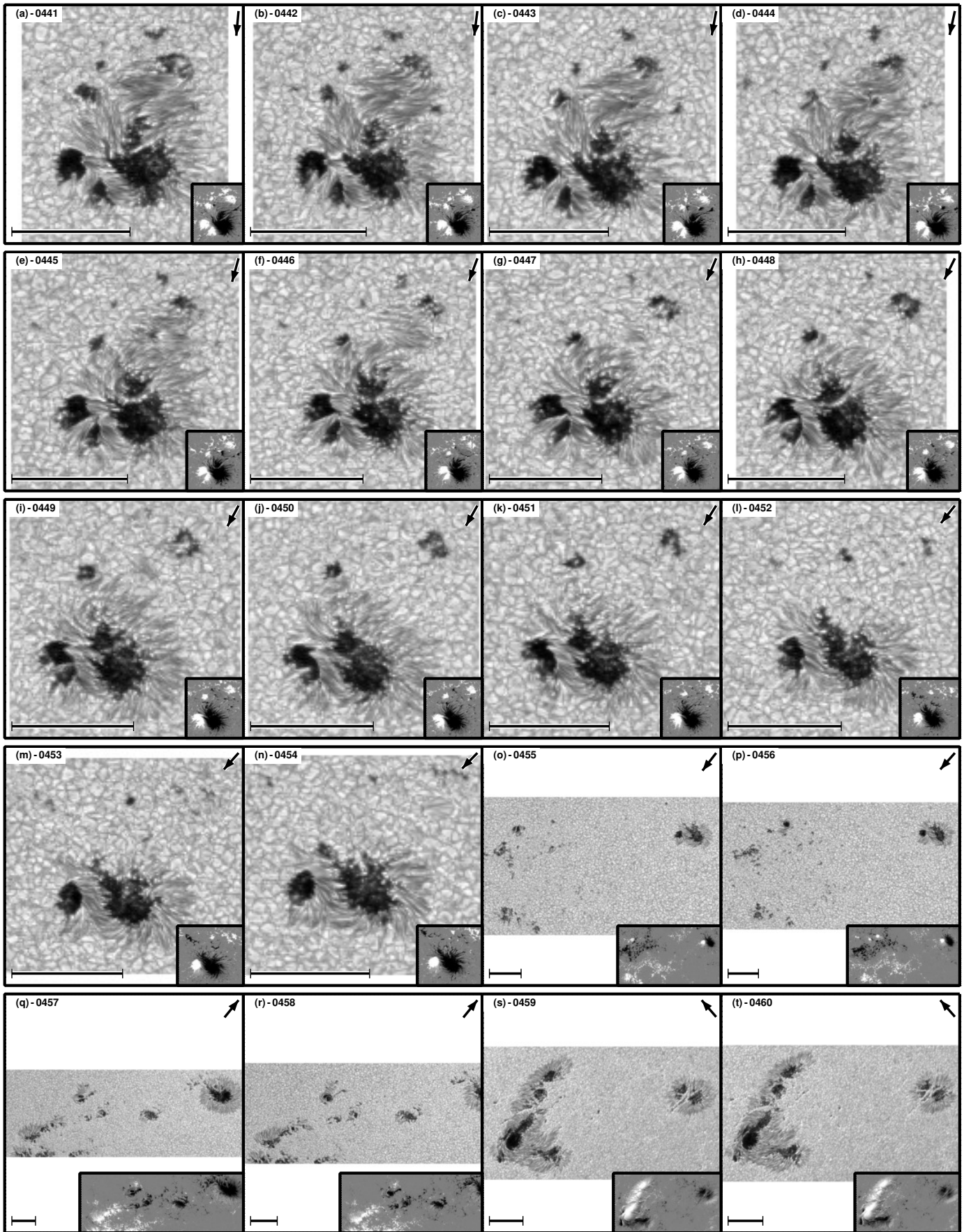


Fig. D.21: Same as Fig. D.1 on page 22. Axes colors display whether the scan was taken in fast mode (black) or normal mode (green).

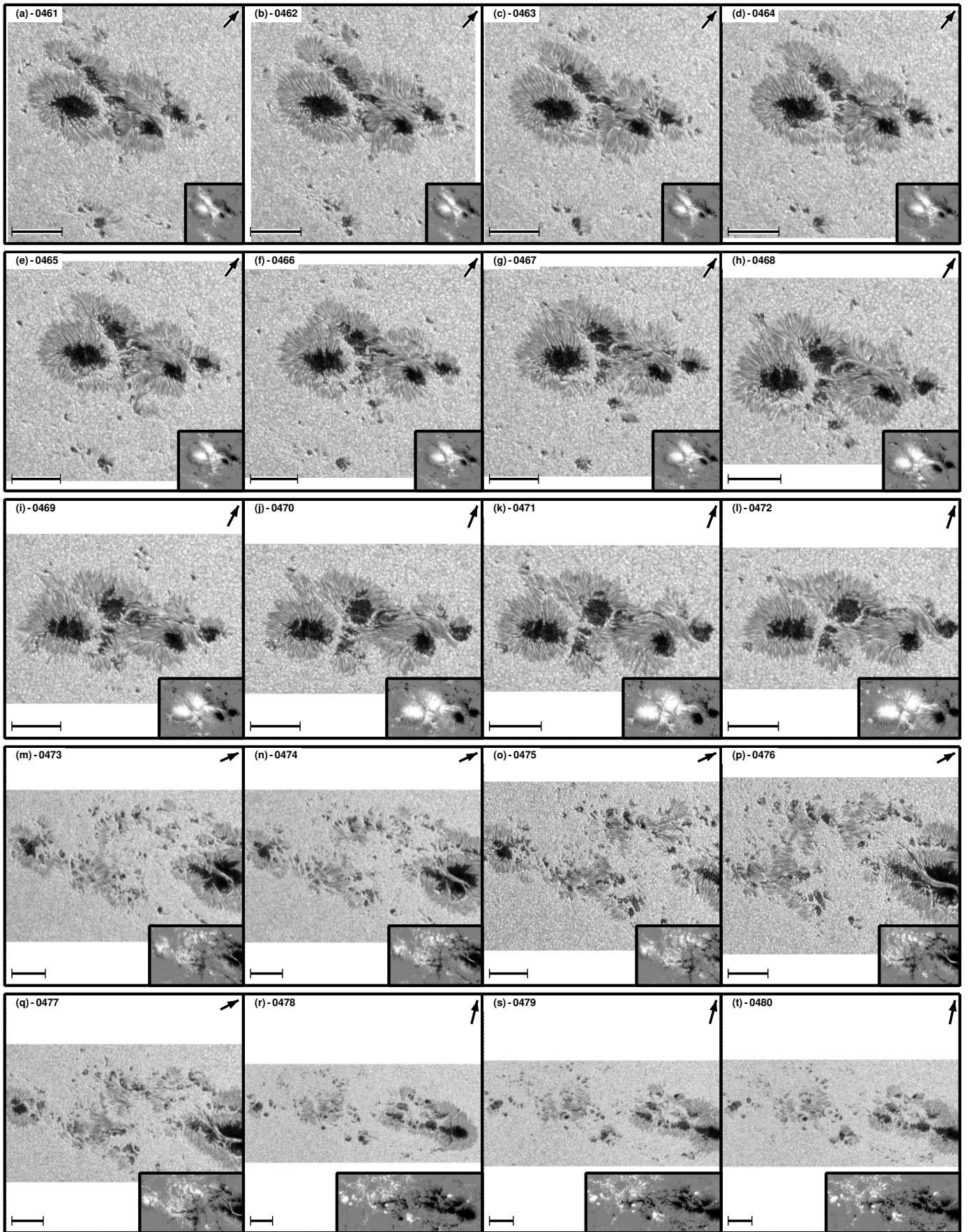


Fig. D.22: Same as Fig. D.1 on page 22. Axes colors display whether the scan was taken in fast mode (black) or normal mode (green).

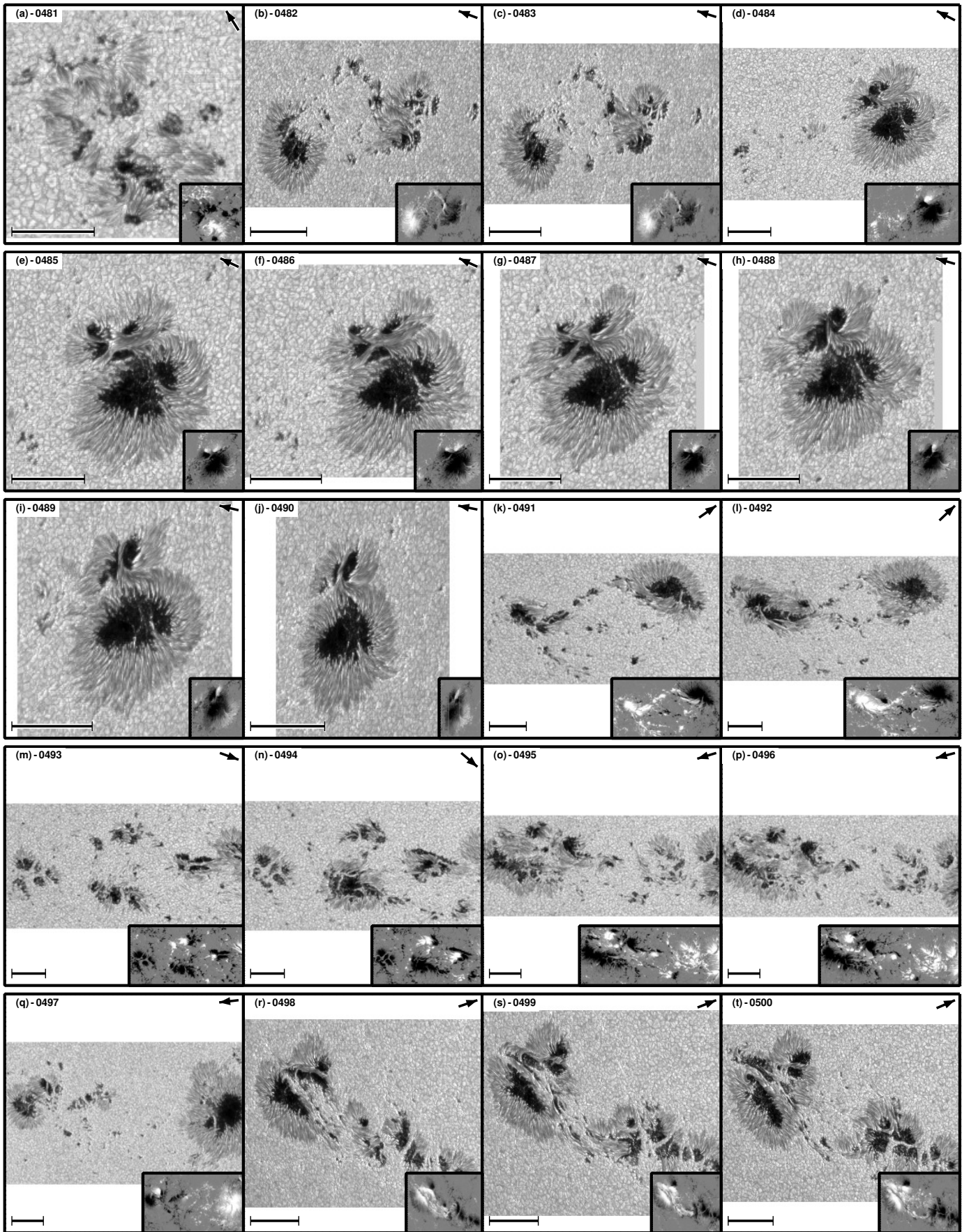


Fig. D.23: Same as Fig. D.1 on page 22. Axes colors display whether the scan was taken in fast mode (black) or normal mode (green).

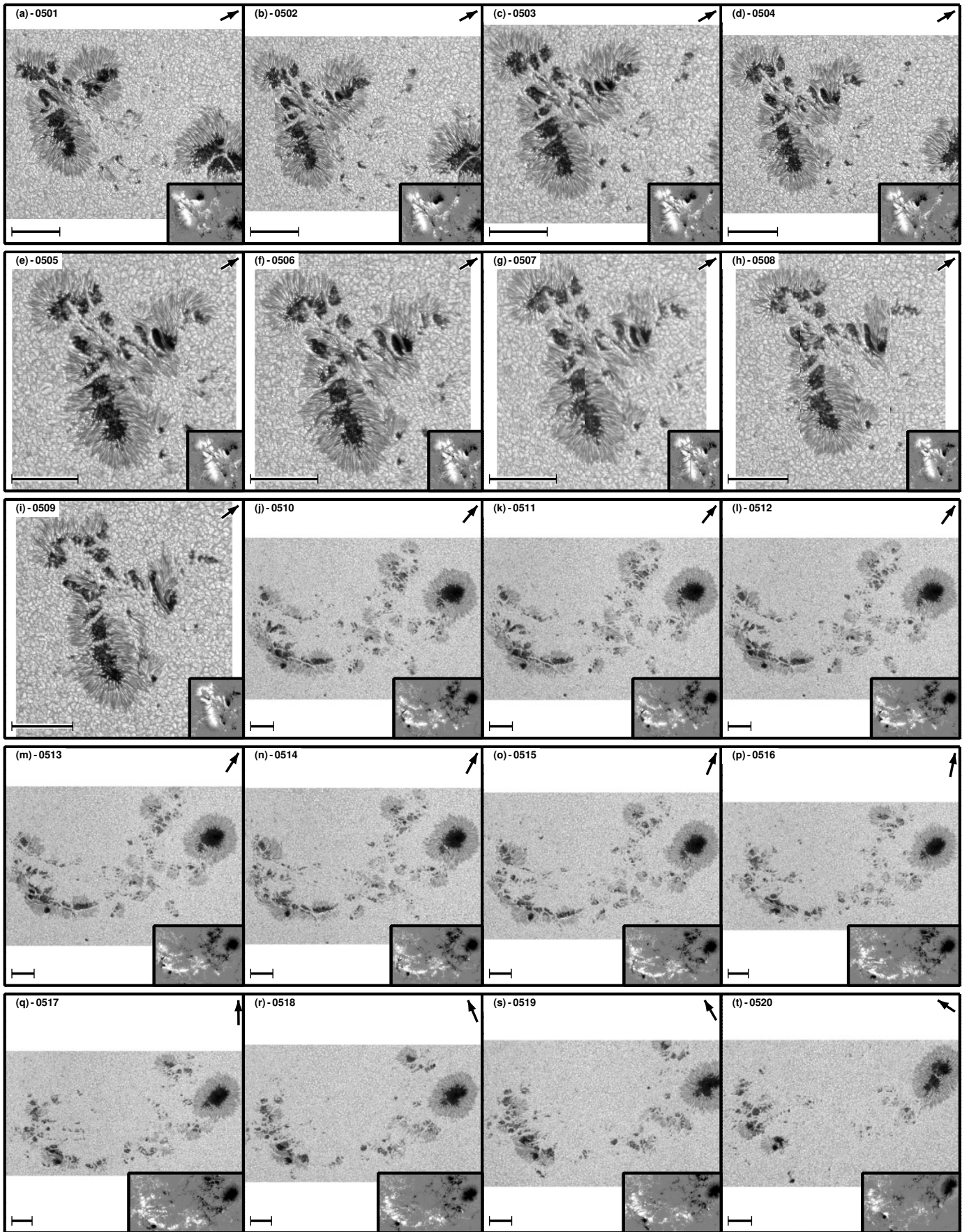


Fig. D.24: Same as Fig. D.1 on page 22. Axes colors display whether the scan was taken in fast mode (black) or normal mode (green).

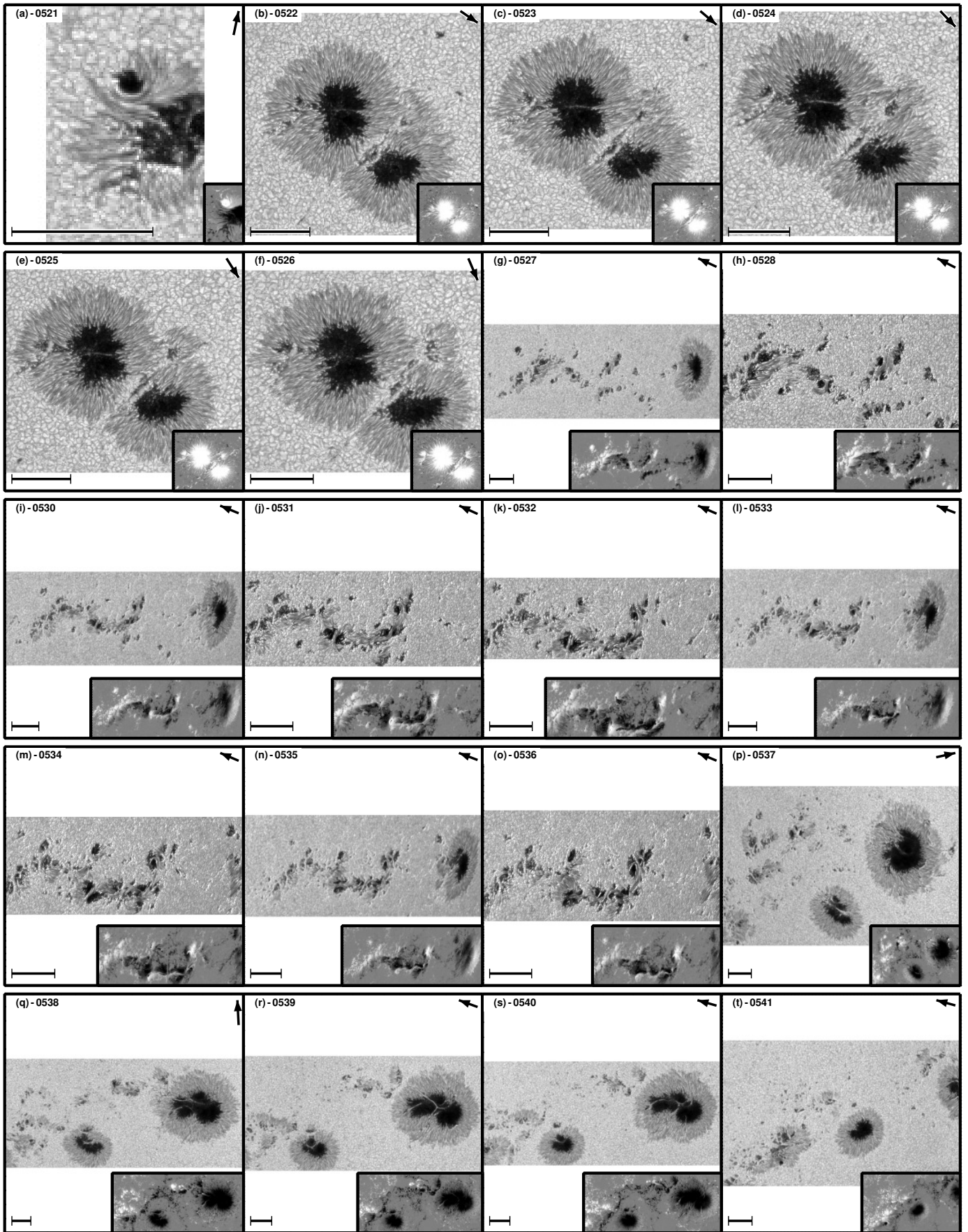


Fig. D.25: Same as Fig. D.1 on page 22. Axes colors display whether the scan was taken in fast mode (black) or normal mode (green).

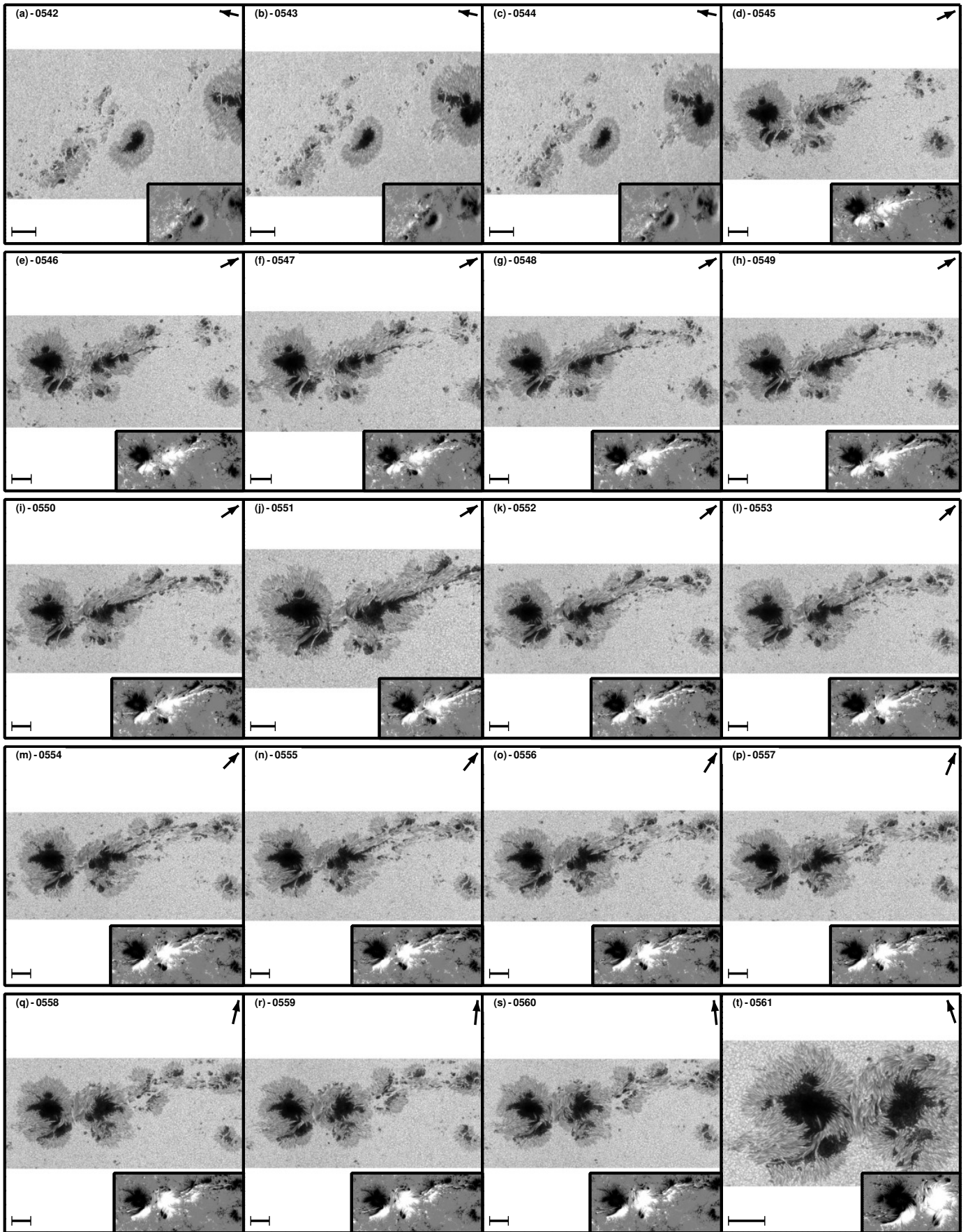


Fig. D.26: Same as Fig. D.1 on page 22. Axes colors display whether the scan was taken in fast mode (black) or normal mode (green).

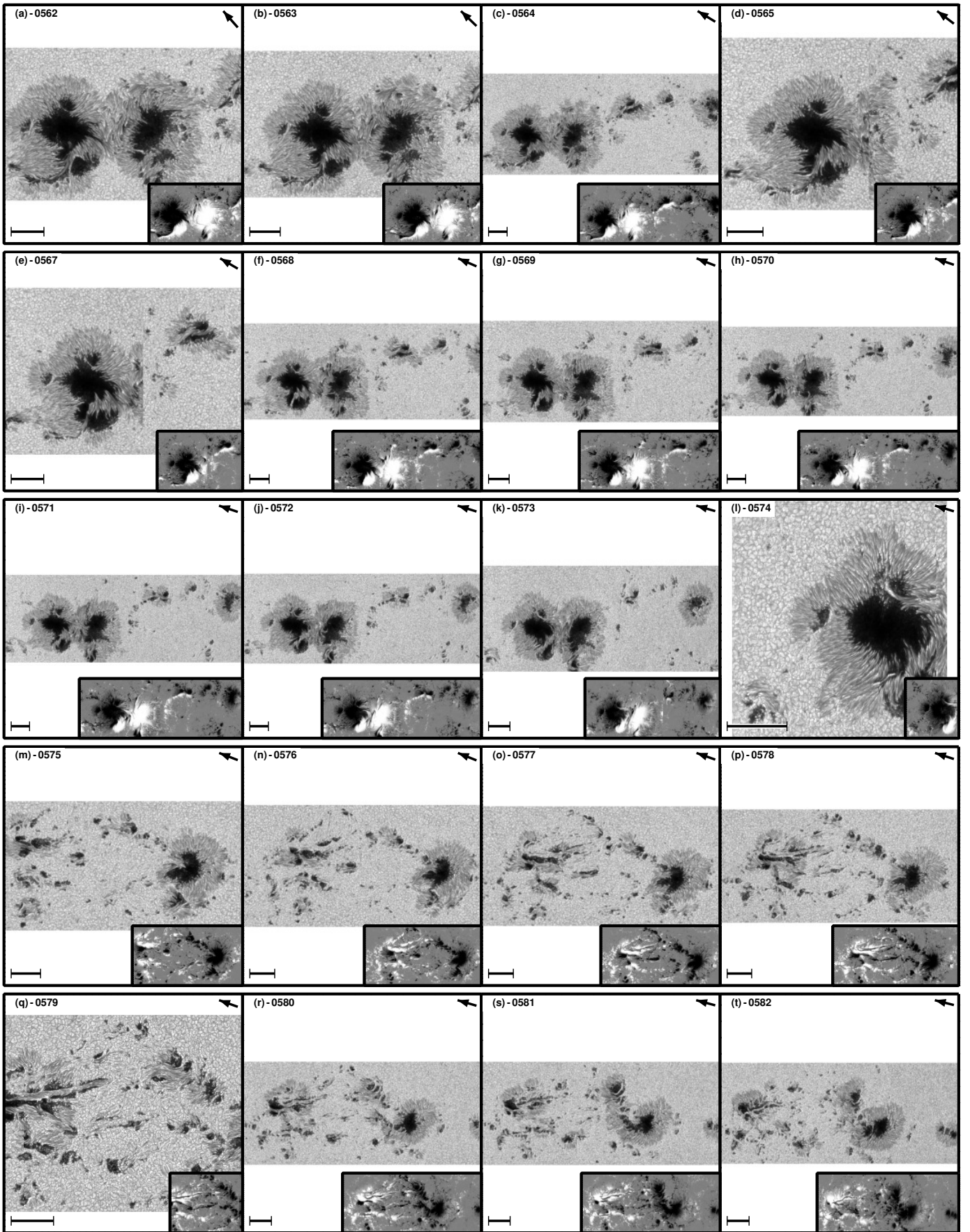


Fig. D.27: Same as Fig. D.1 on page 22. Axes colors display whether the scan was taken in fast mode (black) or normal mode (green).

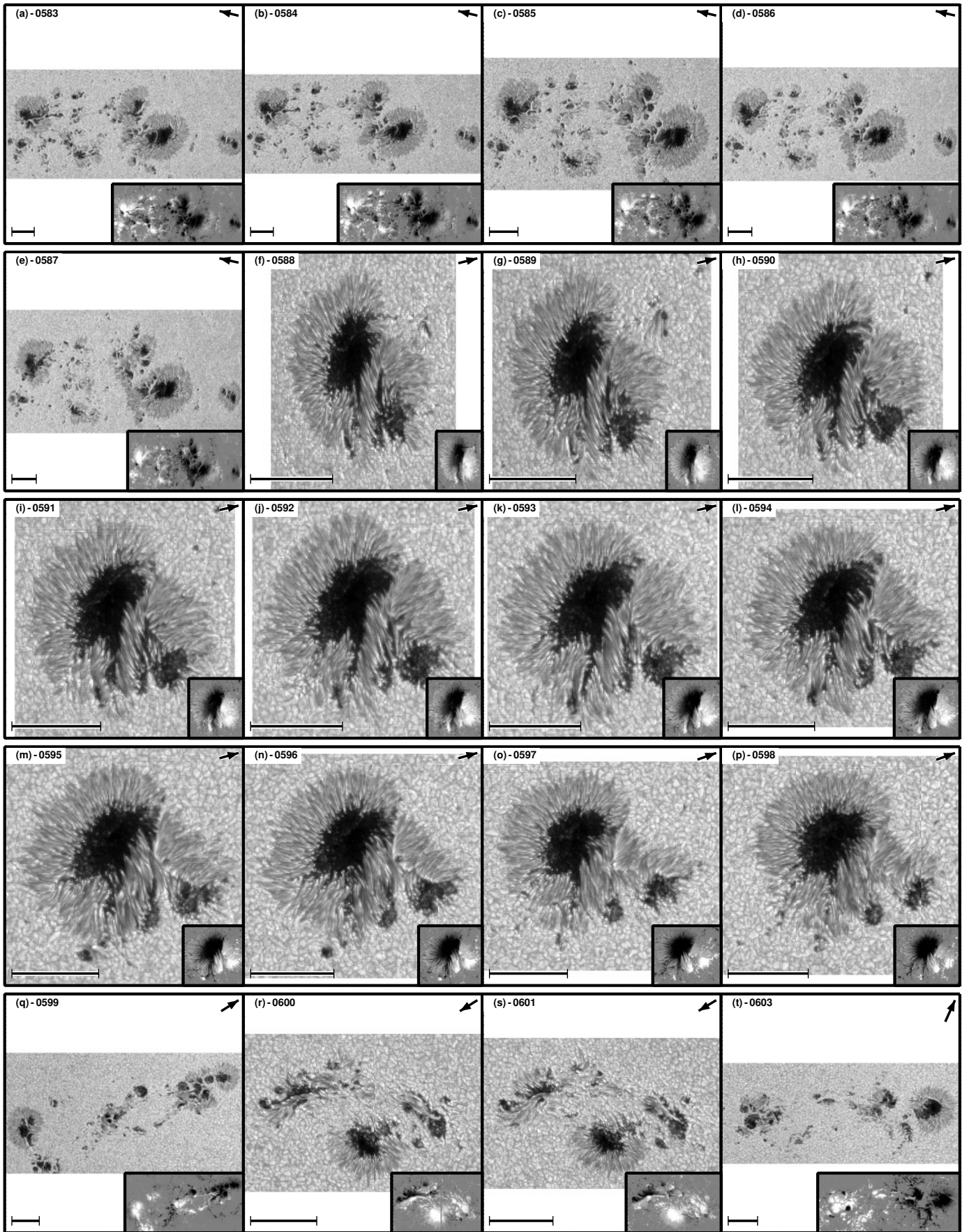


Fig. D.28: Same as Fig. D.1 on page 22. Axes colors display whether the scan was taken in fast mode (black) or normal mode (green).

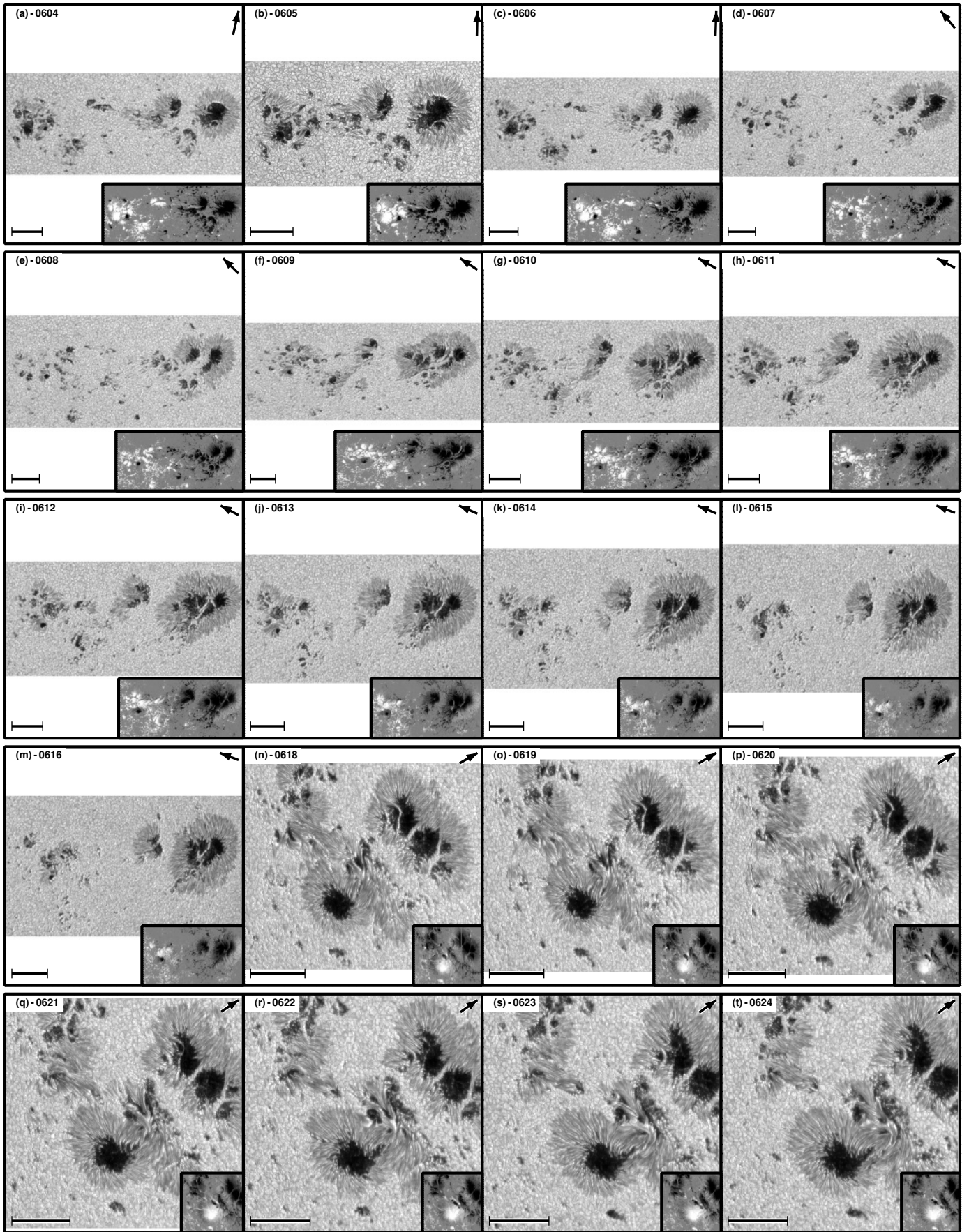


Fig. D.29: Same as Fig. D.1 on page 22. Axes colors display whether the scan was taken in fast mode (black) or normal mode (green).

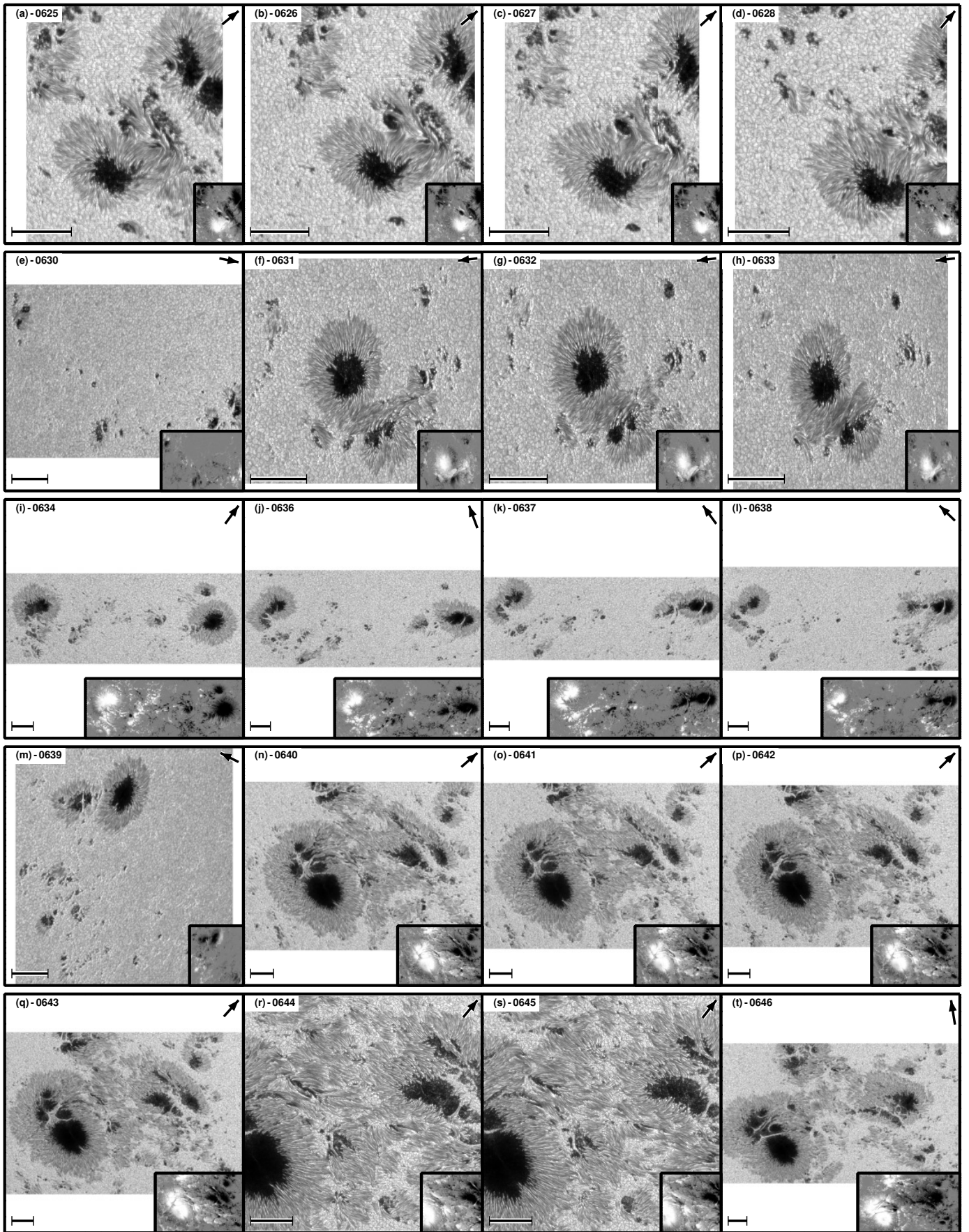


Fig. D.30: Same as Fig. D.1 on page 22. Axes colors display whether the scan was taken in fast mode (black) or normal mode (green).

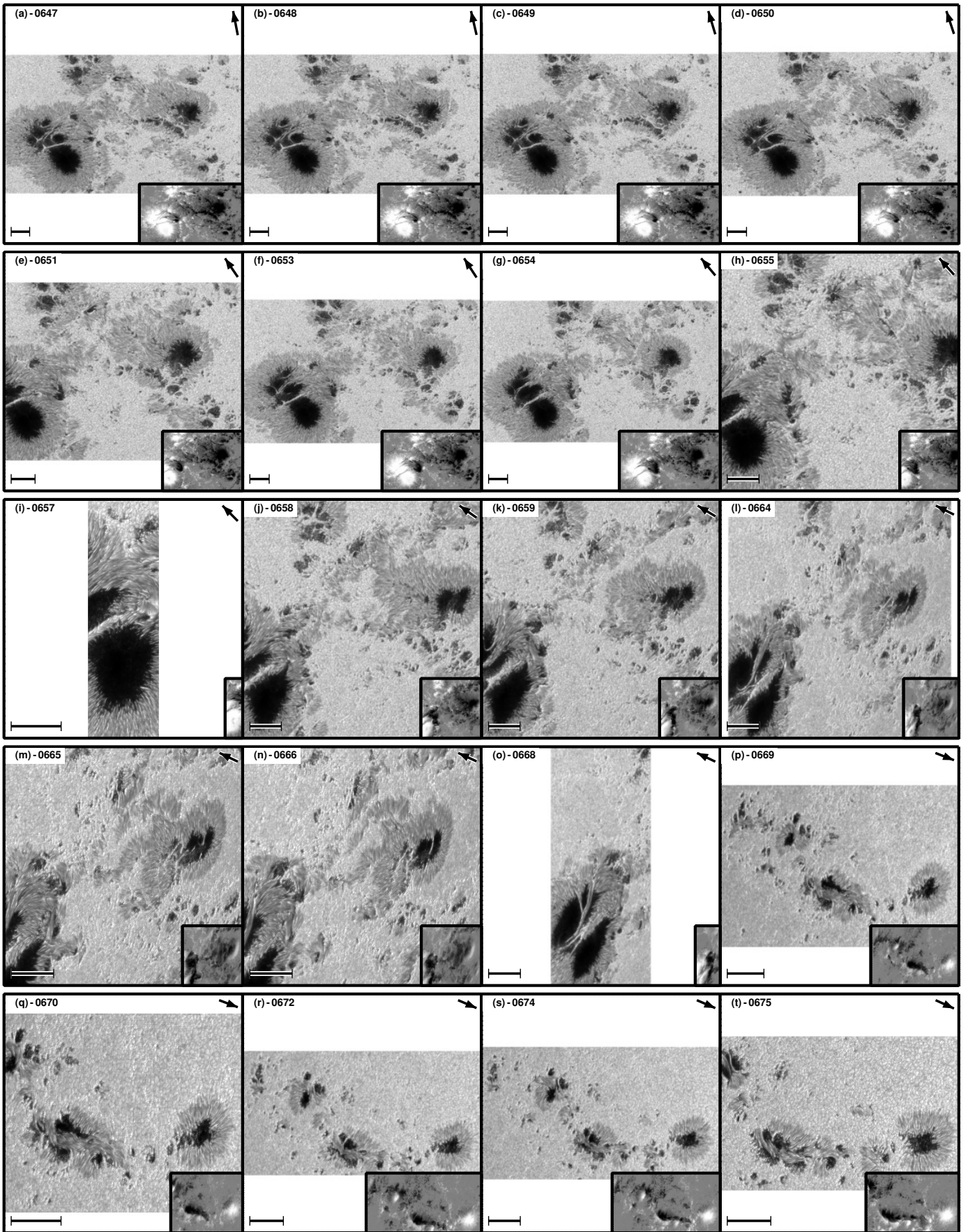


Fig. D.31: Same as Fig. D.1 on page 22. Axes colors display whether the scan was taken in fast mode (black) or normal mode (green).

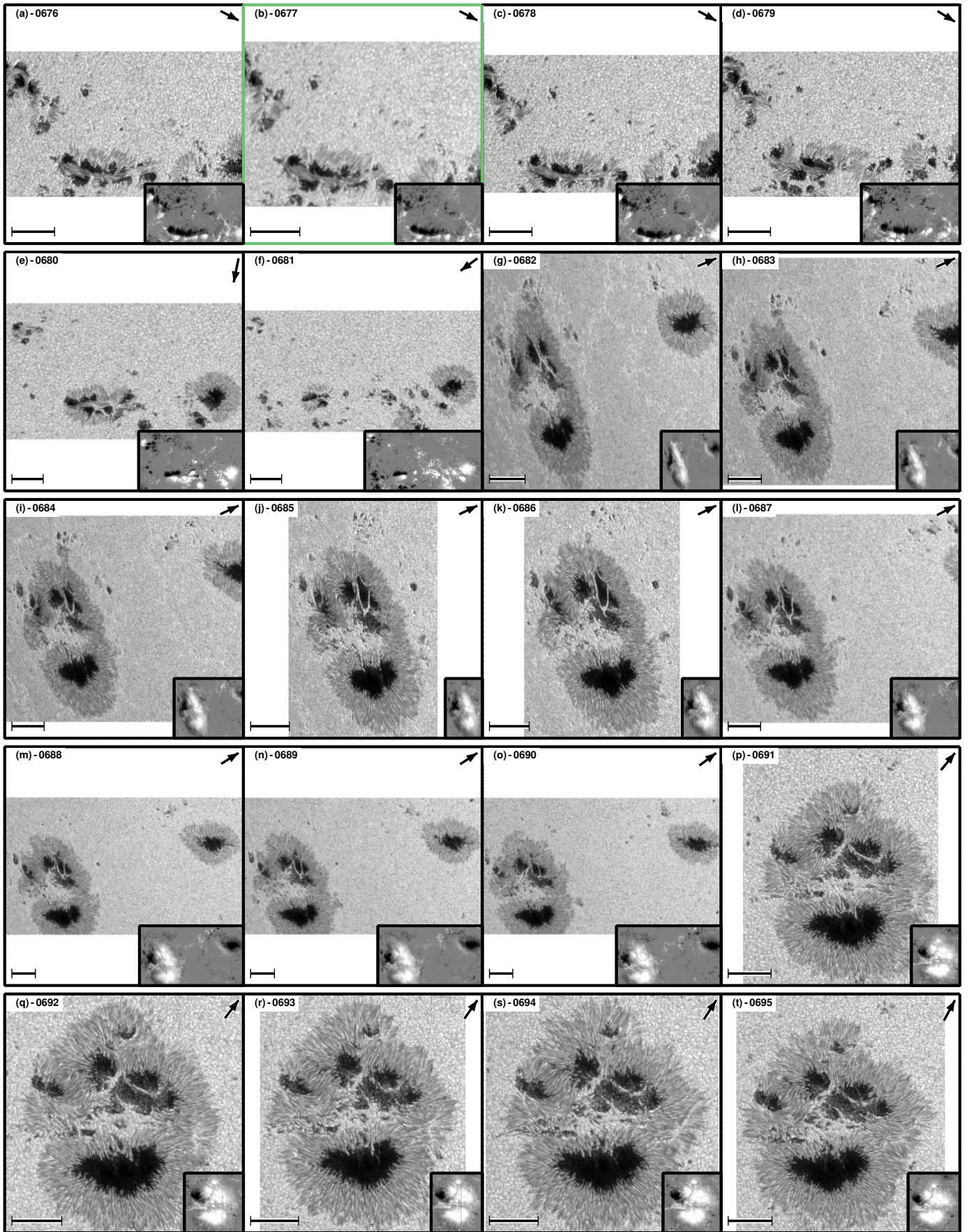


Fig. D.32: Same as Fig. D.1 on page 22. Axes colors display whether the scan was taken in fast mode (black) or normal mode (green).

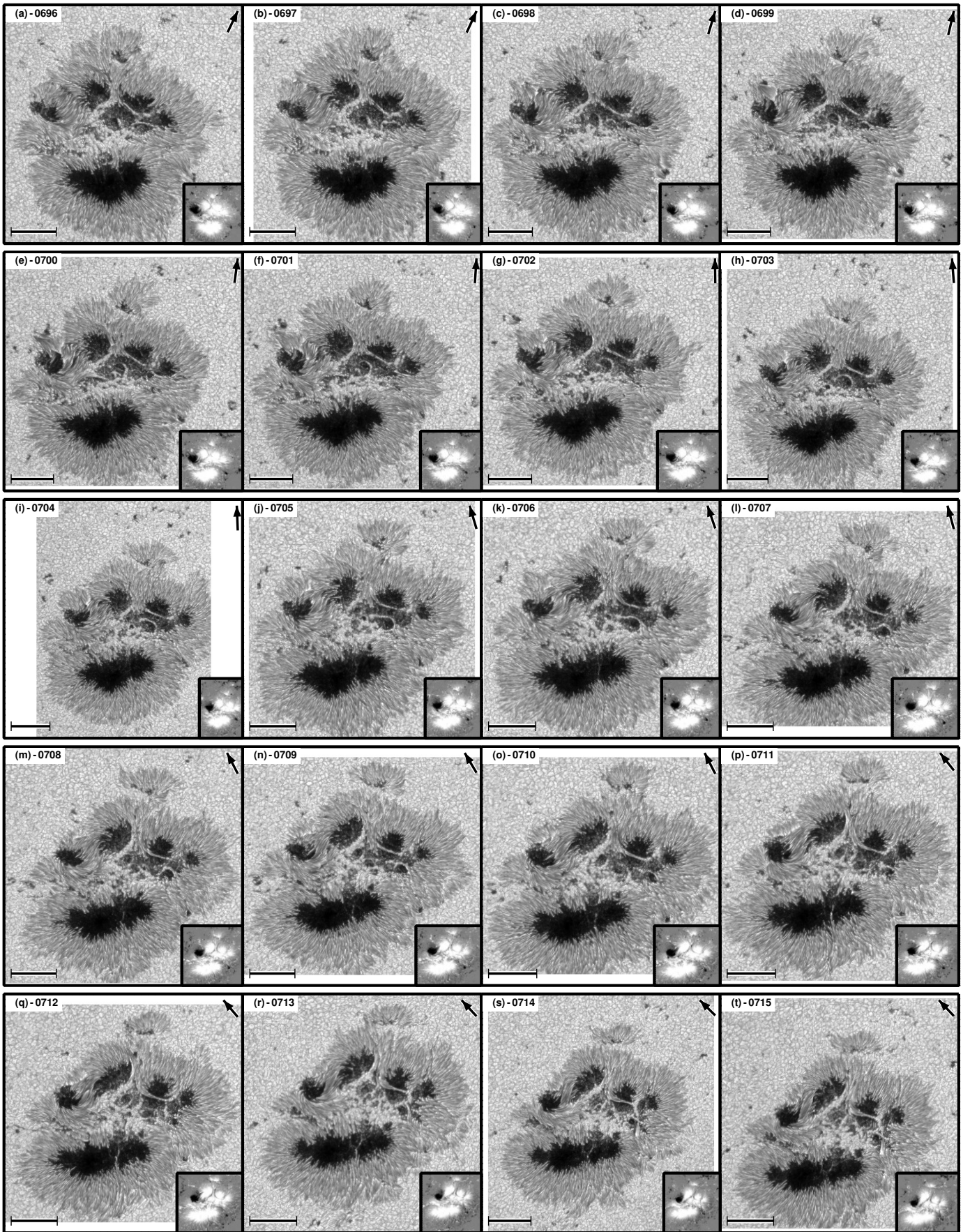


Fig. D.33: Same as Fig. D.1 on page 22. Axes colors display whether the scan was taken in fast mode (black) or normal mode (green).

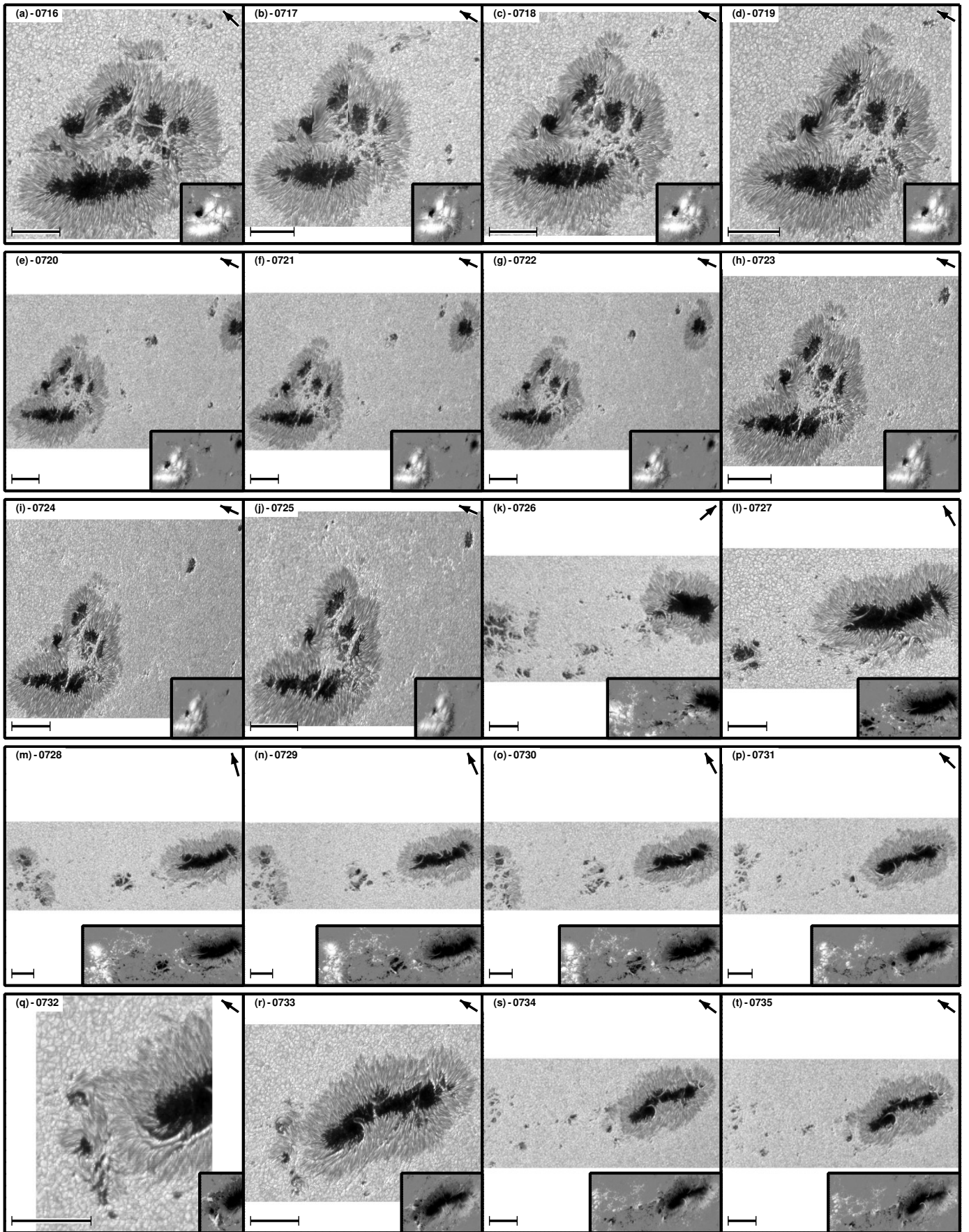


Fig. D.34: Same as Fig. D.1 on page 22. Axes colors display whether the scan was taken in fast mode (black) or normal mode (green).

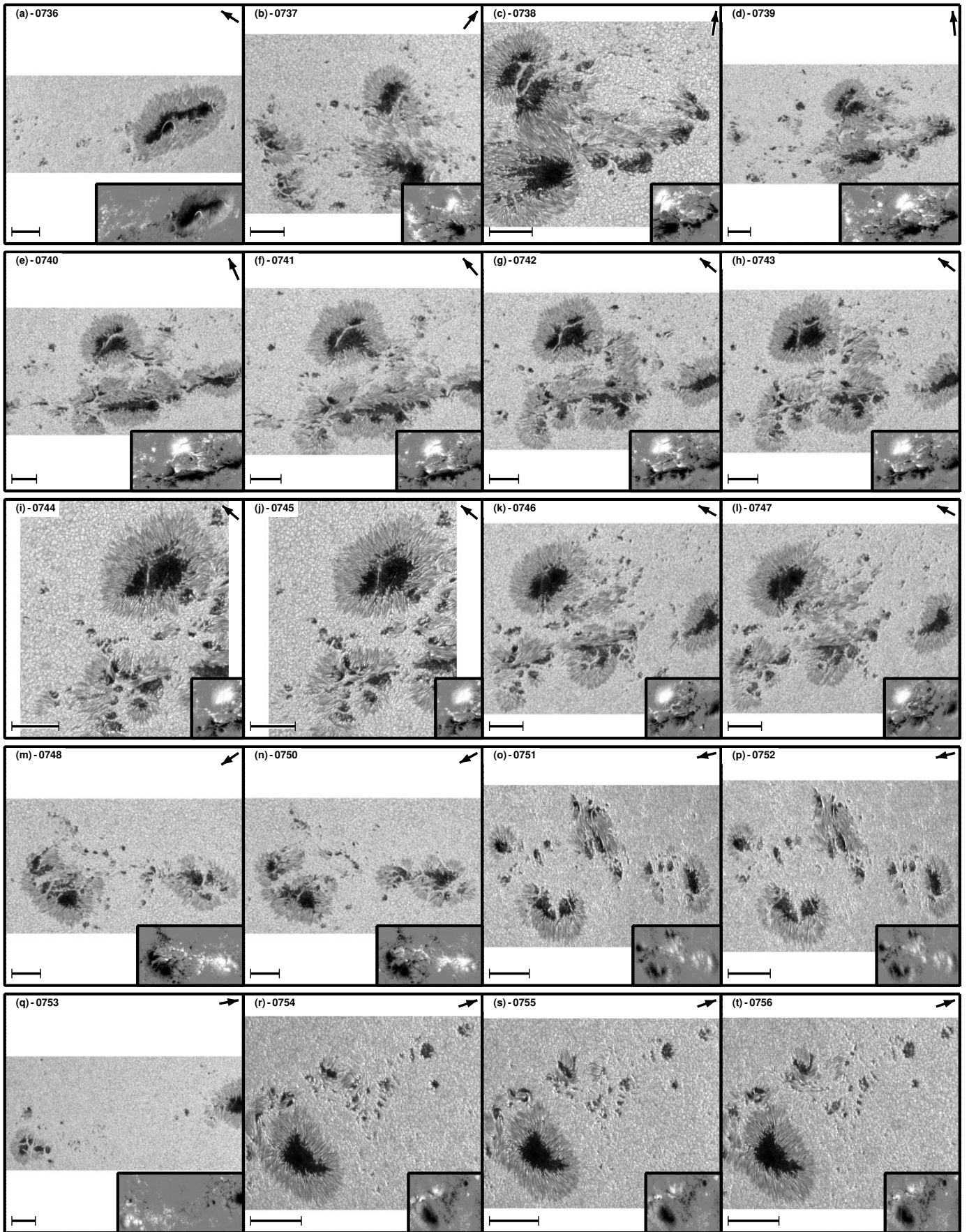


Fig. D.35: Same as Fig. D.1 on page 22. Axes colors display whether the scan was taken in fast mode (black) or normal mode (green).

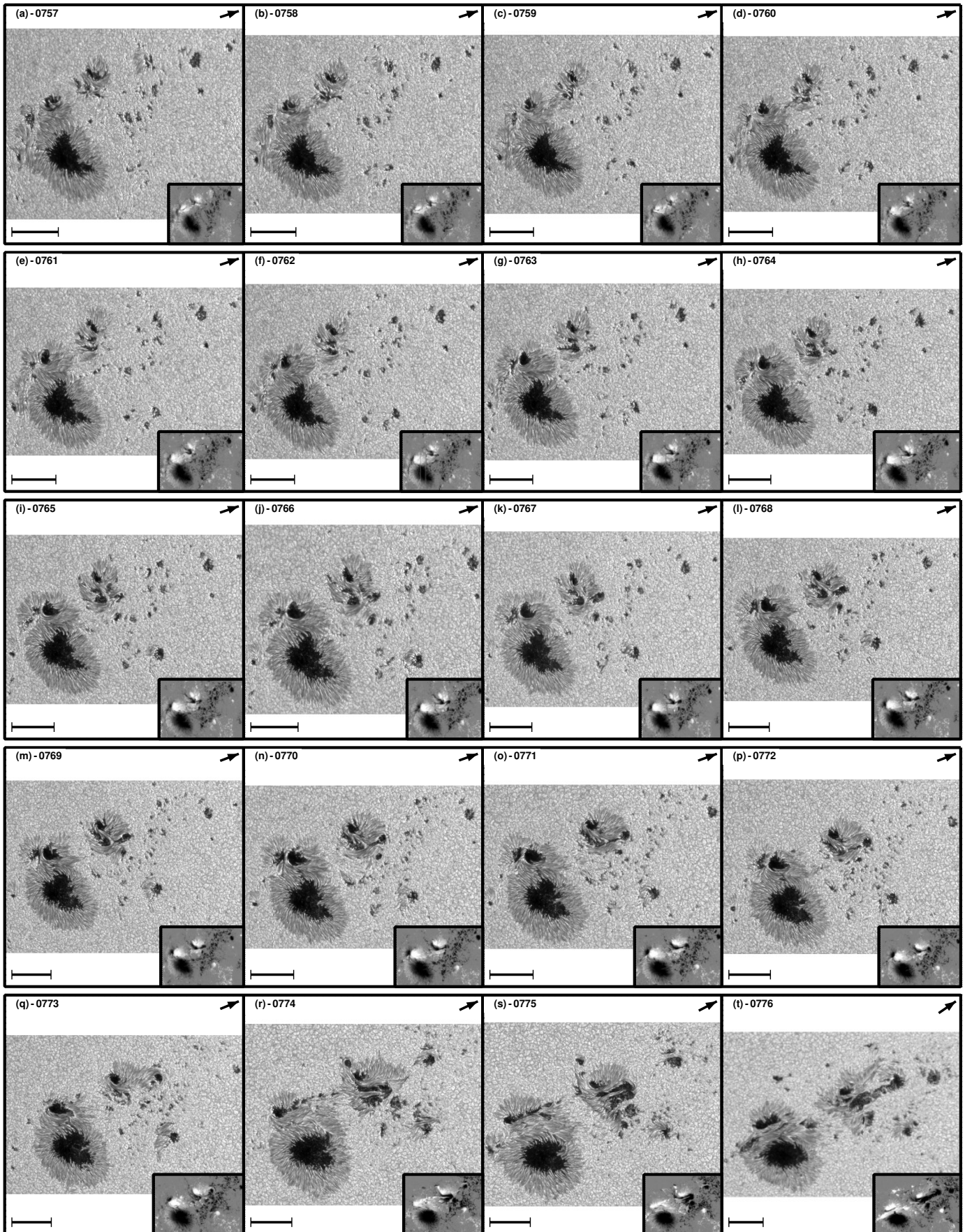


Fig. D.36: Same as Fig. D.1 on page 22. Axes colors display whether the scan was taken in fast mode (black) or normal mode (green).

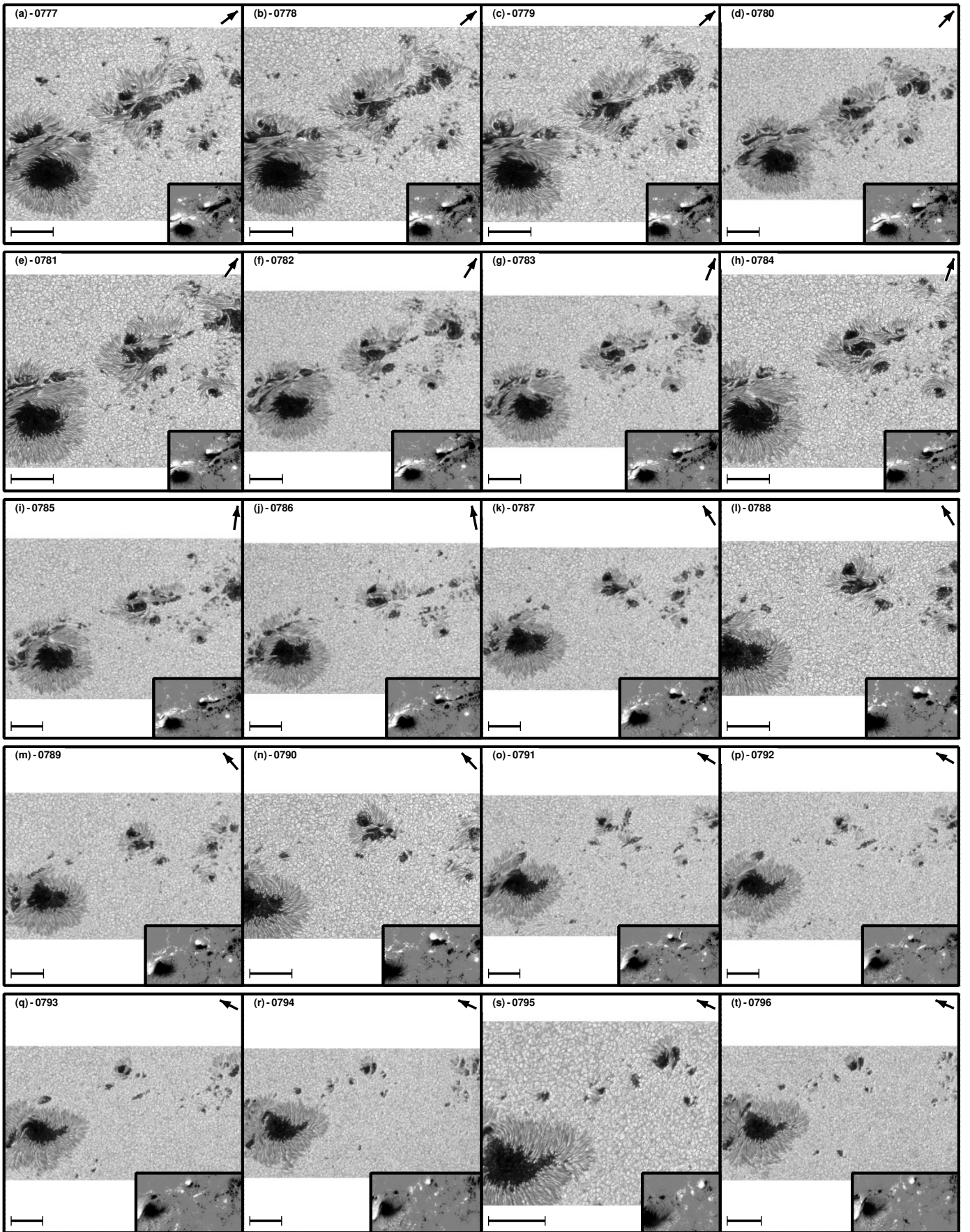


Fig. D.37: Same as Fig. D.1 on page 22. Axes colors display whether the scan was taken in fast mode (black) or normal mode (green).

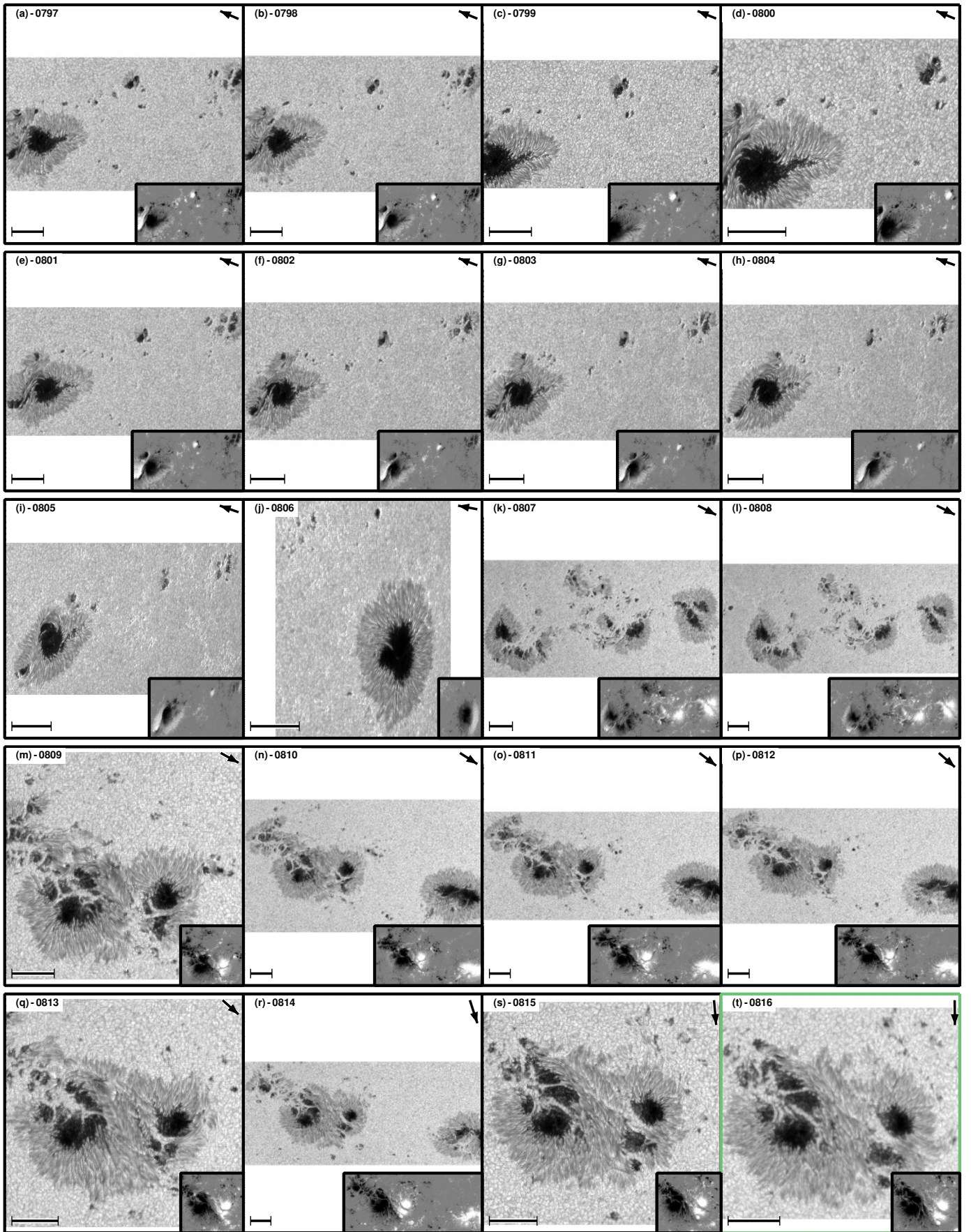


Fig. D.38: Same as Fig. D.1 on page 22. Axes colors display whether the scan was taken in fast mode (black) or normal mode (green).

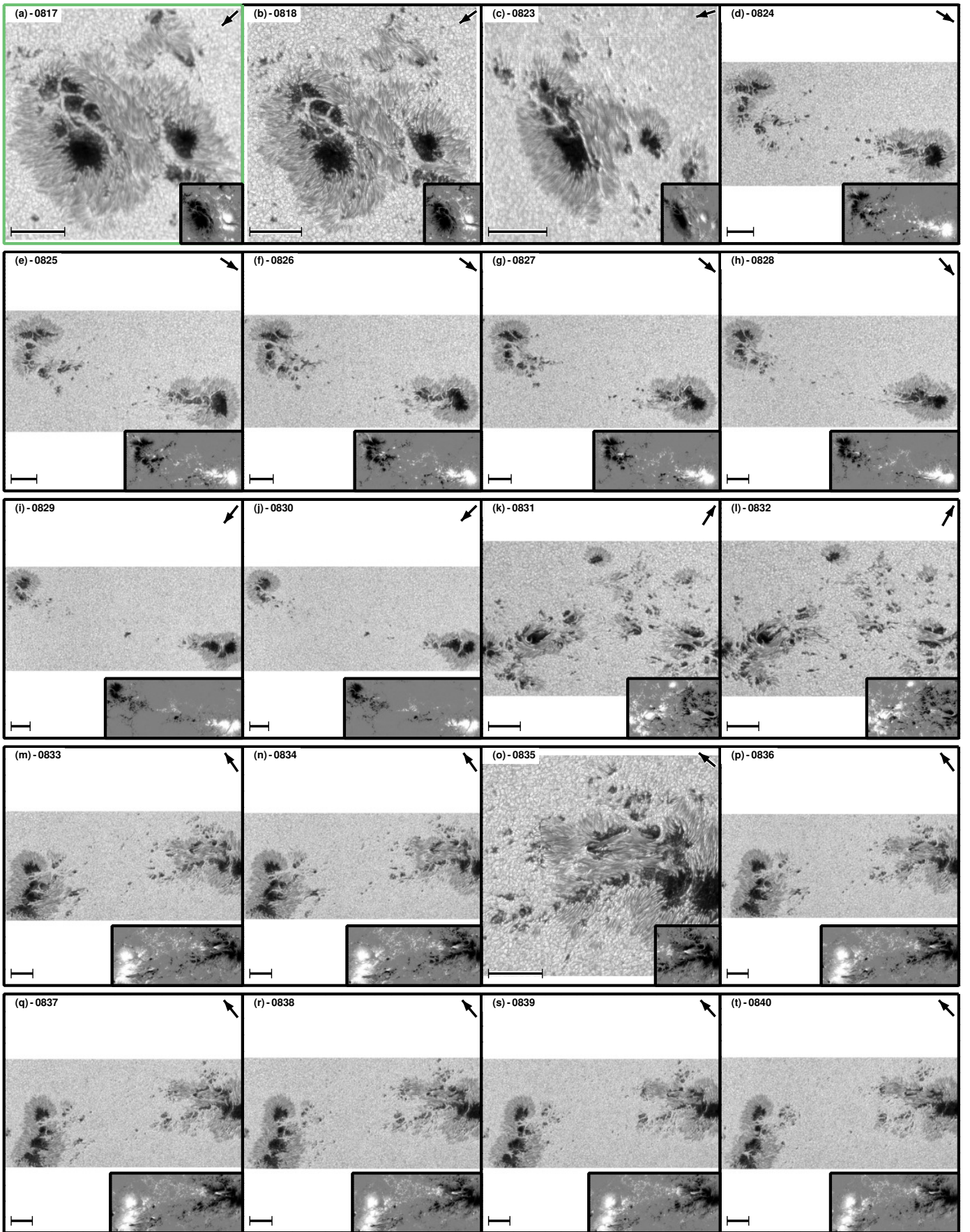


Fig. D.39: Same as Fig. D.1 on page 22. Axes colors display whether the scan was taken in fast mode (black) or normal mode (green).

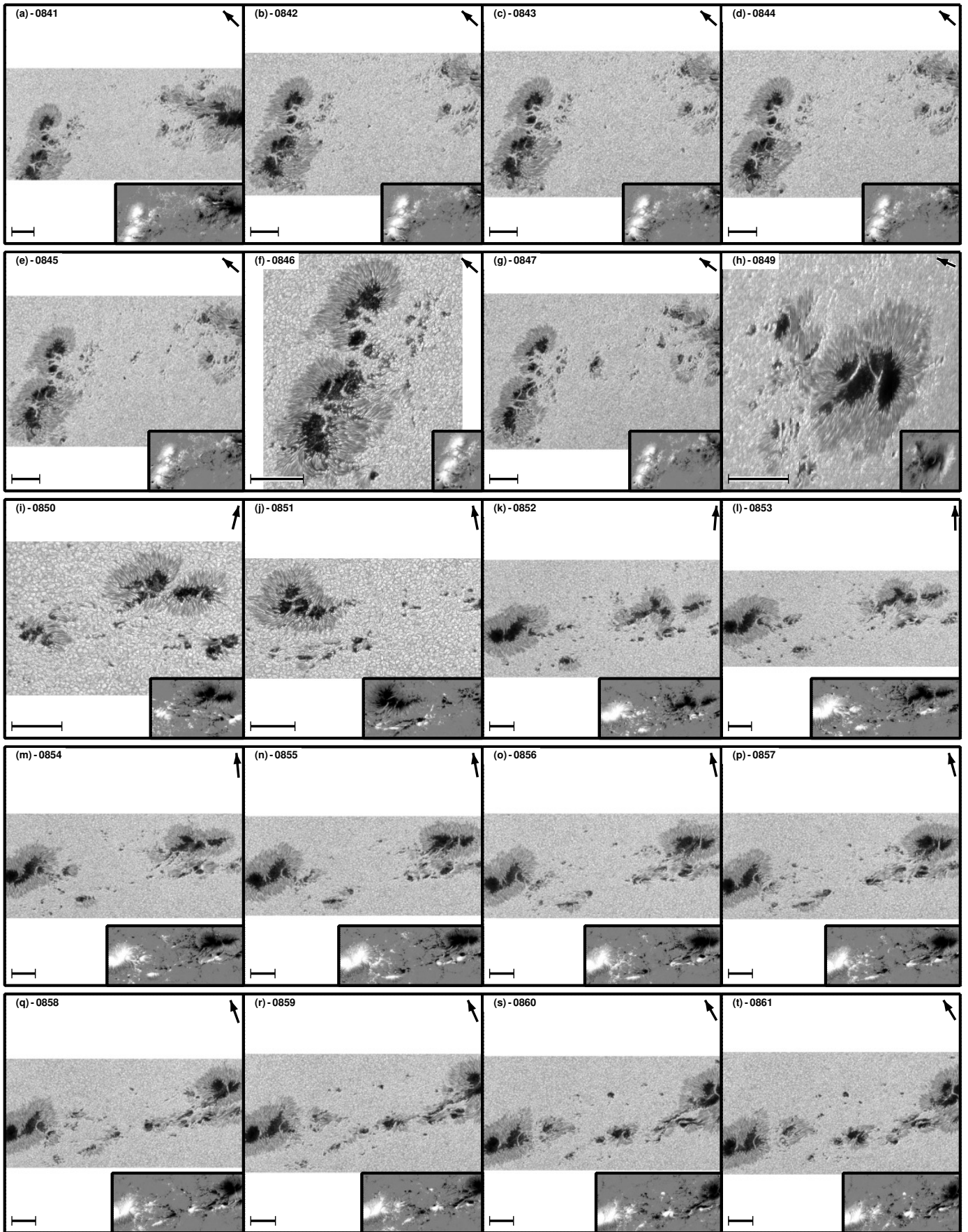


Fig. D.40: Same as Fig. D.1 on page 22. Axes colors display whether the scan was taken in fast mode (black) or normal mode (green).

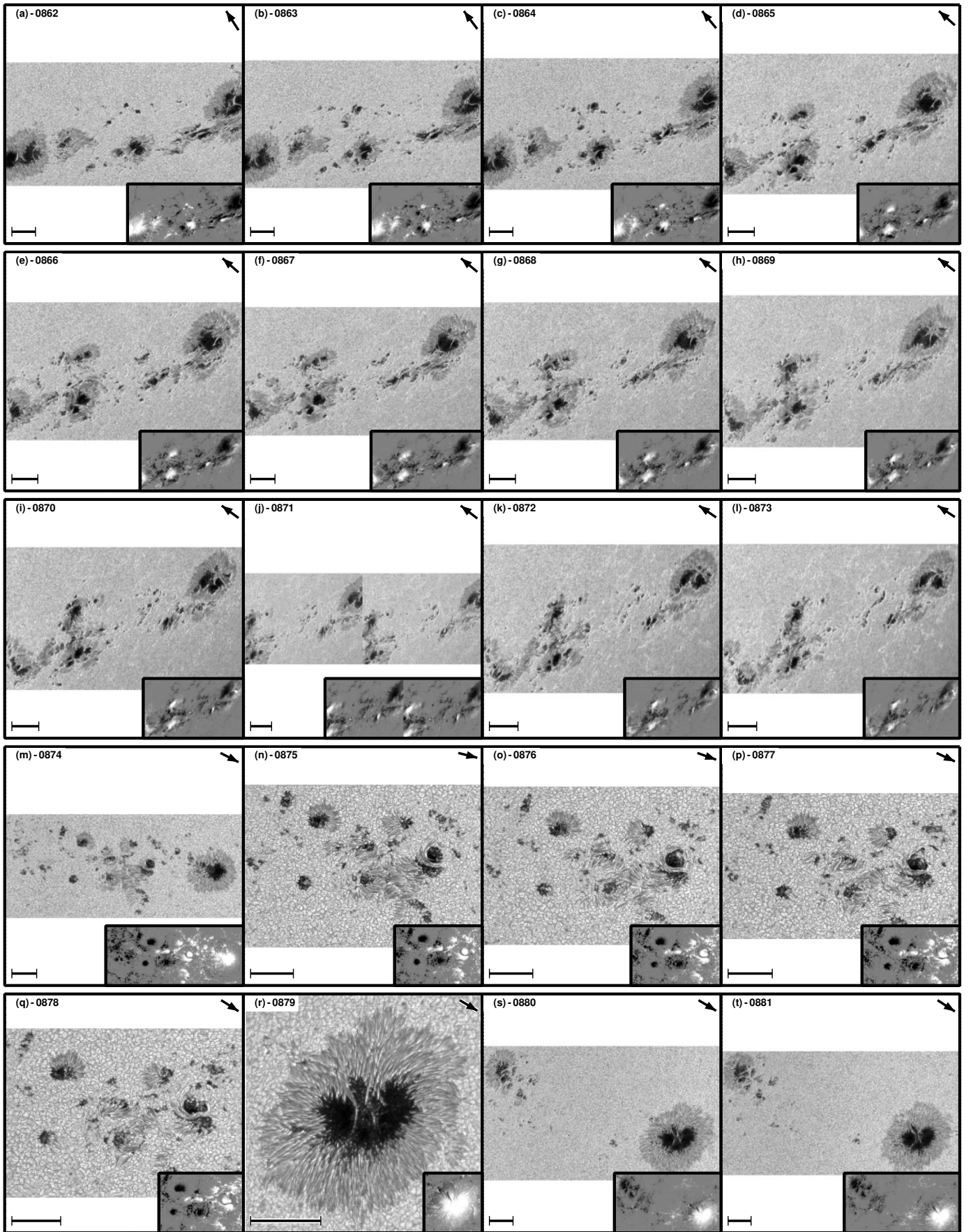


Fig. D.41: Same as Fig. D.1 on page 22. Axes colors display whether the scan was taken in fast mode (black) or normal mode (green).

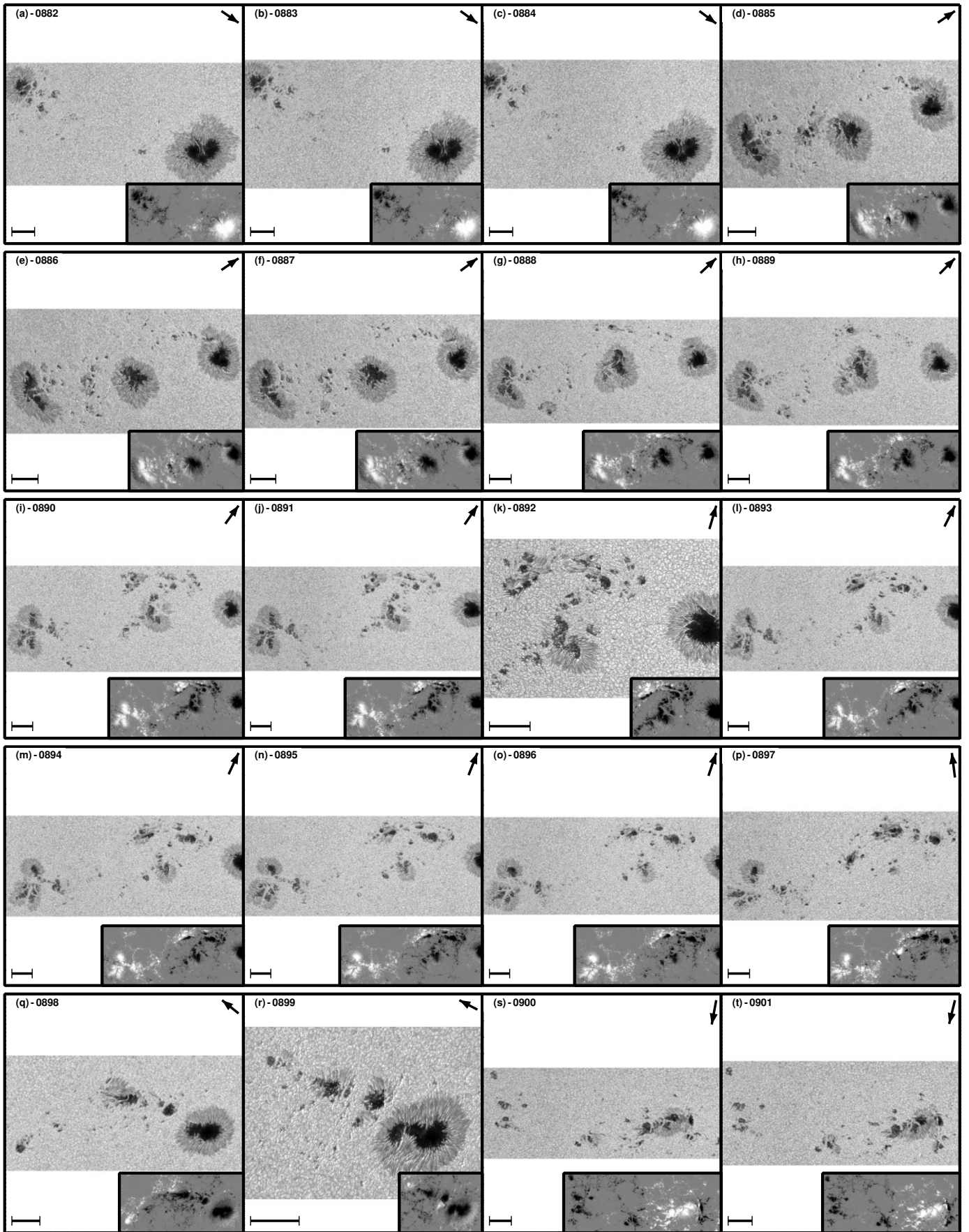


Fig. D.42: Same as Fig. D.1 on page 22. Axes colors display whether the scan was taken in fast mode (black) or normal mode (green).

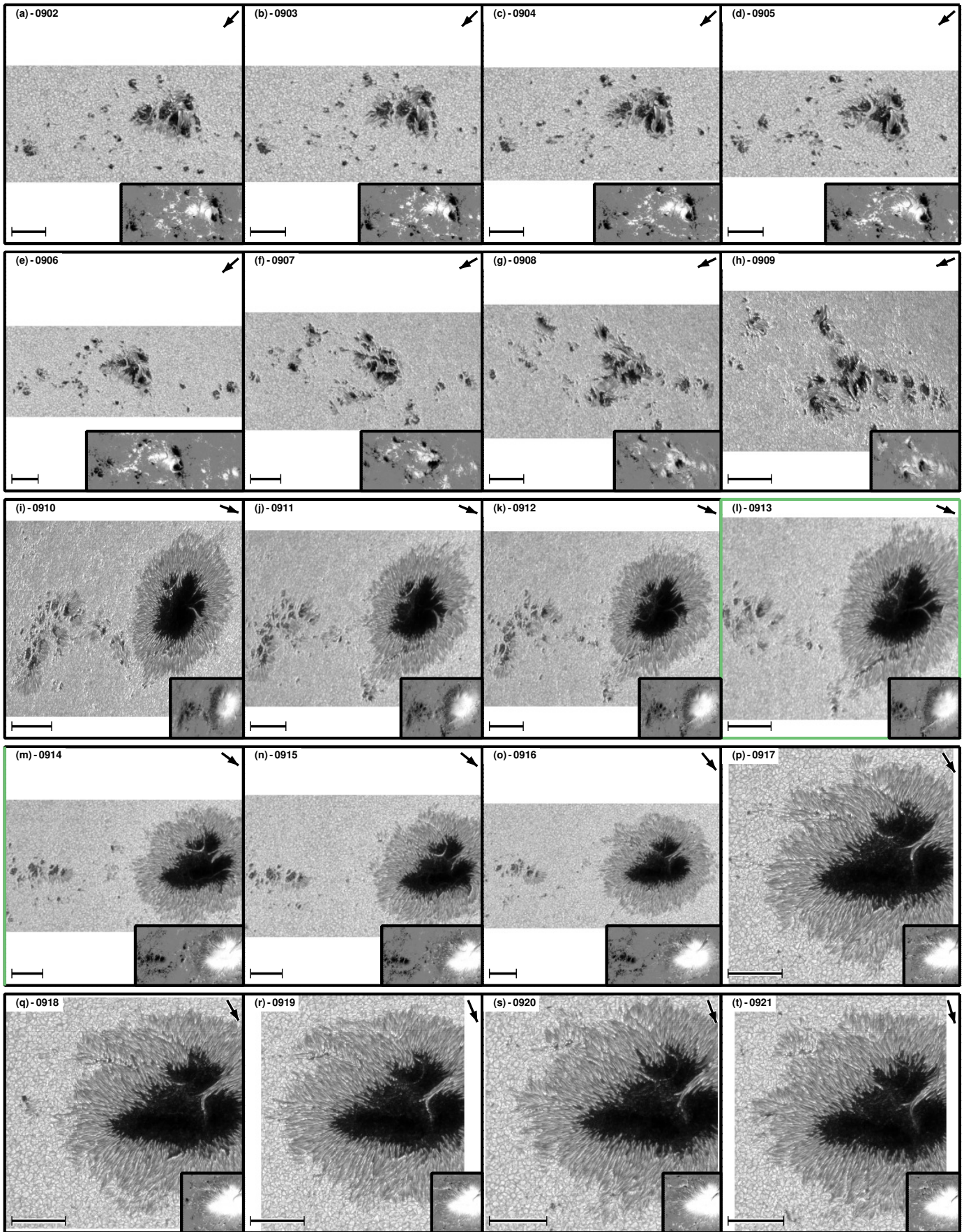


Fig. D.43: Same as Fig. D.1 on page 22. Axes colors display whether the scan was taken in fast mode (black) or normal mode (green).

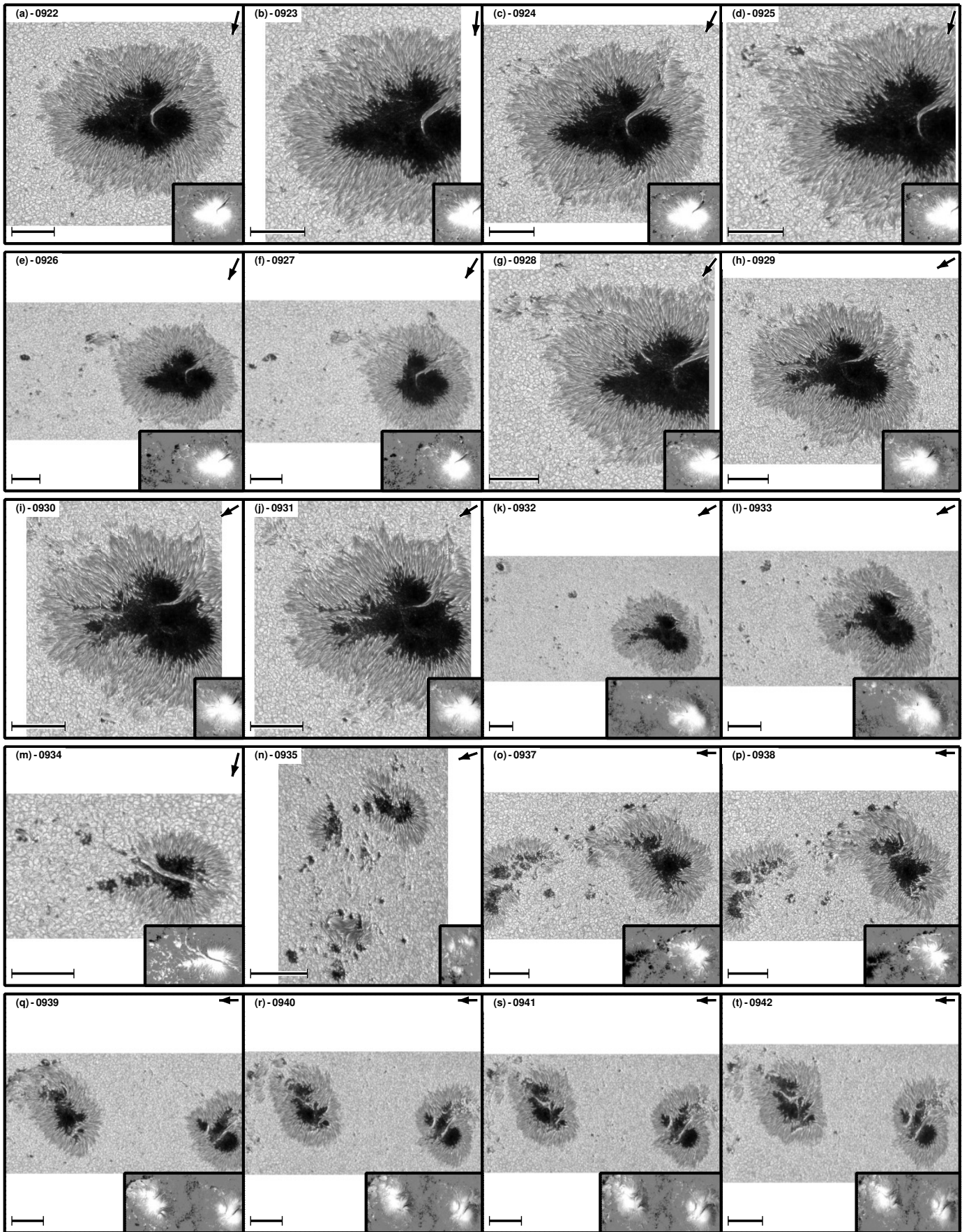


Fig. D.44: Same as Fig. D.1 on page 22. Axes colors display whether the scan was taken in fast mode (black) or normal mode (green).

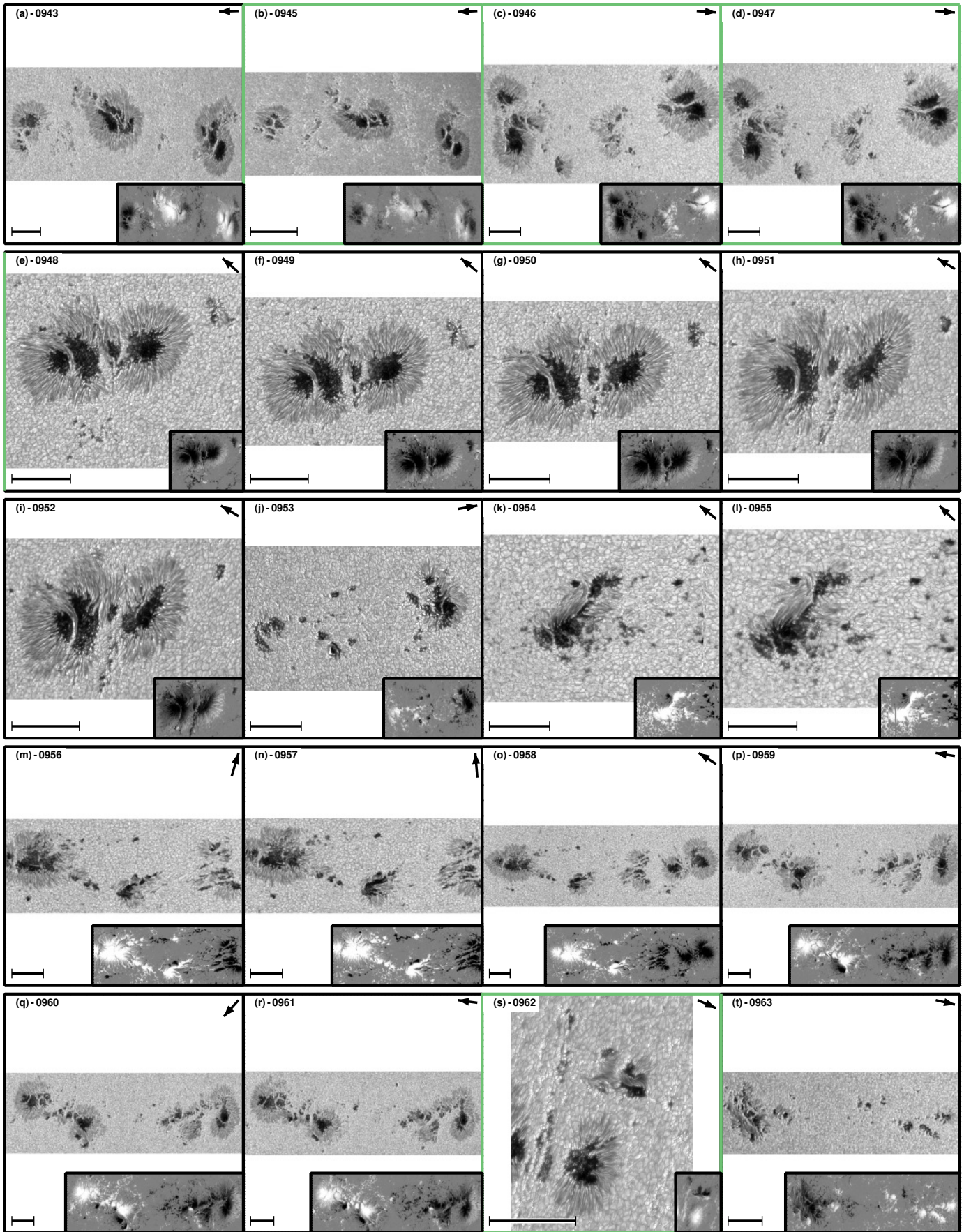


Fig. D.45: Same as Fig. D.1 on page 22. Axes colors display whether the scan was taken in fast mode (black) or normal mode (green).

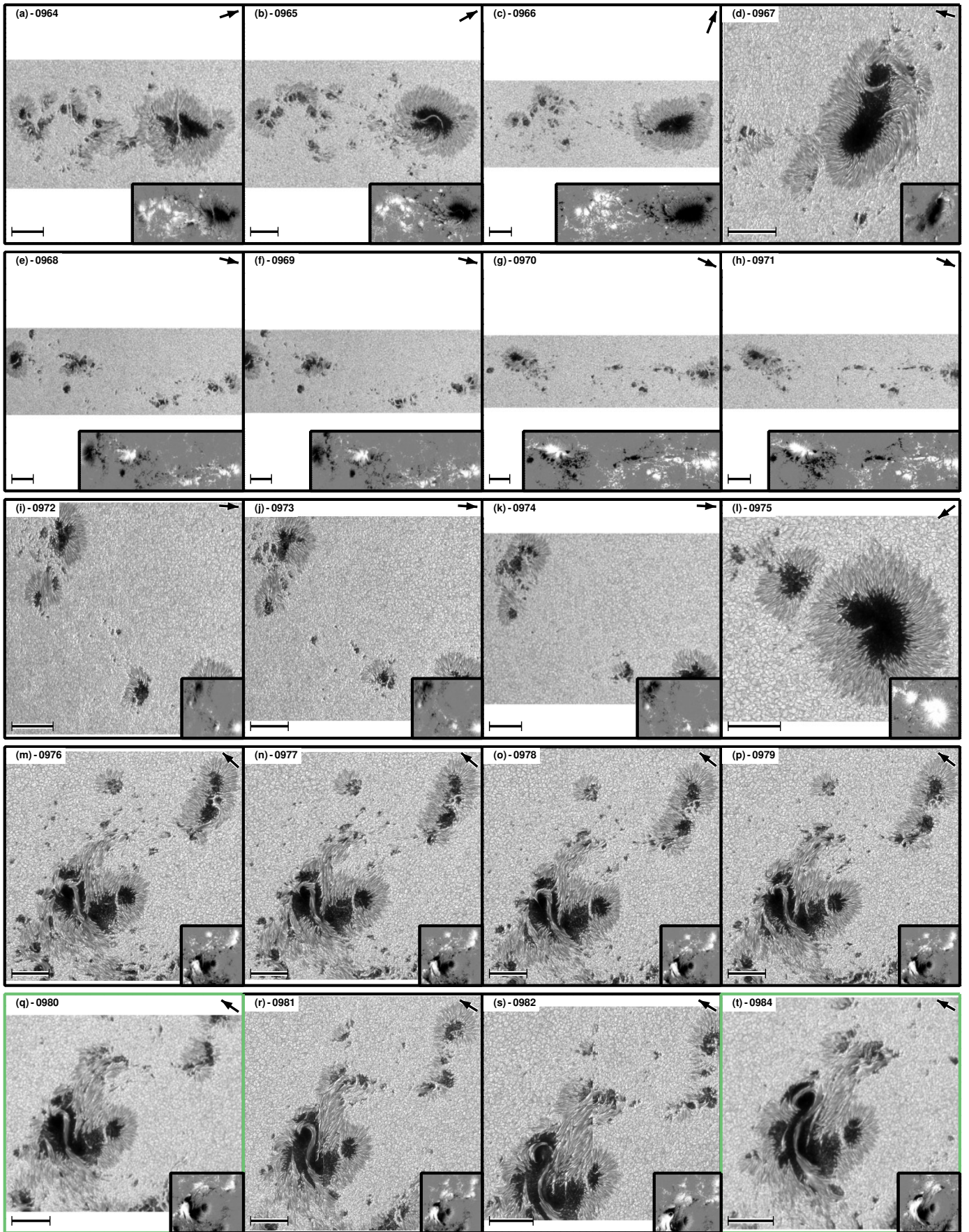


Fig. D.46: Same as Fig. D.1 on page 22. Axes colors display whether the scan was taken in fast mode (black) or normal mode (green).

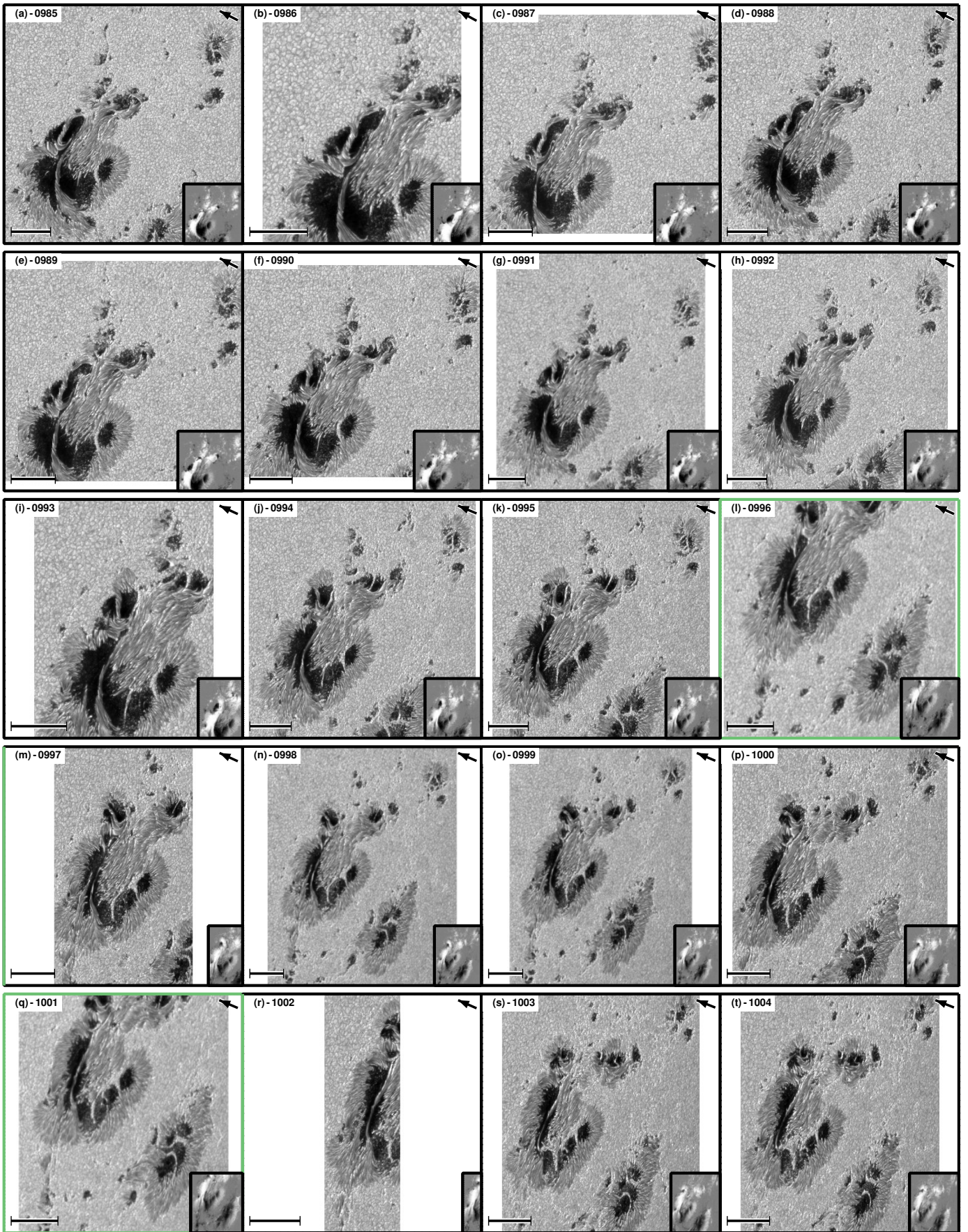


Fig. D.47: Same as Fig. D.1 on page 22. Axes colors display whether the scan was taken in fast mode (black) or normal mode (green).

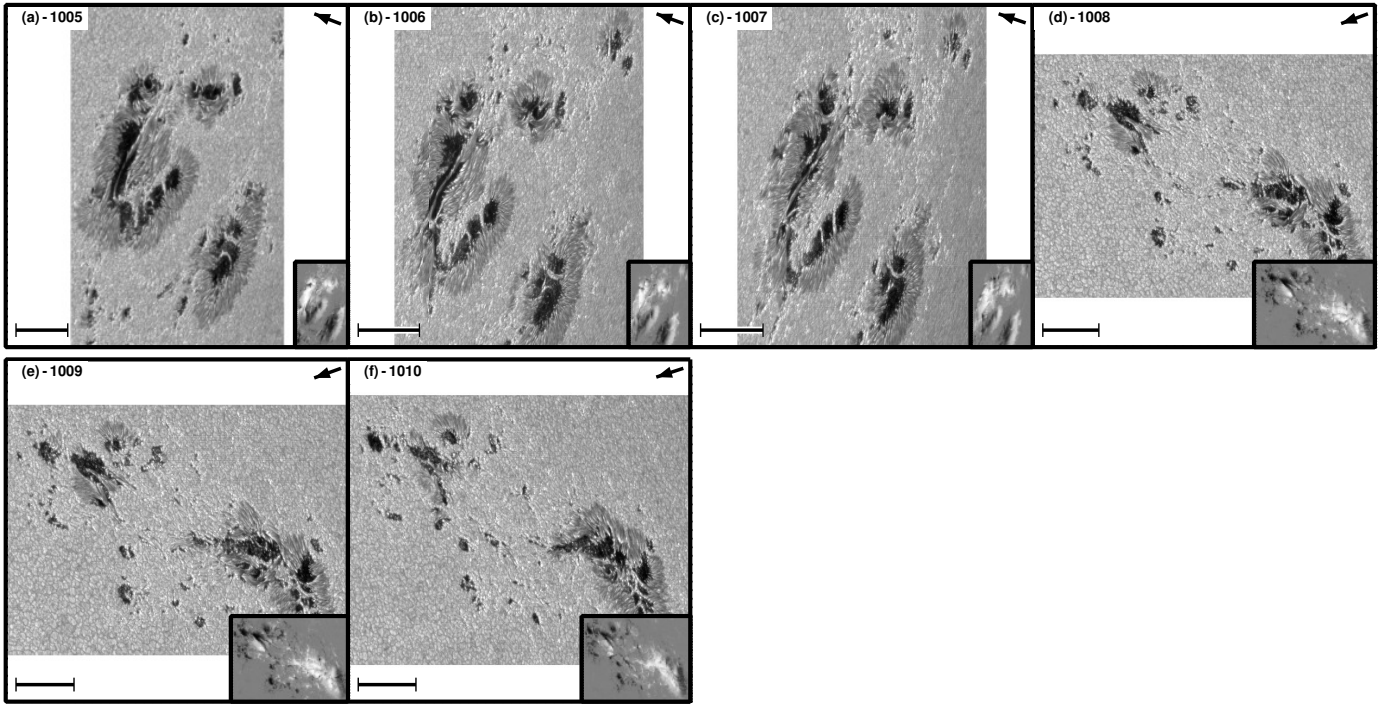


Fig. D.48: Same as Fig. D.1 on page 22. Axes colors display whether the scan was taken in fast mode (black) or normal mode (green).

Table D.1: Sample of sunspot groups part of the MODEST catalog

index	inv_id	obs_id (date)_time	NOAA AR num	type scan	x_c (")	y_c (")	μ	num tiles	size FOV	area (MSH)	Zürich class	magnetic class	Fig. (panel)
1	0000	20061208_061114	10930	Nor.	-797	-72	0.56	100	89" × 95"	430	Dki	$\beta\gamma\delta$	D.1 on page 22(a)
2	0001	20061208_105104	10930	Fast	-670	-58	0.60	25	89" × 95"	430	Dki	$\beta\gamma\delta$	D.1 on page 22(b)
3	0002	20061208_121357	10930	Fast	-661	-58	0.61	25	89" × 95"	430	Dki	$\beta\gamma\delta$	D.1 on page 22(c)
4	0003	20061208_131320	10930	Fast	-634	-57	0.62	25	89" × 95"	430	Dki	$\beta\gamma\delta$	D.1 on page 22(d)
5	0004	20061208_145005	10930	Fast	-643	-53	0.63	25	89" × 95"	430	Dki	$\beta\gamma\delta$	D.1 on page 22(e)
6	0005	20061208_180506	10930	Fast	-621	-54	0.66	25	89" × 95"	430	Dki	$\beta\gamma\delta$	D.1 on page 22(f)
7	0006	20061208_212005	10930	Fast	-598	-54	0.69	25	89" × 95"	430	Dki	$\beta\gamma\delta$	D.1 on page 22(g)
8	0007	20061209_034005	10930	Fast	-548	-53	0.74	25	89" × 95"	430	Dki	$\beta\gamma\delta$	D.1 on page 22(h)
9	0008	20061209_070005	10930	Fast	-517	-51	0.77	25	89" × 95"	430	Dki	$\beta\gamma\delta$	D.1 on page 22(i)
10	0009	20061209_100005	10930	Fast	-493	-54	0.79	25	89" × 95"	430	Dki	$\beta\gamma\delta$	D.1 on page 22(j)
11	0010	20061209_112005	10930	Fast	-482	-53	0.80	25	89" × 95"	430	Dki	$\beta\gamma\delta$	D.1 on page 22(k)
12	0011	20061209_124005	10930	Fast	-471	-53	0.80	25	89" × 95"	430	Dki	$\beta\gamma\delta$	D.1 on page 22(l)
13	0012	20061209_140005	10930	Fast	-459	-53	0.81	25	89" × 95"	430	Dki	$\beta\gamma\delta$	D.1 on page 22(m)
14	0013	20061209_171005	10930	Fast	-434	-54	0.83	25	89" × 95"	430	Dki	$\beta\gamma\delta$	D.1 on page 22(n)
15	0014	20061209_220004	10930	Fast	-391	-49	0.86	25	89" × 95"	430	Dki	$\beta\gamma\delta$	D.1 on page 22(o)
16	0015	20061210_010005	10930	Fast	-363	-51	0.87	25	89" × 95"	430	Dki	$\beta\gamma\delta$	D.1 on page 22(p)
17	0016	20061210_105507	10930	Nor.	-270	-51	0.92	100	89" × 95"	430	Dki	$\beta\gamma\delta$	D.2 on page 23(a)
18	0017	20061210_210007	10930	Fast	-176	-50	0.95	25	89" × 95"	430	Dki	$\beta\gamma\delta$	D.2 on page 23(b)
19	0018	20061211_031004	10930	Fast	-116	-46	0.97	25	89" × 95"	440	Cki	$\beta\gamma\delta$	D.2 on page 23(c)
20	0019	20061211_080004	10930	Fast	-72	-43	0.98	25	89" × 95"	440	Cki	$\beta\gamma\delta$	D.2 on page 23(d)
21	0020	20061211_111006	10930	Fast	-48	-47	0.98	25	89" × 95"	440	Cki	$\beta\gamma\delta$	D.2 on page 23(e)
22	0021	20061211_131009	10930	Nor.	-32	-48	0.99	100	89" × 95"	440	Cki	$\beta\gamma\delta$	D.2 on page 23(f)
23	0022	20061211_170008	10930	Fast	5	-48	0.99	25	89" × 95"	440	Cki	$\beta\gamma\delta$	D.2 on page 23(g)
24	0023	20061211_200005	10930	Fast	32	-47	0.99	25	89" × 95"	440	Cki	$\beta\gamma\delta$	D.2 on page 23(h)
25	0024	20061211_231005	10930	Fast	64	-47	1.00	25	89" × 95"	440	Cki	$\beta\gamma\delta$	D.2 on page 23(i)
26	0025	20061212_035005	10930	Fast	107	-48	1.00	25	89" × 95"	480	Dki	$\beta\gamma\delta$	D.2 on page 23(j)

Table D.1: continued.

index	inv_id	obs_id (date)_(time)	NOAA AR num	type scan	x_c (")	y_c (")	μ	num tiles	size FOV	area (MSH)	Zürich class	magnetic class	Fig. (panel)
27	0026	20061212_101008	10930	Nor.	164	-51	0.99	100	89" × 95"	480	Dki	$\beta\gamma\delta$	D.2 on page 23(k)
28	0027	20061212_153008	10930	Fast	206	-52	0.99	25	89" × 95"	480	Dki	$\beta\gamma\delta$	D.2 on page 23(l)
29	0028	20061212_174005	10930	Fast	230	-53	0.99	25	89" × 95"	480	Dki	$\beta\gamma\delta$	D.2 on page 23(m)
30	0029	20061212_203005	10930	Fast	252	-52	0.98	25	89" × 95"	480	Dki	$\beta\gamma\delta$	D.2 on page 23(n)
31	0030	20061213_043005	10930	Fast	324	-58	0.97	25	89" × 95"	680	Dki	$\beta\gamma\delta$	D.2 on page 23(o)
32	0031	20061213_075005	10930	Fast	355	-58	0.96	25	89" × 95"	680	Dki	$\beta\gamma\delta$	D.2 on page 23(p)
33	0032	20061213_125104	10930	Nor.	396	-51	0.94	100	89" × 95"	680	Dki	$\beta\gamma\delta$	D.2 on page 23(q)
34	0033	20061213_162104	10930	Fast	425	-56	0.94	25	89" × 95"	680	Dki	$\beta\gamma\delta$	D.2 on page 23(r)
35	0034	20061214_002005	10930	Fast	487	-58	0.91	25	89" × 95"	670	Dki	$\beta\gamma\delta$	D.2 on page 23(s)
36	0035	20061214_050005	10930	Fast	522	-58	0.89	25	89" × 95"	670	Dki	$\beta\gamma\delta$	D.2 on page 23(t)
37	0036	20061214_112602	10930	Nor.	569	-60	0.87	100	89" × 95"	670	Dki	$\beta\gamma\delta$	D.3 on page 24(a)
38	0037	20061214_140103	10930	Fast	589	-63	0.86	25	89" × 95"	670	Dki	$\beta\gamma\delta$	D.3 on page 24(b)
39	0038	20061214_170005	10930	Fast	610	-62	0.84	25	89" × 95"	670	Dki	$\beta\gamma\delta$	D.3 on page 24(c)
40	0039	20061214_220005	10930	Fast	641	-64	0.82	25	89" × 95"	670	Dki	$\beta\gamma\delta$	D.3 on page 24(d)
41	0040	20061215_054505	10930	Fast	692	-63	0.79	25	89" × 95"	620	Dkc	$\beta\gamma\delta$	D.3 on page 24(e)
42	0041	20061215_130205	10930	Nor.	737	-62	0.76	100	89" × 95"	620	Dkc	$\beta\gamma\delta$	D.3 on page 24(f)
43	0046	20070108_195005	10933	Nor.	665	-33	0.75	48	49" × 74"	180	Hkx	α	D.3 on page 24(g)
44	0047	20070109_001036	10933	Nor.	744	-33	0.71	56	57" × 73"	230	Cki	β	D.3 on page 24(h)
45	0048	20070109_063005	10933	Nor.	742	-39	0.68	48	52" × 76"	230	Cki	β	D.3 on page 24(i)
46	0049	20070109_081505	10933	Nor.	747	-41	0.67	63	54" × 77"	230	Cki	β	D.3 on page 24(j)
47	0051	20070430_045105	10953	Fast	-283	-71	0.94	25	78" × 82"	500	Dki	$\beta\gamma\delta$	D.3 on page 24(k)
48	0052	20070430_084005	10953	Fast	-235	-60	0.95	20	77" × 75"	500	Dki	$\beta\gamma\delta$	D.3 on page 24(l)
49	0053	20070501_163005	10953	Fast	82	-74	1.00	25	76" × 81"	480	Dki	$\beta\gamma\delta$	D.3 on page 24(m)
50	0054	20070501_193005	10953	Fast	115	-81	1.00	20	72" × 88"	480	Dki	$\beta\gamma\delta$	D.3 on page 24(n)
51	0055	20070501_210006	10953	Nor.	133	-71	0.99	80	70" × 87"	480	Dki	$\beta\gamma\delta$	D.3 on page 24(o)
52	0056	20070502_001506	10953	Fast	152	-72	0.99	20	73" × 89"	440	Cko	$\beta\gamma$	D.3 on page 24(p)
53	0057	20070516_154512	10956	Nor.	-545	87	0.79	81	76" × 80"	130	Dso	$\beta\gamma$	D.3 on page 24(q)
54	0058	20070516_190522	10956	Fast	-502	89	0.81	25	80" × 82"	130	Dso	$\beta\gamma$	D.3 on page 24(r)
55	0059	20070516_204206	10956	Fast	-486	90	0.82	20	83" × 79"	130	Dso	$\beta\gamma$	D.3 on page 24(s)
56	0060	20070516_222006	10956	Fast	-482	88	0.83	25	85" × 83"	130	Dso	$\beta\gamma$	D.3 on page 24(t)
57	0061	20070517_130101	10956	Nor.	-390	97	0.90	80	81" × 72"	220	Dkc	$\beta\gamma\delta$	D.4 on page 25(a)
58	0062	20070517_161737	10956	Fast	-338	94	0.91	30	107" × 82"	220	Dkc	$\beta\gamma\delta$	D.4 on page 25(b)
59	0063	20070517_181820	10956	Fast	-318	96	0.92	24	103" × 75"	220	Dkc	$\beta\gamma\delta$	D.4 on page 25(c)
60	0064	20070518_034650	10956	Fast	-274	83	0.95	30	92" × 86"	300	Dkc	$\beta\gamma\delta$	D.4 on page 25(d)
61	0065	20070519_074205	10956	Fast	-25	84	1.00	24	95" × 79"	280	Dko	$\beta\gamma\delta$	D.4 on page 25(e)
62	0066	20070519_123821	10956	Nor.	25	84	1.00	72	77" × 75"	280	Dko	$\beta\gamma\delta$	D.4 on page 25(f)
63	0067	20070521_185012	10956	Fast	544	77	0.86	6	37" × 44"	190	Dai	β	D.4 on page 25(g)
64	0068	20070604_125036	10960	Fast	-584	-88	0.74	55	186" × 81"	540	Fkc	$\beta\gamma\delta$	D.4 on page 25(h)
65	0069	20070604_224005	10960	Fast	-526	-88	0.80	60	198" × 84"	540	Fkc	$\beta\gamma\delta$	D.4 on page 25(i)
66	0070	20070710_072505	10963	Fast	-556	-116	0.65	32	139" × 65"	260	Dai	$\beta\gamma$	D.4 on page 25(j)
67	0071	20070710_122136	10963	Fast	-614	-116	0.64	15	90" × 61"	260	Dai	$\beta\gamma$	D.4 on page 25(k)
68	0072	20070710_141031	10963	Fast	-603	-116	0.65	15	90" × 56"	260	Dai	$\beta\gamma$	D.4 on page 25(l)
69	0073	20070710_155025	10963	Fast	-596	-116	0.66	15	90" × 59"	260	Dai	$\beta\gamma$	D.4 on page 25(m)
70	0074	20070710_191156	10963	Fast	-574	-120	0.69	15	91" × 58"	260	Dai	$\beta\gamma$	D.4 on page 25(n)
71	0075	20091027_012004	11029	Fast	496	188	0.85	20	76" × 63"	190	Dai	$\beta\gamma$	D.4 on page 25(o)
72	0076	20091027_104525	11029	Fast	591	198	0.78	24	102" × 67"	190	Dai	$\beta\gamma$	D.4 on page 25(p)
73	0077	20091027_164506	11029	Fast	629	202	0.75	24	100" × 69"	190	Dai	$\beta\gamma$	D.4 on page 25(q)
74	0078	20091027_184506	11029	Fast	640	202	0.74	24	102" × 67"	190	Dai	$\beta\gamma$	D.4 on page 25(r)
75	0079	20091027_212005	11029	Fast	657	204	0.72	24	105" × 69"	190	Dai	$\beta\gamma$	D.4 on page 25(s)
76	0081	20091217_223005	11035	Fast	495	515	0.72	12	68" × 58"	140	Eac	$\beta\delta$	D.4 on page 25(t)
77	0082	20091218_140740	11035	Fast	531	534	0.68	55	185" × 94"	210	Eac	β	D.5 on page 26(a)

Table D.1: continued.

index	inv_id	obs_id (date)_(time)	NOAA AR num	type scan	x_c (")	y_c (")	μ	num tiles	size FOV	area (MSH)	Zürich class	magnetic class	Fig. (panel)
78	0083	20100111_013004	11040	Fast	-317	540	0.76	24	92" × 71"	130	Eao	β	D.5 on page 26(b)
79	0084	20100208_100405	11045	Fast	64	511	0.87	36	148" × 78"	320	Fkc	$\beta\gamma$	D.5 on page 26(c)
80	0085	20100208_154505	11045	Fast	147	505	0.87	32	126" × 69"	320	Fkc	$\beta\gamma$	D.5 on page 26(d)
81	0086	20100209_104106	11045	Fast	345	501	0.82	52	230" × 73"	420	Fkc	$\beta\gamma\delta$	D.5 on page 26(e)
82	0087	20100209_161206	11045	Fast	392	497	0.81	56	241" × 78"	420	Fkc	$\beta\gamma\delta$	D.5 on page 26(f)
83	0088	20100209_224006	11045	Fast	443	495	0.78	56	238" × 77"	420	Fkc	$\beta\gamma\delta$	D.5 on page 26(g)
84	0090	20101027_020005	11117	Fast	281	277	0.93	54	158" × 102"	360	Ehi	$\beta\gamma$	D.5 on page 26(h)
85	0091	20101027_112005	11117	Fast	361	278	0.90	54	151" × 102"	360	Ehi	$\beta\gamma$	D.5 on page 26(i)
86	0092	20101029_030042	11117	Fast	662	293	0.71	42	116" × 100"	520	Dkc	β	D.5 on page 26(j)
87	0093	20101029_110005	11117	Fast	724	299	0.66	30	99" × 95"	520	Dkc	β	D.5 on page 26(k)
88	0094	20110214_000004	11158	Fast	-32	-216	0.97	54	150" × 108"	120	Eac	$\beta\gamma$	D.5 on page 26(l)
89	0095	20110214_063004	11158	Fast	23	-214	0.97	54	151" × 109"	120	Eac	$\beta\gamma$	D.5 on page 26(m)
90	0096	20110215_101126	11158	Fast	272	-223	0.93	55	195" × 90"	450	Ekc	$\beta\gamma$	D.5 on page 26(n)
91	0097	20110215_121106	11158	Fast	288	-224	0.93	56	196" × 89"	450	Ekc	$\beta\gamma$	D.5 on page 26(o)
92	0098	20110215_141106	11158	Fast	306	-224	0.92	55	195" × 92"	450	Ekc	$\beta\gamma$	D.5 on page 26(p)
93	0099	20110215_154006	11158	Fast	316	-224	0.92	55	192" × 88"	450	Ekc	$\beta\gamma$	D.5 on page 26(q)
94	0100	20110215_184006	11158	Fast	343	-225	0.91	55	194" × 87"	450	Ekc	$\beta\gamma$	D.5 on page 26(r)
95	0101	20110215_204005	11158	Fast	359	-224	0.90	55	192" × 88"	450	Ekc	$\beta\gamma$	D.5 on page 26(s)
96	0102	20110215_233005	11158	Fast	381	-227	0.89	55	192" × 87"	450	Ekc	$\beta\gamma$	D.5 on page 26(t)
97	0103	20110216_010005	11158	Fast	393	-227	0.89	55	193" × 87"	600	Ekc	$\beta\gamma\delta$	D.6 on page 27(a)
98	0104	20110216_023005	11158	Fast	404	-228	0.88	55	195" × 88"	600	Ekc	$\beta\gamma\delta$	D.6 on page 27(b)
99	0105	20110216_043005	11158	Fast	419	-229	0.87	55	192" × 87"	600	Ekc	$\beta\gamma\delta$	D.6 on page 27(c)
100	0106	20110216_073005	11158	Fast	441	-231	0.86	55	190" × 86"	600	Ekc	$\beta\gamma\delta$	D.6 on page 27(d)
101	0107	20110216_092005	11158	Fast	454	-231	0.86	55	187" × 86"	600	Ekc	$\beta\gamma\delta$	D.6 on page 27(e)
102	0108	20110216_113005	11158	Fast	468	-231	0.85	55	187" × 83"	600	Ekc	$\beta\gamma\delta$	D.6 on page 27(f)
103	0109	20110217_101805	11158	Fast	628	-245	0.73	50	169" × 81"	620	Ekc	$\beta\gamma\delta$	D.6 on page 27(g)
104	0110	20110217_130005	11158	Fast	648	-247	0.71	50	166" × 83"	620	Ekc	$\beta\gamma\delta$	D.6 on page 27(h)
105	0111	20110217_170005	11158	Fast	671	-250	0.69	50	162" × 84"	620	Ekc	$\beta\gamma\delta$	D.6 on page 27(i)
106	0112	20110217_200005	11158	Fast	688	-253	0.67	50	164" × 81"	620	Ekc	$\beta\gamma\delta$	D.6 on page 27(j)
107	0114	20110218_020005	11158	Fast	722	-257	0.63	45	157" × 81"	290	Eac	$\beta\gamma\delta$	D.6 on page 27(k)
108	0115	20110218_070005	11158	Fast	745	-261	0.60	45	148" × 80"	290	Eac	$\beta\gamma\delta$	D.6 on page 27(l)
109	0116	20110218_100505	11158	Fast	763	-263	0.58	40	143" × 83"	290	Eac	$\beta\gamma\delta$	D.6 on page 27(m)
110	0117	20110218_130005	11158	Fast	787	-265	0.55	40	137" × 82"	290	Eac	$\beta\gamma\delta$	D.6 on page 27(n)
111	0118	20110219_103406	11162	Fast	190	432	0.89	32	133" × 71"	260	Dai	$\beta\gamma$	D.6 on page 27(o)
112	0119	20110219_142006	11162	Fast	224	431	0.88	32	134" × 71"	260	Dai	$\beta\gamma$	D.6 on page 27(p)
113	0120	20110219_181705	11162	Fast	253	429	0.87	24	140" × 52"	260	Dai	$\beta\gamma$	D.6 on page 27(q)
114	0121	20110301_073504	11164	Fast	-439	539	0.68	36	106" × 102"	350	Ehc	$\beta\gamma$	D.6 on page 27(r)
115	0122	20110301_090503	11164	Fast	-420	539	0.69	36	106" × 100"	350	Ehc	$\beta\gamma$	D.6 on page 27(s)
116	0123	20110302_080005	11164	Fast	-284	540	0.78	48	131" × 110"	550	Ekc	$\beta\gamma\delta$	D.6 on page 27(t)
117	0124	20110304_230505	11164	Fast	242	527	0.80	54	148" × 111"	470	Ekc	$\beta\gamma$	D.7 on page 28(a)
118	0125	20110305_020005	11164	Fast	265	527	0.80	54	150" × 111"	570	Ekc	$\beta\gamma\delta$	D.7 on page 28(b)
119	0128	20110305_095308	11164	Fast	403	518	0.77	66	193" × 117"	570	Ekc	$\beta\gamma\delta$	D.7 on page 28(c)
120	0129	20110305_114006	11164	Fast	416	518	0.76	77	191" × 117"	570	Ekc	$\beta\gamma\delta$	D.7 on page 28(d)
121	0132	20110305_165006	11164	Fast	455	515	0.74	77	187" × 117"	570	Ekc	$\beta\gamma\delta$	D.7 on page 28(e)
122	0134	20110310_094136	11166	Fast	315	276	0.92	72	201" × 105"	630	Ekc	$\beta\gamma\delta$	D.7 on page 28(f)
123	0135	20110310_144005	11166	Fast	358	274	0.91	72	199" × 113"	630	Ekc	$\beta\gamma\delta$	D.7 on page 28(g)
124	0136	20110310_225505	11166	Fast	428	274	0.88	66	191" × 104"	630	Ekc	$\beta\gamma\delta$	D.7 on page 28(h)
125	0137	20110311_033108	11166	Fast	413	272	0.87	54	151" × 101"	750	Ekc	$\beta\gamma$	D.7 on page 28(i)
126	0138	20110330_140005	11176	Fast	486	-165	0.89	28	120" × 75"	210	Fsi	$\beta\gamma$	D.7 on page 28(j)
127	0139	20110506_012650	11203+11204	Fast	140	343	0.92	48	203" × 66"	80+120	Hsx+Cao	$\alpha+\beta$	D.7 on page 28(k)

Table D.1: continued.

index	inv_id	obs_id (date)_(time)	NOAA AR num	type scan	x_c (")	y_c (")	μ	num tiles	size FOV	area (MSH)	Zürich class	magnetic class	Fig. (panel)
128	0140	20110506_090106	11203+11204	Fast	192	342	0.91	48	203" × 68"	80+120	Hsx+Cao	$\alpha+\beta$	D.7 on page 28(l)
129	0141	20110531_125814	11226	Fast	-464	-358	0.75	35	122" × 96"	360	Dki	$\beta\gamma$	D.7 on page 28(m)
130	0142	20110616_111806	11236	Fast	-655	232	0.59	35	124" × 88"	350	Ehi	$\beta\delta$	D.7 on page 28(n)
131	0143	20110616_130006	11236	Fast	-641	232	0.61	35	121" × 93"	350	Ehi	$\beta\delta$	D.7 on page 28(o)
132	0144	20110616_143906	11236	Fast	-633	231	0.62	35	122" × 89"	350	Ehi	$\beta\delta$	D.7 on page 28(p)
133	0145	20110728_124012	11260	Fast	-358	220	0.89	55	181" × 80"	110	Dsi	$\beta\gamma$	D.7 on page 28(q)
134	0146	20110728_142336	11260	Fast	-345	226	0.90	44	181" × 73"	110	Dsi	$\beta\gamma$	D.7 on page 28(r)
135	0147	20110802_112411	11263	Fast	-227	184	0.95	45	149" × 83"	460	Dki	$\beta\gamma\delta$	D.7 on page 28(s)
136	0148	20110803_113623	11263	Fast	-21	181	0.98	36	151" × 75"	560	Eki	$\beta\gamma\delta$	D.7 on page 28(t)
137	0149	20110803_130305	11263	Fast	-8	180	0.98	36	147" × 78"	560	Eki	$\beta\gamma\delta$	D.8 on page 29(a)
138	0150	20110803_144135	11263	Fast	7	179	0.98	36	147" × 77"	560	Eki	$\beta\gamma\delta$	D.8 on page 29(b)
139	0151	20110803_163635	11263	Fast	21	183	0.99	36	153" × 75"	560	Eki	$\beta\gamma\delta$	D.8 on page 29(c)
140	0152	20110803_182805	11263	Fast	39	184	0.98	45	151" × 80"	560	Eki	$\beta\gamma\delta$	D.8 on page 29(d)
141	0153	20110803_195005	11263	Fast	45	184	0.98	36	146" × 76"	560	Eki	$\beta\gamma\delta$	D.8 on page 29(e)
142	0154	20110803_212735	11263	Fast	64	183	0.98	36	148" × 78"	560	Eki	$\beta\gamma\delta$	D.8 on page 29(f)
143	0155	20110803_230235	11263	Fast	78	184	0.98	36	146" × 78"	560	Eki	$\beta\gamma\delta$	D.8 on page 29(g)
144	0156	20110804_021034	11263	Fast	100	181	0.98	36	150" × 73"	600	Dki	$\beta\gamma\delta$	D.8 on page 29(h)
145	0157	20110804_034904	11263	Fast	114	181	0.98	36	150" × 79"	600	Dki	$\beta\gamma\delta$	D.8 on page 29(i)
146	0158	20110804_070605	11263	Fast	143	184	0.98	36	151" × 79"	600	Dki	$\beta\gamma\delta$	D.8 on page 29(j)
147	0159	20110804_084405	11263	Fast	158	182	0.97	45	149" × 81"	600	Dki	$\beta\gamma\delta$	D.8 on page 29(k)
148	0160	20110804_153706	11263	Fast	212	186	0.96	36	149" × 77"	600	Dki	$\beta\gamma\delta$	D.8 on page 29(l)
149	0161	20110804_171305	11263	Fast	228	189	0.96	36	149" × 77"	600	Dki	$\beta\gamma\delta$	D.8 on page 29(m)
150	0162	20110806_072004	11263	Fast	519	189	0.82	15	75" × 59"	570	Ekc	$\beta\gamma\delta$	D.8 on page 29(n)
151	0163	20110806_120558	11263	Fast	514	215	0.82	40	164" × 78"	570	Ekc	$\beta\gamma\delta$	D.8 on page 29(o)
152	0164	20110806_170006	11263	Fast	547	216	0.79	50	161" × 80"	570	Ekc	$\beta\gamma\delta$	D.8 on page 29(p)
153	0165	20110806_220006	11263	Fast	578	216	0.76	45	156" × 82"	570	Ekc	$\beta\gamma\delta$	D.8 on page 29(q)
154	0166	20110807_024006	11263	Fast	606	214	0.74	36	153" × 72"	440	Ekc	$\beta\gamma\delta$	D.8 on page 29(r)
155	0167	20110807_110005	11263	Fast	692	215	0.65	12	60" × 49"	440	Ekc	$\beta\gamma\delta$	D.8 on page 29(s)
156	0169	20110819_083005	11271	Fast	-471	158	0.85	16	61" × 76"	290	Ehc	β	D.8 on page 29(t)
157	0170	20110907_050002	11283	Fast	341	138	0.93	24	94" × 68"	200	Eai	$\beta\gamma\delta$	D.9 on page 30(a)
158	0171	20110909_113005	11283	Fast	794	160	0.62	20	82" × 71"	200	Cao	$\beta\gamma\delta$	D.9 on page 30(b)
159	0172	20110909_130125	11283	Fast	801	161	0.61	20	76" × 70"	200	Cao	$\beta\gamma\delta$	D.9 on page 30(c)
160	0173	20110913_103405	11289	Fast	111	271	0.96	20	85" × 76"	300	Cko	β	D.9 on page 30(d)
161	0174	20110913_120405	11289	Fast	126	269	0.96	20	81" × 75"	300	Cko	β	D.9 on page 30(e)
162	0175	20110918_051205	11295	Fast	14	234	0.97	48	141" × 99"	210	Dai	β	D.9 on page 30(f)
163	0176	20110918_065504	11295	Fast	22	237	0.97	40	142" × 93"	210	Dai	β	D.9 on page 30(g)
164	0177	20110920_072004	11295	Fast	441	267	0.89	54	160" × 109"	300	Dhc	$\beta\gamma$	D.9 on page 30(h)
165	0179	20110921_082351	11295	Fast	622	286	0.77	48	143" × 108"	310	Dhc	$\beta\gamma$	D.9 on page 30(i)
166	0182	20110922_114005	11295	Fast	718	279	0.60	20	90" × 73"	380	Ehc	$\beta\gamma$	D.9 on page 30(j)
167	0183	20110924_104905	11302	Fast	-768	152	0.55	56	123" × 138"	840	Ekc	$\beta\gamma$	D.9 on page 30(k)
168	0184	20110924_130005	11302	Fast	-749	148	0.56	64	139" × 139"	840	Ekc	$\beta\gamma$	D.9 on page 30(l)
169	0185	20110924_222528	11302	Fast	-703	139	0.64	72	155" × 141"	840	Ekc	$\beta\gamma$	D.9 on page 30(m)
170	0186	20110925_012335	11302	Fast	-693	135	0.66	80	162" × 141"	1300	Fkc	$\beta\gamma\delta$	D.9 on page 30(n)
171	0188	20110925_043921	11302	Fast	-675	137	0.68	80	166" × 136"	1300	Fkc	$\beta\gamma\delta$	D.9 on page 30(o)
172	0189	20110926_065034	11302	Fast	-558	169	0.81	30	99" × 87"	980	Ekc	$\beta\gamma\delta$	D.9 on page 30(p)
173	0190	20110926_110209	11302	Fast	-470	128	0.87	84	205" × 126"	980	Ekc	$\beta\gamma\delta$	D.9 on page 30(q)
174	0191	20110926_130004	11302	Fast	-506	165	0.84	30	105" × 87"	980	Ekc	$\beta\gamma\delta$	D.9 on page 30(r)
175	0192	20110926_184634	11302	Fast	-432	125	0.89	63	158" × 125"	980	Ekc	$\beta\gamma\delta$	D.9 on page 30(s)
176	0193	20110927_010005	11302	Fast	-391	134	0.91	48	139" × 115"	950	Ekc	$\beta\gamma$	D.9 on page 30(t)
177	0194	20110927_104259	11302	Fast	-268	108	0.96	104	218" × 140"	950	Ekc	$\beta\gamma$	D.10 on page 31(a)

Table D.1: continued.

index	inv_id	obs_id (date)_(time)	NOAA AR num	type scan	x_c (")	y_c (")	μ	num tiles	size FOV	area (MSH)	Zürich class	magnetic class	Fig. (panel)
178	0195	20110927_140006	11302	Fast	-118	101	0.98	40	141" × 97"	950	Ekc	$\beta\gamma$	D.10 on page 31(b)
179	0197	20110927_223605	11302	Fast	-36	103	0.99	40	139" × 95"	950	Ekc	$\beta\gamma$	D.10 on page 31(c)
180	0198	20110928_031135	11302	Fast	5	101	0.99	40	136" × 97"	980	Fkc	$\beta\gamma\delta$	D.10 on page 31(d)
181	0199	20110928_110005	11302	Fast	89	101	1.00	40	129" × 93"	980	Fkc	$\beta\gamma\delta$	D.10 on page 31(e)
182	0200	20110928_150006	11302	Fast	117	103	1.00	40	134" × 93"	980	Fkc	$\beta\gamma\delta$	D.10 on page 31(f)
183	0202	20110928_213705	11302	Fast	180	102	0.99	40	133" × 95"	980	Fkc	$\beta\gamma\delta$	D.10 on page 31(g)
184	0203	20110929_004505	11302	Fast	220	104	0.99	40	137" × 92"	1070	Fkc	$\beta\gamma\delta$	D.10 on page 31(h)
185	0204	20110929_041004	11302	Fast	251	103	0.98	35	125" × 95"	1070	Fkc	$\beta\gamma\delta$	D.10 on page 31(i)
186	0205	20110929_073004	11302	Fast	283	104	0.98	35	123" × 95"	1070	Fkc	$\beta\gamma\delta$	D.10 on page 31(j)
187	0206	20110929_101606	11302	Fast	286	100	0.97	42	125" × 100"	1070	Fkc	$\beta\gamma\delta$	D.10 on page 31(k)
188	0207	20111001_050403	11302	Fast	643	133	0.80	36	102" × 101"	750	Fkc	$\beta\gamma\delta$	D.10 on page 31(l)
189	0208	20111001_110406	11302	Fast	678	140	0.77	24	102" × 76"	750	Fkc	$\beta\gamma\delta$	D.10 on page 31(m)
190	0209	20111001_180235	11302	Fast	724	145	0.73	30	103" × 80"	750	Fkc	$\beta\gamma\delta$	D.10 on page 31(n)
191	0210	20111002_010504	11302	Fast	769	151	0.68	24	95" × 79"	700	Fkc	$\beta\gamma\delta$	D.10 on page 31(o)
192	0211	20111002_070514	11302	Fast	741	138	0.65	20	91" × 74"	700	Fkc	$\beta\gamma\delta$	D.10 on page 31(p)
193	0212	20111002_113449	11302	Fast	818	149	0.61	25	90" × 89"	700	Fkc	$\beta\gamma\delta$	D.10 on page 31(q)
194	0213	20111002_151148	11302	Fast	785	146	0.59	20	86" × 75"	700	Fkc	$\beta\gamma\delta$	D.10 on page 31(r)
195	0214	20111006_152406	11309	Fast	-189	322	0.90	6	32" × 46"	160	Dso	β	D.10 on page 31(s)
196	0215	20111007_023104	11309	Fast	-134	321	0.93	9	48" × 50"	170	Cso	β	D.10 on page 31(t)
197	0218	20111104_233139	11339	Fast	-680	271	0.65	24	94" × 78"	1400	Ekc	$\beta\gamma\delta$	D.11 on page 32(a)
198	0219	20111105_034209	11339	Fast	-654	272	0.68	42	112" × 113"	1540	Fkc	$\beta\gamma\delta$	D.11 on page 32(b)
199	0222	20111105_210005	11339	Fast	-522	267	0.80	66	181" × 109"	1540	Fkc	$\beta\gamma\delta$	D.11 on page 32(c)
200	0223	20111106_010506	11339	Fast	-488	263	0.82	66	191" × 111"	1250	Ekc	$\beta\gamma\delta$	D.11 on page 32(d)
201	0224	20111106_042005	11339	Fast	-456	262	0.84	72	202" × 111"	1250	Ekc	$\beta\gamma\delta$	D.11 on page 32(e)
202	0225	20111106_080205	11339	Fast	-429	263	0.86	72	202" × 111"	1250	Ekc	$\beta\gamma\delta$	D.11 on page 32(f)
203	0227	20111106_120041	11339	Fast	-396	263	0.87	72	202" × 106"	1250	Ekc	$\beta\gamma\delta$	D.11 on page 32(g)
204	0229	20111106_200005	11339	Fast	-332	264	0.90	72	201" × 100"	1250	Ekc	$\beta\gamma\delta$	D.11 on page 32(h)
205	0230	20111107_000005	11339	Fast	-300	262	0.91	72	202" × 105"	1230	Fkc	$\beta\gamma\delta$	D.11 on page 32(i)
206	0231	20111107_034004	11339	Fast	-270	260	0.92	72	201" × 101"	1230	Fkc	$\beta\gamma\delta$	D.11 on page 32(j)
207	0232	20111107_081004	11339	Fast	-231	262	0.93	72	201" × 100"	1230	Fkc	$\beta\gamma\delta$	D.11 on page 32(k)
208	0235	20111108_160006	11339	Fast	29	258	0.97	60	203" × 98"	1240	Fkc	$\beta\gamma\delta$	D.11 on page 32(l)
209	0236	20111109_200005	11339	Fast	274	263	0.92	72	200" × 102"	940	Ekc	$\beta\gamma$	D.11 on page 32(m)
210	0237	20111109_231005	11339	Fast	300	262	0.91	72	198" × 104"	940	Ekc	$\beta\gamma$	D.11 on page 32(n)
211	0238	20111110_021005	11339	Fast	330	262	0.90	72	199" × 105"	1030	Fkc	$\beta\gamma$	D.11 on page 32(o)
212	0239	20111110_051005	11339	Fast	345	263	0.90	66	183" × 106"	1030	Fkc	$\beta\gamma$	D.11 on page 32(p)
213	0240	20111110_100239	11339	Fast	450	266	0.86	54	155" × 104"	1030	Fkc	$\beta\gamma$	D.11 on page 32(q)
214	0241	20111111_000005	11339	Fast	528	273	0.80	45	157" × 94"	1020	Fkc	$\beta\gamma$	D.11 on page 32(r)
215	0242	20111119_113006	11354	Fast	-744	-283	0.55	36	96" × 104"	210	Dso	β	D.11 on page 32(s)
216	0243	20111119_123006	11354	Fast	-738	-284	0.56	36	99" × 104"	210	Dso	β	D.11 on page 32(t)
217	0244	20111119_133005	11354	Fast	-733	-284	0.57	36	99" × 102"	210	Dso	β	D.12 on page 33(a)
218	0245	20111119_143006	11354	Fast	-728	-285	0.57	36	100" × 106"	210	Dso	β	D.12 on page 33(b)
219	0246	20111119_163005	11354	Fast	-718	-286	0.59	36	99" × 105"	210	Dso	β	D.12 on page 33(c)
220	0247	20111119_181506	11354	Fast	-708	-286	0.60	36	100" × 109"	210	Dso	β	D.12 on page 33(d)
221	0248	20111119_192005	11354	Fast	-701	-288	0.61	36	100" × 108"	210	Dso	β	D.12 on page 33(e)
222	0249	20111119_195245	11354	Fast	-698	-286	0.61	36	96" × 105"	210	Dso	β	D.12 on page 33(f)
223	0250	20111227_120042	11387	Fast	729	-330	0.63	24	103" × 73"	130	Dai	$\beta\gamma$	D.12 on page 33(g)
224	0251	20111231_004005	11389	Fast	-622	-375	0.59	35	123" × 81"	500	Ekc	$\beta\gamma$	D.12 on page 33(h)
225	0252	20111231_085005	11389	Fast	-582	-372	0.64	28	117" × 75"	500	Ekc	$\beta\gamma$	D.12 on page 33(i)
226	0253	20120102_032504	11389	Fast	-315	-362	0.84	24	95" × 69"	420	Fko	β	D.12 on page 33(j)
227	0254	20120223_224505	11420	Fast	774	360	0.61	16	71" × 72"	30	Hrx	α	D.12 on page 33(k)
228	0255	20120306_100006	11429	Fast	-560	388	0.71	48	138" × 108"	770	Dkc	$\beta\delta$	D.12 on page 33(l)

Table D.1: continued.

index	inv_id	obs_id (date)_(time)	NOAA AR num	type scan	x_c (")	y_c (")	μ	num tiles	size FOV	area (MSH)	Zürich class	magnetic class	Fig. (panel)
229	0256	20120306_120006	11429	Fast	-542	390	0.73	48	140" × 111"	770	Dkc	$\beta\delta$	D.12 on page 33(m)
230	0258	20120306_140104	11429	Fast	-528	391	0.74	48	143" × 111"	770	Dkc	$\beta\delta$	D.12 on page 33(n)
231	0259	20120306_155006	11429	Fast	-515	396	0.75	54	145" × 106"	770	Dkc	$\beta\delta$	D.12 on page 33(o)
232	0260	20120306_173006	11429	Fast	-503	397	0.76	54	145" × 106"	770	Dkc	$\beta\delta$	D.12 on page 33(p)
233	0261	20120306_221040	11429	Fast	-472	399	0.78	54	147" × 110"	770	Dkc	$\beta\delta$	D.12 on page 33(q)
234	0262	20120307_020006	11429	Fast	-460	384	0.79	30	87" × 104"	1120	Dkc	$\beta\gamma\delta$	D.12 on page 33(r)
235	0263	20120307_080005	11429	Fast	-399	407	0.82	54	149" × 111"	1120	Dkc	$\beta\gamma\delta$	D.12 on page 33(s)
236	0264	20120307_090005	11429	Fast	-391	405	0.82	54	150" × 111"	1120	Dkc	$\beta\gamma\delta$	D.12 on page 33(t)
237	0265	20120307_140005	11429	Fast	-338	404	0.85	42	126" × 107"	1120	Dkc	$\beta\gamma\delta$	D.13 on page 34(a)
238	0266	20120307_160005	11429	Fast	-333	405	0.85	54	151" × 115"	1120	Dkc	$\beta\gamma\delta$	D.13 on page 34(b)
239	0267	20120308_012005	11429	Fast	-255	406	0.88	63	149" × 117"	1270	Dkc	$\beta\gamma\delta$	D.13 on page 34(c)
240	0268	20120308_080004	11429	Fast	-197	421	0.89	54	149" × 101"	1270	Dkc	$\beta\gamma\delta$	D.13 on page 34(d)
241	0269	20120308_131128	11429	Fast	-181	425	0.89	36	93" × 100"	1270	Dkc	$\beta\gamma\delta$	D.13 on page 34(e)
242	0270	20120308_163652	11429	Fast	-106	422	0.91	35	119" × 83"	1270	Dkc	$\beta\gamma\delta$	D.13 on page 34(f)
243	0271	20120308_183006	11429	Fast	-105	421	0.91	54	151" × 103"	1270	Dkc	$\beta\gamma\delta$	D.13 on page 34(g)
244	0272	20120308_213005	11429	Fast	-78	424	0.91	54	150" × 100"	1270	Dkc	$\beta\gamma\delta$	D.13 on page 34(h)
245	0273	20120308_230005	11429	Fast	-108	436	0.91	20	67" × 86"	1270	Dkc	$\beta\gamma\delta$	D.13 on page 34(i)
246	0274	20120309_023602	11429	Fast	-68	433	0.91	25	82" × 88"	950	Ekc	$\beta\gamma\delta$	D.13 on page 34(j)
247	0275	20120426_130548	11465	Fast	535	-207	0.82	16	62" × 74"	280	Dko	β	D.13 on page 34(k)
248	0276	20120426_220006	11465	Fast	606	-218	0.78	15	56" × 80"	280	Dko	β	D.13 on page 34(l)
249	0277	20120508_095806	11476	Fast	-678	258	0.66	24	93" × 71"	810	Fkc	$\beta\gamma$	D.13 on page 34(m)
250	0278	20120508_114506	11476	Fast	-640	218	0.70	48	139" × 112"	810	Fkc	$\beta\gamma$	D.13 on page 34(n)
251	0279	20120508_132006	11476	Fast	-626	217	0.72	54	151" × 111"	810	Fkc	$\beta\gamma$	D.13 on page 34(o)
252	0280	20120508_150506	11476	Fast	-613	217	0.73	54	151" × 113"	810	Fkc	$\beta\gamma$	D.13 on page 34(p)
253	0281	20120508_200505	11476	Fast	-579	219	0.76	54	151" × 113"	810	Fkc	$\beta\gamma$	D.13 on page 34(q)
254	0282	20120508_232005	11476	Fast	-508	221	0.79	42	119" × 107"	810	Fkc	$\beta\gamma$	D.13 on page 34(r)
255	0283	20120509_010005	11476	Fast	-563	267	0.77	18	100" × 60"	940	Fkc	$\beta\gamma\delta$	D.13 on page 34(s)
256	0284	20120509_040340	11476	Fast	-521	221	0.80	54	150" × 111"	940	Fkc	$\beta\gamma\delta$	D.13 on page 34(t)
257	0285	20120509_072005	11476	Fast	-464	221	0.83	48	130" × 109"	940	Fkc	$\beta\gamma\delta$	D.14 on page 35(a)
258	0286	20120509_090005	11476	Fast	-456	222	0.84	48	134" × 107"	940	Fkc	$\beta\gamma\delta$	D.14 on page 35(b)
259	0287	20120509_121526	11476	Fast	-490	278	0.82	6	32" × 49"	940	Fkc	$\beta\gamma\delta$	D.14 on page 35(c)
260	0288	20120509_140021	11476	Fast	-422	223	0.86	48	137" × 112"	940	Fkc	$\beta\gamma\delta$	D.14 on page 35(d)
261	0289	20120509_222005	11476	Fast	-351	224	0.89	48	135" × 111"	940	Fkc	$\beta\gamma\delta$	D.14 on page 35(e)
262	0290	20120510_080005	11476	Fast	-272	225	0.92	48	138" × 114"	1050	Fkc	$\beta\gamma\delta$	D.14 on page 35(f)
263	0291	20120510_093906	11476	Fast	-260	226	0.93	48	139" × 112"	1050	Fkc	$\beta\gamma\delta$	D.14 on page 35(g)
264	0292	20120510_111405	11476	Fast	-251	226	0.93	48	140" × 110"	1050	Fkc	$\beta\gamma\delta$	D.14 on page 35(h)
265	0293	20120510_130006	11476	Fast	-279	271	0.92	16	60" × 69"	1050	Fkc	$\beta\gamma\delta$	D.14 on page 35(i)
266	0294	20120510_144006	11476	Fast	-200	226	0.95	42	112" × 113"	1050	Fkc	$\beta\gamma\delta$	D.14 on page 35(j)
267	0295	20120512_023835	11476	Fast	135	183	0.97	72	144" × 143"	1040	Fkc	$\beta\gamma\delta$	D.14 on page 35(k)
268	0296	20120512_091334	11476	Fast	228	182	0.96	56	123" × 138"	1040	Fkc	$\beta\gamma\delta$	D.14 on page 35(l)
269	0297	20120512_123050	11476	Fast	306	191	0.94	77	191" × 128"	1040	Fkc	$\beta\gamma\delta$	D.14 on page 35(m)
270	0298	20120512_223006	11476	Fast	381	188	0.92	54	154" × 102"	1040	Fkc	$\beta\gamma\delta$	D.14 on page 35(n)
271	0300	20120513_081505	11476	Fast	474	186	0.88	45	149" × 95"	960	Fkc	$\beta\gamma\delta$	D.14 on page 35(o)
272	0303	20120513_183005	11476	Fast	514	184	0.84	50	173" × 98"	960	Fkc	$\beta\gamma\delta$	D.14 on page 35(p)
273	0304	20120513_213005	11476	Fast	543	183	0.82	50	167" × 97"	960	Fkc	$\beta\gamma\delta$	D.14 on page 35(q)
274	0305	20120514_004505	11476	Fast	567	181	0.80	60	164" × 99"	810	Fki	$\beta\gamma\delta$	D.14 on page 35(r)
275	0306	20120514_040005	11476	Fast	589	180	0.79	60	168" × 102"	810	Fki	$\beta\gamma\delta$	D.14 on page 35(s)
276	0308	20120514_103004	11476	Fast	625	166	0.76	60	164" × 110"	810	Fki	$\beta\gamma\delta$	D.14 on page 35(t)
277	0310	20120514_171605	11476	Fast	746	163	0.69	30	106" × 97"	810	Fki	$\beta\gamma\delta$	D.15 on page 36(a)
278	0311	20120514_203239	11476	Fast	769	162	0.66	30	103" × 90"	810	Fki	$\beta\gamma\delta$	D.15 on page 36(b)
279	0312	20120515_030004	11476	Fast	807	161	0.62	30	97" × 93"	600	Fko	$\beta\gamma$	D.15 on page 36(c)
280	0313	20120515_061504	11476	Fast	795	158	0.61	42	114" × 103"	600	Fko	$\beta\gamma$	D.15 on page 36(d)

Table D.1: continued.

index	inv_id	obs_id (date)_(time)	NOAA AR num	type scan	x_c (")	y_c (")	μ	num tiles	size FOV	area (MSH)	Zürich class	magnetic class	Fig. (panel)
281	0315	20120613_110505	11504	Fast	-282	-301	0.87	55	195" × 98"	310	Eki	β	D.15 on page 36(e)
282	0316	20120629_224835	11513	Fast	-417	193	0.83	25	79" × 96"	90	Dso	$\beta\gamma$	D.15 on page 36(f)
283	0317	20120704_224035	11515	Fast	325	-349	0.86	40	165" × 70"	570	Fkc	$\beta\gamma\delta$	D.15 on page 36(g)
284	0318	20120705_015535	11515	Fast	350	-348	0.85	40	164" × 71"	640	Fkc	$\beta\gamma\delta$	D.15 on page 36(h)
285	0319	20120705_034535	11515	Fast	365	-349	0.84	40	164" × 76"	640	Fkc	$\beta\gamma\delta$	D.15 on page 36(i)
286	0320	20120705_065135	11515	Fast	388	-347	0.83	36	161" × 74"	640	Fkc	$\beta\gamma\delta$	D.15 on page 36(j)
287	0321	20120706_190513	11515	Fast	688	-339	0.61	50	163" × 95"	670	Ekc	$\beta\gamma\delta$	D.15 on page 36(k)
288	0322	20120710_231041	11520	Fast	-336	-371	0.85	66	181" × 103"	1370	Fkc	$\beta\gamma\delta$	D.15 on page 36(l)
289	0323	20120711_173528	11520	Fast	-210	-352	0.89	80	172" × 137"	1370	Fkc	$\beta\gamma\delta$	D.15 on page 36(m)
290	0324	20120711_202646	11520	Fast	-154	-357	0.90	91	216" × 134"	1370	Fkc	$\beta\gamma\delta$	D.15 on page 36(n)
291	0325	20120712_111228	11520	Fast	-10	-372	0.92	66	187" × 102"	1320	Fkc	$\beta\gamma\delta$	D.15 on page 36(o)
292	0327	20120713_004708	11520	Fast	63	-375	0.91	63	159" × 118"	1460	Fkc	$\beta\gamma\delta$	D.15 on page 36(p)
293	0331	20120715_045105	11520	Fast	514	-365	0.75	36	99" × 115"	990	Fkc	$\beta\gamma\delta$	D.15 on page 36(q)
294	0333	20120729_020305	11532	Fast	-609	-407	0.59	72	204" × 115"	510	Fho	β	D.15 on page 36(r)
295	0334	20120729_052005	11532	Fast	-590	-411	0.62	91	214" × 118"	510	Fho	β	D.15 on page 36(s)
296	0335	20120729_083605	11532	Fast	-575	-413	0.63	78	213" × 117"	510	Fho	β	D.15 on page 36(t)
297	0336	20120729_120005	11532	Fast	-559	-416	0.65	91	222" × 117"	510	Fho	β	D.16 on page 37(a)
298	0338	20120730_024005	11532	Fast	-480	-423	0.73	98	248" × 124"	500	Fko	β	D.16 on page 37(b)
299	0339	20120730_060005	11532	Fast	-462	-425	0.74	105	257" × 122"	500	Fko	β	D.16 on page 37(c)
300	0340	20120731_113345	11532	Fast	-240	-453	0.83	119	292" × 129"	350	Dkc	β	D.16 on page 37(d)
301	0341	20120809_052420	11542	Fast	-641	-305	0.57	25	91" × 87"	160	Dai	β	D.16 on page 37(e)
302	0342	20120809_070119	11542	Fast	-644	-300	0.59	30	93" × 85"	160	Dai	β	D.16 on page 37(f)
303	0343	20120814_000004	11543	Fast	113	243	0.96	16	71" × 64"	250	Dko	$\beta\gamma$	D.16 on page 37(g)
304	0344	20120814_143505	11543	Fast	261	260	0.94	20	88" × 67"	250	Dko	$\beta\gamma$	D.16 on page 37(h)
305	0345	20120814_180906	11543	Fast	285	265	0.93	20	87" × 67"	250	Dko	$\beta\gamma$	D.16 on page 37(i)
306	0346	20120815_003105	11543	Fast	307	253	0.91	12	63" × 61"	250	Cko	$\beta\gamma$	D.16 on page 37(j)
307	0347	20120815_013142	11543	Fast	344	270	0.91	20	80" × 65"	250	Cko	$\beta\gamma$	D.16 on page 37(k)
308	0348	20120902_090505	11560	Nor.	164	-65	0.98	42	60" × 55"	220	Dai	$\beta\gamma$	D.16 on page 37(l)
309	0349	20120902_130005	11560	Nor.	204	-61	0.98	35	58" × 48"	220	Dai	$\beta\gamma$	D.16 on page 37(m)
310	0350	20120903_113004	11560	Nor.	406	-48	0.90	48	69" × 56"	260	Ehi	$\beta\gamma$	D.16 on page 37(n)
311	0351	20120903_130004	11560	Nor.	418	-50	0.89	48	69" × 57"	260	Ehi	$\beta\gamma$	D.16 on page 37(o)
312	0352	20121023_150006	11598	Fast	-684	-255	0.58	30	99" × 92"	370	Dhi	β	D.16 on page 37(p)
313	0353	20121023_181635	11598	Fast	-665	-255	0.61	30	104" × 92"	370	Dhi	β	D.16 on page 37(q)
314	0354	20121023_212005	11598	Fast	-646	-262	0.63	30	102" × 90"	370	Dhi	β	D.16 on page 37(r)
315	0355	20121024_003005	11598	Fast	-617	-262	0.66	30	102" × 87"	420	Dki	$\beta\delta$	D.16 on page 37(s)
316	0356	20121024_034005	11598	Fast	-597	-272	0.68	30	102" × 97"	420	Dki	$\beta\delta$	D.16 on page 37(t)
317	0357	20121024_065005	11598	Fast	-577	-272	0.70	30	105" × 92"	420	Dki	$\beta\delta$	D.17 on page 38(a)
318	0358	20121024_091322	11598	Fast	-601	-275	0.70	25	90" × 90"	420	Dki	$\beta\delta$	D.17 on page 38(b)
319	0359	20121024_120026	11598	Fast	-565	-274	0.73	35	110" × 86"	420	Dki	$\beta\delta$	D.17 on page 38(c)
320	0360	20121024_151505	11598	Fast	-540	-278	0.75	35	116" × 90"	420	Dki	$\beta\delta$	D.17 on page 38(d)
321	0361	20121024_190005	11598	Fast	-499	-274	0.78	35	111" × 84"	420	Dki	$\beta\delta$	D.17 on page 38(e)
322	0362	20121025_010005	11598	Fast	-450	-277	0.81	35	111" × 94"	360	Dki	$\beta\delta$	D.17 on page 38(f)
323	0363	20121025_110506	11598	Fast	-367	-280	0.86	42	113" × 100"	360	Dki	$\beta\delta$	D.17 on page 38(g)
324	0364	20121025_141505	11598	Fast	-350	-280	0.87	35	121" × 98"	360	Dki	$\beta\delta$	D.17 on page 38(h)
325	0365	20121025_164005	11598	Fast	-328	-282	0.88	42	112" × 99"	360	Dki	$\beta\delta$	D.17 on page 38(i)
326	0366	20121025_195005	11598	Fast	-300	-283	0.89	42	112" × 100"	360	Dki	$\beta\delta$	D.17 on page 38(j)
327	0367	20121025_230005	11598	Fast	-280	-285	0.90	42	117" × 102"	360	Dki	$\beta\delta$	D.17 on page 38(k)
328	0368	20121026_021005	11598	Fast	-251	-285	0.91	42	117" × 103"	370	Dko	$\beta\delta$	D.17 on page 38(l)
329	0369	20121026_083005	11598	Fast	-197	-288	0.92	42	114" × 106"	370	Dko	$\beta\delta$	D.17 on page 38(m)
330	0370	20121026_121006	11598	Fast	-166	-288	0.93	42	118" × 103"	370	Dko	$\beta\delta$	D.17 on page 38(n)
331	0371	20121026_145006	11598	Fast	-138	-285	0.94	42	121" × 102"	370	Dko	$\beta\delta$	D.17 on page 38(o)

Table D.1: continued.

index	inv_id	obs_id (date)_(time)	NOAA AR num	type scan	x_c (")	y_c (")	μ	num tiles	size FOV	area (MSH)	Zürich class	magnetic class	Fig. (panel)
332	0372	20121026_231006	11598	Fast	-61	-285	0.95	42	114" × 104"	370	Dko	$\beta\delta$	D.17 on page 38(p)
333	0373	20121027_034505	11598	Fast	-11	-264	0.95	35	110" × 82"	340	Dko	$\beta\delta$	D.17 on page 38(q)
334	0374	20121027_091505	11598	Fast	38	-257	0.95	28	109" × 79"	340	Dko	$\beta\delta$	D.17 on page 38(r)
335	0375	20121027_210005	11598	Fast	179	-260	0.95	25	86" × 84"	340	Dko	$\beta\delta$	D.17 on page 38(s)
336	0376	20121027_234005	11598	Fast	185	-253	0.94	24	96" × 77"	340	Dko	$\beta\delta$	D.17 on page 38(t)
337	0377	20121028_014005	11598	Fast	199	-254	0.94	30	100" × 80"	330	Dkc	$\beta\delta$	D.18 on page 39(a)
338	0378	20121028_104005	11598	Fast	297	-252	0.92	20	84" × 72"	330	Dkc	$\beta\delta$	D.18 on page 39(b)
339	0379	20121028_124005	11598	Fast	314	-249	0.92	20	87" × 74"	330	Dkc	$\beta\delta$	D.18 on page 39(c)
340	0380	20121028_144004	11598	Fast	329	-246	0.91	20	85" × 73"	330	Dkc	$\beta\delta$	D.18 on page 39(d)
341	0381	20121028_164004	11598	Fast	356	-246	0.90	20	83" × 70"	330	Dkc	$\beta\delta$	D.18 on page 39(e)
342	0382	20121028_193004	11598	Fast	373	-244	0.90	20	83" × 70"	330	Dkc	$\beta\delta$	D.18 on page 39(f)
343	0383	20121028_213004	11598	Fast	395	-243	0.89	20	83" × 67"	330	Dkc	$\beta\delta$	D.18 on page 39(g)
344	0384	20121029_034504	11598	Fast	454	-240	0.87	20	75" × 74"	240	Dac	β	D.18 on page 39(h)
345	0385	20121029_053004	11598	Fast	472	-240	0.86	20	87" × 71"	240	Dac	β	D.18 on page 39(i)
346	0386	20121113_111206	11613	Fast	-505	-425	0.67	20	76" × 76"	170	Dso	β	D.18 on page 39(j)
347	0387	20121123_073005	11618	Fast	370	121	0.95	55	192" × 89"	350	Ekc	$\beta\gamma\delta$	D.18 on page 39(k)
348	0388	20121123_121122	11618	Fast	315	108	0.94	28	111" × 78"	350	Ekc	$\beta\gamma\delta$	D.18 on page 39(l)
349	0389	20121123_130123	11618	Fast	422	127	0.93	55	181" × 89"	350	Ekc	$\beta\gamma\delta$	D.18 on page 39(m)
350	0390	20121123_192205	11618	Fast	480	129	0.91	50	177" × 88"	350	Ekc	$\beta\gamma\delta$	D.18 on page 39(n)
351	0391	20121124_122005	11618	Fast	591	138	0.83	40	169" × 75"	450	Ekc	$\beta\gamma\delta$	D.18 on page 39(o)
352	0392	20121124_150005	11618	Fast	596	145	0.82	40	162" × 69"	450	Ekc	$\beta\gamma\delta$	D.18 on page 39(p)
353	0395	20121125_003005	11618	Fast	684	148	0.76	36	145" × 69"	340	Ekc	$\beta\gamma\delta$	D.18 on page 39(q)
354	0396	20121125_034005	11618	Fast	711	148	0.74	36	149" × 68"	340	Ekc	$\beta\gamma\delta$	D.18 on page 39(r)
355	0397	20121125_070005	11618	Fast	734	148	0.72	36	154" × 74"	340	Ekc	$\beta\gamma\delta$	D.18 on page 39(s)
356	0398	20121125_131505	11618	Fast	774	141	0.67	36	155" × 75"	340	Ekc	$\beta\gamma\delta$	D.18 on page 39(t)
357	0399	20121125_154505	11618	Fast	792	148	0.66	36	144" × 74"	340	Ekc	$\beta\gamma\delta$	D.19 on page 40(a)
358	0400	20121125_190005	11618	Fast	813	143	0.63	36	146" × 79"	340	Ekc	$\beta\gamma\delta$	D.19 on page 40(b)
359	0401	20121125_221005	11618	Fast	828	143	0.61	32	138" × 79"	340	Ekc	$\beta\gamma\delta$	D.19 on page 40(c)
360	0402	20130109_203505	11652	Fast	-408	410	0.79	60	206" × 82"	210	Fac	$\beta\gamma$	D.19 on page 40(d)
361	0404	20130112_133006	11654	Fast	-449	198	0.86	78	229" × 108"	1100	Fki	$\beta\gamma$	D.19 on page 40(e)
362	0405	20130112_160006	11654	Fast	-427	199	0.88	78	229" × 108"	1100	Fki	$\beta\gamma$	D.19 on page 40(f)
363	0406	20130112_191506	11654	Fast	-400	200	0.89	78	229" × 107"	1100	Fki	$\beta\gamma$	D.19 on page 40(g)
364	0407	20130112_210505	11654	Fast	-385	200	0.90	78	229" × 104"	1100	Fki	$\beta\gamma$	D.19 on page 40(h)
365	0408	20130112_215759	11654	Fast	-358	200	0.90	24	99" × 70"	1100	Fki	$\beta\gamma$	D.19 on page 40(i)
366	0409	20130210_143004	11670	Fast	183	422	0.91	27	149" × 58"	150	Dsi	$\beta\gamma$	D.19 on page 40(j)
367	0410	20130210_190004	11670	Fast	228	421	0.90	24	143" × 54"	150	Dsi	$\beta\gamma$	D.19 on page 40(k)
368	0411	20130314_120112	11692	Fast	-193	283	0.92	15	78" × 53"	190	Cso	β	D.19 on page 40(l)
369	0412	20130314_210005	11692	Fast	-122	285	0.94	12	66" × 52"	190	Cso	β	D.19 on page 40(m)
370	0413	20130402_161006	11711	Fast	-584	-203	0.71	25	84" × 90"	480	Cki	β	D.19 on page 40(n)
371	0414	20130402_173505	11711	Fast	-575	-208	0.71	20	71" × 93"	480	Cki	β	D.19 on page 40(o)
372	0416	20130423_105459	11726	Fast	626	271	0.73	72	208" × 106"	550	Ekc	$\beta\gamma\delta$	D.19 on page 40(p)
373	0417	20130423_143005	11726	Fast	653	270	0.70	72	209" × 107"	550	Ekc	$\beta\gamma\delta$	D.19 on page 40(q)
374	0418	20130423_173805	11726	Fast	674	266	0.68	72	201" × 107"	550	Ekc	$\beta\gamma\delta$	D.19 on page 40(r)
375	0419	20130423_210505	11726	Fast	698	263	0.66	66	195" × 109"	550	Ekc	$\beta\gamma\delta$	D.19 on page 40(s)
376	0420	20130430_215439	11731	Nor.	26	238	0.98	185	202" × 75"	350	Ekc	$\beta\gamma$	D.19 on page 40(t)
377	0421	20130501_061517	11731	Fast	116	238	0.97	70	239" × 93"	380	Ekc	$\beta\gamma\delta$	D.20 on page 41(a)
378	0422	20130513_103605	11745	Fast	-631	218	0.66	30	104" × 94"	600	Ekc	$\beta\gamma$	D.20 on page 41(b)
379	0423	20130513_121739	11745	Fast	-621	219	0.67	30	107" × 91"	600	Ekc	$\beta\gamma$	D.20 on page 41(c)
380	0424	20130513_135528	11745	Fast	-615	219	0.68	42	110" × 100"	600	Ekc	$\beta\gamma$	D.20 on page 41(d)
381	0425	20130513_153428	11745	Fast	-603	221	0.69	35	112" × 96"	600	Ekc	$\beta\gamma$	D.20 on page 41(e)

Table D.1: continued.

index	inv_id	obs_id (date)_(time)	NOAA AR num	type scan	x_c (")	y_c (")	μ	num tiles	size FOV	area (MSH)	Zürich class	magnetic class	Fig. (panel)
382	0426	20130513_165426	11745	Fast	-592	220	0.70	35	112" × 90"	600	Ekc	$\beta\gamma$	D.20 on page 41(f)
383	0427	20130513_202929	11745	Fast	-568	222	0.73	35	114" × 87"	600	Ekc	$\beta\gamma$	D.20 on page 41(g)
384	0428	20130513_234629	11745	Fast	-542	222	0.75	35	122" × 88"	600	Ekc	$\beta\gamma$	D.20 on page 41(h)
385	0429	20130516_154529	11748	Fast	-589	190	0.71	42	125" × 110"	260	Dki	$\beta\gamma\delta$	D.20 on page 41(i)
386	0430	20130516_235827	11748	Fast	-535	193	0.76	42	123" × 102"	260	Dki	$\beta\gamma\delta$	D.20 on page 41(j)
387	0431	20130517_025928	11748	Fast	-509	193	0.78	48	141" × 103"	270	Dki	$\beta\gamma\delta$	D.20 on page 41(k)
388	0432	20130517_061806	11748	Fast	-481	194	0.80	54	144" × 104"	270	Dki	$\beta\gamma\delta$	D.20 on page 41(l)
389	0433	20130517_094005	11748	Fast	-458	194	0.82	54	145" × 99"	270	Dki	$\beta\gamma\delta$	D.20 on page 41(m)
390	0434	20130517_130305	11748	Fast	-438	194	0.83	48	140" × 101"	270	Dki	$\beta\gamma\delta$	D.20 on page 41(n)
391	0435	20130518_065702	11748	Fast	-99	253	0.94	4	28" × 41"	220	Dai	$\beta\gamma\delta$	D.20 on page 41(o)
392	0436	20130518_115505	11748	Fast	-62	253	0.95	4	35" × 42"	220	Dai	$\beta\gamma\delta$	D.20 on page 41(p)
393	0437	20130518_133303	11748	Fast	-46	251	0.95	6	35" × 43"	220	Dai	$\beta\gamma\delta$	D.20 on page 41(q)
394	0438	20130518_150304	11748	Fast	-31	250	0.95	6	36" × 45"	220	Dai	$\beta\gamma\delta$	D.20 on page 41(r)
395	0439	20130518_165005	11748	Fast	-13	254	0.96	6	38" × 44"	220	Dai	$\beta\gamma\delta$	D.20 on page 41(s)
396	0440	20130518_200305	11748	Fast	11	249	0.96	6	35" × 47"	220	Dai	$\beta\gamma\delta$	D.20 on page 41(t)
397	0441	20130518_213306	11748	Fast	29	252	0.97	6	34" × 43"	220	Dai	$\beta\gamma\delta$	D.21 on page 42(a)
398	0442	20130518_231505	11748	Fast	41	251	0.97	6	38" × 44"	220	Dai	$\beta\gamma\delta$	D.21 on page 42(b)
399	0443	20130519_004505	11748	Fast	58	252	0.97	6	38" × 43"	140	Dao	$\beta\delta$	D.21 on page 42(c)
400	0444	20130519_022005	11748	Fast	71	252	0.97	6	35" × 43"	140	Dao	$\beta\delta$	D.21 on page 42(d)
401	0445	20130519_041005	11748	Fast	87	250	0.97	6	39" × 44"	140	Dao	$\beta\delta$	D.21 on page 42(e)
402	0446	20130519_071505	11748	Fast	116	248	0.98	9	40" × 45"	140	Dao	$\beta\delta$	D.21 on page 42(f)
403	0447	20130519_085405	11748	Fast	133	248	0.98	9	41" × 45"	140	Dao	$\beta\delta$	D.21 on page 42(g)
404	0448	20130519_105005	11748	Fast	158	250	0.98	6	35" × 44"	140	Dao	$\beta\delta$	D.21 on page 42(h)
405	0449	20130519_122005	11748	Fast	171	249	0.98	4	37" × 42"	140	Dao	$\beta\delta$	D.21 on page 42(i)
406	0450	20130519_134905	11748	Fast	182	250	0.98	4	37" × 41"	140	Dao	$\beta\delta$	D.21 on page 42(j)
407	0451	20130519_154205	11748	Fast	198	249	0.98	9	39" × 42"	140	Dao	$\beta\delta$	D.21 on page 42(k)
408	0452	20130519_221223	11748	Fast	253	247	0.97	9	42" × 45"	140	Dao	$\beta\delta$	D.21 on page 42(l)
409	0453	20130520_011905	11748	Fast	281	247	0.97	6	43" × 41"	110	Fao	$\beta\gamma\delta$	D.21 on page 42(m)
410	0454	20130520_043605	11748	Fast	308	247	0.97	6	40" × 39"	110	Fao	$\beta\gamma\delta$	D.21 on page 42(n)
411	0455	20130520_112004	11748	Fast	189	193	0.97	45	150" × 93"	110	Fao	$\beta\gamma\delta$	D.21 on page 42(o)
412	0456	20130520_162004	11748	Fast	218	192	0.96	45	157" × 90"	110	Fao	$\beta\gamma\delta$	D.21 on page 42(p)
413	0457	20130524_104005	11756	Fast	-333	-317	0.86	48	202" × 79"	250	Ehi	$\beta\gamma$	D.21 on page 42(q)
414	0458	20130524_122306	11756	Fast	-329	-317	0.87	55	179" × 80"	250	Ehi	$\beta\gamma$	D.21 on page 42(r)
415	0459	20130604_121436	11762	Fast	529	-476	0.65	40	142" × 84"	300	Dki	$\beta\gamma\delta$	D.21 on page 42(s)
416	0460	20130604_135306	11762	Fast	540	-477	0.64	40	137" × 84"	300	Dki	$\beta\gamma\delta$	D.21 on page 42(t)
417	0461	20130618_110138	11775	Fast	-535	-459	0.62	36	92" × 102"	380	Dko	$\beta\delta$	D.22 on page 43(a)
418	0462	20130618_142006	11775	Fast	-521	-461	0.64	30	88" × 102"	380	Dko	$\beta\delta$	D.22 on page 43(b)
419	0463	20130618_192638	11775	Fast	-483	-462	0.67	36	93" × 103"	380	Dko	$\beta\delta$	D.22 on page 43(c)
420	0464	20130618_224137	11775	Fast	-465	-460	0.68	30	94" × 96"	380	Dko	$\beta\delta$	D.22 on page 43(d)
421	0465	20130619_032837	11775	Fast	-434	-462	0.71	30	98" × 97"	410	Dkc	β	D.22 on page 43(e)
422	0466	20130619_064537	11775	Fast	-411	-460	0.72	30	101" × 97"	410	Dkc	β	D.22 on page 43(f)
423	0467	20130619_100236	11775	Fast	-387	-459	0.74	30	97" × 92"	410	Dkc	β	D.22 on page 43(g)
424	0468	20130619_131937	11775	Fast	-345	-442	0.76	20	90" × 76"	410	Dkc	β	D.22 on page 43(h)
425	0469	20130619_200505	11775	Fast	-295	-438	0.78	24	97" × 74"	410	Dkc	β	D.22 on page 43(i)
426	0470	20130620_040405	11775	Fast	-230	-440	0.81	24	96" × 64"	360	Dkc	$\beta\delta$	D.22 on page 43(j)
427	0471	20130620_054305	11775	Fast	-214	-437	0.81	18	92" × 60"	360	Dkc	$\beta\delta$	D.22 on page 43(k)
428	0472	20130620_092306	11775	Fast	-191	-439	0.82	18	95" × 60"	360	Dkc	$\beta\delta$	D.22 on page 43(l)
429	0473	20130704_223846	11785	Fast	-604	-215	0.72	40	142" × 97"	570	Fkc	$\beta\gamma$	D.22 on page 43(m)
430	0474	20130705_014935	11785	Fast	-593	-220	0.74	54	149" × 103"	630	Fkc	$\beta\gamma\delta$	D.22 on page 43(n)
431	0475	20130705_050632	11785	Fast	-583	-216	0.75	35	125" × 95"	630	Fkc	$\beta\gamma\delta$	D.22 on page 43(o)
432	0476	20130705_081348	11785	Fast	-502	-214	0.79	35	120" × 95"	630	Fkc	$\beta\gamma\delta$	D.22 on page 43(p)
433	0477	20130705_114005	11785	Fast	-526	-212	0.79	45	151" × 94"	630	Fkc	$\beta\gamma\delta$	D.22 on page 43(q)

Table D.1: continued.

index	inv_id	obs_id (date)_(time)	NOAA AR num	type scan	x_c (")	y_c (")	μ	num tiles	size FOV	area (MSH)	Zürich class	magnetic class	Fig. (panel)
434	0478	20130707_093903	11785	Fast	-73	-233	0.95	65	217" × 96"	650	Ekc	$\beta\gamma\delta$	D.22 on page 43(r)
435	0479	20130707_143916	11785	Fast	-80	-236	0.96	60	199" × 95"	650	Ekc	$\beta\gamma\delta$	D.22 on page 43(s)
436	0480	20130707_162405	11785	Fast	-65	-235	0.96	60	201" × 96"	650	Ekc	$\beta\gamma\delta$	D.22 on page 43(t)
437	0481	20130708_221858	11785	Fast	203	-247	0.94	12	57" × 59"	610	Ekc	$\beta\gamma\delta$	D.23 on page 44(a)
438	0482	20130727_084736	11800	Fast	710	-204	0.63	20	85" × 63"	160	Dai	$\beta\gamma$	D.23 on page 44(b)
439	0483	20130727_102859	11800	Fast	787	-192	0.61	24	92" × 66"	160	Dai	$\beta\gamma$	D.23 on page 44(c)
440	0484	20130817_101750	11818	Fast	454	-181	0.89	28	112" × 76"	330	Dki	$\beta\gamma\delta$	D.23 on page 44(d)
441	0485	20130817_184136	11818	Fast	509	-187	0.84	16	65" × 70"	330	Dki	$\beta\gamma\delta$	D.23 on page 44(e)
442	0486	20130817_201708	11818	Fast	504	-181	0.84	16	67" × 64"	330	Dki	$\beta\gamma\delta$	D.23 on page 44(f)
443	0487	20130817_220443	11818	Fast	593	-166	0.82	13	57" × 71"	330	Dki	$\beta\gamma\delta$	D.23 on page 44(g)
444	0488	20130818_092928	11818	Fast	702	-160	0.76	13	57" × 72"	300	Dko	$\beta\gamma\delta$	D.23 on page 44(h)
445	0489	20130818_210006	11818	Fast	781	-147	0.69	12	53" × 63"	300	Dko	$\beta\gamma\delta$	D.23 on page 44(i)
446	0490	20130819_093505	11818	Fast	867	-138	0.59	12	46" × 69"	260	Cko	$\beta\delta$	D.23 on page 44(j)
447	0491	20131010_191608	11861	Fast	-408	-223	0.84	32	129" × 76"	60	Cao	β	D.23 on page 44(k)
448	0492	20131011_063405	11861	Fast	-310	-230	0.89	32	141" × 79"	200	Eac	β	D.23 on page 44(l)
449	0493	20131022_183221	11875	Fast	-169	47	0.98	32	141" × 79"	250	Ekc	$\beta\gamma\delta$	D.23 on page 44(m)
450	0494	20131023_061805	11875	Fast	-63	42	1.00	40	141" × 82"	420	Ekc	$\beta\gamma\delta$	D.23 on page 44(n)
451	0495	20131024_060011	11875	Fast	187	44	0.98	36	151" × 68"	610	Ekc	$\beta\gamma\delta$	D.23 on page 44(o)
452	0496	20131024_103406	11875	Fast	228	48	0.97	36	150" × 69"	610	Ekc	$\beta\gamma\delta$	D.23 on page 44(p)
453	0497	20131026_061556	11875	Fast	593	51	0.79	45	151" × 96"	660	Ekc	$\beta\gamma\delta$	D.23 on page 44(q)
454	0498	20131026_223109	11882	Fast	-693	-183	0.60	30	99" × 83"	280	Dko	$\beta\gamma\delta$	D.23 on page 44(r)
455	0499	20131027_080005	11882	Fast	-626	-190	0.67	30	97" × 90"	300	Dki	$\beta\gamma\delta$	D.23 on page 44(s)
456	0500	20131027_170005	11882	Fast	-583	-196	0.73	30	106" × 84"	300	Dki	$\beta\gamma\delta$	D.23 on page 44(t)
457	0501	20131028_040005	11882	Fast	-494	-194	0.79	30	99" × 84"	390	Dkc	$\beta\gamma\delta$	D.24 on page 45(a)
458	0502	20131028_100004	11882	Fast	-450	-189	0.82	24	99" × 78"	390	Dkc	$\beta\gamma\delta$	D.24 on page 45(b)
459	0503	20131028_113628	11882	Fast	-469	-211	0.82	20	82" × 73"	390	Dkc	$\beta\gamma\delta$	D.24 on page 45(c)
460	0504	20131028_140520	11882	Fast	-413	-192	0.84	24	96" × 77"	390	Dkc	$\beta\gamma\delta$	D.24 on page 45(d)
461	0505	20131028_144914	11882	Fast	-446	-211	0.84	16	67" × 77"	390	Dkc	$\beta\gamma\delta$	D.24 on page 45(e)
462	0506	20131028_151910	11882	Fast	-440	-209	0.84	16	63" × 76"	390	Dkc	$\beta\gamma\delta$	D.24 on page 45(f)
463	0507	20131028_154459	11882	Fast	-436	-214	0.84	16	62" × 76"	390	Dkc	$\beta\gamma\delta$	D.24 on page 45(g)
464	0508	20131028_190020	11882	Fast	-376	-203	0.86	20	69" × 86"	390	Dkc	$\beta\gamma\delta$	D.24 on page 45(h)
465	0509	20131029_000004	11882	Fast	-351	-204	0.88	20	70" × 84"	330	Dkc	$\beta\gamma\delta$	D.24 on page 45(i)
466	0510	20131107_094107	11890	Fast	-273	-254	0.90	96	208" × 151"	910	Ekc	$\beta\gamma\delta$	D.24 on page 45(j)
467	0511	20131107_111006	11890	Fast	-260	-255	0.91	96	207" × 151"	910	Ekc	$\beta\gamma\delta$	D.24 on page 45(k)
468	0512	20131107_150005	11890	Fast	-233	-255	0.92	96	210" × 152"	910	Ekc	$\beta\gamma\delta$	D.24 on page 45(l)
469	0513	20131107_164506	11890	Fast	-212	-256	0.92	104	213" × 153"	910	Ekc	$\beta\gamma\delta$	D.24 on page 45(m)
470	0514	20131107_214005	11890	Fast	-169	-252	0.93	104	214" × 151"	910	Ekc	$\beta\gamma\delta$	D.24 on page 45(n)
471	0515	20131108_021005	11890	Fast	-137	-248	0.94	104	217" × 143"	920	Ehc	$\beta\gamma\delta$	D.24 on page 45(o)
472	0516	20131108_113005	11890	Fast	-62	-243	0.96	98	236" × 136"	920	Ehc	$\beta\gamma\delta$	D.24 on page 45(p)
473	0517	20131108_190005	11890	Fast	3	-236	0.96	98	235" × 131"	920	Ehc	$\beta\gamma\delta$	D.24 on page 45(q)
474	0518	20131109_074004	11890	Fast	135	-244	0.96	104	228" × 140"	920	Ehc	$\beta\gamma\delta$	D.24 on page 45(r)
475	0519	20131109_104806	11890	Fast	186	-251	0.95	104	213" × 140"	920	Ehc	$\beta\gamma\delta$	D.24 on page 45(s)
476	0520	20131110_183005	11890	Fast	492	-255	0.87	84	203" × 134"	660	Ekc	$\beta\gamma\delta$	D.24 on page 45(t)
477	0521	20131115_214505	11897	Fast	-91	-333	0.87	3	22" × 36"	310	Fkc	$\beta\gamma$	D.25 on page 46(a)
478	0522	20131214_094105	11921	Fast	-276	146	0.94	25	80" × 80"	350	Cko	β	D.25 on page 46(b)
479	0523	20131214_150005	11921	Fast	-224	149	0.96	20	81" × 76"	350	Cko	β	D.25 on page 46(c)
480	0524	20131214_200005	11921	Fast	-181	147	0.97	20	78" × 78"	350	Cko	β	D.25 on page 46(d)
481	0525	20131215_020005	11921	Fast	-121	151	0.98	20	81" × 74"	380	Cko	β	D.25 on page 46(e)
482	0526	20131215_064235	11921	Fast	-83	155	0.99	20	76" × 69"	380	Cko	β	D.25 on page 46(f)
483	0527	20131221_190404	11928	Fast	668	-241	0.72	60	200" × 85"	400	Ekc	$\beta\gamma$	D.25 on page 46(g)

Table D.1: continued.

index	inv_id	obs_id (date)_(time)	NOAA AR num	type scan	x_c (")	y_c (")	μ	num tiles	size FOV	area (MSH)	Zürich class	magnetic class	Fig. (panel)
484	0528	20131221_200353	11928	Fast	618	-247	0.73	21	110" × 56"	400	Ekc	$\beta\gamma$	D.25 on page 46(h)
485	0530	20131222_080005	11928	Fast	753	-243	0.65	40	177" × 74"	460	Ekc	$\beta\gamma$	D.25 on page 46(i)
486	0531	20131222_085954	11928	Fast	700	-248	0.64	21	113" × 48"	460	Ekc	$\beta\gamma$	D.25 on page 46(j)
487	0532	20131222_151010	11928	Fast	735	-250	0.60	14	112" × 40"	460	Ekc	$\beta\gamma$	D.25 on page 46(k)
488	0533	20131222_163103	11928	Fast	803	-243	0.58	40	169" × 75"	460	Ekc	$\beta\gamma$	D.25 on page 46(l)
489	0534	20131222_190412	11928	Fast	758	-250	0.57	21	111" × 48"	460	Ekc	$\beta\gamma$	D.25 on page 46(m)
490	0535	20131222_213103	11928	Fast	820	-241	0.55	36	156" × 71"	460	Ekc	$\beta\gamma$	D.25 on page 46(n)
491	0536	20131222_223054	11928	Fast	775	-252	0.55	21	113" × 56"	460	Ekc	$\beta\gamma$	D.25 on page 46(o)
492	0537	20140105_000405	11944	Fast	-608	-108	0.77	96	209" × 150"	1470	Fkc	$\beta\gamma\delta$	D.25 on page 46(p)
493	0538	20140107_212006	11944	Fast	5	-82	1.00	105	251" × 122"	1415	Fkc	$\beta\gamma\delta$	D.25 on page 46(q)
494	0539	20140109_040506	11944	Fast	299	-84	0.95	78	227" × 117"	1560	Fkc	$\beta\gamma\delta$	D.25 on page 46(r)
495	0540	20140109_160024	11944	Fast	380	-85	0.92	84	235" × 110"	1560	Fkc	$\beta\gamma\delta$	D.25 on page 46(s)
496	0541	20140110_144924	11944	Fast	565	-119	0.84	84	203" × 133"	1420	Fkc	$\beta\gamma\delta$	D.25 on page 46(t)
497	0542	20140111_065506	11944	Fast	693	-126	0.75	84	199" × 134"	1300	Fkc	$\beta\gamma\delta$	D.26 on page 47(a)
498	0543	20140111_154006	11944	Fast	754	-130	0.69	84	198" × 129"	1300	Fkc	$\beta\gamma\delta$	D.26 on page 47(b)
499	0544	20140111_190006	11944	Fast	775	-130	0.66	84	199" × 126"	1300	Fkc	$\beta\gamma\delta$	D.26 on page 47(c)
500	0545	20140201_104205	11967	Fast	-378	-137	0.91	105	248" × 123"	1000	Fkc	$\beta\gamma\delta$	D.26 on page 47(d)
501	0546	20140201_140005	11967	Fast	-356	-136	0.92	98	246" × 124"	1000	Fkc	$\beta\gamma\delta$	D.26 on page 47(e)
502	0547	20140201_165405	11967	Fast	-341	-135	0.92	98	233" × 126"	1000	Fkc	$\beta\gamma\delta$	D.26 on page 47(f)
503	0548	20140201_201319	11967	Fast	-305	-134	0.94	105	253" × 126"	1000	Fkc	$\beta\gamma\delta$	D.26 on page 47(g)
504	0549	20140201_231906	11967	Fast	-280	-130	0.95	105	254" × 122"	1000	Fkc	$\beta\gamma\delta$	D.26 on page 47(h)
505	0550	20140202_022005	11967	Fast	-249	-131	0.96	105	252" × 123"	1410	Fkc	$\beta\gamma\delta$	D.26 on page 47(i)
506	0551	20140202_041505	11967	Fast	-264	-128	0.95	77	195" × 121"	1410	Fkc	$\beta\gamma\delta$	D.26 on page 47(j)
507	0552	20140202_071205	11967	Fast	-206	-129	0.97	105	252" × 124"	1410	Fkc	$\beta\gamma\delta$	D.26 on page 47(k)
508	0553	20140202_102005	11967	Fast	-178	-128	0.97	105	251" × 123"	1410	Fkc	$\beta\gamma\delta$	D.26 on page 47(l)
509	0554	20140202_130005	11967	Fast	-157	-127	0.98	105	253" × 122"	1410	Fkc	$\beta\gamma\delta$	D.26 on page 47(m)
510	0555	20140202_160005	11967	Fast	-128	-128	0.98	105	254" × 125"	1410	Fkc	$\beta\gamma\delta$	D.26 on page 47(n)
511	0556	20140202_192005	11967	Fast	-101	-128	0.99	105	252" × 126"	1410	Fkc	$\beta\gamma\delta$	D.26 on page 47(o)
512	0557	20140202_223004	11967	Fast	-67	-127	0.99	105	253" × 125"	1410	Fkc	$\beta\gamma\delta$	D.26 on page 47(p)
513	0558	20140203_013005	11967	Fast	-39	-127	0.99	105	252" × 125"	1510	Fkc	$\beta\gamma\delta$	D.26 on page 47(q)
514	0559	20140203_044004	11967	Fast	-15	-126	0.99	105	256" × 125"	1510	Fkc	$\beta\gamma\delta$	D.26 on page 47(r)
515	0560	20140203_075004	11967	Fast	16	-126	0.99	105	254" × 124"	1510	Fkc	$\beta\gamma\delta$	D.26 on page 47(s)
516	0561	20140203_182306	11967	Fast	48	-107	0.99	40	131" × 86"	1510	Fkc	$\beta\gamma\delta$	D.26 on page 47(t)
517	0562	20140204_003801	11967	Fast	122	-108	0.99	54	145" × 99"	1490	Fkc	$\beta\gamma\delta$	D.27 on page 48(a)
518	0563	20140204_034005	11967	Fast	143	-108	0.98	54	157" × 103"	1490	Fkc	$\beta\gamma\delta$	D.27 on page 48(b)
519	0564	20140204_070214	11967	Fast	228	-109	0.97	90	256" × 116"	1490	Fkc	$\beta\gamma\delta$	D.27 on page 48(c)
520	0565	20140204_100005	11967	Fast	187	-111	0.97	48	133" × 103"	1490	Fkc	$\beta\gamma\delta$	D.27 on page 48(d)
521	0567	20140204_154250	11967	Fast	244	-112	0.96	54	146" × 109"	1490	Fkc	$\beta\gamma\delta$	D.27 on page 48(e)
522	0568	20140204_190005	11967	Fast	322	-108	0.94	84	246" × 106"	1490	Fkc	$\beta\gamma\delta$	D.27 on page 48(f)
523	0569	20140205_011005	11967	Fast	368	-112	0.92	79	230" × 105"	1580	Fkc	$\beta\gamma\delta$	D.27 on page 48(g)
524	0570	20140205_073005	11967	Fast	433	-115	0.89	90	259" × 103"	1580	Fkc	$\beta\gamma\delta$	D.27 on page 48(h)
525	0571	20140205_104005	11967	Fast	460	-118	0.87	90	258" × 101"	1580	Fkc	$\beta\gamma\delta$	D.27 on page 48(i)
526	0572	20140205_145005	11967	Fast	495	-120	0.85	90	257" × 103"	1580	Fkc	$\beta\gamma\delta$	D.27 on page 48(j)
527	0573	20140206_000004	11967	Fast	556	-125	0.81	78	222" × 105"	1500	Fkc	$\beta\gamma\delta$	D.27 on page 48(k)
528	0574	20140206_032004	11967	Fast	533	-125	0.83	20	71" × 86"	1500	Fkc	$\beta\gamma\delta$	D.27 on page 48(l)
529	0575	20140213_103140	11974	Fast	332	-99	0.95	50	162" × 94"	460	Fkc	$\beta\gamma\delta$	D.27 on page 48(m)
530	0576	20140213_143006	11974	Fast	318	-100	0.95	66	191" × 105"	460	Fkc	$\beta\gamma\delta$	D.27 on page 48(n)
531	0577	20140213_193104	11974	Fast	368	-103	0.93	66	192" × 103"	460	Fkc	$\beta\gamma\delta$	D.27 on page 48(o)
532	0578	20140214_000005	11974	Fast	404	-101	0.92	66	195" × 99"	780	Fkc	$\beta\gamma\delta$	D.27 on page 48(p)
533	0579	20140214_030859	11974	Fast	386	-105	0.91	42	112" × 99"	780	Fkc	$\beta\gamma\delta$	D.27 on page 48(q)
534	0580	20140214_063104	11974	Fast	473	-106	0.89	78	221" × 102"	780	Fkc	$\beta\gamma\delta$	D.27 on page 48(r)
535	0581	20140214_120005	11974	Fast	519	-109	0.86	78	221" × 102"	780	Fkc	$\beta\gamma\delta$	D.27 on page 48(s)
536	0582	20140214_200005	11974	Fast	585	-115	0.82	65	218" × 98"	780	Fkc	$\beta\gamma\delta$	D.27 on page 48(t)

Table D.1: continued.

index	inv_id	obs_id (date)_(time)	NOAA AR num	type scan	x_c (")	y_c (")	μ	num tiles	size FOV	area (MSH)	Zürich class	magnetic class	Fig. (panel)
537	0583	20140215_003005	11974	Fast	623	-118	0.79	72	212" × 104"	990	Fkc	$\beta\gamma\delta$	D.28 on page 49(a)
538	0584	20140215_040005	11974	Fast	645	-120	0.77	60	210" × 93"	990	Fkc	$\beta\gamma\delta$	D.28 on page 49(b)
539	0585	20140215_090005	11974	Fast	658	-124	0.76	60	167" × 99"	990	Fkc	$\beta\gamma\delta$	D.28 on page 49(c)
540	0586	20140215_103600	11974	Fast	687	-124	0.74	72	202" × 103"	990	Fkc	$\beta\gamma\delta$	D.28 on page 49(d)
541	0587	20140215_154106	11974	Fast	718	-126	0.71	66	194" × 108"	990	Fkc	$\beta\gamma\delta$	D.28 on page 49(e)
542	0588	20140226_235108	11990	Fast	-667	-132	0.60	12	44" × 62"	210	Dkc	$\beta\delta$	D.28 on page 49(f)
543	0589	20140227_030005	11990	Fast	-646	-127	0.63	9	50" × 59"	210	Dkc	$\beta\delta$	D.28 on page 49(g)
544	0590	20140227_120038	11990	Fast	-666	-120	0.68	9	48" × 60"	210	Dkc	$\beta\delta$	D.28 on page 49(h)
545	0591	20140227_133005	11990	Fast	-656	-118	0.69	9	49" × 57"	210	Dkc	$\beta\delta$	D.28 on page 49(i)
546	0592	20140227_181805	11990	Fast	-623	-113	0.72	9	48" × 55"	210	Dkc	$\beta\delta$	D.28 on page 49(j)
547	0593	20140227_233505	11990	Fast	-589	-111	0.76	9	50" × 56"	250	Dkc	$\beta\delta$	D.28 on page 49(k)
548	0594	20140228_021505	11990	Fast	-573	-109	0.77	9	55" × 54"	250	Dkc	$\beta\delta$	D.28 on page 49(l)
549	0595	20140228_113006	11990	Fast	-499	-108	0.83	9	54" × 58"	250	Dkc	$\beta\delta$	D.28 on page 49(m)
550	0596	20140228_140005	11990	Fast	-483	-105	0.84	12	57" × 57"	250	Dkc	$\beta\delta$	D.28 on page 49(n)
551	0597	20140228_233534	11990	Fast	-362	-100	0.89	12	61" × 57"	250	Dkc	$\beta\delta$	D.28 on page 49(o)
552	0598	20140301_022804	11990	Fast	-347	-100	0.90	12	59" × 58"	250	Dkc	$\beta\delta$	D.28 on page 49(p)
553	0599	20140311_143005	12002	Fast	-433	-213	0.85	50	174" × 94"	150	Dac	$\beta\gamma\delta$	D.28 on page 49(q)
554	0600	20140329_150006	12017	Fast	605	295	0.80	12	72" × 51"	150	Dao	$\beta\delta$	D.28 on page 49(r)
555	0601	20140329_170006	12017	Fast	615	292	0.79	15	75" × 50"	150	Dao	$\beta\delta$	D.28 on page 49(s)
556	0603	20140607_145319	12080	Fast	-115	-201	0.96	40	162" × 73"	160	Dai	$\beta\gamma\delta$	D.28 on page 49(t)
557	0604	20140607_195436	12080	Fast	-60	-203	0.96	36	157" × 71"	160	Dai	$\beta\gamma\delta$	D.29 on page 50(a)
558	0605	20140607_231505	12080	Fast	-5	-199	0.97	28	112" × 63"	160	Dai	$\beta\gamma\delta$	D.29 on page 50(b)
559	0606	20140608_022356	12080	Fast	-7	-203	0.97	40	166" × 69"	230	Dac	$\beta\gamma\delta$	D.29 on page 50(c)
560	0607	20140609_043534	12080	Fast	226	-215	0.96	50	175" × 83"	340	Dkc	$\beta\gamma\delta$	D.29 on page 50(d)
561	0608	20140609_093452	12080	Fast	276	-213	0.95	50	173" × 87"	340	Dkc	$\beta\gamma\delta$	D.29 on page 50(e)
562	0609	20140610_001635	12080	Fast	414	-217	0.90	55	191" × 83"	300	Ekc	$\beta\gamma\delta$	D.29 on page 50(f)
563	0610	20140610_033335	12080	Fast	451	-203	0.88	36	154" × 71"	300	Ekc	$\beta\gamma\delta$	D.29 on page 50(g)
564	0611	20140610_082905	12080	Fast	495	-206	0.86	36	153" × 76"	300	Ekc	$\beta\gamma\delta$	D.29 on page 50(h)
565	0612	20140610_114536	12080	Fast	512	-211	0.85	36	154" × 79"	300	Ekc	$\beta\gamma\delta$	D.29 on page 50(i)
566	0613	20140610_231505	12080	Fast	618	-210	0.78	40	142" × 82"	300	Ekc	$\beta\gamma\delta$	D.29 on page 50(j)
567	0614	20140611_023135	12080	Fast	639	-211	0.77	40	139" × 87"	320	Dkc	$\beta\gamma\delta$	D.29 on page 50(k)
568	0615	20140611_090858	12085	Fast	692	-209	0.72	40	137" × 91"	460	Ekc	$\beta\gamma$	D.29 on page 50(l)
569	0616	20140611_122235	12085	Fast	712	-211	0.70	40	134" × 84"	460	Ekc	$\beta\gamma$	D.29 on page 50(m)
570	0618	20140701_194405	12104	Fast	-554	-249	0.68	25	87" × 81"	350	Dkc	$\beta\gamma\delta$	D.29 on page 50(n)
571	0619	20140701_212105	12104	Fast	-544	-252	0.69	25	87" × 83"	350	Dkc	$\beta\gamma\delta$	D.29 on page 50(o)
572	0620	20140702_003105	12104	Fast	-519	-252	0.71	25	83" × 82"	410	Dkc	$\beta\gamma\delta$	D.29 on page 50(p)
573	0621	20140702_034805	12104	Fast	-496	-256	0.73	25	82" × 84"	410	Dkc	$\beta\gamma\delta$	D.29 on page 50(q)
574	0622	20140702_070505	12104	Fast	-471	-258	0.74	25	80" × 86"	410	Dkc	$\beta\gamma\delta$	D.29 on page 50(r)
575	0623	20140702_102205	12104	Fast	-453	-259	0.76	25	79" × 86"	410	Dkc	$\beta\gamma\delta$	D.29 on page 50(s)
576	0624	20140702_120005	12104	Fast	-436	-260	0.77	25	78" × 86"	410	Dkc	$\beta\gamma\delta$	D.29 on page 50(t)
577	0625	20140702_140005	12104	Fast	-410	-260	0.78	20	65" × 86"	410	Dkc	$\beta\gamma\delta$	D.30 on page 51(a)
578	0626	20140702_170605	12104	Fast	-399	-264	0.80	25	76" × 88"	410	Dkc	$\beta\gamma\delta$	D.30 on page 51(b)
579	0627	20140702_202220	12104	Fast	-362	-262	0.81	20	65" × 86"	410	Dkc	$\beta\gamma\delta$	D.30 on page 51(c)
580	0628	20140703_074304	12104	Fast	-281	-264	0.86	20	69" × 84"	470	Dkc	$\beta\gamma\delta$	D.30 on page 51(d)
581	0630	20140824_011822	12149	Fast	-698	112	0.65	48	132" × 103"	120	Eac	$\beta\gamma$	D.30 on page 51(e)
582	0631	20140826_105321	12146	Fast	733	70	0.67	25	85" × 86"	290	Dki	$\beta\delta$	D.30 on page 51(f)
583	0632	20140826_141206	12146	Fast	751	73	0.65	25	82" × 83"	290	Dki	$\beta\delta$	D.30 on page 51(g)
584	0633	20140826_212506	12148	Fast	796	77	0.59	25	76" × 91"	60	Cao	β	D.30 on page 51(h)
585	0634	20140925_142206	12172	Fast	-259	-273	0.90	65	222" × 90"	440	Ekc	$\beta\gamma$	D.30 on page 51(i)
586	0636	20140927_110005	12172	Fast	137	-287	0.94	84	240" × 104"	500	Ekc	$\beta\gamma$	D.30 on page 51(j)

Table D.1: continued.

index	inv_id	obs_id (date)_(time)	NOAA AR num	type scan	x_c (")	y_c (")	μ	num tiles	size FOV	area (MSH)	Zürich class	magnetic class	Fig. (panel)
587	0637	20140928_011505	12172	Fast	268	-288	0.91	70	240" × 89"	460	Ekc	$\beta\gamma$	D.30 on page 51(k)
588	0638	20140928_134005	12172	Fast	381	-290	0.87	84	238" × 111"	460	Ekc	$\beta\gamma$	D.30 on page 51(l)
589	0639	20140929_220004	12172	Fast	790	-309	0.61	56	119" × 142"	460	Ekc	$\beta\gamma$	D.30 on page 51(m)
590	0640	20141021_130127	12192	Fast	-465	-318	0.81	108	209" × 158"	2180	Fkc	$\beta\gamma\delta$	D.30 on page 51(n)
591	0641	20141021_154005	12192	Fast	-437	-319	0.82	108	212" × 158"	2180	Fkc	$\beta\gamma\delta$	D.30 on page 51(o)
592	0642	20141021_190005	12192	Fast	-414	-321	0.84	117	220" × 160"	2180	Fkc	$\beta\gamma\delta$	D.30 on page 51(p)
593	0643	20141021_220005	12192	Fast	-374	-323	0.85	117	220" × 160"	2180	Fkc	$\beta\gamma\delta$	D.30 on page 51(q)
594	0644	20141022_013937	12192	Fast	-344	-324	0.87	49	113" × 119"	2410	Fkc	$\beta\gamma\delta$	D.30 on page 51(r)
595	0645	20141022_041102	12192	Fast	-322	-324	0.88	49	112" × 120"	2410	Fkc	$\beta\gamma\delta$	D.30 on page 51(s)
596	0646	20141024_003106	12192	Fast	68	-327	0.94	135	256" × 161"	2740	Fkc	$\beta\gamma\delta$	D.30 on page 51(t)
597	0647	20141024_021005	12192	Fast	82	-327	0.94	135	257" × 159"	2740	Fkc	$\beta\gamma\delta$	D.31 on page 52(a)
598	0648	20141024_040005	12192	Fast	98	-326	0.93	135	256" × 159"	2740	Fkc	$\beta\gamma\delta$	D.31 on page 52(b)
599	0649	20141024_070006	12192	Fast	124	-326	0.93	135	255" × 160"	2740	Fkc	$\beta\gamma\delta$	D.31 on page 52(c)
600	0650	20141024_084505	12192	Fast	139	-326	0.93	135	248" × 160"	2740	Fkc	$\beta\gamma\delta$	D.31 on page 52(d)
601	0651	20141024_203004	12192	Fast	283	-322	0.90	108	199" × 159"	2740	Fkc	$\beta\gamma\delta$	D.31 on page 52(e)
602	0653	20141024_234105	12192	Fast	267	-321	0.90	126	247" × 159"	2740	Fkc	$\beta\gamma\delta$	D.31 on page 52(f)
603	0654	20141025_074004	12192	Fast	337	-319	0.88	135	251" × 160"	2510	Fkc	$\beta\gamma\delta$	D.31 on page 52(g)
604	0655	20141025_110049	12192	Fast	367	-320	0.86	81	149" × 162"	2510	Fkc	$\beta\gamma\delta$	D.31 on page 52(h)
605	0657	20141025_230021	12192	Fast	400	-315	0.85	12	28" × 102"	2510	Fkc	$\beta\gamma\delta$	D.31 on page 52(i)
606	0658	20141026_110005	12192	Fast	553	-308	0.75	81	151" × 160"	2570	Fkc	$\beta\gamma\delta$	D.31 on page 52(j)
607	0659	20141026_233004	12192	Fast	639	-301	0.68	81	151" × 160"	2570	Fkc	$\beta\gamma\delta$	D.31 on page 52(k)
608	0664	20141027_191004	12192	Fast	752	-289	0.55	72	138" × 160"	2750	Fkc	$\beta\gamma\delta$	D.31 on page 52(l)
609	0665	20141027_221951	12192	Fast	771	-287	0.52	49	112" × 119"	2750	Fkc	$\beta\gamma\delta$	D.31 on page 52(m)
610	0666	20141028_025431	12192	Fast	793	-284	0.49	49	112" × 120"	2380	Fkc	$\beta\gamma\delta$	D.31 on page 52(n)
611	0668	20141028_044051	12192	Fast	758	-283	0.54	36	62" × 161"	2380	Fkc	$\beta\gamma\delta$	D.31 on page 52(o)
612	0669	20141106_062834	12205	Fast	-751	228	0.54	40	130" × 95"	250	Ekc	$\beta\gamma\delta$	D.31 on page 52(p)
613	0670	20141106_072825	12205	Fast	-769	224	0.57	30	95" × 85"	250	Ekc	$\beta\gamma\delta$	D.31 on page 52(q)
614	0672	20141106_170111	12205	Fast	-702	232	0.60	32	142" × 79"	250	Ekc	$\beta\gamma\delta$	D.31 on page 52(r)
615	0674	20141106_203419	12205	Fast	-693	231	0.63	45	150" × 89"	250	Ekc	$\beta\gamma\delta$	D.31 on page 52(s)
616	0675	20141107_040201	12205	Fast	-651	226	0.70	28	109" × 75"	360	Ekc	$\beta\gamma\delta$	D.31 on page 52(t)
617	0676	20141107_182005	12205	Fast	-553	223	0.79	28	111" × 72"	360	Ekc	$\beta\gamma\delta$	D.32 on page 53(a)
618	0677	20141107_184601	12205	Nor.	-547	222	0.79	88	97" × 71"	360	Ekc	$\beta\gamma\delta$	D.32 on page 53(b)
619	0678	20141107_222544	12205	Fast	-521	222	0.81	28	112" × 69"	360	Ekc	$\beta\gamma\delta$	D.32 on page 53(c)
620	0679	20141108_063905	12205	Fast	-460	219	0.85	28	112" × 73"	410	Ekc	$\beta\gamma\delta$	D.32 on page 53(d)
621	0680	20141110_075739	12205	Fast	52	201	0.98	45	152" × 93"	350	Ekc	$\beta\gamma\delta$	D.32 on page 53(e)
622	0681	20141111_183840	12205	Fast	353	205	0.93	45	153" × 84"	280	Dkc	$\beta\gamma\delta$	D.32 on page 53(f)
623	0682	20141115_102421	12209	Fast	-818	-273	0.43	64	133" × 143"	680	Eac	$\beta\gamma$	D.32 on page 53(g)
624	0683	20141115_231101	12209	Fast	-762	-276	0.53	72	144" × 147"	680	Fkc	$\beta\gamma$	D.32 on page 53(h)
625	0684	20141116_014605	12209	Fast	-754	-277	0.55	72	147" × 136"	800	Fkc	$\beta\gamma\delta$	D.32 on page 53(i)
626	0685	20141116_080039	12209	Fast	-755	-280	0.55	35	76" × 132"	800	Fkc	$\beta\gamma\delta$	D.32 on page 53(j)
627	0686	20141116_110005	12209	Fast	-735	-280	0.57	35	78" × 129"	800	Fkc	$\beta\gamma\delta$	D.32 on page 53(k)
628	0687	20141116_150004	12209	Fast	-682	-282	0.64	72	147" × 138"	800	Fkc	$\beta\gamma\delta$	D.32 on page 53(l)
629	0688	20141116_200048	12209	Fast	-582	-284	0.70	84	202" × 125"	800	Fkc	$\beta\gamma\delta$	D.32 on page 53(m)
630	0689	20141116_230004	12209	Fast	-558	-285	0.72	84	200" × 123"	800	Fkc	$\beta\gamma\delta$	D.32 on page 53(n)
631	0690	20141117_090004	12209	Fast	-489	-286	0.78	84	204" × 125"	940	Fkc	$\beta\gamma\delta$	D.32 on page 53(o)
632	0691	20141118_120006	12209	Fast	-316	-302	0.86	35	90" × 119"	990	Fkc	$\beta\gamma\delta$	D.32 on page 53(p)
633	0692	20141118_133006	12209	Fast	-292	-302	0.87	36	94" × 103"	990	Fkc	$\beta\gamma\delta$	D.32 on page 53(q)
634	0693	20141118_160506	12209	Fast	-273	-302	0.87	30	85" × 107"	990	Fkc	$\beta\gamma\delta$	D.32 on page 53(r)
635	0694	20141118_193006	12209	Fast	-248	-302	0.89	36	95" × 105"	990	Fkc	$\beta\gamma\delta$	D.32 on page 53(s)
636	0695	20141118_224006	12209	Fast	-211	-304	0.90	36	94" × 117"	990	Fkc	$\beta\gamma\delta$	D.32 on page 53(t)
637	0696	20141119_013005	12209	Fast	-187	-304	0.91	36	104" × 113"	990	Fkc	$\beta\gamma\delta$	D.33 on page 54(a)
638	0697	20141119_031505	12209	Fast	-177	-304	0.91	36	95" × 112"	1100	Fkc	$\beta\gamma\delta$	D.33 on page 54(b)
639	0698	20141119_100005	12209	Fast	-117	-304	0.93	36	108" × 116"	1100	Fkc	$\beta\gamma\delta$	D.33 on page 54(c)

Table D.1: continued.

index	inv_id	obs_id (date)_(time)	NOAA AR num	type scan	x_c (")	y_c (")	μ	num tiles	size FOV	area (MSH)	Zürich class	magnetic class	Fig. (panel)
640	0699	20141119_130005	12209	Fast	-93	-305	0.93	42	110" × 113"	1100	Fkc	$\beta\gamma\delta$	D.33 on page 54(d)
641	0700	20141119_164505	12209	Fast	-53	-302	0.94	42	112" × 116"	1100	Fkc	$\beta\gamma\delta$	D.33 on page 54(e)
642	0701	20141119_200005	12209	Fast	-25	-304	0.94	42	111" × 117"	1100	Fkc	$\beta\gamma\delta$	D.33 on page 54(f)
643	0702	20141119_231005	12209	Fast	4	-303	0.95	42	110" × 113"	1100	Fkc	$\beta\gamma\delta$	D.33 on page 54(g)
644	0703	20141120_021005	12209	Fast	30	-304	0.95	49	110" × 126"	930	Fko	$\beta\gamma\delta$	D.33 on page 54(h)
645	0704	20141120_070048	12209	Fast	15	-294	0.95	35	89" × 132"	930	Fko	$\beta\gamma\delta$	D.33 on page 54(i)
646	0705	20141120_120048	12209	Fast	116	-304	0.95	36	97" × 111"	930	Fko	$\beta\gamma\delta$	D.33 on page 54(j)
647	0706	20141120_140005	12209	Fast	132	-302	0.95	36	99" × 109"	930	Fko	$\beta\gamma\delta$	D.33 on page 54(k)
648	0707	20141120_195942	12209	Fast	105	-303	0.94	36	103" × 100"	930	Fko	$\beta\gamma\delta$	D.33 on page 54(l)
649	0708	20141120_221104	12209	Fast	198	-301	0.94	36	105" × 111"	930	Fko	$\beta\gamma\delta$	D.33 on page 54(m)
650	0709	20141121_011005	12209	Fast	230	-302	0.94	36	105" × 103"	970	Fko	$\beta\gamma\delta$	D.33 on page 54(n)
651	0710	20141121_044536	12209	Fast	196	-302	0.93	30	98" × 96"	970	Fko	$\beta\gamma\delta$	D.33 on page 54(o)
652	0711	20141121_091903	12209	Fast	303	-301	0.92	36	98" × 102"	970	Fko	$\beta\gamma\delta$	D.33 on page 54(p)
653	0712	20141121_121804	12209	Fast	329	-301	0.92	36	103" × 101"	970	Fko	$\beta\gamma\delta$	D.33 on page 54(q)
654	0713	20141121_211048	12209	Fast	343	-289	0.89	36	101" × 108"	970	Fko	$\beta\gamma\delta$	D.33 on page 54(r)
655	0714	20141122_001504	12209	Fast	376	-290	0.88	42	106" × 121"	900	Fko	$\beta\gamma\delta$	D.33 on page 54(s)
656	0715	20141122_005652	12209	Fast	362	-296	0.88	36	103" × 106"	900	Fko	$\beta\gamma\delta$	D.33 on page 54(t)
657	0716	20141122_033802	12209	Fast	389	-297	0.87	36	99" × 102"	900	Fko	$\beta\gamma\delta$	D.34 on page 55(a)
658	0717	20141122_220054	12209	Fast	609	-292	0.78	42	109" × 101"	900	Fko	$\beta\gamma\delta$	D.34 on page 55(b)
659	0718	20141123_023004	12209	Fast	637	-291	0.76	36	100" × 101"	950	Fko	$\beta\gamma\delta$	D.34 on page 55(c)
660	0719	20141123_062123	12209	Fast	654	-289	0.75	30	85" × 100"	950	Fko	$\beta\gamma\delta$	D.34 on page 55(d)
661	0720	20141123_110004	12209	Fast	735	-288	0.68	70	175" × 121"	950	Fko	$\beta\gamma\delta$	D.34 on page 55(e)
662	0721	20141123_160004	12209	Fast	766	-286	0.65	70	172" × 121"	950	Fko	$\beta\gamma\delta$	D.34 on page 55(f)
663	0722	20141123_210004	12209	Fast	794	-285	0.61	70	173" × 122"	950	Fko	$\beta\gamma\delta$	D.34 on page 55(g)
664	0723	20141124_020043	12209	Fast	753	-284	0.61	35	111" × 95"	1000	Fki	$\beta\gamma\delta$	D.34 on page 55(h)
665	0724	20141124_080004	12209	Fast	798	-283	0.55	42	124" × 111"	1000	Fki	$\beta\gamma\delta$	D.34 on page 55(i)
666	0725	20141124_140006	12209	Fast	821	-281	0.52	30	101" × 97"	1000	Fki	$\beta\gamma\delta$	D.34 on page 55(j)
667	0726	20141129_224005	12224	Fast	-498	-344	0.78	50	166" × 94"	10	Bxo	β	D.34 on page 55(k)
668	0727	20141202_211505	12222	Fast	244	-338	0.92	28	124" × 78"	650	Eki	$\beta\gamma$	D.34 on page 55(l)
669	0728	20141203_001505	12222	Fast	129	-348	0.92	65	217" × 87"	620	Eki	$\beta\gamma$	D.34 on page 55(m)
670	0729	20141203_081505	12222	Fast	200	-348	0.91	65	217" × 84"	620	Eki	$\beta\gamma$	D.34 on page 55(n)
671	0730	20141203_111005	12222	Fast	235	-347	0.91	60	209" × 83"	620	Eki	$\beta\gamma$	D.34 on page 55(o)
672	0731	20141204_141506	12222	Fast	446	-342	0.82	60	199" × 86"	570	Ekc	$\beta\gamma$	D.34 on page 55(p)
673	0732	20141204_210005	12222	Fast	616	-336	0.78	12	44" × 64"	570	Ekc	$\beta\gamma$	D.34 on page 55(q)
674	0733	20141205_030005	12222	Fast	675	-331	0.73	24	99" × 79"	770	Ekc	$\beta\gamma$	D.34 on page 55(r)
675	0734	20141205_075005	12222	Fast	594	-343	0.73	50	172" × 84"	770	Ekc	$\beta\gamma$	D.34 on page 55(s)
676	0735	20141205_105005	12222	Fast	614	-337	0.72	50	171" × 83"	770	Ekc	$\beta\gamma$	D.34 on page 55(t)
677	0736	20141205_163408	12222	Fast	658	-330	0.68	40	172" × 75"	770	Ekc	$\beta\gamma$	D.35 on page 56(a)
678	0737	20141216_110511	12242	Fast	-290	-299	0.89	48	142" × 114"	360	Dkc	$\beta\gamma\delta$	D.35 on page 56(b)
679	0738	20141217_100116	12242	Fast	-53	-296	0.95	42	111" × 102"	630	Dkc	$\beta\gamma\delta$	D.35 on page 56(c)
680	0739	20141217_233104	12242	Fast	36	-294	0.95	78	214" × 115"	630	Dkc	$\beta\gamma\delta$	D.35 on page 56(d)
681	0740	20141218_151342	12242	Fast	170	-292	0.94	66	193" × 110"	700	Ekc	$\beta\gamma\delta$	D.35 on page 56(e)
682	0741	20141218_223006	12242	Fast	318	-293	0.92	63	156" × 117"	700	Ekc	$\beta\gamma\delta$	D.35 on page 56(f)
683	0742	20141219_100006	12242	Fast	442	-293	0.88	60	163" × 115"	970	Ekc	$\beta\gamma\delta$	D.35 on page 56(g)
684	0743	20141219_150006	12242	Fast	487	-293	0.86	63	161" × 118"	970	Ekc	$\beta\gamma\delta$	D.35 on page 56(h)
685	0744	20141219_223124	12242	Fast	434	-292	0.85	30	88" × 109"	970	Ekc	$\beta\gamma\delta$	D.35 on page 56(i)
686	0745	20141220_003053	12242	Fast	459	-293	0.85	30	83" × 115"	1080	Ekc	$\beta\gamma\delta$	D.35 on page 56(j)
687	0746	20141220_101605	12242	Fast	665	-294	0.77	56	142" × 121"	1080	Ekc	$\beta\gamma\delta$	D.35 on page 56(k)
688	0747	20141220_154505	12242	Fast	705	-293	0.74	56	143" × 121"	1080	Ekc	$\beta\gamma\delta$	D.35 on page 56(l)
689	0748	20150109_092006	12257	Fast	340	183	0.93	60	166" × 100"	170	Dai	β	D.35 on page 56(m)
690	0750	20150109_182020	12257	Fast	419	183	0.90	60	166" × 101"	170	Dai	β	D.35 on page 56(n)
691	0751	20150111_210105	12257	Fast	826	159	0.59	35	119" × 87"	470	Ekc	$\beta\delta$	D.35 on page 56(o)

Table D.1: continued.

index	inv_id	obs_id (date)_(time)	NOAA AR num	type scan	x_c (")	y_c (")	μ	num tiles	size FOV	area (MSH)	Zürich class	magnetic class	Fig. (panel)
692	0752	20150111_234445	12262	Fast	820	161	0.59	35	113" × 87"	20	Cro	β	D.35 on page 56(p)
693	0753	20150126_000204	12268	Fast	-534	-74	0.79	72	202" × 103"	360	Eki	$\beta\gamma$	D.35 on page 56(q)
694	0754	20150309_025047	12297	Fast	-758	-200	0.57	30	94" × 81"	260	Dhc	$\beta\gamma\delta$	D.35 on page 56(r)
695	0755	20150309_051505	12297	Fast	-743	-199	0.59	30	97" × 82"	260	Dhc	$\beta\gamma\delta$	D.35 on page 56(s)
696	0756	20150309_070504	12297	Fast	-733	-197	0.60	30	94" × 80"	260	Dhc	$\beta\gamma\delta$	D.35 on page 56(t)
697	0757	20150309_103622	12297	Fast	-704	-179	0.63	30	102" × 87"	260	Dhc	$\beta\gamma\delta$	D.36 on page 57(a)
698	0758	20150309_123006	12297	Fast	-693	-175	0.64	30	106" × 84"	260	Dhc	$\beta\gamma\delta$	D.36 on page 57(b)
699	0759	20150309_140005	12297	Fast	-686	-176	0.65	35	109" × 87"	260	Dhc	$\beta\gamma\delta$	D.36 on page 57(c)
700	0760	20150309_154006	12297	Fast	-672	-173	0.67	35	109" × 86"	260	Dhc	$\beta\gamma\delta$	D.36 on page 57(d)
701	0761	20150309_171106	12297	Fast	-664	-171	0.68	30	108" × 81"	260	Dhc	$\beta\gamma\delta$	D.36 on page 57(e)
702	0762	20150309_184806	12297	Fast	-654	-170	0.69	35	109" × 86"	260	Dhc	$\beta\gamma\delta$	D.36 on page 57(f)
703	0763	20150309_204806	12297	Fast	-642	-172	0.70	35	111" × 88"	260	Dhc	$\beta\gamma\delta$	D.36 on page 57(g)
704	0764	20150309_223805	12297	Fast	-630	-168	0.71	35	114" × 84"	260	Dhc	$\beta\gamma\delta$	D.36 on page 57(h)
705	0765	20150310_000005	12297	Fast	-623	-168	0.72	35	112" × 85"	260	Dac	$\beta\delta$	D.36 on page 57(i)
706	0766	20150310_010006	12297	Fast	-623	-167	0.72	30	101" × 86"	260	Dac	$\beta\delta$	D.36 on page 57(j)
707	0767	20150310_024006	12297	Fast	-605	-168	0.74	35	113" × 89"	260	Dac	$\beta\delta$	D.36 on page 57(k)
708	0768	20150310_043005	12297	Fast	-595	-169	0.75	35	118" × 86"	260	Dac	$\beta\delta$	D.36 on page 57(l)
709	0769	20150310_061705	12297	Fast	-583	-171	0.76	35	122" × 94"	260	Dac	$\beta\delta$	D.36 on page 57(m)
710	0770	20150310_074505	12297	Fast	-582	-162	0.76	35	111" × 81"	260	Dac	$\beta\delta$	D.36 on page 57(n)
711	0771	20150310_093005	12297	Fast	-568	-162	0.78	35	110" × 81"	260	Dac	$\beta\delta$	D.36 on page 57(o)
712	0772	20150310_110406	12297	Fast	-540	-162	0.79	35	114" × 90"	260	Dac	$\beta\delta$	D.36 on page 57(p)
713	0773	20150310_165005	12297	Fast	-500	-159	0.82	35	121" × 86"	260	Dac	$\beta\delta$	D.36 on page 57(q)
714	0774	20150311_031505	12297	Fast	-425	-157	0.87	35	116" × 95"	280	Dkc	$\beta\gamma\delta$	D.36 on page 57(r)
715	0775	20150311_081005	12297	Fast	-382	-153	0.89	35	118" × 97"	280	Dkc	$\beta\gamma\delta$	D.36 on page 57(s)
716	0776	20150311_220105	12297	Fast	-279	-149	0.94	48	139" × 103"	280	Dkc	$\beta\gamma\delta$	D.36 on page 57(t)
717	0777	20150311_223546	12297	Fast	-279	-167	0.94	35	113" × 98"	280	Dkc	$\beta\gamma\delta$	D.37 on page 58(a)
718	0778	20150312_032226	12297	Fast	-238	-161	0.95	35	111" × 97"	350	Dkc	$\beta\gamma\delta$	D.37 on page 58(b)
719	0779	20150312_044309	12297	Fast	-226	-161	0.96	42	112" × 99"	350	Dkc	$\beta\gamma\delta$	D.37 on page 58(c)
720	0780	20150312_103721	12297	Fast	-174	-146	0.97	54	149" × 101"	350	Dkc	$\beta\gamma\delta$	D.37 on page 58(d)
721	0781	20150312_135257	12297	Fast	-145	-163	0.97	35	112" × 98"	350	Dkc	$\beta\gamma\delta$	D.37 on page 58(e)
722	0782	20150312_155021	12297	Fast	-119	-148	0.98	54	145" × 105"	350	Dkc	$\beta\gamma\delta$	D.37 on page 58(f)
723	0783	20150312_210006	12297	Fast	-77	-146	0.98	54	148" × 101"	350	Dkc	$\beta\gamma\delta$	D.37 on page 58(g)
724	0784	20150312_214800	12297	Fast	-75	-164	0.98	35	113" × 98"	350	Dkc	$\beta\gamma\delta$	D.37 on page 58(h)
725	0785	20150313_030121	12297	Fast	-27	-147	0.98	54	151" × 109"	340	Dkc	$\beta\gamma\delta$	D.37 on page 58(i)
726	0786	20150313_103036	12297	Fast	38	-151	0.98	54	151" × 102"	340	Dkc	$\beta\gamma\delta$	D.37 on page 58(j)
727	0787	20150313_200005	12297	Fast	122	-156	0.98	45	149" × 95"	340	Dkc	$\beta\gamma\delta$	D.37 on page 58(k)
728	0788	20150313_204115	12297	Fast	127	-165	0.98	28	112" × 78"	340	Dkc	$\beta\gamma\delta$	D.37 on page 58(l)
729	0789	20150314_015020	12297	Fast	170	-153	0.97	45	147" × 97"	420	Dkc	$\beta\gamma\delta$	D.37 on page 58(m)
730	0790	20150314_042951	12297	Fast	195	-167	0.96	28	113" × 74"	420	Dkc	$\beta\gamma\delta$	D.37 on page 58(n)
731	0791	20150315_001106	12297	Fast	362	-172	0.91	45	152" × 96"	320	Ekc	$\beta\gamma\delta$	D.37 on page 58(o)
732	0792	20150315_030005	12297	Fast	384	-174	0.90	54	150" × 100"	320	Ekc	$\beta\gamma\delta$	D.37 on page 58(p)
733	0793	20150315_093005	12297	Fast	435	-173	0.87	45	151" × 91"	320	Ekc	$\beta\gamma\delta$	D.37 on page 58(q)
734	0794	20150315_200005	12297	Fast	513	-183	0.82	45	150" × 87"	320	Ekc	$\beta\gamma\delta$	D.37 on page 58(r)
735	0795	20150315_224638	12297	Fast	518	-189	0.82	20	84" × 69"	320	Ekc	$\beta\gamma\delta$	D.37 on page 58(s)
736	0796	20150316_000020	12297	Fast	537	-185	0.81	40	139" × 84"	370	Ekc	$\beta\gamma\delta$	D.37 on page 58(t)
737	0797	20150316_030005	12297	Fast	564	-189	0.79	45	151" × 90"	370	Ekc	$\beta\gamma\delta$	D.38 on page 59(a)
738	0798	20150316_100004	12297	Fast	610	-195	0.75	45	151" × 92"	370	Ekc	$\beta\gamma\delta$	D.38 on page 59(b)
739	0799	20150316_104729	12297	Fast	616	-195	0.74	28	113" × 65"	370	Ekc	$\beta\gamma\delta$	D.38 on page 59(c)
740	0800	20150316_125916	12297	Fast	613	-198	0.74	20	82" × 63"	370	Ekc	$\beta\gamma\delta$	D.38 on page 59(d)
741	0801	20150316_140019	12297	Fast	643	-197	0.72	45	150" × 86"	370	Ekc	$\beta\gamma\delta$	D.38 on page 59(e)
742	0802	20150316_230004	12297	Fast	687	-202	0.67	40	140" × 87"	370	Ekc	$\beta\gamma\delta$	D.38 on page 59(f)
743	0803	20150317_020004	12297	Fast	706	-204	0.65	40	138" × 86"	380	Ekc	$\beta\gamma\delta$	D.38 on page 59(g)
744	0804	20150317_082405	12297	Fast	734	-210	0.61	40	137" × 82"	380	Ekc	$\beta\gamma\delta$	D.38 on page 59(h)

Table D.1: continued.

index	inv_id	obs_id (date)_(time)	NOAA AR num	type scan	x_c (")	y_c (")	μ	num tiles	size FOV	area (MSH)	Zürich class	magnetic class	Fig. (panel)
745	0805	20150317_170554	12297	Fast	827	-224	0.55	35	121" × 82"	380	Ekc	$\beta\gamma\delta$	D.38 on page 59(i)
746	0806	20150331_160005	12315	Fast	882	-130	0.55	24	71" × 105"	30	Cro	β	D.38 on page 59(j)
747	0807	20150508_101508	12339	Fast	-597	239	0.71	72	206" × 108"	730	Fkc	$\beta\gamma$	D.38 on page 59(k)
748	0808	20150508_120005	12339	Fast	-620	241	0.71	84	232" × 114"	730	Fkc	$\beta\gamma$	D.38 on page 59(l)
749	0809	20150620_102106	12371	Fast	-400	173	0.89	42	112" × 115"	1020	Ekc	$\beta\gamma\delta$	D.38 on page 59(m)
750	0810	20150620_144749	12371	Fast	-291	145	0.93	91	223" × 133"	1020	Ekc	$\beta\gamma\delta$	D.38 on page 59(n)
751	0811	20150620_194105	12371	Fast	-253	152	0.94	78	228" × 111"	1020	Ekc	$\beta\gamma\delta$	D.38 on page 59(o)
752	0812	20150621_003746	12371	Fast	-211	145	0.96	91	226" × 117"	1120	Ekc	$\beta\gamma\delta$	D.38 on page 59(p)
753	0813	20150621_061125	12371	Fast	-234	161	0.96	36	103" × 105"	1120	Ekc	$\beta\gamma\delta$	D.38 on page 59(q)
754	0814	20150621_184013	12371	Fast	-62	149	0.99	84	235" × 109"	1120	Ekc	$\beta\gamma\delta$	D.38 on page 59(r)
755	0815	20150622_062148	12371	Fast	-16	152	0.99	36	100" × 100"	1180	Fkc	$\beta\gamma\delta$	D.38 on page 59(s)
756	0816	20150622_074504	12371	Nor.	-2	158	0.99	110	92" × 87"	1180	Fkc	$\beta\gamma\delta$	D.38 on page 59(t)
757	0817	20150623_082141	12371	Nor.	214	154	0.96	100	88" × 92"	1070	Fkc	$\beta\gamma\delta$	D.39 on page 60(a)
758	0818	20150623_145506	12371	Fast	271	153	0.95	30	88" × 99"	1070	Fkc	$\beta\gamma\delta$	D.39 on page 60(b)
759	0823	20150625_180921	12371	Fast	670	162	0.71	25	79" × 88"	740	Fkc	$\beta\gamma$	D.39 on page 60(c)
760	0824	20150707_100806	12381	Fast	-345	166	0.90	66	181" × 100"	350	Ekc	$\beta\gamma$	D.39 on page 60(d)
761	0825	20150707_150606	12381	Fast	-309	161	0.92	66	186" × 101"	350	Ekc	$\beta\gamma$	D.39 on page 60(e)
762	0826	20150707_200754	12381	Fast	-276	158	0.93	72	203" × 103"	350	Ekc	$\beta\gamma$	D.39 on page 60(f)
763	0827	20150708_005701	12381	Fast	-234	153	0.95	72	210" × 107"	450	Ekc	$\beta\gamma$	D.39 on page 60(g)
764	0828	20150708_090505	12381	Fast	-164	146	0.97	78	222" × 111"	450	Ekc	$\beta\gamma$	D.39 on page 60(h)
765	0829	20150709_211604	12381	Fast	136	135	0.98	90	251" × 117"	550	Eko	β	D.39 on page 60(i)
766	0830	20150710_020434	12381	Fast	173	135	0.97	105	253" × 119"	500	Eko	β	D.39 on page 60(j)
767	0831	20150822_144608	12403	Fast	-275	-338	0.87	54	150" × 104"	350	Dkc	$\beta\gamma$	D.39 on page 60(k)
768	0832	20150822_181735	12403	Fast	-244	-339	0.88	54	151" × 105"	350	Dkc	$\beta\gamma$	D.39 on page 60(l)
769	0833	20150825_103138	12403	Fast	323	-366	0.86	78	219" × 107"	930	Fkc	$\beta\gamma\delta$	D.39 on page 60(m)
770	0834	20150825_120006	12403	Fast	332	-366	0.86	78	218" × 104"	930	Fkc	$\beta\gamma\delta$	D.39 on page 60(n)
771	0835	20150825_134505	12403	Fast	540	-348	0.82	25	88" × 87"	930	Fkc	$\beta\gamma\delta$	D.39 on page 60(o)
772	0836	20150825_145006	12403	Fast	345	-365	0.85	78	228" × 106"	930	Fkc	$\beta\gamma\delta$	D.39 on page 60(p)
773	0837	20150825_182005	12403	Fast	375	-363	0.84	78	224" × 109"	930	Fkc	$\beta\gamma\delta$	D.39 on page 60(q)
774	0838	20150825_200005	12403	Fast	395	-362	0.83	78	215" × 107"	930	Fkc	$\beta\gamma\delta$	D.39 on page 60(r)
775	0839	20150825_231006	12403	Fast	415	-361	0.82	78	223" × 109"	930	Fkc	$\beta\gamma\delta$	D.39 on page 60(s)
776	0840	20150826_022005	12403	Fast	443	-360	0.80	78	221" × 111"	1190	Fki	$\beta\gamma\delta$	D.39 on page 60(t)
777	0841	20150826_053005	12403	Fast	466	-359	0.79	78	216" × 108"	1190	Fki	$\beta\gamma\delta$	D.40 on page 61(a)
778	0842	20150826_083510	12403	Fast	517	-374	0.78	60	172" × 110"	1190	Fki	$\beta\gamma\delta$	D.40 on page 61(b)
779	0843	20150826_100505	12403	Fast	533	-373	0.77	60	173" × 113"	1190	Fki	$\beta\gamma\delta$	D.40 on page 61(c)
780	0844	20150826_113005	12403	Fast	543	-372	0.76	60	170" × 112"	1190	Fki	$\beta\gamma\delta$	D.40 on page 61(d)
781	0845	20150826_130005	12403	Fast	560	-371	0.75	60	171" × 116"	1190	Fki	$\beta\gamma\delta$	D.40 on page 61(e)
782	0846	20150826_171351	12403	Fast	537	-369	0.77	25	75" × 97"	1190	Fki	$\beta\gamma\delta$	D.40 on page 61(f)
783	0847	20150826_234235	12403	Fast	637	-364	0.69	70	170" × 119"	1190	Fki	$\beta\gamma\delta$	D.40 on page 61(g)
784	0849	20150827_192810	12403	Fast	810	-281	0.50	25	79" × 85"	1100	Fkc	$\beta\gamma\delta$	D.40 on page 61(h)
785	0850	20150916_110553	12415	Fast	-137	-427	0.87	24	95" × 65"	150	Cai	$\beta\gamma$	D.40 on page 61(i)
786	0851	20150917_102655	12415	Fast	102	-418	0.87	18	107" × 58"	190	Dac	$\beta\gamma$	D.40 on page 61(j)
787	0852	20150926_180815	12422	Fast	-44	-421	0.88	67	196" × 103"	310	Eko	$\beta\gamma$	D.40 on page 61(k)
788	0853	20150927_000005	12422	Fast	8	-428	0.88	60	207" × 89"	410	Ekc	$\beta\gamma\delta$	D.40 on page 61(l)
789	0854	20150927_050004	12422	Fast	50	-431	0.88	60	203" × 95"	410	Ekc	$\beta\gamma\delta$	D.40 on page 61(m)
790	0855	20150927_110515	12422	Fast	99	-420	0.87	60	196" × 87"	410	Ekc	$\beta\gamma\delta$	D.40 on page 61(n)
791	0856	20150927_140004	12422	Fast	124	-422	0.87	60	197" × 92"	410	Ekc	$\beta\gamma\delta$	D.40 on page 61(o)
792	0857	20150927_170004	12422	Fast	152	-426	0.86	60	199" × 95"	410	Ekc	$\beta\gamma\delta$	D.40 on page 61(p)
793	0858	20150927_230004	12422	Fast	199	-429	0.85	60	200" × 98"	410	Ekc	$\beta\gamma\delta$	D.40 on page 61(q)
794	0859	20150928_051504	12422	Fast	249	-432	0.84	66	193" × 103"	650	Ekc	$\beta\gamma\delta$	D.40 on page 61(r)
795	0860	20150928_110523	12422	Fast	299	-416	0.82	72	200" × 102"	650	Ekc	$\beta\gamma\delta$	D.40 on page 61(s)

Table D.1: continued.

index	inv_id	obs_id (date)_(time)	NOAA AR num	type scan	x_c (")	y_c (")	μ	num tiles	size FOV	area (MSH)	Zürich class	magnetic class	Fig. (panel)
796	0861	20150928_140004	12422	Fast	322	-419	0.82	72	197" × 108"	650	Ekc	$\beta\gamma\delta$	D.40 on page 61(t)
797	0862	20150928_171504	12422	Fast	346	-418	0.81	72	202" × 111"	650	Ekc	$\beta\gamma\delta$	D.41 on page 62(a)
798	0863	20150929_000003	12422	Fast	398	-417	0.78	72	203" × 116"	690	Fkc	$\beta\gamma\delta$	D.41 on page 62(b)
799	0864	20150929_044003	12422	Fast	432	-417	0.76	84	203" × 119"	690	Fkc	$\beta\gamma\delta$	D.41 on page 62(c)
800	0865	20150929_181615	12422	Fast	565	-395	0.69	66	183" × 115"	690	Fkc	$\beta\gamma\delta$	D.41 on page 62(d)
801	0866	20150929_210042	12422	Fast	583	-396	0.68	66	183" × 113"	690	Fkc	$\beta\gamma\delta$	D.41 on page 62(e)
802	0867	20150930_001534	12422	Fast	605	-391	0.66	66	195" × 112"	950	Fkc	$\beta\gamma\delta$	D.41 on page 62(f)
803	0868	20150930_033005	12422	Fast	623	-388	0.64	66	182" × 113"	950	Fkc	$\beta\gamma\delta$	D.41 on page 62(g)
804	0869	20150930_064004	12422	Fast	645	-389	0.62	70	175" × 119"	950	Fkc	$\beta\gamma\delta$	D.41 on page 62(h)
805	0870	20150930_120004	12422	Fast	670	-385	0.59	60	176" × 113"	950	Fkc	$\beta\gamma\delta$	D.41 on page 62(i)
806	0871	20150930_132025	12422	Fast	636	-385	0.63	65	227" × 92"	950	Fkc	$\beta\gamma\delta$	D.41 on page 62(j)
807	0872	20150930_183541	12422	Fast	702	-379	0.55	60	166" × 111"	950	Fkc	$\beta\gamma\delta$	D.41 on page 62(k)
808	0873	20150930_233004	12422	Fast	726	-375	0.52	60	167" × 112"	950	Fkc	$\beta\gamma\delta$	D.41 on page 62(l)
809	0874	20151103_141549	12443	Fast	-153	60	0.98	55	191" × 89"	590	Fkc	$\beta\delta$	D.41 on page 62(m)
810	0875	20151103_160105	12443	Fast	-196	38	0.98	35	111" × 81"	590	Fkc	$\beta\delta$	D.41 on page 62(n)
811	0876	20151103_210505	12443	Fast	-149	41	0.99	28	109" × 78"	590	Fkc	$\beta\delta$	D.41 on page 62(o)
812	0877	20151103_225005	12443	Fast	-130	47	0.99	24	108" × 71"	590	Fkc	$\beta\delta$	D.41 on page 62(p)
813	0878	20151104_011005	12443	Fast	-91	44	0.99	24	97" × 74"	560	Fkc	$\beta\delta$	D.41 on page 62(q)
814	0879	20151216_170513	12470	Fast	-475	221	0.83	16	66" × 73"	610	Eko	β	D.41 on page 62(r)
815	0880	20151216_200611	12470	Fast	-534	251	0.80	84	201" × 121"	610	Eko	β	D.41 on page 62(s)
816	0881	20151217_002935	12470	Fast	-504	254	0.82	72	208" × 115"	530	Eko	β	D.41 on page 62(t)
817	0882	20151217_040005	12470	Fast	-478	258	0.84	72	209" × 115"	530	Eko	β	D.42 on page 63(a)
818	0883	20151217_065605	12470	Fast	-458	257	0.85	72	202" × 117"	530	Eko	β	D.42 on page 63(b)
819	0884	20151217_083304	12470	Fast	-444	259	0.86	84	205" × 118"	530	Eko	β	D.42 on page 63(c)
820	0885	20151224_092605	12473	Fast	-612	-325	0.65	60	173" × 99"	420	Ekc	$\beta\gamma$	D.42 on page 63(d)
821	0886	20151224_150016	12473	Fast	-604	-322	0.68	66	182" × 102"	420	Ekc	$\beta\gamma$	D.42 on page 63(e)
822	0887	20151224_182135	12473	Fast	-556	-321	0.71	55	189" × 96"	420	Ekc	$\beta\gamma$	D.42 on page 63(f)
823	0888	20151225_110004	12473	Fast	-443	-325	0.80	78	220" × 102"	500	Ekc	$\beta\gamma$	D.42 on page 63(g)
824	0889	20151225_153204	12473	Fast	-411	-322	0.82	78	226" × 110"	500	Ekc	$\beta\gamma$	D.42 on page 63(h)
825	0890	20151226_061533	12473	Fast	-298	-318	0.87	78	229" × 109"	570	Ekc	$\beta\gamma$	D.42 on page 63(i)
826	0891	20151226_090003	12473	Fast	-277	-319	0.88	84	233" × 109"	570	Ekc	$\beta\gamma$	D.42 on page 63(j)
827	0892	20151226_120003	12473	Fast	-108	-292	0.91	35	117" × 83"	570	Ekc	$\beta\gamma$	D.42 on page 63(k)
828	0893	20151226_181332	12473	Fast	-202	-313	0.91	84	231" × 109"	570	Ekc	$\beta\gamma$	D.42 on page 63(l)
829	0894	20151226_210003	12473	Fast	-185	-308	0.91	84	234" × 106"	570	Ekc	$\beta\gamma$	D.42 on page 63(m)
830	0895	20151227_000003	12473	Fast	-157	-310	0.92	84	236" × 106"	590	Fkc	$\beta\gamma\delta$	D.42 on page 63(n)
831	0896	20151227_030703	12473	Fast	-131	-306	0.92	84	236" × 103"	590	Fkc	$\beta\gamma\delta$	D.42 on page 63(o)
832	0897	20151228_003002	12473	Fast	50	-307	0.94	78	223" × 109"	530	Fhc	$\beta\delta$	D.42 on page 63(p)
833	0898	20151229_113620	12473	Fast	449	-280	0.87	50	169" × 87"	510	Fhc	$\beta\delta$	D.42 on page 63(q)
834	0899	20151230_080545	12473	Fast	691	-281	0.75	24	98" × 76"	470	Fhc	β	D.42 on page 63(r)
835	0900	20160211_224006	12497	Fast	81	345	0.95	65	217" × 88"	240	Eac	$\beta\gamma$	D.42 on page 63(s)
836	0901	20160212_013506	12497	Fast	109	343	0.94	60	200" × 93"	180	Eac	$\beta\gamma\delta$	D.42 on page 63(t)
837	0902	20160212_195805	12497	Fast	393	336	0.90	32	140" × 73"	180	Eac	$\beta\gamma\delta$	D.43 on page 64(a)
838	0903	20160212_231005	12497	Fast	428	334	0.89	32	136" × 71"	180	Eac	$\beta\gamma\delta$	D.43 on page 64(b)
839	0904	20160213_021005	12497	Fast	451	331	0.88	32	139" × 71"	250	Eac	$\beta\gamma\delta$	D.43 on page 64(c)
840	0905	20160213_070005	12497	Fast	498	333	0.87	32	136" × 65"	250	Eac	$\beta\gamma\delta$	D.43 on page 64(d)
841	0906	20160213_101204	12497	Fast	479	328	0.85	44	181" × 74"	250	Eac	$\beta\gamma\delta$	D.43 on page 64(e)
842	0907	20160214_110104	12497	Fast	677	301	0.72	45	158" × 84"	220	Eac	$\beta\gamma\delta$	D.43 on page 64(f)
843	0908	20160215_001040	12497	Fast	767	288	0.64	40	139" × 83"	200	Eac	$\beta\gamma\delta$	D.43 on page 64(g)
844	0909	20160215_120103	12497	Fast	862	284	0.54	28	109" × 79"	200	Eac	$\beta\gamma\delta$	D.43 on page 64(h)
845	0910	20160410_000205	12529	Fast	-783	229	0.51	42	120" × 105"	820	Ehi	β	D.43 on page 64(i)
846	0911	20160410_120405	12529	Fast	-728	237	0.61	48	135" × 107"	820	Ehi	β	D.43 on page 64(j)
847	0912	20160410_150604	12529	Fast	-707	237	0.63	48	140" × 110"	820	Ehi	β	D.43 on page 64(k)

Table D.1: continued.

index	inv_id	obs_id (date)_(time)	NOAA AR num	type scan	x_c (")	y_c (")	μ	num tiles	size FOV	area (MSH)	Zürich class	magnetic class	Fig. (panel)
848	0913	20160410_183420	12529	Nor.	-678	226	0.67	143	111" × 100"	820	Ehi	β	D.43 on page 64(l)
849	0914	20160412_000504	12529	Fast	-469	272	0.84	45	154" × 91"	850	Eki	β	D.43 on page 64(m)
850	0915	20160412_042303	12529	Fast	-433	272	0.86	45	150" × 96"	850	Eki	β	D.43 on page 64(n)
851	0916	20160412_123504	12529	Fast	-284	271	0.89	60	177" × 99"	850	Eki	β	D.43 on page 64(o)
852	0917	20160412_180021	12529	Fast	-215	273	0.92	25	82" × 95"	850	Eki	β	D.43 on page 64(p)
853	0918	20160412_210905	12529	Fast	-198	274	0.93	25	89" × 92"	850	Eki	β	D.43 on page 64(q)
854	0919	20160413_001305	12529	Fast	-146	272	0.94	25	75" × 95"	800	Eho	β	D.43 on page 64(r)
855	0920	20160413_032105	12529	Fast	-129	276	0.94	25	80" × 89"	800	Eho	β	D.43 on page 64(s)
856	0921	20160413_050705	12529	Fast	-108	277	0.95	25	75" × 92"	800	Eho	β	D.43 on page 64(t)
857	0922	20160413_183219	12529	Fast	90	269	0.96	42	112" × 103"	800	Eho	β	D.44 on page 65(a)
858	0923	20160413_201103	12529	Fast	35	277	0.96	20	71" × 95"	800	Eho	β	D.44 on page 65(b)
859	0924	20160414_022103	12529	Fast	172	276	0.97	30	107" × 95"	780	Eko	β	D.44 on page 65(c)
860	0925	20160414_053304	12529	Fast	105	276	0.97	25	82" × 93"	780	Eko	β	D.44 on page 65(d)
861	0926	20160414_124504	12529	Fast	163	274	0.96	60	169" × 105"	780	Eko	β	D.44 on page 65(e)
862	0927	20160414_181520	12529	Fast	207	274	0.96	45	152" × 97"	780	Eko	β	D.44 on page 65(f)
863	0928	20160415_000104	12529	Fast	260	269	0.94	31	91" × 104"	790	Eki	β	D.44 on page 65(g)
864	0929	20160416_031518	12529	Fast	595	257	0.84	42	119" × 99"	740	Eki	$\beta\gamma$	D.44 on page 65(h)
865	0930	20160416_060302	12529	Fast	544	256	0.84	20	73" × 96"	740	Eki	$\beta\gamma$	D.44 on page 65(i)
866	0931	20160416_070005	12529	Fast	541	257	0.83	25	82" × 98"	740	Eki	$\beta\gamma$	D.44 on page 65(j)
867	0932	20160416_184203	12529	Fast	587	255	0.80	72	205" × 115"	740	Eki	$\beta\gamma$	D.44 on page 65(k)
868	0933	20160416_220005	12529	Fast	675	256	0.76	45	146" × 88"	740	Eki	$\beta\gamma$	D.44 on page 65(l)
869	0934	20160510_080133	12542	Fast	84	248	0.98	15	76" × 50"	150	Dai	$\beta\gamma$	D.44 on page 65(m)
870	0935	20160513_130705	12542	Fast	664	175	0.72	20	59" × 90"	160	Dai	$\beta\gamma$	D.44 on page 65(n)
871	0937	20160720_010205	12567	Fast	385	0	0.91	28	120" × 79"	390	Dki	$\beta\gamma$	D.44 on page 65(o)
872	0938	20160720_041105	12565+12567	Fast	411	1	0.90	35	120" × 81"	300+390	Cko+Dki	$\beta+\beta\gamma$	D.44 on page 65(p)
873	0939	20160720_091551	12565+12567	Fast	519	4	0.83	45	151" × 81"	300+390	Cko+Dki	$\beta+\beta\gamma$	D.44 on page 65(q)
874	0940	20160720_223047	12565+12567	Fast	616	4	0.76	45	150" × 83"	300+390	Cko+Dki	$\beta+\beta\gamma$	D.44 on page 65(r)
875	0941	20160721_000005	12565+12567	Fast	628	5	0.74	36	149" × 79"	310+510	Cko+Dki	$\beta+\beta$	D.44 on page 65(s)
876	0942	20160721_014005	12565+12567	Fast	637	0	0.74	40	139" × 86"	310+510	Cko+Dki	$\beta+\beta$	D.44 on page 65(t)
877	0943	20160721_181004	12565+12567	Fast	796	14	0.65	50	166" × 84"	310+510	Cko+Dki	$\beta+\beta$	D.45 on page 66(a)
878	0945	20160722_233504	12565+12567	Nor.	879	31	0.43	60	102" × 95"	250+380	Hkx+Dki	$\alpha+\beta\gamma$	D.45 on page 66(b)
879	0946	20160903_074908	12585	Nor.	-593	34	0.77	162	152" × 81"	460	Ekc	$\beta\gamma$	D.45 on page 66(c)
880	0947	20160903_104306	12585	Nor.	-571	34	0.79	162	150" × 82"	460	Ekc	$\beta\gamma$	D.45 on page 66(d)
881	0948	20161011_144054	12599	Fast	502	-346	0.80	20	81" × 71"	250	Cko	β	D.45 on page 66(e)
882	0949	20161011_160006	12599	Fast	508	-326	0.80	15	82" × 55"	250	Cko	β	D.45 on page 66(f)
883	0950	20161011_192106	12599	Fast	533	-320	0.78	15	79" × 49"	250	Cko	β	D.45 on page 66(g)
884	0951	20161012_132104	12599	Fast	656	-313	0.69	12	68" × 50"	270	Cko	β	D.45 on page 66(h)
885	0952	20161012_152005	12599	Fast	673	-314	0.68	12	70" × 51"	270	Cko	β	D.45 on page 66(i)
886	0953	20161130_130006	12615	Fast	-646	-88	0.69	18	94" × 61"	30	Dsi	β	D.45 on page 66(j)
887	0954	20161203_184119	12615	Fast	129	-80	0.99	15	79" × 59"	110	Dao	β	D.45 on page 66(k)
888	0955	20161204_001834	12615	Fast	106	-82	0.99	12	69" × 55"	140	Dai	β	D.45 on page 66(l)
889	0956	20170401_061405	12645	Fast	-19	-50	1.00	36	151" × 64"	380	Ekc	$\beta\gamma$	D.45 on page 66(m)
890	0957	20170401_090005	12645	Fast	5	-53	1.00	36	150" × 64"	380	Ekc	$\beta\gamma$	D.45 on page 66(n)
891	0958	20170401_110049	12645	Fast	79	-39	1.00	65	229" × 84"	380	Ekc	$\beta\gamma$	D.45 on page 66(o)
892	0959	20170403_100542	12645	Fast	495	-62	0.87	65	218" × 82"	600	Ehc	$\beta\gamma\delta$	D.45 on page 66(p)
893	0960	20170403_173711	12645	Fast	40	34	1.00	52	216" × 78"	600	Ehc	$\beta\gamma\delta$	D.45 on page 66(q)
894	0961	20170404_000104	12645	Fast	602	-62	0.80	48	205" × 77"	700	Ekc	$\beta\gamma\delta$	D.45 on page 66(r)
895	0962	20170420_071538	12651	Nor.	-762	257	0.55	35	42" × 59"	110	Dao	β	D.45 on page 66(s)
896	0963	20170603_190143	12661	Fast	-576	102	0.71	24	140" × 51"	200	Dao	β	D.45 on page 66(t)
897	0964	20170708_230346	12665	Fast	-593	-156	0.74	45	151" × 87"	310	Ekc	β	D.46 on page 67(a)

Table D.1: continued.

index	inv_id	obs_id (date)_(time)	NOAA AR num	type scan	x_c ($''$)	y_c ($''$)	μ	num tiles	size FOV	area (MSH)	Zürich class	magnetic class	Fig. (panel)
898	0965	20170709_233834	12665	Fast	-404	-177	0.87	60	174'' × 99''	480	Ekc	β	D.46 on page 67(b)
899	0966	20170711_114358	12665	Fast	-90	-177	0.97	65	217'' × 84''	690	Ekc	$\beta\gamma$	D.46 on page 67(c)
900	0967	20170714_232204	12665	Fast	748	-169	0.69	36	97'' × 107''	440	Ehi	β	D.46 on page 67(d)
901	0968	20170817_160006	12671	Fast	-615	114	0.76	65	223'' × 87''	380	Ehc	$\beta\gamma\delta$	D.46 on page 67(e)
902	0969	20170817_203005	12671	Fast	-579	113	0.79	65	228'' × 85''	380	Ehc	$\beta\gamma\delta$	D.46 on page 67(f)
903	0970	20170819_083144	12671	Fast	-232	84	0.96	56	234'' × 76''	410	Fkc	$\beta\gamma$	D.46 on page 67(g)
904	0971	20170819_115106	12671	Fast	-192	64	0.97	52	216'' × 72''	410	Fkc	$\beta\gamma$	D.46 on page 67(h)
905	0972	20170822_171104	12672	Fast	-732	38	0.60	49	115'' × 120''	160	Dao	β	D.46 on page 67(i)
906	0973	20170823_061405	12672	Fast	-650	31	0.70	48	126'' × 116''	270	Dao	β	D.46 on page 67(j)
907	0974	20170823_224005	12672	Fast	-502	20	0.81	54	148'' × 114''	270	Dao	β	D.46 on page 67(k)
908	0975	20170905_030404	12674	Fast	135	79	0.99	25	91'' × 84''	740	Fhi	β	D.46 on page 67(l)
909	0976	20170905_105108	12673	Fast	352	-254	0.90	56	128'' × 132''	680	Dkc	$\beta\gamma\delta$	D.46 on page 67(m)
910	0977	20170905_140006	12673	Fast	378	-252	0.88	56	128'' × 131''	680	Dkc	$\beta\gamma\delta$	D.46 on page 67(n)
911	0978	20170905_160006	12673	Fast	400	-250	0.88	56	127'' × 136''	680	Dkc	$\beta\gamma\delta$	D.46 on page 67(o)
912	0979	20170905_180902	12673	Fast	417	-250	0.87	56	128'' × 135''	680	Dkc	$\beta\gamma\delta$	D.46 on page 67(p)
913	0980	20170906_000205	12673	Nor.	470	-247	0.84	180	125'' × 110''	880	Dkc	$\beta\gamma\delta$	D.46 on page 67(q)
914	0981	20170906_061405	12673	Fast	512	-244	0.81	56	127'' × 134''	880	Dkc	$\beta\gamma\delta$	D.46 on page 67(r)
915	0982	20170906_090339	12673	Fast	516	-242	0.80	42	109'' × 104''	880	Dkc	$\beta\gamma\delta$	D.46 on page 67(s)
916	0984	20170906_120847	12673	Nor.	547	-240	0.79	144	105'' × 110''	880	Dkc	$\beta\gamma\delta$	D.46 on page 67(t)
917	0985	20170906_161754	12673	Fast	593	-237	0.76	49	119'' × 130''	880	Dkc	$\beta\gamma\delta$	D.47 on page 68(a)
918	0986	20170906_174028	12673	Fast	558	-237	0.77	20	68'' × 89''	880	Dkc	$\beta\gamma\delta$	D.47 on page 68(b)
919	0987	20170906_181045	12673	Fast	586	-236	0.75	36	109'' × 107''	880	Dkc	$\beta\gamma\delta$	D.47 on page 68(c)
920	0988	20170906_183650	12673	Fast	605	-235	0.75	49	115'' × 127''	880	Dkc	$\beta\gamma\delta$	D.47 on page 68(d)
921	0989	20170906_191722	12673	Fast	592	-236	0.74	36	108'' × 107''	880	Dkc	$\beta\gamma\delta$	D.47 on page 68(e)
922	0990	20170907_000129	12673	Fast	623	-233	0.72	42	112'' × 107''	960	Ekc	$\beta\gamma\delta$	D.47 on page 68(f)
923	0991	20170907_002734	12673	Fast	646	-231	0.71	56	113'' × 140''	960	Ekc	$\beta\gamma\delta$	D.47 on page 68(g)
924	0992	20170907_031405	12673	Fast	662	-229	0.70	42	108'' × 129''	960	Ekc	$\beta\gamma\delta$	D.47 on page 68(h)
925	0993	20170907_050218	12673	Fast	633	-228	0.71	20	64'' × 92''	960	Ekc	$\beta\gamma\delta$	D.47 on page 68(i)
926	0994	20170907_064318	12673	Fast	688	-226	0.67	42	109'' × 124''	960	Ekc	$\beta\gamma\delta$	D.47 on page 68(j)
927	0995	20170907_100004	12673	Fast	705	-224	0.65	49	109'' × 129''	960	Ekc	$\beta\gamma\delta$	D.47 on page 68(k)
928	0996	20170907_112906	12673	Nor.	697	-249	0.64	144	99'' × 111''	960	Ekc	$\beta\gamma\delta$	D.47 on page 68(l)
929	0997	20170907_143319	12673	Fast	693	-246	0.63	28	63'' × 118''	960	Ekc	$\beta\gamma\delta$	D.47 on page 68(m)
930	0998	20170907_144813	12673	Fast	722	-246	0.61	56	111'' × 152''	960	Ekc	$\beta\gamma\delta$	D.47 on page 68(n)
931	0999	20170907_164809	12673	Fast	734	-244	0.60	48	106'' × 150''	960	Ekc	$\beta\gamma\delta$	D.47 on page 68(o)
932	1000	20170907_182845	12673	Fast	734	-242	0.58	42	100'' × 120''	960	Ekc	$\beta\gamma\delta$	D.47 on page 68(p)
933	1001	20170907_185450	12673	Nor.	740	-241	0.59	120	88'' × 109''	960	Ekc	$\beta\gamma\delta$	D.47 on page 68(q)
934	1002	20170907_202403	12673	Fast	710	-240	0.62	12	30'' × 102''	960	Ekc	$\beta\gamma\delta$	D.47 on page 68(r)
935	1003	20170908_001907	12673	Fast	767	-238	0.54	42	93'' × 121''	1000	Ekc	$\beta\gamma\delta$	D.47 on page 68(s)
936	1004	20170908_004457	12673	Fast	785	-237	0.54	42	93'' × 121''	1000	Ekc	$\beta\gamma\delta$	D.47 on page 68(t)
937	1005	20170908_011519	12673	Fast	783	-234	0.54	40	82'' × 142''	1000	Ekc	$\beta\gamma\delta$	D.48 on page 69(a)
938	1006	20170908_090038	12673	Fast	816	-229	0.47	35	81'' × 120''	1000	Ekc	$\beta\gamma\delta$	D.48 on page 69(b)
939	1007	20170908_163731	12673	Fast	845	-221	0.42	35	79'' × 118''	1000	Ekc	$\beta\gamma\delta$	D.48 on page 69(c)
940	1008	20190322_002307	12736	Fast	703	201	0.67	35	122'' × 93''	210	Dac	$\beta\gamma\delta$	D.48 on page 69(d)
941	1009	20190322_010205	12736	Fast	789	221	0.66	35	117'' × 92''	210	Dac	$\beta\gamma\delta$	D.48 on page 69(e)
942	1010	20190322_061746	12736	Fast	744	189	0.62	42	118'' × 100''	210	Dac	$\beta\gamma\delta$	D.48 on page 69(f)